



DIGITAL ACCESS TO SCHOLARSHIP AT HARVARD

Chemical Probes and the Exploration of Bromodomains in Cancer Biology

The Harvard community has made this article openly available.
[Please share](#) how this access benefits you. Your story matters.

| | |
|---------------------|--|
| Citation | McKeown, Michael Robert. 2014. Chemical Probes and the Exploration of Bromodomains in Cancer Biology. Doctoral dissertation, Harvard University. |
| Accessed | April 17, 2018 4:58:26 PM EDT |
| Citable Link | http://nrs.harvard.edu/urn-3:HUL.InstRepos:12269851 |
| Terms of Use | This article was downloaded from Harvard University's DASH repository, and is made available under the terms and conditions applicable to Other Posted Material, as set forth at http://nrs.harvard.edu/urn-3:HUL.InstRepos:dash.current.terms-of-use#LAA |

(Article begins on next page)

Chemical Probes and the Exploration of Bromodomains in Cancer Biology

A dissertation presented
by
Michael Robert McKeown
to
The Chemical Biology PhD Program

in partial fulfillment of the requirements
for the degree of
Doctor of Philosophy
in the subject of
Chemical Biology

Harvard University
Cambridge, Massachusetts

April 2014

© 2014. Michael Robert McKeown
All Rights Reserved.

Chemical Probes and the Exploration of Bromodomains in Cancer Biology

Abstract:

The post-translational modification of histones and their interaction with transcription factors is essential to gene regulation. Furthermore, these targets would greatly benefit from probe molecules to fully elucidate their biological actions and to potentially lead to therapeutics. However, these protein-protein interactions have been considered difficult to inhibit and few high-quality chemical probes currently exist for the study of epigenetic biological systems in particular.

The bromodomain and extra-terminal (BET) domain family are readers of acetyl lysine marks on histones and some nuclear proteins. They share a common domain architecture comprising two N-terminal bromodomains which exhibit high levels of sequence conservation. BETs are important to transcription in a number of systems, especially transcriptional elongation, making them interesting targets for biological investigation and cancer therapeutics. My work developed and improved direct inhibitors of these targets. Here we present an improved derivative, JQ35, and novel chemistry for targeting BETs and other bromodomains.

Overexpression of *MYC* has been detected in 30% of all human cancers and, in many cases, correlates with aggressive cancers of poor clinical outcome and increased frequency of relapse. While *MYC* can have a restrictive effect on cell growth under

normal conditions of tight regulation, it contributes to all six hallmarks of cancer when deregulated by amplification, translocation, enhancer mutation, or aberrant expression. Thus, we engaged in a deep literature search for strategies to inhibit MYC as well as an effort to develop novel direct inhibitors.

Diffuse Large B-Cell Lymphoma is the most common non-Hodgkin lymphoma accounting for 30-40% of new cases. The heterogeneity of this disease makes treatment difficult with remission in 40-50% of patients while others suffer from aggressive progression. Collaborative research from our group and others has recently identified a role for BET bromodomains in supporting the transcription of known DLBCL oncogenes (*MYC* and *BCL2*) in studies of acute leukemia, multiple myeloma and Burkitt lymphoma. Interestingly, overexpression of *BRD2* from an engineered immunoglobulin heavy-chain promoter-enhancer construct caused an aggressive B-cell neoplasm resembling DLBCL in mice. Therefore, we embarked on a study of the efficacy and mechanisms of bromodomain inhibition in DLBCL.

Table of Contents

| <u>Section</u> | <u>Page</u> |
|--|-------------|
| Abstract | iii |
| Table of Contents | iv |
| List of Figures | vi |
| List of Tables | ix |
| List of Schemes | x |
| Acknowledgements | xi |
| Introduction | 1 |
| Chapter 1 Development of an Improved BET Inhibitor for In Vivo and Human Trials | 6 |
| Chapter 2 Development of Novel 3,5-Dimethylisoxazoles as Selective Inhibitors of BET-bromodomain proteins | 54 |
| Chapter 3 Therapeutic Strategies to Inhibit MYC | 99 |
| Chapter 4 Disruption of Super Enhancer-Driven Cancer Dependencies in Diffuse Large B-Cell Lymphoma | 144 |

| <u>List of Figures</u> | <u>Page</u> |
|--|-------------|
| Figure 1.1 BET inhibitors and synthetic strategy | 12 |
| Figure 1.2 Biochemical screening assay | 14 |
| Figure 1.3 Assay optimization | 15 |
| Figure 1.4 Assay performance | 16 |
| Figure 1.5 Dose response of chemical probes | 17 |
| Figure 1.6 Medicinal chemistry regions | 22 |
| Figure 1.7 Lead Series | 35 |
| Figure 1.8 Lead series dose response | 37 |
| Figure 1.9 JQ35 crystal structure | 39 |
| Figure 1.10 Gene Expression | 42 |
| Figure 1.11 Additional ChIP-seq | 44 |
| Figure 1.12 <i>In vivo</i> studies | 47 |
| Figure 2.1 Approach to chemistry | 60 |
| Figure 2.2 Lead series biochemistry | 67 |
| Figure 3.1 Assay optimization for cMYC dependent signal | 105 |
| Figure 3.2 Z-prime analysis for assay robustness | 106 |
| Figure 3.3 MYC Screening | 107 |
| Figure 3.4 MYC dose response | 109 |
| Figure 3.5 Structural studies of MYC | 117 |
| Figure 3.6 Small molecule inhibitors of MYC | 120 |
| Figure 3.7 A model of MYC transcriptional complex | 124 |

| | | |
|--------------------|--|-----|
| Figure 3.8 | The MYC protein interactome | 127 |
| Figure 4.1 | <i>In vitro</i> analyses of BET Bromodomain inhibition in various B-cell lymphomas | 154 |
| Figure 4.2 | Dose response curves, assessment of apoptosis, and an additional xenograft model of JQ1 treatment | 158 |
| Figure 4.3 | Transcriptional modulation | 161 |
| Figure 4.4 | Transcriptional response to BET inhibition in representative DLBCL cell lines | 169 |
| Figure 4.5 | Visualization of leading edge E2F1-target genes in all cell lines and knockdown of E2F1 in representative DLBCL cell lines | 173 |
| Figure 4.6 | Co-localization and function of BRD4 and E2F1 at active promoters | 177 |
| Figure 4.7 | Asymmetric BRD4 loading at enhancer elements of actively transcribed genes | 180 |
| Figure 4.8 | Modulation of BRD4 loading at <i>CD79B</i> and <i>MYC</i> enhancers following JQ1 treatment | 183 |
| Figure 4.9 | Modulation of BRD4 super-loading at the <i>POU2AF1</i> locus following JQ1 treatment | 185 |
| Figure 4.10 | OCA-B abundance and target genes in DLBCL cell lines treated with JQ1 | 187 |
| Figure 4.11 | Modulation of super-enhancers of B-cell transcription factors following JQ1 treatment | 189 |
| Figure 4.12 | JQ1 effect on the <i>BCL6</i> locus | 191 |
| Figure 4.13 | Analysis of super enhancers in additional DLBCL cell lines and normal lymphoid | 193 |
| Figure 4.14 | H3K27ac tracks of <i>POU2AF1</i> locus, GSEA plots of germinal center B-cell signature in individual cell lines and unsupervised hierarchical clustering of super-enhancers in DLBCL cell lines. | 195 |

| | |
|--|-----|
| Figure 4.15 Analysis of super enhancers in primary DLBCLs | 198 |
| Figure 4.16 Unsupervised hierarchical clustering of super-enhancers in four primary DLBCL samples | 200 |

| <u>List of Tables</u> | <u>Page</u> |
|---|-------------|
| Table 1.1 Known bromodomain inhibitors | 20 |
| Table 1.2 Medicinal chemistry series | 23 |
| Table 2.1 Exploration of compounds scaffold region | 63 |
| Table 2.2 Elaboration of imidazopyridine scaffold | 65 |
| Table 2.3 Variations to UMB-32 linker | 69 |
| Table 3.1 MYC pathway and regulator inhibitors | 129 |

| <u>List of Schemes</u> | <u>Page</u> |
|---|-------------|
| Scheme 2.1 Synthesis of UMB11 near analogs | 64 |
| Scheme 2.2 General procedures for the synthesis of UMB-6, -11, -20, -21, -23, -25, -28 to -32, -56, -57, -60 to -62, -65, -76, -82, and -83 | 73 |
| Scheme 2.3 Procedures for the synthesis of ethyl-3-(4-(3,5-dimethylisoxazol-4-yl)phenyl)-5-ethyl-1-methyl-4,6-dioxooctahydropyrrolo[3,4-c]pyrrole-1-carboxylate UMB-17 | 78 |
| Scheme 2.4 Procedures for the synthesis of UMB-1, -2, -3, -4, -8, -9, -10, -12, and -15 | 79 |
| Scheme 2.5 Synthesis of Ethyl-2-(N-(4-(3,5-dimethylisoxazol-4-yl)benzyl)-4-methoxybenzamido)-propanoate UMB-5 | 81 |
| Scheme 2.6 Synthesis of 4-butyl-3-(4-(3,5-dimethylisoxazol-4-yl)-3-methoxyphenyl)-3,4-dihydro-1H-benzo[e][1,4]diazepine-2,5-dione UMB-18 | 82 |
| Scheme 2.7 Synthesis of 10-(3-(3,5-dimethylisoxazol-4-yl)phenyl)-3,4,9,10-tetrahydro-1H-benzo[b]furo[3,4-e][1,4]diazepin-1-one UMB-27 | 83 |
| Scheme 2.8 Synthesis of UMB-13 and UMB-14 | 84 |
| Scheme 2.9 General procedures for the synthesis of UMB-53 to -55, UMB-58 and -59 | 85 |
| Scheme 2.10 Synthesis of Ethyl 2-((2-(4-(3,5-dimethylisoxazol-4-yl)phenyl)imidazo[1,2-a]pyrazin-3-yl)amino)acetate (DB-1-038) | 86 |
| Scheme 2.11 tert-butyl 2-((2-(4-(3,5-dimethylisoxazol-4-yl)phenyl)imidazo[1,2-a]pyrazin-3-yl)amino)acetate (DB-1-057) | 88 |
| Scheme 3.1 Chemical Progression | 110 |

Acknowledgements

Science is no longer the purview of a lone monk laboring in the isolation of an ivory tower. The massive interdisciplinary endeavors of the chemical biology projects require more skill sets and hands than any one scientist could hope to supply. Moreover, the pressures, training, and support of each of those scientists necessitate a collaborative effort in their life to get them to and keep them in the lab. There are many more people to thank than I can cover, but I would like to highlight several.

First, I would like to thank my adviser, Dr. James Bradner, for his training, support, and leadership over the last several years. His vision for drug discovery and science have been an incredible learning experience. I would also like to thank the whole of the Bradner lab for their support academically, scientifically, and collegially. After five years, this is more a group of friends to me than a work place. Katharin not only put up with sitting next to me in lab and spending a ton of time together outside of lab, but honored me with a place in her wedding party.

I would like to thank my committee members: Drs. Jon Clardy, Tim Mitchison, and Ralph Mazitschek. They have lent me their advice and guidance over the course of my graduate school work and have helped chart my course moving forward. Furthermore, I have benefited from some wonderful collaborators and friends in the Shipp Lab, especially Bjoern Chapuy and Kelly Yeda. While Kelly was taken from us before getting to see the full fruits of our labor against lymphoma, she made a great contribution to science and was a good friend.

In addition, I would like to thank the Tsien lab at UC San Diego for giving me an amazing opportunity to do real-world lab science as an undergraduate. Dr. Roger Tsien is an inspirational figure that embodied all I could hope for as a scientist and Dr. Michael Lin was an outstanding mentor.

Also, thanks belong to all my teachers along the way. All of them have helped get me here, but I would like to especially single out my high school chemistry teachers Mrs. House and Mrs. Garfinkle for helping choose a field of study.

Finally, I would like to thank my friends and family. They have helped keep me on track with support to try harder and reminding me to have fun too. My parents instilled in me purpose, dedication, and fostered an early interest in science. Moreover, their support was crucial for college, Harvard, and beyond. I wish my father could read this and say it in person; I know that this accomplishment makes him proud.

Introduction:

The use of chemical probes in biological studies empowers researchers with the tools to manipulate and perturb a system to gain insights that would be difficult from interpreting still-life snapshots or totally deconstructed systems. However, there exists relatively few high-quality and selective chemical probes fit for this purpose. The lack of chemical probes available for the study of transcriptional regulation presents a barrier to understanding the dynamic events underlying cell identity and fate. Therefore, my work sought to discover, develop, and explore the ramifications of chemical probes in cancer. This involved screening to find compounds, medicinal chemistry to improve leads, and a variety of biological tools to investigate the biological systems related to the transcriptional regulatory proteins that I was targeting.

In my first major project in the Bradner lab, I contributed to the probe discovery and biological effort in Nut Midline Carcinoma (NMC) that led to JQ1¹, a first in class inhibitor of bromodomains used in cancer. Bromodomains are a family of proteins involved in the readout of the posttranslational mark of acetyl lysine primarily on nuclear factors and histones. In this breakthrough work, a cell-permeable small molecule, JQ1, was found that competitively binds to acetyl-lysine recognition motif of the BET subfamily of bromodomains. This probe was then deployed against NMC, which hosts a recurrent translocation of BRD3 or BRD4 forming a fusion protein and making it oncogenically addicted to BET bromodomain activity. It was found that inhibition by JQ1 displaces the BRD4 fusion oncoprotein from chromatin which leads to growth arrest and differentiation of these cells. Moreover, this established a rationale for the use of

bromodomain inhibition in cancer and provided an academic, open-source probe to the scientific community.

Next, I became involved in one of my most entertaining projects based on the observation that JQ1 could inhibit a BET subfamily bromodomain called BRDT², which shows tissue restriction to the testes. As of yet, a pharmacologic method for male contraception remains an elusive for biomedical research. To investigate the potential for inhibitors of epigenetic targets for this purpose, we explored the anti-spermatogenic effects of JQ1. Importantly, BRDT is essential for chromatin remodeling and compaction during spermatogenesis. It was found by biochemistry and crystallographic studies that JQ1 does indeed block the BRDT acetyl-lysine binding from engaging acetylated histone H4. In addition, dosing male mice with JQ1 reduced seminiferous tubule volume, testis mass, the quantity of spermatozoa, and the motility of sperm. Moreover, associated hormone levels were unchanged. JQ1 did not adversely affect mouse behavior but was found to reversibly confer a contraceptive effect on mice.

From these early projects, I engaged in several highly collaborative probe and drug discovery efforts in addition to building a stronger understanding of cancer biology by deploying these tools. By pairing probe development with cancer biology I could learn not just about the effects of the compounds, but about the nature of the cancer specific biology itself.

Chapter one covers the discovery of JQ35. This work presents a next-generation optimized BET bromodomain inhibitor with improved *in vivo* properties. In addition, I developed robust assays and using novel pull-down tools enabling further research on bromodomain biochemistry and biology. While the existing probe molecule JQ1 is

incredibly useful for interrogating biology in an academic setting, reaching improved, drug-like properties must be achieved to enable potential therapeutics. With the overall likelihood of approval in oncology is only 6.7% from Phase I trials³ and the dire need of new targeted therapies in oncology, we engaged in focused effort to build a second generation inhibitor from JQ1, with longer half-life, potency, and *in vivo* efficacy. In addition, this compound was utilized to investigate the nature of NMC, which remains a tumor of unknown origin⁴.

Chapter two describes efforts to develop alternative chemistries for bromodomain inhibition to empower new probes and to engage new targets. BET bromodomain inhibition has emerged as both a viable method to probe gene regulation and a promising therapeutic option in cancer treatment. As small molecule inhibitors of bromodomains begin clinical trials as anti-cancer drugs, there is an obvious opportunity and need for novel inhibitors to support medical advances and to elucidate the chemical biology of these proteins. Using pioneering, fluororous multicomponent reactions we have rapidly developed a chemical library of bromodomain inhibitors around a 3,5-dimethylisoxazole biasing element with an initial biochemical IC₅₀ of 16 μ M. A robust chemical screening and development program has allowed rapid optimization of novel and selective BET bromodomain pharmacophores with 637 nM biochemical potency and 724 nM cellular potency. In addition, these compounds show inhibitory effects against TAF1, which currently lacks a probe compound. Computational studies of interaction with BET-bromodomain BRD4 suggest the binding modality of this compound class is consistent with previous modes of engagement. These compounds

showcase novel chemical synthesis methods for the development bromodomain inhibitors.

Chapter three details our deep literature search for methods and strategies to inhibit the proto-oncogene MYC. In addition, it describes our effort to make our own direct MYC inhibitors in collaboration with the Young Lab. MYC is a master regulator of stem cell state, embryogenesis, tissue homeostasis, aging and has been the subject of much study in cancer. Many years of biomedical research have demonstrated a central role for MYC in the pathophysiology of cancer, inflammation, and heart disease. However, it has thus far proven intractable for drug discovery efforts. This chapter reviews strategies toward the development of inhibitors of MYC-dependent transcriptional signaling, efforts to modulate MYC stability, and the elusive goal of developing direct-acting inhibitors of MYC.

Finally, chapter four describes our study⁵ of the efficacy and mechanisms underlying bromodomain inhibition in Diffuse Large B-Cell Lymphoma (DLBCL). This malignancy is a biologically heterogeneous and clinically aggressive disease. Using integrative chemical genetics and functional epigenomics we probed effects of bromodomain inhibition in this disease. We found highly asymmetric loading of BRD4 with almost half at enhancers. Moreover, these enhancers show a skewed distribution with approximately 33% of all BRD4 localizing to enhancers at 1.6% of occupied genes. These “super-enhancers” are particularly sensitive to disruption by bromodomain inhibition leading to depletion of their target gene. This helps explain the selective effect of BET inhibitors on oncogenic and lineage-specific transcriptional circuits. In addition,

functional studies of the super-enhancer marked genes in DLBCL cell lines and primary tumors can elucidate novel dependencies.

Thus, the development of chemical probes enables a path toward clinically useful compounds and empowers deeper exploration of the biology related to the probe's target. In this case, I worked on new and improved chemical probes for the BET bromodomains and MYC which were then deployed to study transcriptional regulation in the setting of cancer biology.

- 1 Filippakopoulos, P. *et al.* Selective inhibition of BET bromodomains. *Nature* **468**, 1067-1073, doi:10.1038/nature09504 (2010).
- 2 Matzuk, M. M. *et al.* Small-Molecule Inhibition of BRDT for Male Contraception. *Cell* **150**, 673-684, doi:10.1016/j.cell.2012.06.045 (2012).
- 3 Hay, M., Thomas, D. W., Craighead, J. L., Economides, C. & Rosenthal, J. Clinical development success rates for investigational drugs. *Nature biotechnology* **32**, 40-51, doi:10.1038/nbt.2786 (2014).
- 4 French, C. A. NUT midline carcinoma. *Cancer genetics and cytogenetics* **203**, 16-20, doi:10.1016/j.cancergencyto.2010.06.007
S0165-4608(10)00262-1 [pii] (2010).
- 5 Chapuy, B. *et al.* Discovery and characterization of super-enhancer-associated dependencies in diffuse large B cell lymphoma. *Cancer cell* **24**, 777-790, doi:10.1016/j.ccr.2013.11.003 (2013).

Chapter 1

Development of an Improved BET Inhibitor for *In Vivo* and Human Trials

Contributors

Michael McKeown, Jun Qi, Katharin Shaw, Xiang Xu, Chris Ott, Charles Lin,

Jaime Reyes, Andrew Kung, Teri Bowman, James Bradner

Introduction:

After the discovery of bromodomain inhibitors and their potential against cancer with JQ1¹, we sought to explore the SAR around this scaffold and to develop a compound with properties adequate for *in vivo* use. As part of this effort, I became well acquainted with the equipment and technologies employed in high-throughput screening. Our lab is equipped with a Biotek liquid handler, a Janus workstation, and an Envision. I have learned how to calibrate, program, and repair most all aspects of this equipment. In addition to training and running this equipment for numerous projects, I also developed novel capabilities for the lab, including 1536 well plates for HTS.

For this project, I first created AlphaScreen assays for all the BET proteins with independent site one and two assays for all except BRDT. This enabled both screening for novel warheads (not shown in chapter) and to generate large numbers of IC₅₀ curves for medicinal chemistry efforts. In conjunction with Jun Qi and Jason Marineau, a large set of aldehyde containing compounds was selected and coupled to build a screening deck of about 400 compounds based on the JQ1 structure. After analyzing the hits from this initial screen, I worked closely with Jun to iteratively improve the properties of JQ1 derivatives. We created an excellent synergy of biochemistry and synthetic chemistry where I would run AlphaScreen assays and cellular viability on compounds made that week, analyze the data over the weekend, and Jun would start a new round of chemistry based on the SAR established by the recent assays data.

In the end, JQ35 was the best compound in terms of solubility and potency. Moreover, it proved to have a vastly improved half-life over JQ1. I used this compound for in depth cellular investigations performing expression studies analyzed with Chris Ott, ChIP-seq processed with Charles Lin, and mouse studies with Andrew Kung. This improved compound has expanded our understanding of Nut-Midline Carcinoma and is superior in mouse studies.

Another important milestone achieved in this project was the use of formulated JQ35 in the clinic. It is rare for a scientist to see their work achieve the full transition from early bench research to use at the bedside, but I am very happy to have been part of this process.

Contribution:

MRM wrote the text, composed figures, developed and executed biochemical and cellular assays, and planned and analyzed *in vivo* experiments. JQ synthesized compounds. KS synthesized compounds and collaborated on biochemistry. XX did crystallography. CO analyzed transcriptional data. CL and JR processed ChIP-seq data. AK oversaw execution of *in vivo*. TB processed samples for histology. JB oversaw and mentored research.

Background:

The functional interpretation of epigenetic modifications of chromatin is an essential component of gene regulation². The marks are placed by nuclear enzymes called 'writers' and removed by a set of enzymes called 'erasers' in a creating a system of transcriptionally activating and inhibiting post translational histone modifications. Thus, a diverse set of chromatin-recognition – or 'reader' - proteins is critical for the transmission of posttranslational modifications to cellular transcriptional machinery by coordinating the local area network of transcription factors, polymerases, and remodeling enzymes³. The bromodomain containing proteins are readers of lysine acetylation with a conserved structural motif composed of a four alpha helix bundle and forming a binding pocket that mediates interactions with acetylated lysine side chain on substrates⁴⁻⁷. In particular, the bromodomain and extra terminal domain (BET) family of proteins, including BRD2, BRD3, BRD4, and BRDT, contains a pair of bromodomains with high sequence homology for site 1 and site 2, respectively, among the family members. BRD4 has been shown to be important transcriptional coactivators by promoting RNA polymerase II (RNAP) pause release and transcript elongation through recruitment of the positive transcriptional elongation factor –B (pTEFB)⁸⁻¹⁰. Moreover, BRD4 appears to both directly interact with pTEFB through its second bromodomain site and promote elongation independent of pTEFB by increasing the effective molarity of transcription factors^{11,12}. BRD4 also appears to colocalize with sites of active transcription during mitosis and exhibits asymmetric loading to enhancers tissue dependencies^{13,14}.

Recently, small molecule inhibitors have been shown to effectively and selectively inhibit BET bromodomains through direct binding to the acetyllysine binding pocket¹⁵. The first reports of selective chemical probes for BET bromodomains, JQ1 and iBET, are based on a 1,4 diazepine scaffold^{1,16}. These compounds have seen considerable utility as tool compounds in a variety of cancer and inflammation-related studies. Since then initial reports, additional studies have found potential fragments, alternative binding motifs such as the dimethylisoxazole in iBET-151, and alternative chemical scaffolds that greatly expand the chemical space for BET bromodomain inhibitors¹⁷⁻²². In addition, compounds have been reported to bind other bromodomain-containing proteins including CREBBP²³. Furthermore, BET bromodomain inhibition shows great therapeutic potential in a wide range of cancer types including NUT-midline carcinoma¹, acute lymphoblastic leukemia²⁴, multiple myeloma²⁵, Burkitt's lymphoma²⁶, glioblastoma²⁷, neuroblastoma²⁸, diffuse large B-cell lymphoma¹⁴, and even HPV²⁹ and HIV³⁰. These chemical probes have established great promise and rationale for the use of bromodomain inhibitors in human therapeutics, but would benefit from further optimization for clinical use. Here we report the development of a novel biochemical screening assay utilizing a derivatized biotinylated JQ1 as a capture reagent³¹. This assay along with cell viability measurements were deployed to discover an improved probe for BET bromodomains which was further validated with ITC, crystallography, pharmacokinetic measurements, and an *in vivo* model of NMC establishing

improved efficacy. This more potent compound also helped shed light on the mechanism of action and cell origins of NUT-midline carcinoma.

The nature of BET inhibition in NUT-midline Carcinoma (NMC) needs further characterization. Based on previous studies, we hypothesized that the observed phenotypic effect would be consistent with an endothelial to epithelial conversion since previous studies in our lab found a transition from poorly differentiated cells with high nucleus to cytosol ratio into flattened enucleated cells with epithelial character¹. It has been established that epithelial cells undergo epithelial to mesenchymal transitions to promote invasion, metastasis, proliferation, repressed growth control, and reduced adhesion^{32,33}. The poor differentiation of NMC is also consistent with the more stem-like properties created by EMT³⁴. Thus, we explored BET inhibition as a method to reverse EMT in NMC on a transcriptional and chromatin level.

Results

Benzodiazepines have been an important scaffold for drug discovery over years. Since our discovery of thienodiazepine as bromodomain inhibitors, we have examined well known benzodiazepine family members, including Alprazolam, the FDA approved drug anxiety medication better known as Xanax (Figure 1.1A).

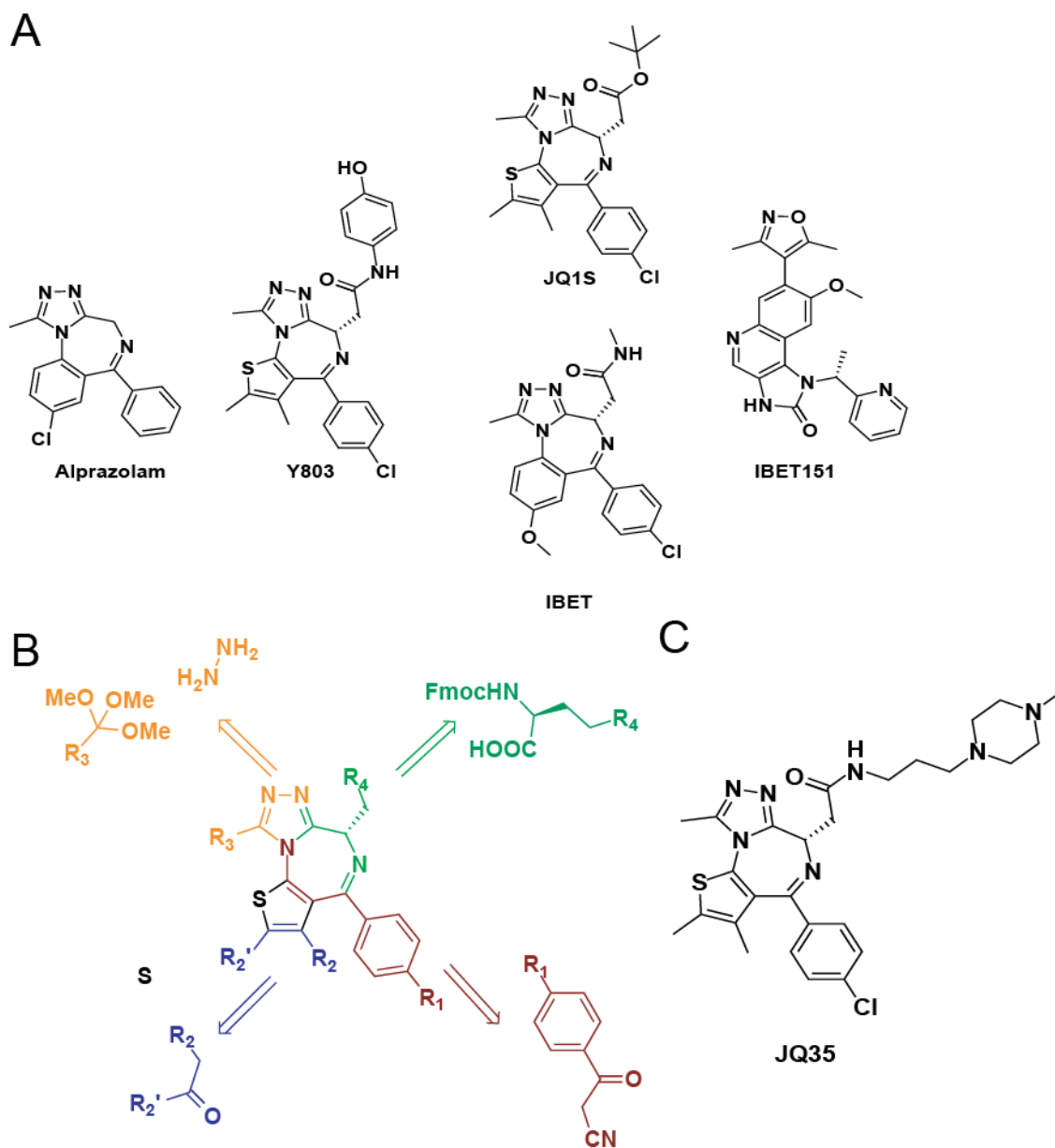


Figure 1.1: BET inhibitors and synthetic strategy (A) Current BET bromodomain inhibitors. Alprazolam is a benzodiazepine (Xanax) that was originally found to weakly bind the acetyl-lysine pocket. Y803, from Mitsubishi, IBET and IBET-151, from GSK, and JQ1S, from the Bradner Lab, were among the first BET bromodomain probes. (B) Schema showing starting components and accessibility to the JQ1 core structure that enables diversification. (C) The optimized probe compound JQ35.

Other bromodomain inhibitors, such as **Y803** (from Mitsubishi), **iBET**, share a similar structure with substitutions at the C6 position larger than a methyl group to prevent binding to the central benzodiazepine receptor and block activity as a platelet aggregating factor antagonist^{35,36}.

The use of a dimethyl isoxazole moiety distinguishes iBET-151 from the other structures. While it demonstrates the potential of alternative structural moieties in targeting BETs, it does not show significantly improved *in vivo* efficacy versus the original iBET-762 (also name just iBET)^{16,22,37}. Thus, we set out to study the structure activity relationships of BET inhibition to build improved inhibitors based on the JQ1 scaffold. Based on the retrosynthetic analysis of JQ1, we have designed an optimized synthetic route to modify a variety of units in and appending to the core structure to establish structure activities relationships (Figure 1.1B).

Assay development

We designed and developed a bead-based proximity assay to facilitate high-throughput screening of compound libraries. Utilizing the well characterized binding of JQ1 to BETs, a capture probe was created by attaching a biotin with a two PEG spacer (Figure 1.2A)³¹. This probe replaces biotinylated tetra acetyl histone H4 tail peptides in pulldowns and biochemical assays⁷. To build a robust, high-throughput assay for inhibition of BET family member subunit the biotinylated probe was used with 6x histidine tagged proteins of each subunit in a Ni⁺² chelate AlphaScreen system (Figure 1.2B). In order to optimize this assay

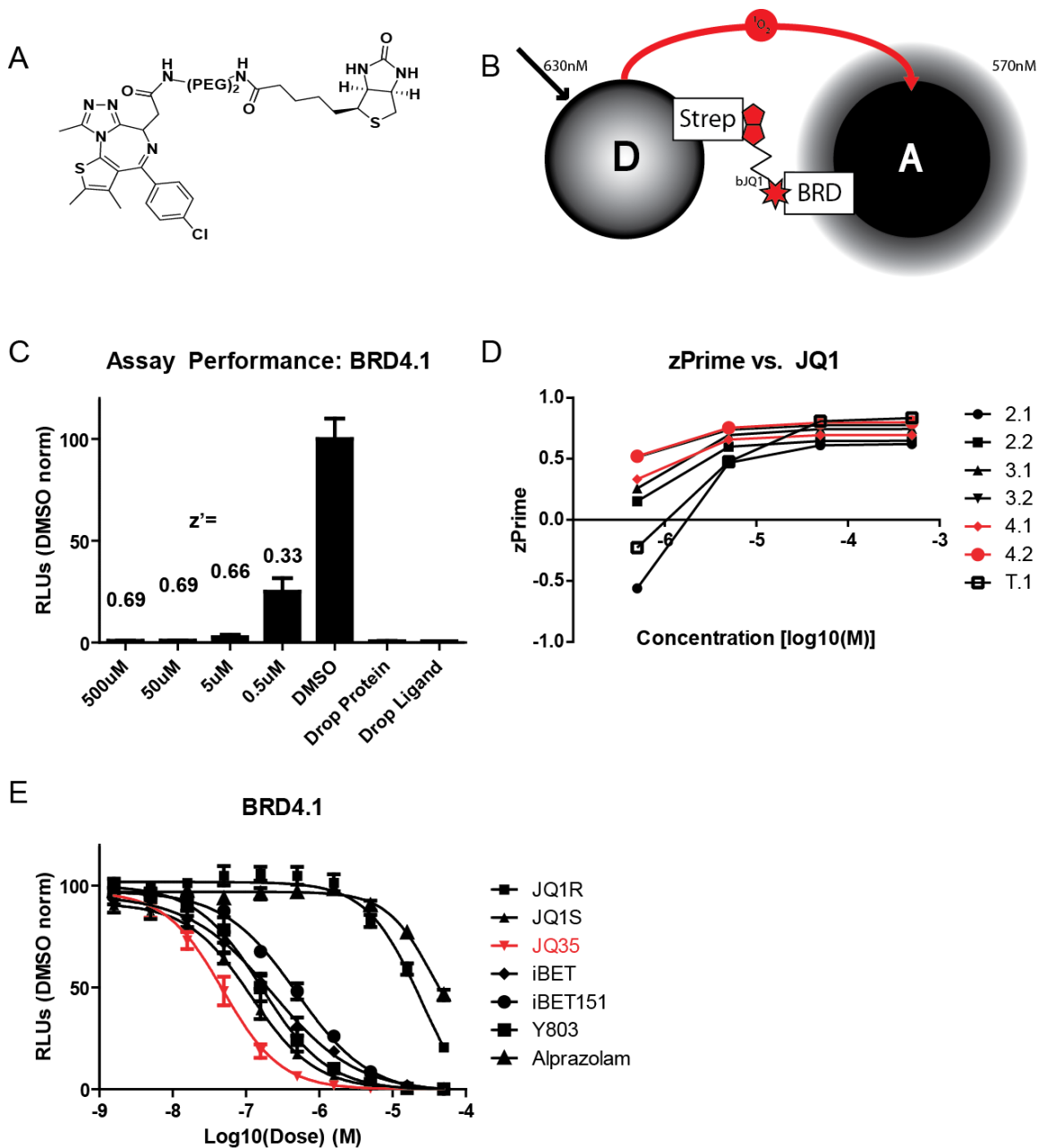
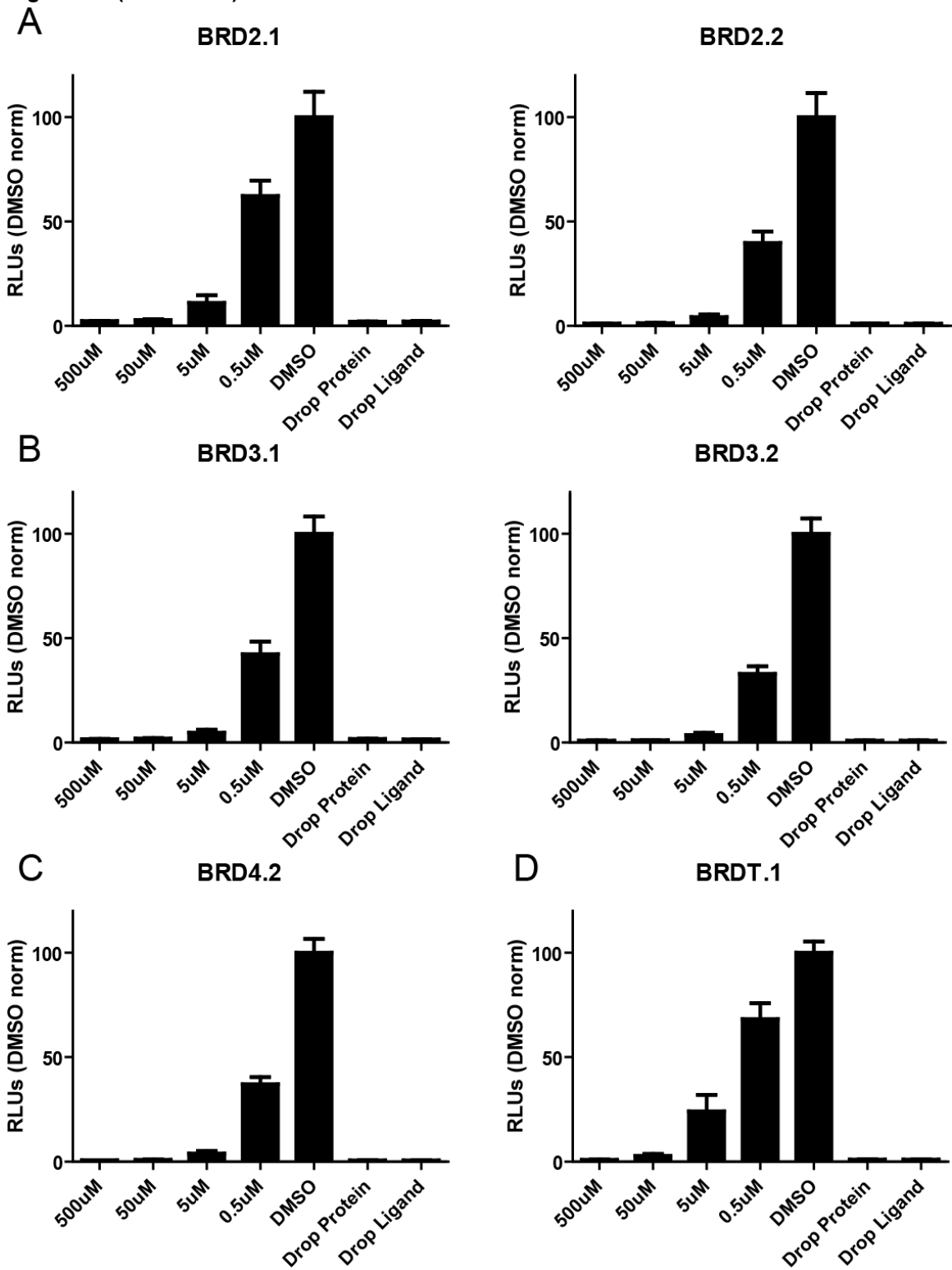


Figure 1.2: Biochemical screening assay. (A) Biotinylated JQ1 probe used in HTS read assay. **(B)** Schematic of assay showing nickel coated acceptor bead A with bromodomain attached (BRD) linked by the biotinylated probe to the donor bead (D) with streptavidin coating. **(C)** Z' performance over varying concentrations of free JQ1 showing good detection sensitivity. **(D)** Data for Z' over dose for all BET proteins by subdomain. **(E)** Dose response for compounds in Figure 1.1A using AlphaScreen assay.

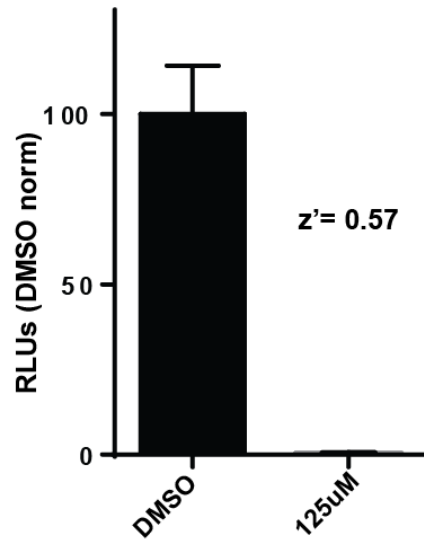
Figure 1.3: Assay optimization. Dose response z-prime data for site one and site two, respectively, of BRD2 (**A**) and BRD3 (**B**). BRD4.2 (**C**) and BRDT.1 (**D**) are also shown. Assay was performed on 384 well plates as described in methods.

Figure 1.3 (Continued)



system, buffer conditions and reagent concentrations were tested. To maximize signal and responsiveness to inhibition while minimizing background signal, protein and ligand were titrated with constant bead concentrations and respective drop-out conditions. Moreover, a buffer at physiologic pH and salinity (see methods) was formulated with high detergent (0.01%) and BSA (0.1%) to minimize non-specific interactions. The final version of this fully optimized assay provides statistical robustness across a broad range of assay screening concentrations for BRD4.1, with a Z' of 0.69 (Figure 1.2C). BRD4 also showed robust performance across a range of doses and with site 2 (Figure 1.2D; 1.3C). In addition, this system works comparably well with all BET bromodomains (Figure 1.2D; 1.3; 1.4D). The z -prime across doses of JQ1 is shown in the table in Figure 1.4B. This assay is also 1536 ready with a Z -prime of 0.57 enabling dramatically higher screening capacity (Figure 1.4A). To test out dose response behavior and benchmark the assay the known bromodomain inhibitors shown in Figure 1.1A were tested and showed potencies in good agreement with previously published values (Figure 1.2e; 1.5; Table 1.1). Furthermore, the biotinylated JQ1 probe performed as well as the tetra acetylated peptide in the same assay configuration (Figure 1.5). Finally, validation of the compounds for cellular activity was performed by cell viability in 797 Nut Midline Carcinoma lines. Performance over a range of JQ1 concentrations showed good dose responsive behavior by ATPlite (Figure 1.4C).

A Assay Performance: 1536



B

BET site

| | 2.1 | 2.2 | 3.1 | 3.2 | 4.1 | 4.2 | T.1 |
|--------------|-------|------|------|------|------|------|-------|
| JQ1 (μM) 500 | 0.62 | 0.65 | 0.74 | 0.78 | 0.69 | 0.80 | 0.83 |
| 50 | 0.61 | 0.65 | 0.74 | 0.78 | 0.69 | 0.80 | 0.81 |
| 5 | 0.47 | 0.60 | 0.69 | 0.74 | 0.66 | 0.75 | 0.48 |
| 0.5 | -0.56 | 0.15 | 0.26 | 0.51 | 0.33 | 0.52 | -0.23 |

C

797

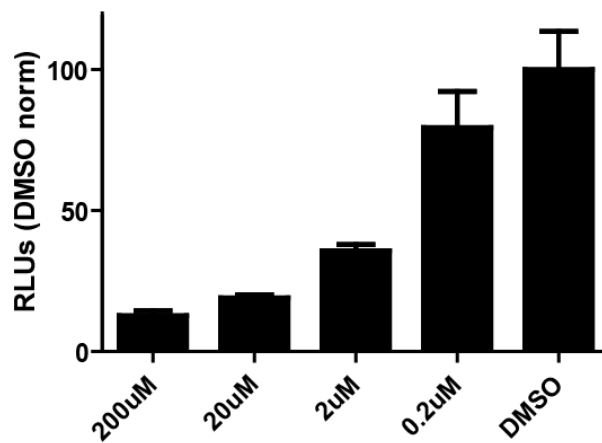


Figure 1.4: Assay performance (A) Z-prime performance of assay in 1536-well configuration. **(B)** Table form of z-prime data for all BET bromodomain sites studied. **(C)** Performance of JQ1 in a ATPlite cellular viability assays against the 797 NMC cell line.

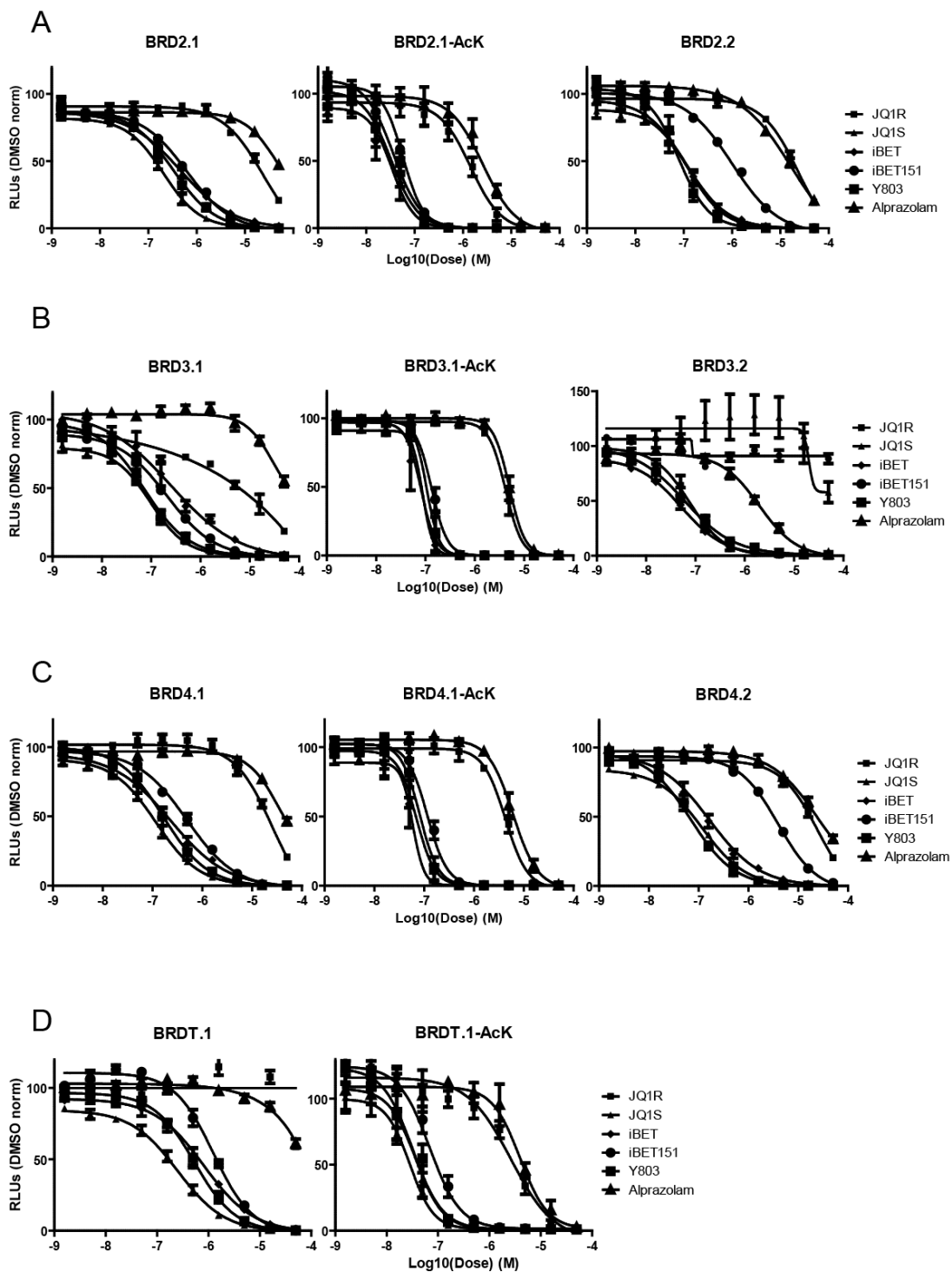


Figure 1.5: Dose response of chemical probes 10 point dose response curves generated for bromodomain probe molecules. Each series of panels shows site on, left, site two, right, and the site one assay using an acetylated peptide instead of the biotinylated JQ1 probe. BRD2 (A), BRD3 (B), and BRD4 (C) show both sites. BRDT data for site one shown in (D).

Table 1.1: Known Bromodomain Probes

| | Pfizer | JQ1R | JQ1S | JQ35 | iBET | iBET151 | Y803 | Alprazolam |
|-------|---------------|-------------|-------------|-------------|-------------|----------------|-------------|-------------------|
| 2.1 | 3.12E-08 | 2.37E-05 | 2.06E-07 | 8.45E-08 | 4.61E-07 | 6.22E-07 | 3.32E-07 | 4.58E-05 |
| 2.1ac | 4.65E-09 | 1.43E-06 | 3.38E-08 | 2.34E-08 | 3.25E-08 | 5.77E-08 | 3.64E-08 | 2.58E-06 |
| 2.2 | 4.97E-08 | 2.39E-05 | 1.26E-07 | 4.56E-08 | 1.13E-07 | 1.00E-06 | 7.87E-08 | 1.72E-05 |
| 3.1 | 2.61E-08 | >100uM | 9.58E-08 | 2.88E-08 | 2.56E-07 | 2.08E-07 | 7.39E-08 | 3.04E-05 |
| 3.1ac | 1.16E-08 | 4.21E-06 | 8.73E-08 | 6.36E-08 | 8.13E-08 | 1.33E-07 | 1.06E-07 | 5.03E-06 |
| 3.2 | 6.27E-08 | >100uM | 5.21E-08 | 1.50E-08 | 6.89E-08 | 1.96E-06 | 7.17E-08 | >100uM |
| 4.1 | 1.78E-08 | 2.48E-05 | 1.17E-07 | 4.85E-08 | 2.31E-07 | 4.90E-07 | 1.64E-07 | 3.48E-05 |
| 4.1ac | 7.35E-09 | 4.26E-06 | 5.86E-08 | 5.24E-08 | 6.97E-08 | 1.15E-07 | 8.16E-08 | 6.07E-06 |
| 4.2 | 1.60E-07 | 2.45E-05 | 1.19E-07 | 3.43E-08 | 1.65E-07 | 3.93E-06 | 6.93E-08 | 2.41E-05 |
| T.1 | 8.13E-08 | >100uM | 2.52E-07 | 6.78E-08 | 8.11E-07 | 1.25E-06 | 5.35E-07 | >100uM |
| T.1ac | 6.53E-09 | 2.62E-06 | 2.83E-08 | 1.67E-08 | 3.68E-08 | 6.89E-08 | 3.20E-08 | 3.95E-06 |

Table shows IC50 values generated by the AlphaScreen assay for bromodomain probe molecules against each bromodomain site tested.

Approach to modifying core

Based on the crystal structure of BRD4 and JQ1¹ the following were considered potential areas for modification of the JQ1 scaffold: the chlorophenyl (I), the thiophene (II), methyl triazole (III), and the C6 position (IV) (Figure 1.6A).

The chlorophenyl region is mostly solvent exposed on one face and sits against a non-polar surface of the BC loop on the other. Attempts to remove this group strongly abrogated binding as seen (JQ9). Also, substitution of the chloro to fluoro in JQ43 or changing to a fourth position pyridine in JQ37 in the hopes of improving solubility were found to hinder binding to a lesser extent likely due to a loss of interaction with this surface (Figure 1.6B).

The thiophene region rests in a narrow channel between WPF shelf and the ZA loop. As expected, the isosteric substitution to phenyl ring in JQGB proved to have no effect on binding while the desmethyl version in KS1 proved extremely deleterious (Figure 1.6C). Adding the methoxy group to the benzyl substituent in JQGB to yield JQG2A caused a tenfold reduction in potency suggesting that mimicking iBET's methoxy substituent was not beneficial in this case. Finally, bulking up the C6 position with a benzyl group in place of the thiophene did not compensate for a loss of the chloro at the group I site yielding a very poor potency.

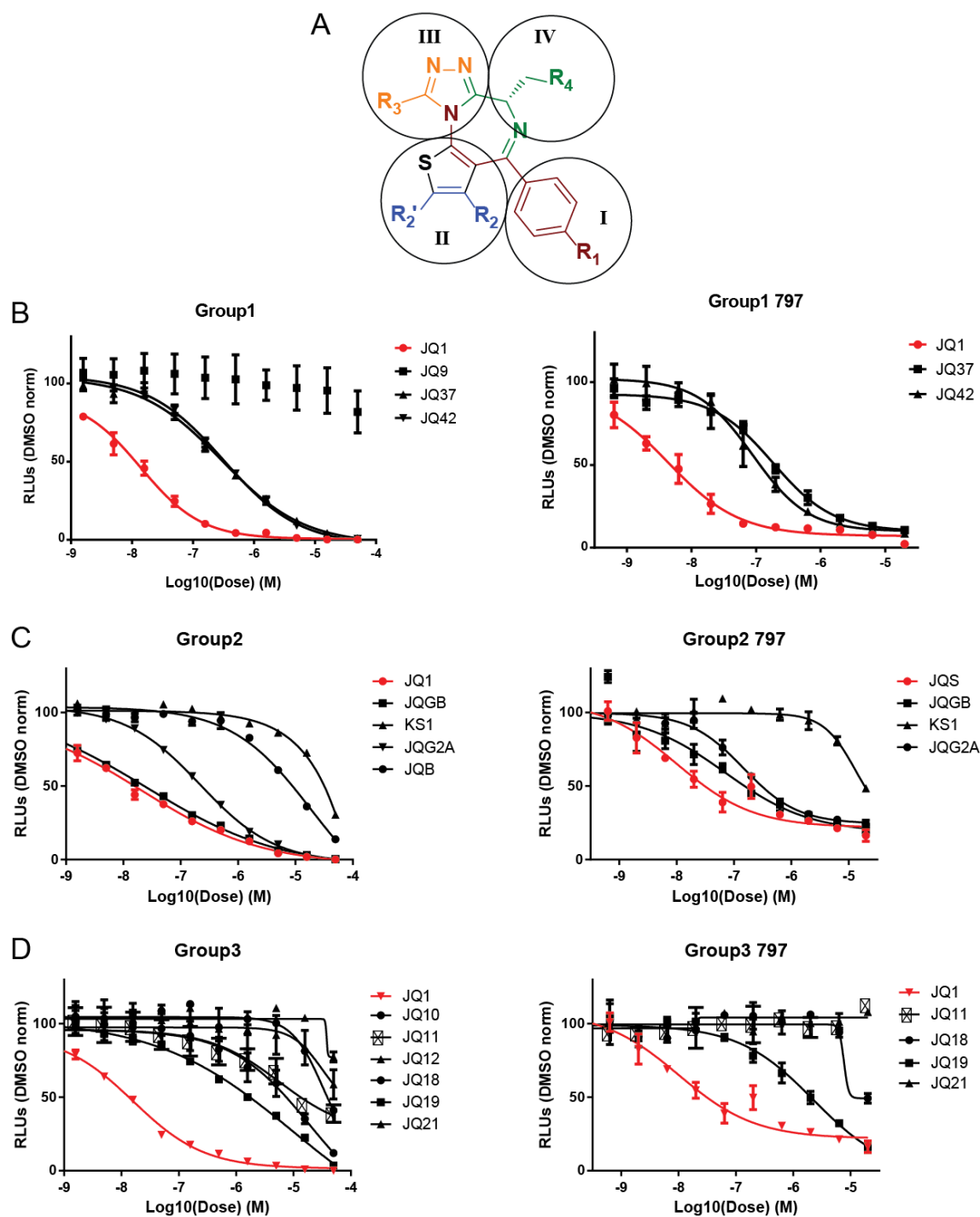


Figure 1.6: Medicinal chemistry regions (A) The generalized structure of JQ1 from which derivatives were made. Color coding illustrates the starting components used in synthesis to access each atom on the molecule. The regions focused on for analogs are circled and labeled with roman numerals. Biochemical (left) and cellular (right) dose response with the 797 NMC cell line are shown for regions I, II, and III in **(B)**, **(C)**, and **(D)** respectively.

Table 1.2: Medicinal chemistry series. Table showing the IC50 generated by AlphaScreen assay against BRD4.1 in column two and the EC50 by cellular viability with the 797 NMC cell line in column three. Compounds are also labelled by region. N/A indicates that the value was not assessed.

Table 1.2 (Continued)

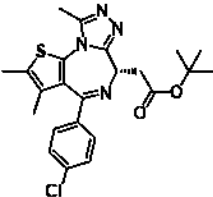
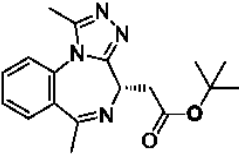
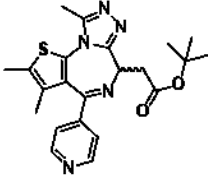
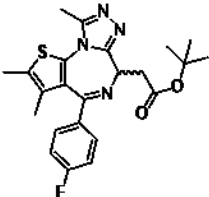
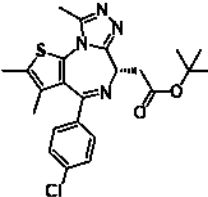
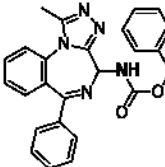
| Compound | IC50 BRD4.1 | EC50 | Group | Structure |
|----------|-------------|----------|-------|--|
| JQ1 | 1.38E-08 | 4.33E-09 | I |  |
| JQ9 | >100 | N/A | I |  |
| JQ37 | 2.98E-07 | 1.82E-07 | I |  |
| JQ42 | 3.20E-07 | 8.88E-08 | I |  |
| JQS | 1.87E-08 | 1.01E-08 | II |  |
| JQGB | 1.92E-08 | 7.09E-08 | II |  |

Table 1.2 (Continued)

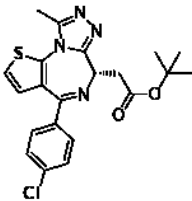
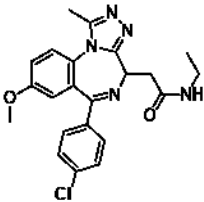
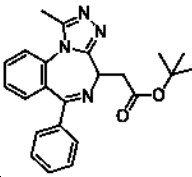
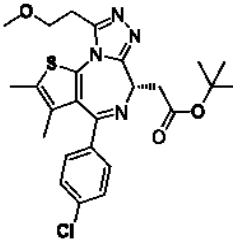
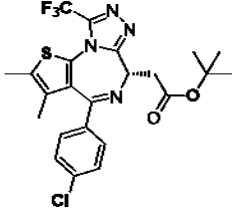
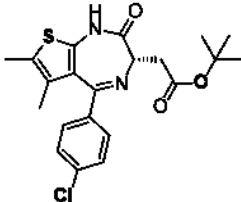
| | | | | |
|-------|----------|----------|-----|--|
| KS1 | 2.55E-05 | 1.33E-05 | II |  |
| JQG2A | 2.04E-07 | 1.48E-07 | II |  |
| JQB | 7.54E-06 | N/A | II |  |
| | | | | |
| JQ10 | 1.86E-05 | N/A | III |  |
| JQ11 | 5.68E-06 | >100 | III |  |
| JQ12 | 3.19E-05 | N/A | III |  |

Table 1.2 (Continued)

| | | | | |
|------|----------|----------|-----|--|
| JQS | 1.61E-08 | 1.80E-08 | III | |
| JQ18 | 3.23E-05 | 1.82E-05 | III | |
| JQ19 | 9.84E-06 | 2.04E-06 | III | |
| JQ21 | 3.78E-05 | >100 | III | |
| JQ1S | 2.10E-08 | 7.69E-08 | IV | |
| JQ25 | 7.07E-05 | N/A | IV | |

Table 1.2 (Continued)

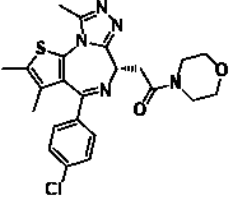
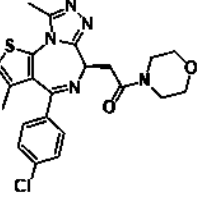
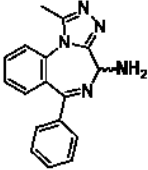
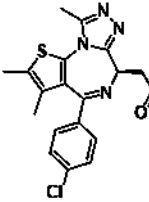
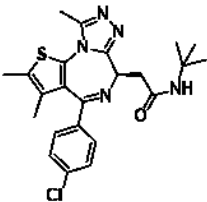
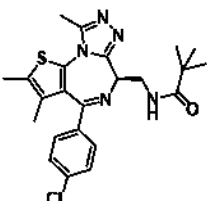
| | | | | |
|--------|----------|----------|----|--|
| JQ26A | 8.30E-08 | 4.25E-08 | IV |  |
| JQ26-R | 2.94E-05 | N/A | IV |  |
| JQ27 | 2.47E-05 | N/A | IV |  |
| JQ29 | 1.65E-08 | 8.03E-09 | IV |  |
| JQ30 | 2.42E-06 | 9.06E-07 | IV |  |
| JQ31 | >100 | 7.37E-06 | IV |  |

Table 1.2 (Continued)

| | | | | |
|------|----------|----------|----|--|
| JQ33 | 9.59E-08 | 3.31E-08 | IV | |
| JQ35 | 2.43E-08 | 1.04E-08 | IV | |
| JQ37 | 2.98E-07 | N/A | IV | |
| JQ38 | 1.53E-07 | N/A | IV | |
| JQ39 | 4.98E-05 | N/A | IV | |
| JQ40 | 2.57E-06 | N/A | IV | |

Table 1.2 (Continued)

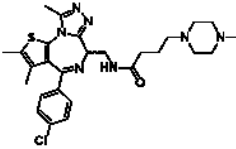
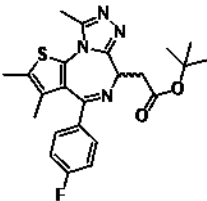
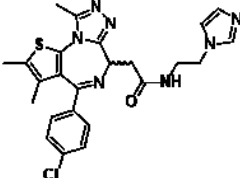
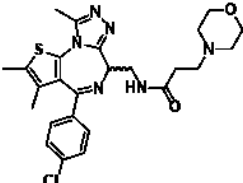
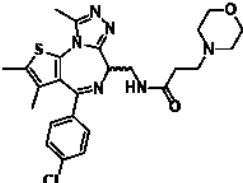
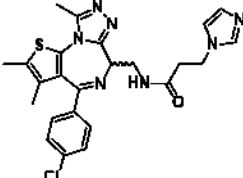
| | | | | |
|---------|----------|----------|----|--|
| JQ41 | 9.71E-07 | N/A | IV |  |
| JQ42 | 3.20E-07 | N/A | IV |  |
| JQ43 | 9.96E-08 | 7.51E-08 | IV |  |
| JQ44rac | 2.56E-06 | 1.56E-06 | IV |  |
| JQ44 | 7.51E-08 | 1.56E-06 | IV |  |
| JQ45rac | 5.78E-06 | 3.18E-06 | IV |  |

Table 1.2 (Continued)

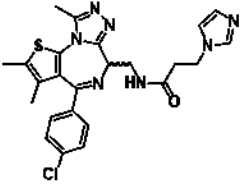
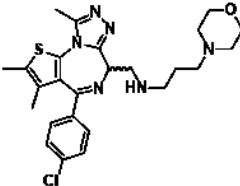
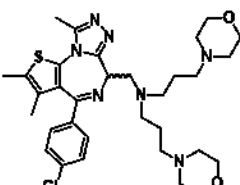
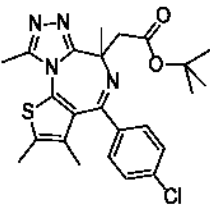
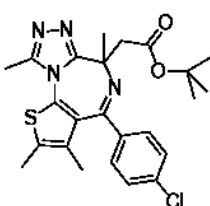
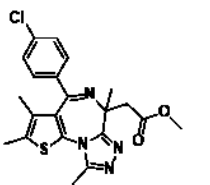
| | | | | |
|--------|----------|----------|----|--|
| JQ45-S | 5.60E-08 | 3.18E-06 | IV |  |
| JQ46 | 2.85E-06 | 1.28E-06 | IV |  |
| JQ47a | 7.57E-06 | 2.74E-06 | IV |  |
| JQ48-1 | 1.70E-05 | N/A | IV |  |
| JQ48-2 | 6.79E-06 | N/A | IV |  |
| JQ49 | 5.00E-06 | 2.79E-07 | IV |  |

Table 1.2 (Continued)

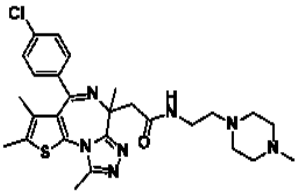
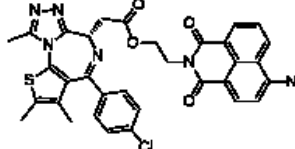
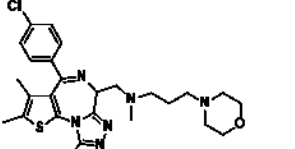
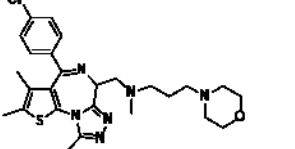
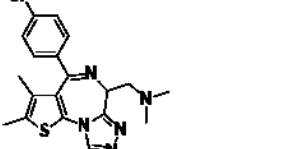
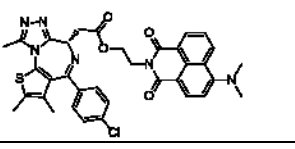
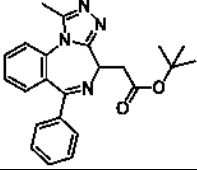
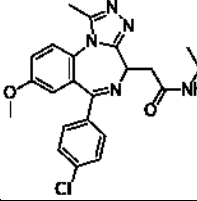
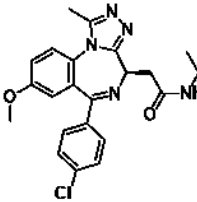
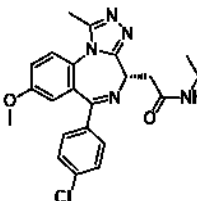
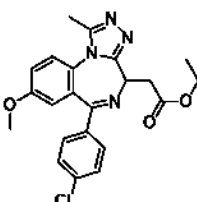
| | | | | |
|---------|----------|----------|----|--|
| JQ50-1 | 1.93E-06 | 1.28E-06 | IV |  |
| JQ51 | 6.26E-08 | 6.35E-08 | IV |  |
| JQ52rac | 2.74E-06 | 6.33E-09 | IV |  |
| JQ52 | 4.05E-08 | 6.33E-09 | IV |  |
| JQ53 | 3.17E-06 | N/A | IV |  |
| JQ54 | 6.64E-06 | 5.79E-06 | IV |  |

Table 1.2 (Continued)

| | | | | |
|--------|----------|-----|----|--|
| JQB | 1.90E-05 | N/A | IV |  |
| JQG2-S | 2.20E-07 | N/A | IV |  |
| JQG2-R | 6.88E-05 | N/A | IV |  |
| JQG2-S | 3.74E-08 | N/A | IV |  |
| JQG3 | 1.72E-06 | N/A | IV |  |

Based on the crystal structure, we hypothesized that the deep waters in the bromodomain binding pocket could be displaced or interacted with to enhance binding. However, exploration of group III around the methyl thiophene proved otherwise (Figure 1.6D). Replacing the methyl group with a methoxy ethyl in JQ10 reduced potency dramatically suggesting a clash instead of replacement with the waters. A shorter methoxy methylene in JQ18 was tenfold more potent, but still less potent than JQ1. A more subtle addition from methyl to ethyl in JQ19 gave another nearly tenfold improvement, but was still a thousand-fold worse than JQ1. Yet the desmethyl JQ21 was one hundred fold weaker than the ethyl suggesting that the original methyl is the ideal substituent. Removing the methyl triazole altogether in JQ12 almost completely eliminated binding establishing that this region is crucial to the binding site interaction. A trifluoro methyl substituent aimed at altering the electronics of the engagement with the conserved asparagine proved similarly ineffective in JQ11.

Biased Library Generation

In order to build a focused library to interrogate the more permissive C6 position, we utilized a hydrazide-aldehyde coupling strategy shown to be successful with the development of histone deacetylase inhibitors at efficiently exploring diversity around a biasing element³⁸. In this strategy, JQ1 was derivatized by hydrolyzing the t-butyl ester to the carboxylic acid and then converting the group to a hydrazide (JQ3) (Figure 1.7A). A library of four hundred commercially available building blocks were assembled and coupled to the

hydrazide by heating the two components at 70⁰C overnight in DMSO (Figure 1.3A). The library was selected to probe diverse chemical functional groups to serve as launching points for a medicinal chemistry lead series. Compounds were then tested in eight point dose response in the BRD4.1 AlphaScreen (Figure 1.7B) assay as well as a cell viability assay against 797 NMC cells (Not shown).

The most potent compounds were resynthesized and retested in ten point dose in the biochemical assay and cell line to verify potency and establish an IC₅₀ (Figure 1.7DE). Based on this screening effort, JQ6 was discovered. However, the hydrazone linkage was judged to be potentially unstable for future *in vivo* work and thus changed to a readily available amide with comparable potency, JQ8. Having established that an amide couple be functionally substituted, we then aimed to remove the histamine component as this is itself bioactive, leading to a piperazine group on JQ13. These compounds were also tested for PK properties yielding half-lives of 2.32, 1.11, and 1.60 hours for JQ6, JQ8, and JQ13 respectively compared to JQ1 with 1.27. While more potent than JQ1, further optimization was required for improved use *in vivo*. Finally, multiple linkers were tested ending the series with JQ35 (Figure 1.3C,D,E). This final series progression was tested against all BET sites with comparable potency (Figure 1.8).

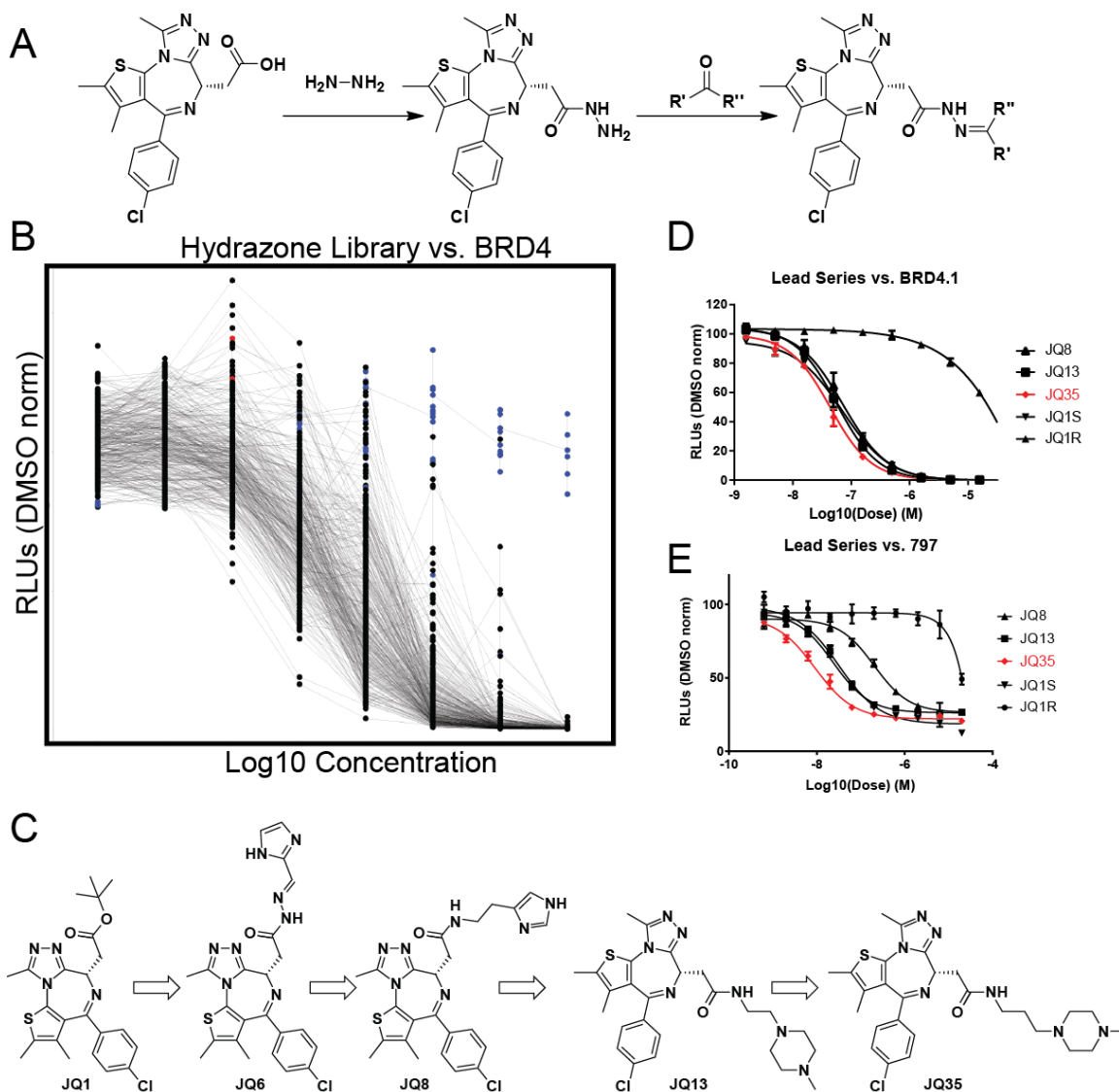


Figure 1.7: Lead series (A) Synthetic strategy for generating hydrazide library. The acid form of JQ1 formed by hydrolyzing the tButyl ester was converted to the hydrazine. This group allows rapid and efficient condensations with a library of 400 aldehydes. **(B)** Eight point dose response data from the aldehyde library against BRD4.1. **(C)** Chemical series leading to the development of JQ35. With JQ1 as a starting point, JQ6 was found from the hydrazide-aldehyde library which led to JQ35 by iterative medicinal chemistry. Dose response for series members is shown for BRD4.1 **(D)** and 797 cells **(E)**. JQ35 is highlighted in red.

Further C6 SAR investigation

Having established extensive structure activity relationships around the potential variable regions in JQ1 and found a promising lead in JQ35, further interrogation of this position was performed to establish a thorough understanding of the SAR (Table 1.2). Numerous amides were tested at this position and found to be suitable replacements for the ester bond as suggested from the ethyl amide at this position in iBET. Other substitutions were found to have negative consequences to binding. The ester/amide compounds form a hydrogen bond and steric interactions with the pocket. Reversing this group, as in JQ1 vs JQ25, JQ30 vs JQ31, JQ35 vs JQ36&41, and JQ13 vs JQ40, all greatly decreased potency. Also, direct amines without substituents (JQ27), secondary amines such as JQ46, and tertiary amines such as JQ52&53, possibly fail to pick up this interaction and as they exhibit reduced potency vs comparable amides and esters. An indole connected by a one carbon linker also proved to lack the potency of JQ1 or JQ35. Finally, an alpha methylation to the C6 carbon was attempted to constrain flexibility in the core while keeping the correct enantiomer during synthesis. However, these proved to have extremely poor potency relative to JQ35 likely due to steric clash with the bromodomain pocket. Thus, these improvement culminated in JQ35 which was maintained as the lead compound for additional biological and *in vivo* studies due to significantly improved biological properties.

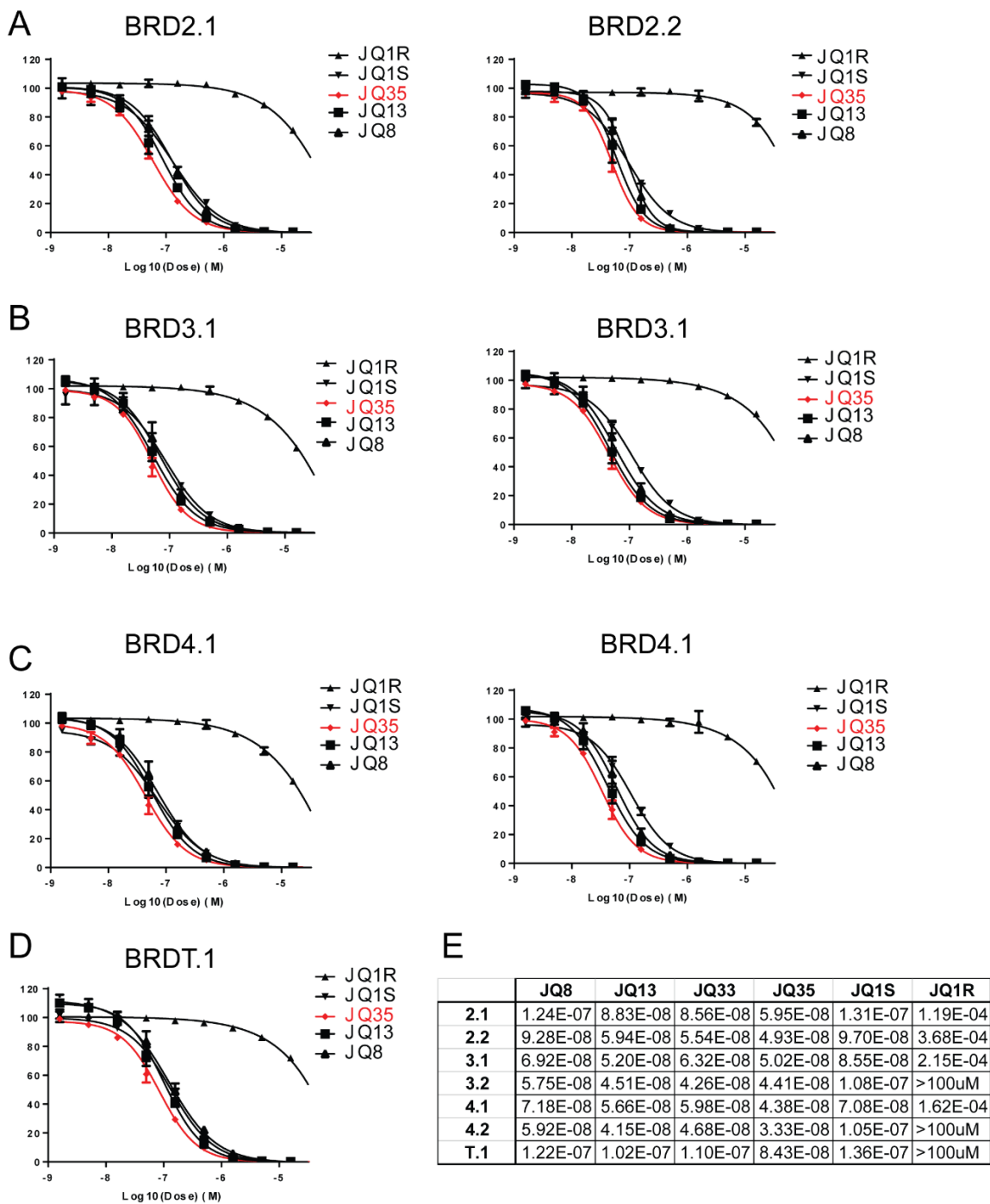


Figure 1.8: Lead series dose response. Dose response of the expanded set of lead series compounds using the AlphaScreen assay is shown with BRD2 (**A**) BRD3 (**B**) BRD4 (**C**) and BRDT.1 (**D**). Site one is in the left panel and site two on the right. IC50 values are compiled in the embedded table (**E**).

Xray Structure Section

To understand the contribution of the piperazine side chain to BET bromodomain engagement, we co-crystallized JQ35 with BRD4 site 1. The critical hydrogen bond to the conserved N140 was preserved, as expected (Figure 1.9A). The elongated side chain rests against the side of the ZA loop between this loop and the BC loop region (Figure 1.9B). Space filling and charge assignment shows not only increased steric interactions, but a favorable charge interaction with the negatively charged area near the aspartic residue on the ZA loop (Figure 1.9C). In addition, an interaction diagram illustrates important hydrogen bonds to structural water molecules present in the binding site (Figure 1.9D). ITC performed on the protein used for crystallography showed a binding stoichiometry of 1:1 for BRD4 site 1 and a K_d of 6.3nM in agreement with the AlphaScreen assay (Figure 1.9E). Moreover, IV cassette PK for this compound showed a dramatic improvement to 5.53 hour half-life by IV injection (Figure 1.12A).

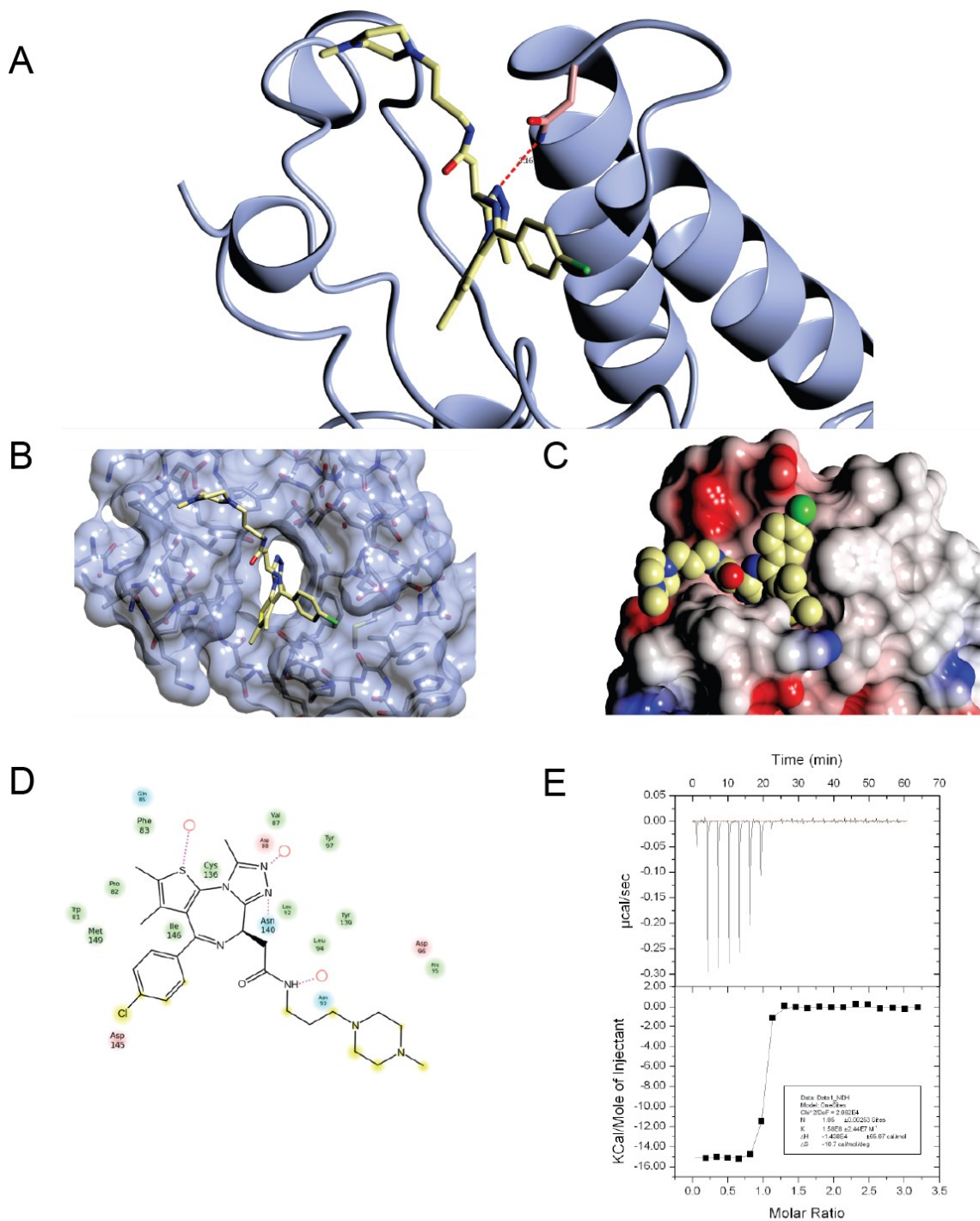


Figure 1.9: JQ35 crystal structure. Crystallographic studies of JQ35 and BRD4.1. The methyl triazole makes the expected hydrogen bond to the conserved asparagine in BRD4 (A). The larger, positive C6 substituent of JQ35 participates in increased surface complementarity (B) and favorable charge interactions (C). The amide picks up and additional hydrogen bond with a fixed water (D). The K_d of JQ35 was assessed by ITC measurement as 15.8nM (E).

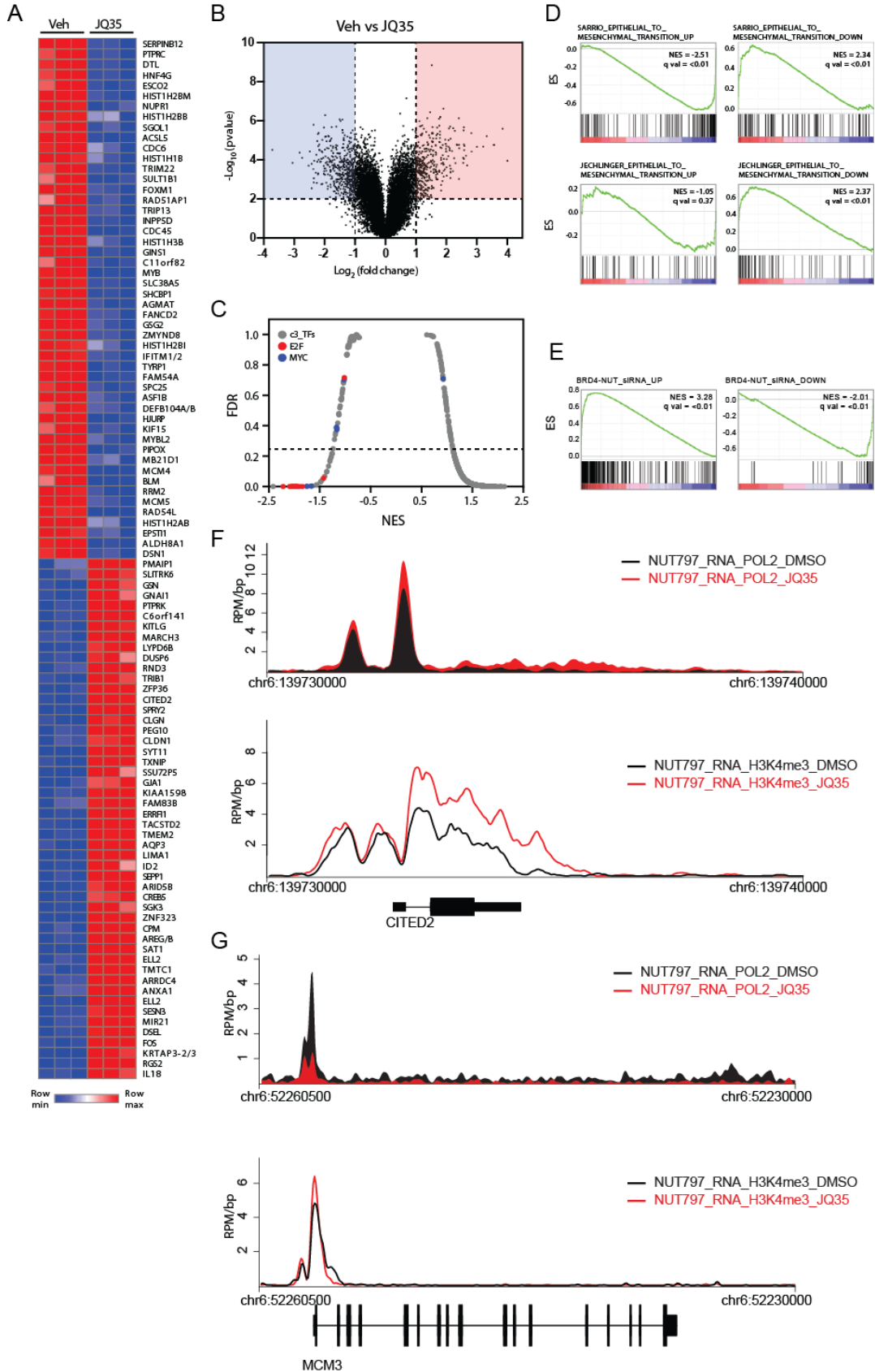
Expression Changes

We hypothesized that the oncogenic dysregulation of BRD4 in NMC is key to its pro-cancerous state and that inhibition could give insight into the original tissue and the programmatic shift enforced by Nut-BRD fusion. To this end, we investigated the effects of JQ35 on NMC cells at the transcriptional level, gene expression profiling, and ChIP-seq. Expression changes in response to JQ35 treatment at 24 hours showed highly significant gene changes both up and down as expected with the pro-differentiation phenotype observed with JQ1 (Figure 1.10A). The top fifty genes with treatment revealed several expected targets such as the upregulation of *Ae1/Ae3*, *ANXA1*, and *cFOS* in agreement with previous studies^{39,40}. Down regulated genes such as the proto-oncogene *MYB* and *ACSL5* were also consistent with previous studies and the noted anti-proliferative effects of JQ35 treatment^{25,41}. Furthermore, JQ35 is not acting simply as a broad transcriptional repressor, but rather causes greater than fourfold and highly significant changes in transcript abundance to both up and down regulate a set of genes at 24 hours of treatment where early phenotypic changes were noted in previous studies (Figure 1.10B)¹. In addition, motif analysis showed a downregulation of growth pathways, such as *Myc* and *E2F*, as seen previously with JQ1 (Figure 1.10C). JQ35 treatment was also significantly consistent with the gene set established by siRNA knockdown of BRD4 in NMC supporting its on-target mechanism of action⁴⁰ (Figure 1.10D).

Since NMC presents as a poorly differentiated squamous carcinoma of unknown origin which undergoes a transition with BET inhibition into strong

epithelial character, we hypothesized that JQ35 could follow the signature of a Mesenchymal to Epithelial transition (MET). We tested established GSEA pathways for Epithelial-to-Mesenchymal (EMT) transition and found a significant anti-correlation with JQ35 treatment (Figure 1.10D)^{42,43}. Importantly, this was true for both directionalities where BET inhibition not only downregulated the expected targets but caused upregulation of epithelial signatures. To further validate this finding, ChIP-seq analysis of the H3K4Me3 promoter mark and RNA Pol II revealed decreased loading and elongation at mesenchymal state genes and increased loading and elongation at epithelial associated genes (Figure 1.10F,G; Figure 1.11). This supports, on a chromatin level, the transcriptional changes seen by affymetrix array. Furthermore, this is consistent with inhibition of BRD4 at these target genes as BETs are important for transcriptional elongation. Thus, inhibition of BET bromodomains appears to disrupt the mesenchymal, pro-oncogenic protocol and allow epithelial character to be restored.

Figure 1.10: Gene expression. Gene expression and ChIP-seq study after 24 hours treatment with 500nM JQ35. **(A)** Top 50 up and down regulated genes by JQ35 treatment. **(B)** Volcano plot comparing significance on y-axis to fold change on x-axis. **(C)** Graph showing gene set for MYC and E2F1 occur at high enrichment, on x-axis by Normalized Enrichment Score, and high significance by being below the False Discovery Threshold shown by the dashed line on the y axis. **(D)** Gene set studies for Epithelial to Mesenchymal shift from Sarrio, top, and Jechlinger, bottom. Data shows significant anti-correlation indicating a Mesenchymal to Epithelial transition. **(E)** JQ35 shows significant correlation with genes sets defined by BRD4 siRNA. **(F)** CITED2 shows increased RNA POL 2 loading and elongation with JQ35 treatment. **(G)** MCM3 shows reduced RNA POL 2. The promoter for both (F) and (G) is shown with H3K4me3 tracks. JQ35 treated is highlighted in red.



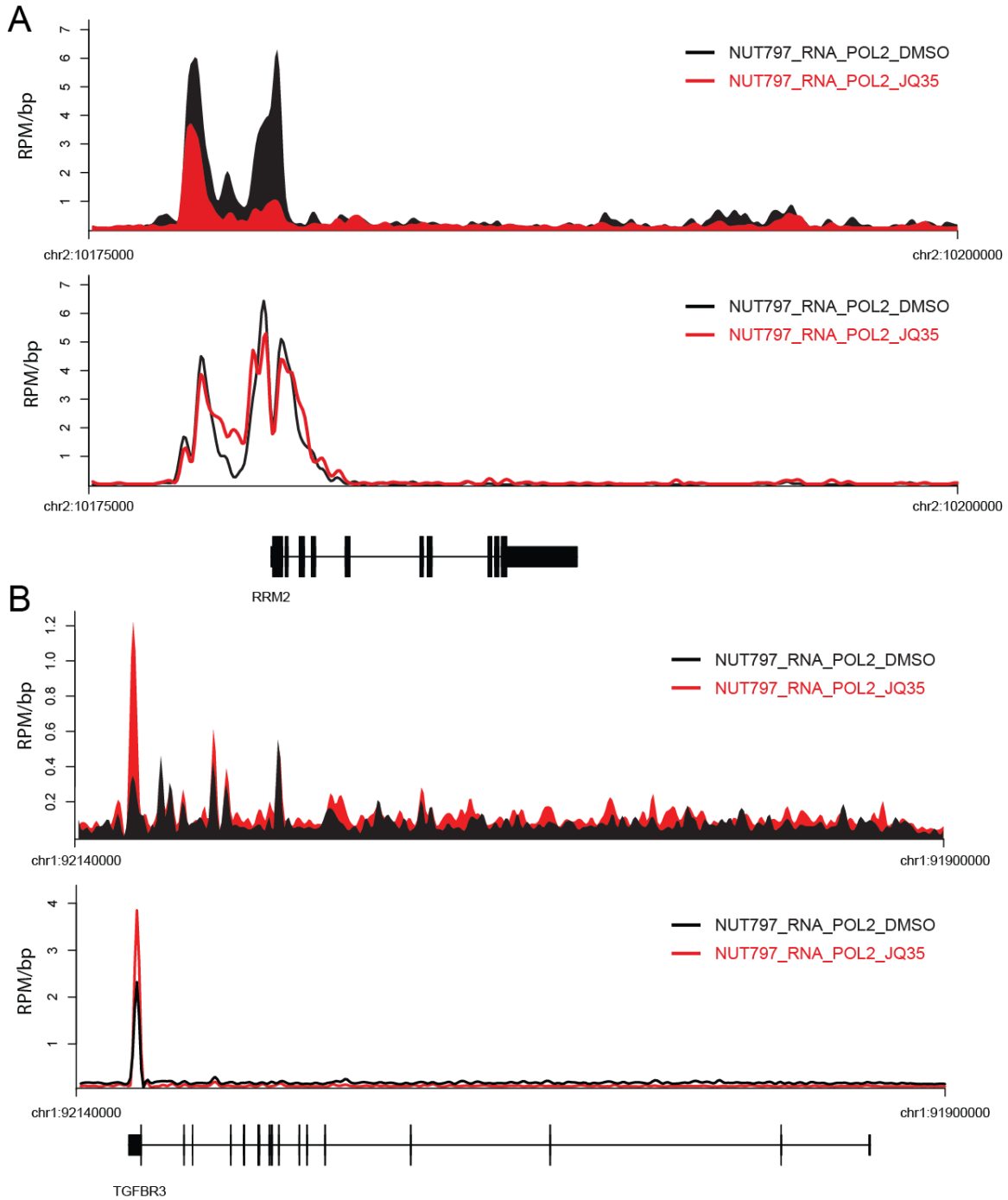


Figure 1.11: Additional ChIP-seq. Tracks shown as with CITED2 and MCM3. **(A)** RRM2 shows loss of RNA POL2 while **(B)** TGFB3 shows gain with JQ35 treatment. 24 hours, 500nM JQ35.

In vivo

Having established improved biochemical characteristics and cellular potency, JQ35 was tested for *in vivo* pharmacokinetic properties and pharmacodynamic efficacy in a xenograft model of NMC. The half-life of JQ1 is less than one hour¹ limiting its therapeutic potential and requiring frequent dosing. JQ35 was found to have 5.61 hour half-life by IP injection which corresponds to the IV value. This enables significantly improved exposure of cells to drug as compared to JQ1 with an IP half-life of 1.24 hours (Figure 1.12A). Moreover, JQ35 is fully soluble in saline eschewing the need for formulation which greatly improves the ease of preparation for treatment and potential irritation at injection sites. Moreover, during the forty two day study there was no significant loss of body mass for the treated versus vehicle only mice indicating a relatively well tolerated compound (Figure 1.12B). Previous studies have used 50mpk¹ QD or even up to 50mpk BID^{14,27} JQ1 to see efficacy. However, even 20mpk QD dosing of JQ35 shows durable tumor regression with an even more pronounced effect at 50mpk as measured by bioluminescent imaging of the mice (Figure 1.12C). A Kaplan-Meier plot showed significant prolongation in survival ($p < 0.01$ log rank test) (Figure 1.12D).

Histology for H&E to show overall morphology, Ki67 to mark proliferating cells, TUNEL to stain apoptotic cells, and the keratin stain Ae1/Ae3 to mark positive differentiation of the tumor further support a strong pharmacodynamic effect (Figure 1.12E). Vehicle treatment shows small, poorly differentiated cells with strong Ki67, minimal TUNEL staining, and weak Ae1/Ae3. In a dose

dependent manner with treatment, the cells take on epithelial characteristics with larger cytosol to nuclear size ratios, reduced proliferation, increased apoptosis, and very strong Ae1/Ae3 indicating differentiation consistent with previous findings⁴⁴. In fact, at 50mg/kg, the tumor size and cellular density is greatly reduced creating the large enucleated regions in the histology. This further supports the genetic findings that BET inhibition reverses EMT.

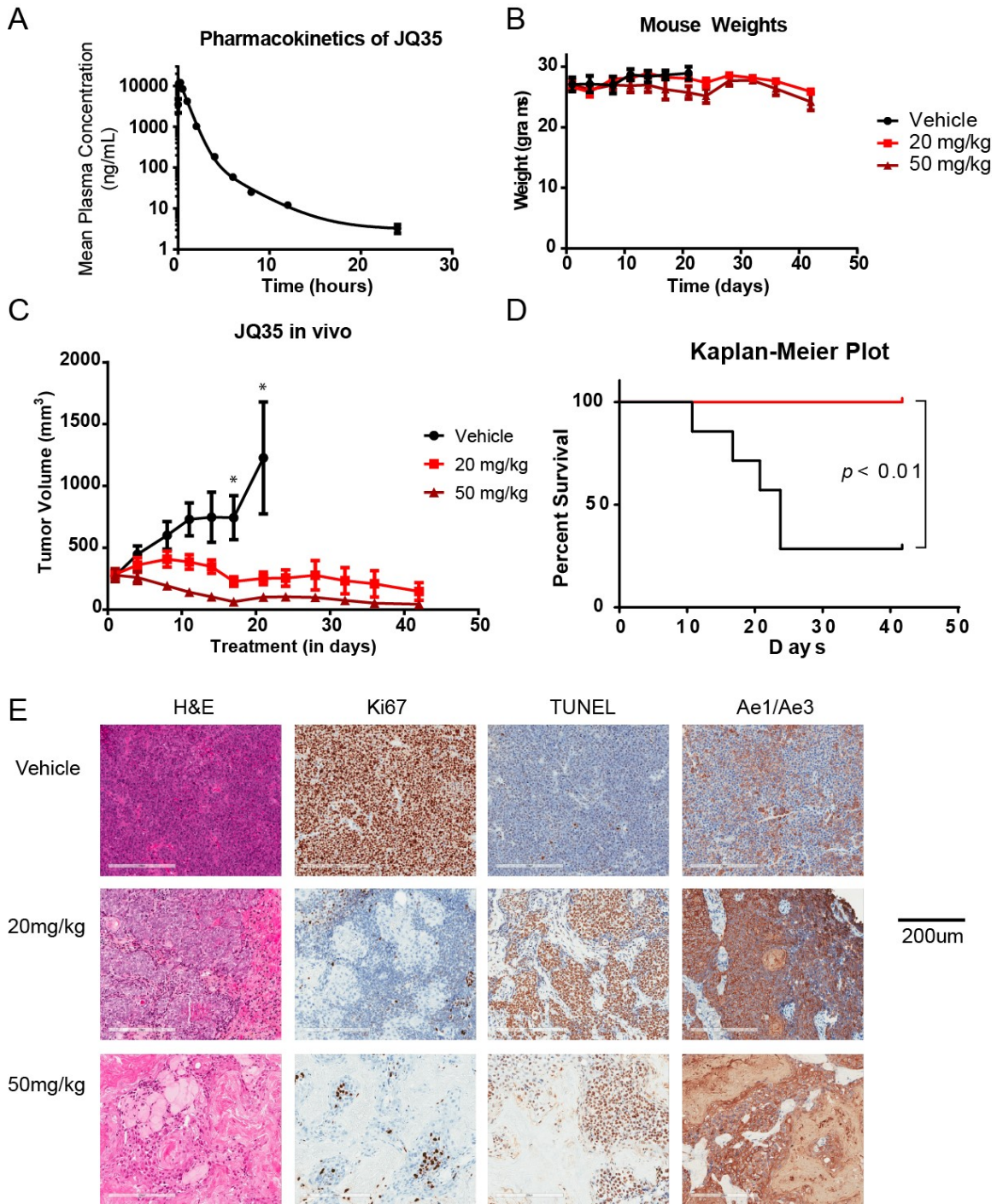


Figure 1.12: *In vivo* studies (A) Pharmacokinetics study of JQ35 in mice for IP injection followed with blood samples by MS. (B) Average weights with SEM for vehicle and treated mice. (C) Tumor volume over time with JQ35 treatment at 20 and 50 mpk QD versus Vehicle. Asterisk shows significance by t-test. (D) Survival of 20mpk versus Vehicle groups. Significance analyzed by Log-Rank test. (E) Histology for H&E, Ki67 (proliferation), TUNEL (apoptosis), and Ae1/Ae3 (keratin, differentiation). Scale bar of 200um shown.

Discussion

Following our work on JQ1, we sought to develop an advanced probe with improved chemical and biological properties. While BET bromodomains have been reported in the literature, we sought to fully understand the structure activity relationships around thienodiazepine binding to the acetyl lysine recognition site and to build a probe capable of enhanced *in vivo* activity. JQ1 is an excellent tool compound but has less than one hour half-life and requires formulation in DMSO and cyclodextrin depending on the route of administration. Thus, a concerted effort to build a next-generation compound was required to provide an agent capable of improve *in vivo* efficacy and potential for human clinical use.

To this end, a high throughput assay was developed to facilitate rapid analysis of compounds. The system incorporates a biotinylated probe for BET bromodomains that can also be used in protein pull downs and Chem-seq, where biotinylated small molecules can be used in place of antibodies in ChIP-seq³¹. The AlphaScreen based system proved robust enough, working over a range of concentrations for a BET family members and sites in 384 well plate format. In addition, the assay even worked in 1536 paving the way for efficient HTS in the future. However, in this application it was primarily applied for replicate ten point dose response formats that generate relative IC50s values that were surprisingly close to those determined by ITC. Ongoing work has deployed this assay for an HTS campaign on nearly 70,000 compounds in an effort to find novel chemical space for acetyl-lysine mimetics both as BET inhibitors and to potentially enable lead hopping.

Our exploration of the JQ1 scaffold concluded that the C6 position is the most amenable to diverse modifications and offered the best opportunity for improving on JQ1's chemical properties. A large, diverse library of 400 compounds was generated using the aldehyde-hydrazide coupling strategy previously employed by our lab for HDAC inhibitors³⁸. In this instance, we doubled the size of the library and once again succeeded in finding a direction for focused medicinal chemistry efforts. From this library, it was determined that improved binding favored nitrogen containing heterocycles and disfavored negative charge. The charge relationship fits with the presence of aspartic acid residues on the loops around the binding pocket. Based on this observation a series of compounds was developed ultimately leading to JQ35 which exhibits greatly improved solubility, potency, and half-life. Thus, the methodology of improving screening hits by building a diversity library around a biasing element followed by iterative medicinal chemistry has proven highly effective and expands beyond what could have been inferred in a linear exploration.

Nut Midline Carcinoma remains a cancer of unknown origin that is driven by an oncogenic translocation of Nut and BRD4 or BRD3. Moreover, it was previously established that BET bromodomain inhibition acts to reverse this oncogenic program based on the altered phenotype seen after treatment. Using JQ35 coupled with transcriptional and ChIP-seq analysis a reversal of an EMT signature was found. This is consistent with the invasive and aggressive nature of NMC having taken on mesenchymal and stem like characteristics. JQ35 blocks the oncogene without totally disrupting or halting transcription, allowing

the cell to redirect RNA Pol II to genes more consistent with its epithelial origin leading to the expression of keratin, cytosol expansion, and growth arrest previously observed.

Indeed, JQ35 strongly induces this phenotype *in vivo* in a dose dependent manner. Actual regression of the tumor was measured as was a significant prolongation of survival. Furthermore, histology found a profound phenotypic change with less proliferation, more apoptosis, massive upregulation of keratin consistent with epithelial cells, and a large expansion of the cytosol relative to the small poorly differentiated cancer cells in the vehicle only.

We present a next-generation optimized BET bromodomain inhibitor with improved *in vivo* properties. In addition, we have developed novel, robust assays and pull-down tools enabling further research on bromodomain biochemistry and biology. While probe molecules are incredibly useful for interrogating biology in an academic setting, drug-like properties must be achieved to enable potential therapeutics to take shape. With the overall likelihood of approval in oncology is only 6.7% from Phase I trials⁴⁵ it is vital to take multiple shots on validated targets for bench research to reach bedside treatments.

- 1 Filippakopoulos, P. *et al.* Selective inhibition of BET bromodomains. *Nature* **468**, 1067-1073, doi:10.1038/nature09504 (2010).
- 2 Sanchez, R. & Zhou, M. M. The role of human bromodomains in chromatin biology and gene transcription. *Current opinion in drug discovery & development* **12**, 659-665 (2009).

- 3 Schreiber, S. L. & Bernstein, B. E. Signaling network model of chromatin. *Cell* **111**, 771-778 (2002).
- 4 Prinjha, R. K., Witherington, J. & Lee, K. Place your BETs: the therapeutic potential of bromodomains. *Trends in pharmacological sciences* **33**, 146-153, doi:10.1016/j.tips.2011.12.002 (2012).
- 5 Mujtaba, S. *et al.* Structural mechanism of the bromodomain of the coactivator CBP in p53 transcriptional activation. *Molecular cell* **13**, 251-263 (2004).
- 6 Mujtaba, S., Zeng, L. & Zhou, M. M. Structure and acetyl-lysine recognition of the bromodomain. *Oncogene* **26**, 5521-5527, doi:10.1038/sj.onc.1210618 (2007).
- 7 Filippakopoulos, P. *et al.* Histone recognition and large-scale structural analysis of the human bromodomain family. *Cell* **149**, 214-231, doi:10.1016/j.cell.2012.02.013 (2012).
- 8 Wu, S. Y. & Chiang, C. M. The double bromodomain-containing chromatin adaptor Brd4 and transcriptional regulation. *J Biol Chem* **282**, 13141-13145, doi:DOI 10.1071/jbc.R700001200 (2007).
- 9 Yang, Z. *et al.* Recruitment of P-TEFb for stimulation of transcriptional elongation by the bromodomain protein Brd4. *Molecular cell* **19**, 535-545, doi:10.1016/j.molcel.2005.06.029 (2005).
- 10 Yang, Z., He, N. & Zhou, Q. Brd4 recruits P-TEFb to chromosomes at late mitosis to promote G1 gene expression and cell cycle progression. *Molecular and cellular biology* **28**, 967-976, doi:10.1128/MCB.01020-07 (2008).
- 11 Schroder, S. *et al.* Two-pronged binding with bromodomain-containing protein 4 liberates positive transcription elongation factor b from inactive ribonucleoprotein complexes. *J Biol Chem* **287**, 1090-1099, doi:10.1074/jbc.M111.282855 (2012).
- 12 Rahman, S. *et al.* The Brd4 extraterminal domain confers transcription activation independent of pTEFb by recruiting multiple proteins, including NSD3. *Molecular and cellular biology* **31**, 2641-2652, doi:10.1128/MCB.01341-10 (2011).
- 13 Dey, A., Chitsaz, F., Abbasi, A., Misteli, T. & Ozato, K. The double bromodomain protein Brd4 binds to acetylated chromatin during interphase and mitosis. *Proceedings of the National Academy of Sciences of the United States of America* **100**, 8758-8763, doi:10.1073/pnas.1433065100 (2003).
- 14 Chapuy, B. *et al.* Discovery and characterization of super-enhancer-associated dependencies in diffuse large B cell lymphoma. *Cancer cell* **24**, 777-790, doi:10.1016/j.ccr.2013.11.003 (2013).
- 15 Gallenkamp, D., Gelato, K. A., Haendler, B. & Weinmann, H. Bromodomains and Their Pharmacological Inhibitors. *ChemMedChem*, doi:10.1002/cmdc.201300434 (2014).
- 16 Nicodeme, E. *et al.* Suppression of inflammation by a synthetic histone mimic. *Nature* **468**, 1119-1123, doi:10.1038/nature09589 (2010).
- 17 Seal, J. *et al.* Identification of a novel series of BET family bromodomain inhibitors: Binding mode and profile of I-BET151 (GSK1210151A). *Bioorganic & medicinal chemistry letters* **22**, 2968-2972, doi:10.1016/j.bmcl.2012.02.041 (2012).

- 18 Bamborough, P. *et al.* Fragment-based discovery of bromodomain inhibitors part 2: optimization of phenylisoxazole sulfonamides. *Journal of medicinal chemistry* **55**, 587-596, doi:10.1021/jm201283q (2012).
- 19 Chung, C. W., Dean, A. W., Woolven, J. M. & Bamborough, P. Fragment-based discovery of bromodomain inhibitors part 1: inhibitor binding modes and implications for lead discovery. *Journal of medicinal chemistry* **55**, 576-586, doi:10.1021/jm201320w (2012).
- 20 Hewings, D. S. *et al.* 3,5-dimethylisoxazoles act as acetyl-lysine-mimetic bromodomain ligands. *Journal of medicinal chemistry* **54**, 6761-6770, doi:10.1021/jm200640v (2011).
- 21 Filippakopoulos, P. *et al.* Benzodiazepines and benzotriazepines as protein interaction inhibitors targeting bromodomains of the BET family. *Bioorganic & medicinal chemistry* **20**, 1878-1886, doi:10.1016/j.bmc.2011.10.080 (2012).
- 22 Dawson, M. A. *et al.* Inhibition of BET recruitment to chromatin as an effective treatment for MLL-fusion leukaemia. *Nature* **478**, 529-533, doi:10.1038/nature10509 (2011).
- 23 Borah, J. C. *et al.* A small molecule binding to the coactivator CREB-binding protein blocks apoptosis in cardiomyocytes. *Chemistry & biology* **18**, 531-541, doi:10.1016/j.chembiol.2010.12.021 (2011).
- 24 Ott, C. J. *et al.* BET bromodomain inhibition targets both c-MYC and IL7R in high-risk acute lymphoblastic leukemia. *Blood*, doi:10.1182/blood-2012-02-413021 (2012).
- 25 Delmore, J. E. *et al.* BET Bromodomain Inhibition as a Therapeutic Strategy to Target c-Myc. *Cell* **146**, 904-917, doi:S0092-8674(11)00943-3 [pii] 10.1016/j.cell.2011.08.017 (2011).
- 26 Mertz, J. A. *et al.* Targeting MYC dependence in cancer by inhibiting BET bromodomains. *Proceedings of the National Academy of Sciences of the United States of America* **108**, 16669-16674, doi:1108190108 [pii] 10.1073/pnas.1108190108 (2011).
- 27 Cheng, Z. *et al.* Inhibition of BET bromodomain targets genetically diverse glioblastoma. *Clinical cancer research : an official journal of the American Association for Cancer Research* **19**, 1748-1759, doi:10.1158/1078-0432.CCR-12-3066 (2013).
- 28 Puissant, A. *et al.* Targeting MYCN in neuroblastoma by BET bromodomain inhibition. *Cancer discovery* **3**, 308-323, doi:10.1158/2159-8290.CD-12-0418 (2013).
- 29 Wang, X., Helfer, C. M., Pancholi, N., Bradner, J. E. & You, J. Recruitment of Brd4 to HPV16 DNA replication complex is essential for viral DNA replication. *J Virol*, doi:JVI.03068-12 [pii] 10.1128/JVI.03068-12 (2013).
- 30 Boehm, D. *et al.* BET bromodomain-targeting compounds reactivate HIV from latency via a Tat-independent mechanism. *Cell Cycle* **12**, 452-462, doi:10.4161/cc.23309 23309 [pii] (2013).
- 31 Anders, L. *et al.* Genome-wide localization of small molecules. *Nature biotechnology* **32**, 92-96, doi:10.1038/nbt.2776 (2014).

- 32 Thiery, J. P. Epithelial-mesenchymal transitions in tumour progression. *Nature reviews. Cancer* **2**, 442-454, doi:10.1038/nrc822 (2002).
- 33 Kalluri, R. & Weinberg, R. A. The basics of epithelial-mesenchymal transition. *The Journal of clinical investigation* **119**, 1420-1428, doi:10.1172/JCI39104 (2009).
- 34 Nieto, M. A. Epithelial plasticity: a common theme in embryonic and cancer cells. *Science* **342**, 1234850, doi:10.1126/science.1234850 (2013).
- 35 Gerecke, M. Chemical structure and properties of midazolam compared with other benzodiazepines. *Br J Clin Pharmacol* **16 Suppl 1**, 11S-16S (1983).
- 36 Walser, A. *et al.* Thienotriazolodiazepines as platelet-activating factor antagonists. Steric limitations for the substituent in position 2. *Journal of medicinal chemistry* **34**, 1440-1446 (1991).
- 37 Mirguet, O. *et al.* Discovery of epigenetic regulator I-BET762: lead optimization to afford a clinical candidate inhibitor of the BET bromodomains. *J Med Chem* **56**, 7501-7515, doi:10.1021/jm401088k (2013).
- 38 Bradner, J. E. *et al.* Chemical phylogenetics of histone deacetylases. *Nat Chem Biol* **6**, 238-243, doi:nchembio.313 [pii] 10.1038/nchembio.313 (2010).
- 39 Yan, J., Diaz, J., Jiao, J., Wang, R. & You, J. Perturbation of BRD4 protein function by BRD4-NUT protein abrogates cellular differentiation in NUT midline carcinoma. *J Biol Chem* **286**, 27663-27675, doi:10.1074/jbc.M111.246975 M111.246975 [pii] (2011).
- 40 Schwartz, B. E. *et al.* Differentiation of NUT midline carcinoma by epigenomic reprogramming. *Cancer Res* **71**, 2686-2696, doi:10.1158/0008-5472.CAN-10-3513 (2011).
- 41 Ott, C. J. *et al.* BET bromodomain inhibition targets both c-Myc and IL7R in high-risk acute lymphoblastic leukemia. *Blood* **120**, 2843-2852, doi:10.1182/blood-2012-02-413021 blood-2012-02-413021 [pii] (2012).
- 42 Sarrio, D. *et al.* Epithelial-mesenchymal transition in breast cancer relates to the basal-like phenotype. *Cancer Res* **68**, 989-997, doi:10.1158/0008-5472.CAN-07-2017 (2008).
- 43 Jechlinger, M. *et al.* Expression profiling of epithelial plasticity in tumor progression. *Oncogene* **22**, 7155-7169, doi:10.1038/sj.onc.1206887 (2003).
- 44 Bunkoczi, G. *et al.* Structural and functional characterization of the human protein kinase ASK1. *Structure* **15**, 1215-1226, doi:10.1016/j.str.2007.08.011 (2007).
- 45 Hay, M., Thomas, D. W., Craighead, J. L., Economides, C. & Rosenthal, J. Clinical development success rates for investigational drugs. *Nature biotechnology* **32**, 40-51, doi:10.1038/nbt.2786 (2014).

Chapter 2

Development of Novel 3,5-Dimethylisoxazoles as Selective Inhibitors of BET-bromodomain proteins

Contributors:

Michael McKeown, Dan Shaw, Harry Fu, Shuai Liu, Jason Marineau, Yibo Huang, Xiaofeng Zhang, Dennis Buckley, Charles Lin, Asha Kadam, Zijuan Zhang, James Bradner, Jun Qi, Wei Zhang

Introduction:

As part of an effort to expand our capabilities on bromodomains, our lab formed a collaboration with Zhang lab at Umass Boston. Based on our previous work with JQ1 derivatives related to the JQ35 work, we had a suite of assays and technological methods prepared to pursue targets. However, we recognized a need for more chemical bandwidth to search for new chemical series and structures to enable expansion into new targets as well as provide more chemical options for development on the BET family.

From the efforts directed at generating JQ35 a robust platform was put in place. Over the course of several years, I performed biochemical and cellular assays for the project. This utilized the previously described AlphaScreen assays and cellular viability on Nut Midline Carcinoma cells. In addition, I used structural information and hypotheses derived from the SAR from our screening efforts in order to advise the chemists at Umass as to what new structures to pursue. Given that the capacity for screening and lead characterization far outstripped synthetic capabilities in house, I very much appreciated the extra bandwidth placed on chemistry. This proved to be a very synergistic and productive relationship.

Out of these collaborative discussions, a novel series of inhibitors was born. While advanced BET bromodomain are available, this new chemistry gave us insights into what features were allowable as bromodomain inhibitors, expanded our inventory of chemical matter, and gave us a first ever foothold against TAF1. Ongoing work hopes to further lead hop, find new and diverse chemistries, and to improve the current chemical series.

Contribution:

MRM wrote text, formatted figures, performed and executed biochemical assays. DS assisted in text assembly. HF, SL, JM, YH, XZ, DB, ZZ, and AK performed chemical synthesis. CL helped with graphic design. JB, JQ, and WZ oversaw research.

Background:

Chemical modifications to chromatin are critical to orchestrating transcriptional activity. Histone post-translational alterations effected by chromatin-modifying enzymes, known as “writers,” lead to both transcription factor localization and gene regulatory complex formation¹⁻⁴. The diverse set of chromatin marks are interpreted by “reader” proteins responsible for real-time transmission of histone marks to transcriptional consequence by mediating the local area network of transcription factors, polymerases, and remodeling enzymes². As end effectors of signaling pathways, regulators of transcription, and potential cancer dependencies, epigenetic reader proteins are attractive therapeutic targets in cancer⁵. However, these events are primarily mediated by protein-protein interactions, which are conventionally considered difficult to inhibit⁶. To date, there are few high-quality chemical probes available to study such interactions⁷. Recent work demonstrates that the chromatin-associated bromodomain and extra-terminal (BET) domain protein family are susceptible to displacement by small molecules capable of mimicking the contacts between acetyl-lysine (KAc) on histones and the binding pocket of the bromodomain⁸⁻¹¹.

The BET family consists of BRD2, BRD3, BRD4 and BRDT, which are characterized by two tandem bromodomains and an external domain. They act as readers of lysine acetylation with a conserved four alpha helix bundle structural motif and a hydrogen bond forming asparagine that mediates the interaction with its peptide substrate¹²⁻¹⁶. In addition to binding histones, the BET family members act as scaffolds for complex formation to regulate transcription and cell cycle progression¹⁶. In particular, the BET bromodomain family is an important transcriptional coactivator for promoting

RNA Polymerase II (POL II) pause release and transcriptional elongation through recruitment of the positive transcription elongation factor B (pTEFB) and the mediator complex¹⁶⁻¹⁹. BRD4 interacts directly with pTEFB through its second bromodomain site binding to CyclinT and promotes elongation independent of pTEFB by increasing the effective molarity of transcription factors^{20,21}. Indeed, BRD4 colocalizes with sites of active transcription during mitosis²² and helps control the reactivation of transcription from the M to G1 phase of cell cycle by mediating decompaction of chromatin^{19,23}.

BET deregulation is observed in various cancers, and notably implicated in the pathogenesis of NUT midline carcinoma^{16,24}. This carcinoma is defined by the recurrent t(15;19) chromosomal translocation, resulting in aberrant expression of the tandem N-terminal bromodomains of BRD4 as an in-frame fusion with the NUT protein²⁴.

Targeting xenotransplanted patient-derived cell lines with recently developed thienodiazepine-based BET bromodomain inhibitor, JQ1, established the therapeutic potential of BRD4 inhibition⁹. Researchers observed complete differentiation of tumor cells to epithelial cells and a significant survival advantage in treated animals.⁹ **JQ1** has demonstrated potent anti-proliferative efficacy in models of multiple myeloma, acute lymphoid leukemia, and acute myeloid leukemia⁸⁻¹¹.

With such promising studies related to drugging the epigenome, it is of the utmost importance to develop new chemistry capable of reaching these targets. Early-stage drug molecules, known as “chemical probes,” are invaluable tools in understanding disease⁷. Complex, non-scalable and wasteful reactions can significantly impede iterative screening efforts. Techniques involving the use of fluororous reagents have shown great versatility, high-yield, rapid deployment, and are relatively eco-

friendly. Complex molecules may be synthesized in multi-component reactions with perfluoroalkyl “phase tags” which can be used to facilitate purification by fluororous solid-phase extraction (F-SPE).²⁵ Subsequent Suzuki-type reactions may replace the fluororous tag to form a biaryl compound.²⁶ Benefits of such reaction include high yielding reactivity with facile purification. Reactions have proven viable to create substituted hydantoins,²⁷ imidazo[1,2-a]-pyridines,²⁸ diazepines²⁹ and others.^{30,31} Such heterocyclic compounds form easily substitutable, drug-like scaffolds for the discovery of probe compounds.

We report a novel class of bromodomain inhibiting compounds using the recently identified 3,5-dimethylisoxazole³² biasing element. Drawing upon previously developed screening capabilities and robust fluororous chemical synthesis, we have rapidly diversified and optimized a set of potent and highly specific inhibitors. In addition to demonstrating a new approach to targeting the BET bromodomains, these compounds and near derivatives could create opportunities to drug other bromodomain-containing of proteins.

RESULTS & DISCUSSION

Analysis of existing small-molecule bromodomain inhibitors, shown in Figure 2.1A, has defined a structure-function model in which the competitive small molecule binds through two chemical features: an acetyl-lysine mimetic warhead (red) and a core region with appending surface-recognition features (black). Kac mimetics, such as the triazole ring in **JQ1** and the 3,5-dimethylisoxazole ring in **iBET151**, form a highly specific hydrogen bond to the conserved asparagine in bromodomains. The core of the

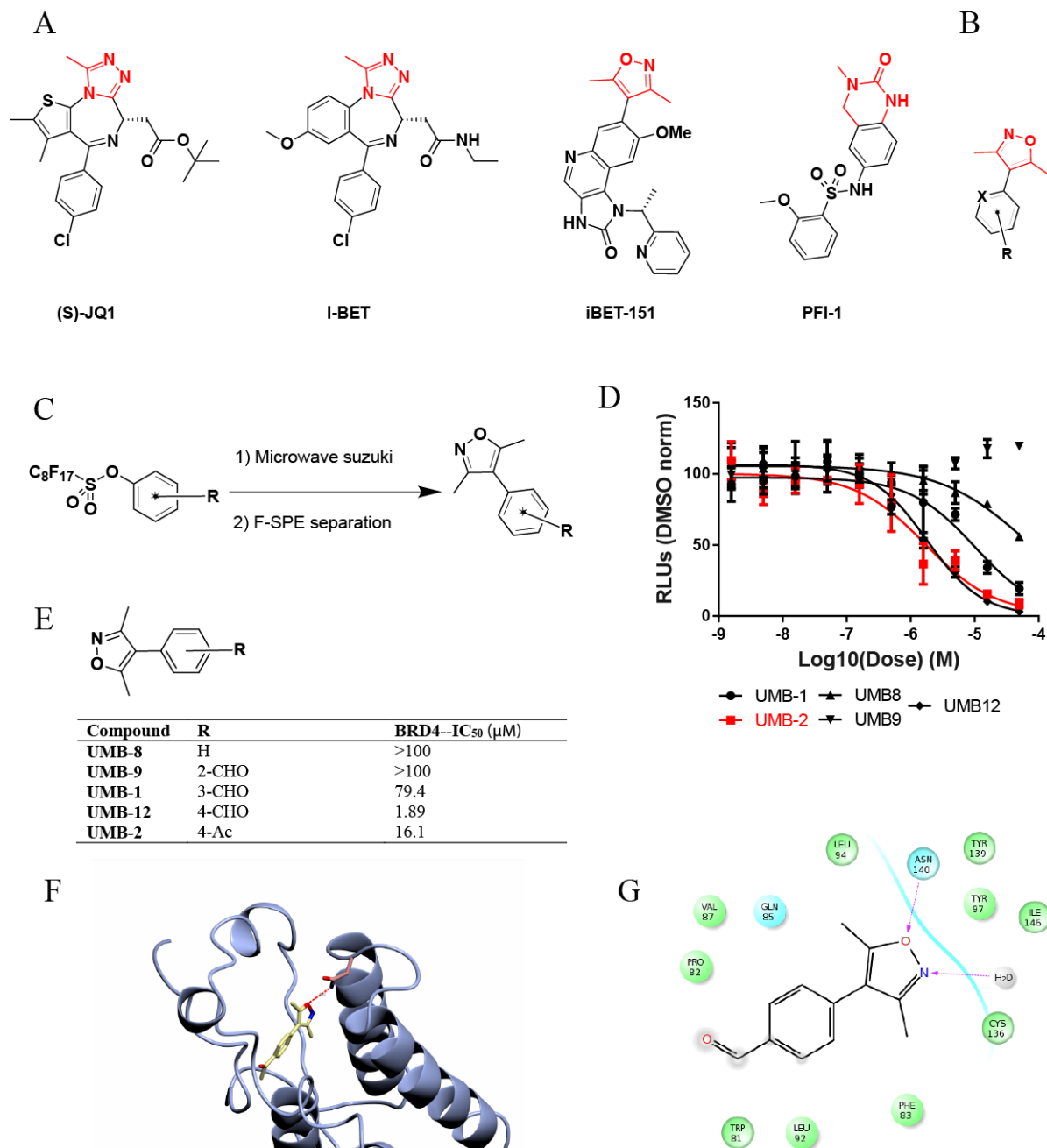


Figure 2.1: Approach to chemistry. Chemical strategies to inhibit BET bromodomain proteins. **A** Existing BET bromodomain inhibitors with biasing moiety in red. **B** Synthetic strategy for the creation of small fragments based on dimethyl isoxazole based BET bromodomain biasing moiety (red). X signifies varied heteroatoms and R signifies varied substituents. **C** Perfluoroalkyl based synthetic strategy. **D** Small fragment dimethylisoxazole inhibitors with potency values indicated. **E** Inhibitory curves for small fragment inhibitors. **F** Docking of UMB-12 into BRD4 crystal structure. **G** Ligand interaction diagram of UMB-12.

molecule establishes shape complementarity with the contour of the binding pocket to increase binding affinity primarily through steric interactions. Appending groups provide an opportunity to enhance potency and selectivity via surface and loop region interactions. The 3,5-dimethylisoxazole head group of **IBET151** was identified as a promising and chemically accessible biasing moiety for further development as a chemical probe. Our screening strategy created an extensive series of diverse chemical features attached to the 4-position of the 3,5-dimethylisoxazole (Figure 2.1B). As a starting point, we focused on small, ligand efficient compounds that could serve as starting points for further derivatization.

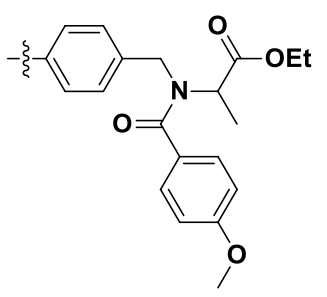
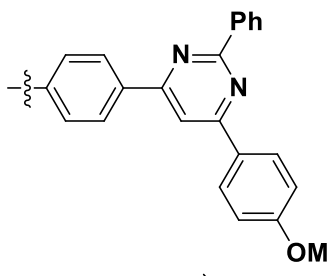
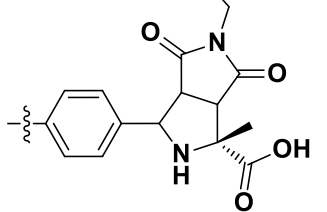
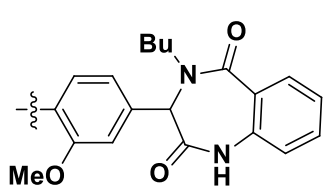
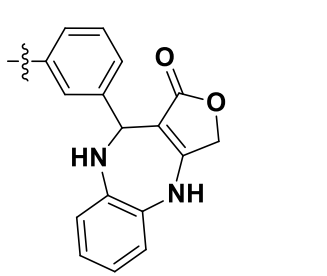
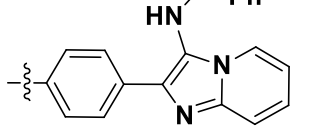
This approach to library development was empowered by recent advances in use of perfluoroalkyl substituents to enable efficient Suzuki-type ring coupling reactions, shown in Figure 2.1C. Purification of reaction intermediates is greatly facilitated by F-SPE. In this case, aryl perfluorooctylsulfonates ($\text{ArOSO}_2(\text{CF}_2)_7\text{CF}_3$) were reacted with 3,5-dimethylisoxazole-4-boronic acid pinacol esters to produce a low-molecular weight chemical series. The resulting compounds were purified using F-SPE. Initial compounds included positional isomers of carbonyl functionalities around the phenyl ring system (Figure 2.1D). Compound potency was assessed by relative IC_{50} potency determined by an AlphaScreen biotin-JQ1 competition assay (Figure 2.1E). IC_{50} values were found to be highly dependent on the steric arrangement of functional groups around the phenyl ring. Ortho- and meta-aldehyde substitutions were poorly tolerated, while a para-aldehyde resulted in excellent potency of 1.89 μM with a ligand efficiency of 54%. Substitution with the more chemically sTable 2.para-acetyl group resulted in a 10-fold

reduction in potency. Previous study of similar compounds had only explored variation at the 3- and 5-ring positions.

We performed computational modeling to better understand the modality of binding and inform further medicinal chemistry (Figure 2.1F). Using previously published crystal structures of both JQ1 and iBET151, we were able to dock fragments into the structure^{9,33}. As is the case with iBET151, UMB-2 binds through a conserved hydrogen bond with D-140 through the ring oxygen, while the ring nitrogen coordinates through a structured water interacting with the hydroxyl group of Y-97 (Figure 2.1G). Based on this interaction, we proceeded to build off the 4-position of the phenyl ring to improve potency by optimizing protein surface interactions near the BC loop region.

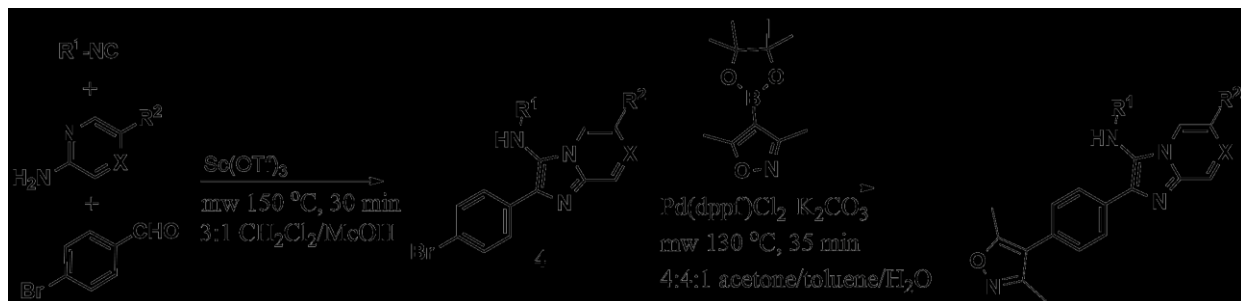
A diverse set of chemical scaffolds was synthesized using reactions previously developed around fluororous-tagged multicomponent reactions (Table 2.1). These reactions create structural diversity by changing the substituent groups on each fractional component, allowing generation of diverse small-molecule libraries around a biasing element. The perfluoroalkyl tags can substituted with a binding motif of choice via Suzuki coupling (Figure 2.1C).²⁶ Synthesized compounds included tertiary amines, pyrimidines and fused heterocyclic ring systems in order to explore the optimal shape for exploiting protein-inhibitor contour interactions. In addition to biochemical IC₅₀, these compounds were selectively evaluated in a BRD4-dependent cell viability study. EC₅₀ was collected by assessing viability using PerkinElmer ATPlite kits against the BRD4-dependent Nut-Midline Carcinoma line 797. The para-imidazo[1,2-*a*]pyridine scaffold²⁸ (UMB-11) was found to be a promising lead with biochemical and cellular inhibitory values of 11.0 μ M and 14.1 μ M, respectively. In addition, the UMB-11 scaffold is

Table 2.1: Exploration of compound scaffold region

| Compound | Ar | BRD4--IC ₅₀ (μM) | 797--IC ₅₀ (μM) |
|----------|---|-----------------------------|----------------------------|
| UMB-5 |  | 16.3 | |
| UMB-13 |  | 69.9 | >100 |
| UMB-17 |  | >100 | 9.42 |
| UMB-18 |  | 13.0 | 9.91 |
| UMB-27 |  | 2.05 | >100 |
| UMB-11 |  | 11.0 | 14.1 |

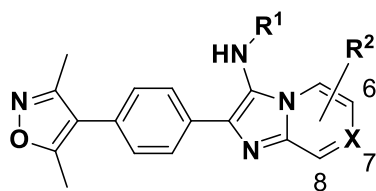
accessible at a variety of positions for diversification to drive potency and understanding of SAR.

Having picked a core scaffold in UMB11, we built a focused library of compounds to optimize placement of heteroatoms and appending groups. Synthesis of the eventual lead compound UMB-32 is shown in Scheme 1 as an exemplar of the route used to assemble the focused SAR series. The compound was synthesized in a two-step reaction. The first step included combination of *t*-butylisocyanide, 2-aminopyrazine, and 4-bromobenzaldehyde. The reaction is catalyzed by scandium triflate and microwaved at 150°C for thirty minute in 3:1 dichloromethane / methanol. Flash chromatography yielded the pure product 80%. This intermediate was then coupled to 3,5-dimethylisoxazole-4-boronic acid pinacol ester in a Suzuki coupling. The resulting crude mixture was purified by flash chromatography with yield 57%.



Scheme 2.1: Synthesis of UMB11 near analogs.

Analogs were synthesized similarly to explore the functional role of both sterics and electronics of the fused bicyclic scaffold on inhibitor function, shown in Table 2.2. Variations of R¹ from UMB-11's benzyl group to bulky, non-aromatic groups like cyclohexane (UMB-28) and *t*-Bu (UMB-29) improved potency. An acid at the R¹ position (DB-1-064) completely inactivated the compound. Appending R² groups at the 6, 7, and

Table 2.2: Elaboration of imidazopyridine scaffold

| Compound | R ¹ | R ² | X | BRD4--IC ₅₀ (μM) | 797--IC ₅₀ (μM) |
|----------|--|-----------------------------------|-----|-----------------------------|----------------------------|
| UMB-65 | H | H | CH | 3.89 | |
| UMB-6 | Bn | 6-Me | CH | >100 | |
| UMB-20 | Bn | 6-Cl | CH | 11.8 | 18.4 |
| UMB-21 | Bn | H | 7-N | 18.8 | 49.1 |
| UMB-28 | cyclohexane | H | CH | 0.904 | 5.07 |
| UMB-30 | 4-(OMe)Ph | H | CH | 2.76 | 7.36 |
| UMB-23 | 4-(OMe)Ph | 6-Cl | CH | 31.5 | 20.7 |
| UMB-24 | 4-(OMe)Ph | 7-OMe | CH | 2.89 | 11.8 |
| UMB-25 | 4-(OMe)Ph | H | 7-N | 7.86 | 32.8 |
| UMB-62 | (S)-1-PhEt | H | 7-N | 2.86 | |
| UMB-29 | <i>t</i> -Bu | H | CH | 0.479 | 2.04 |
| UMB-31 | <i>t</i> -Bu | 6-Cl | CH | 1.17 | 2.19 |
| UMB-76 | <i>t</i> -Bu | 6-Me | CH | 3.17 | |
| UMB-77 | <i>t</i> -Bu | 8-CF ₃ | CH | 11.9 | |
| UMB-82 | <i>t</i> -Bu | 6-CO ₂ CH ₂ | CH | 1.62 | |
| UMB-83 | <i>t</i> -Bu | 6-COOH | CH | 0.968 | |
| UMB-56 | <i>t</i> -Bu | H | 6-N | 20.7 | 2.06 |
| UMB-32 | <i>t</i> -Bu | H | 7-N | 0.637 | 0.724 |
| UMB-84 | <i>t</i> -Bu | H | 8-N | 0.860 | |
| UMB-57 | <i>i</i> -Pr | H | 7-N | 0.807 | 0.494 |
| UMB-61 | <i>n</i> -Bu | H | 7-N | 1.66 | |
| DB-1-064 | -CH ₂ CO ₂ H | H | 7-N | >100 | |
| DB-1-038 | -CH ₂ CO ₂ Et | H | 7-N | 4.53 | |
| UMB-60 | -CH ₂ CO ₂ <i>t</i> Bu | H | 7-N | 4.96 | |

8 positions of the fused ring system universally decreased potency compared to parent compounds. Ring-nitrogens at the 7 and 8 position (UMB-32, and UMB-84, respectively) resulted in little biochemical potency change. A 6-position ring-nitrogen reduced compound potency from 479 nM (UMB-29) to 20 μ M (UMB-56) potency. Cellular potency, however, modestly improved between compound UMB-29 and UMB-32 upon substitution of a 7-N. For this reason, UMB-32 emerged as our lead compound.

Limited structural study around the linking phenyl ring is shown in Table 2.3. Substitution of the phenyl ring for pyridine resulted in decreased potency (UMB-53-54) and the addition of electron-withdrawing fluorine (UMB-55) was detrimental as well. Electron-donating methoxy substituents appear to be mildly beneficial in biochemical assays. Additional work regarding this linking part of the molecule will be a focus of continued medicinal chemistry.

The potency of UMB-32 was driven by two key changes from UMB-11 (Figure 2.2A). UMB-32 has substituted t-Bu for benzyl and inserted a 7-N. Comparison of UMB-11, UMB-21 and UMB-32 show the critical substitutions in the development of UMB-32 which led to an improved biochemical IC₅₀ (Figure 2.2B top). Docking of UMB-32 into the JQ1 crystal structure, (Figure 2.2D) recapitulates binding similar to that of the 3,5-dimethylisoxazole fragment. The dimethylisoxazole makes the expected hydrogen bonds with the conserved asparagine and critical waters. The additional heteroatom at 7-N is likely solvent exposed. Notably, the t-Bu group fits into a pocket between the BC loop and tryptophan shelf. Also, the secondary amine can possibly participate in favorable ionic interaction to the D-145 residue (Figure 2.2E).

Figure 2.2: Lead series biochemistry. UMB-32 is a potent, selective inhibitor of BRD4. **A** Selected compounds leading to UMB-32. **B** Representative biochemical inhibitory curves (top) and 797 viability (bottom). **C** ITC experiment of BRD4 titrated into UMB-32 solution. **D** Docking of UMB-32 in BRD4 crystal structure. **E** Ligand interaction diagram of UMB-32 in BRD4 crystal. **F** Evaluation of UMB-11 and UMB-32 compound selectivity against a panel of bromodomains.

Figure 2.2 (Continued)

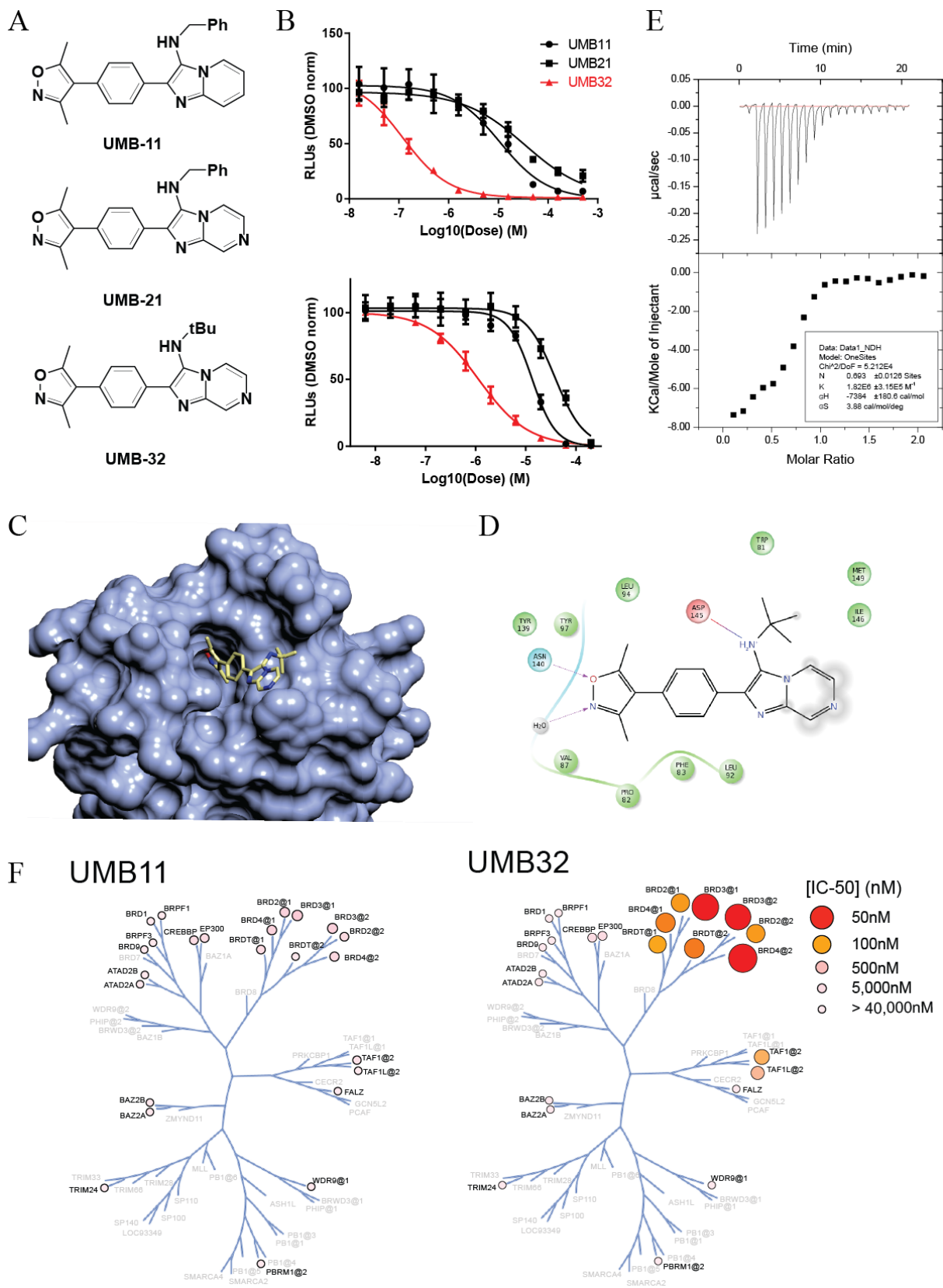
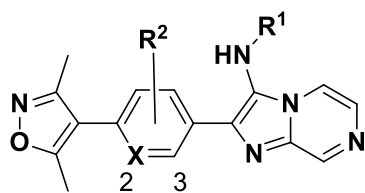


Table 2.3: Variations to UMB-32 linker



| Compound | R ¹ | R ² | X | BRD4--IC ₅₀ (μM) | 797--IC ₅₀ (μM) |
|----------|----------------|----------------|-----|-----------------------------|----------------------------|
| UMB-53 | <i>t</i> -Bu | H | 2-N | 51.9 | >100 |
| UMB-54 | <i>t</i> -Bu | H | 3-N | 12.9 | 8.29 |
| UMB-55 | <i>t</i> -Bu | 2-F | CH | 13.0 | 12.8 |
| UMB-58 | <i>t</i> -Bu | 3-OMe | CH | 0.562 | |
| UMB-59 | <i>i</i> -Pr | 3-OMe | CH | 0.474 | |

Characterization of UMB-32 by isothermal titration calorimetry (ITC) against BRD4 site 1 further supported the biochemical affinity (Figure 2.1E). The resultant K_d was shown to be 550 nM, in good agreement with the biochemical measurements. The binding process is shown to be exothermic and positively entropic with a 1:1 binding ratio. Using Bromoscan (a DiscoverX platform), lead compound UMB-11 and UMB-32 were analyzed for their selectivity (Figure 2.2F). UMB-11 demonstrates broad activity against the tested bromodomains with some selectivity for the BET family. In contrast, UMB-32 showed dramatically increased potency for the BET proteins versus most other targets with low nanomolar K_d affinities. The one exception in selectivity for BETs is against the structurally related TAF1 and TAF1L. While a significantly weaker interaction, this presents a potential scaffold for lead hopping into the development of TAF1-selective agents. Finally, compounds showed effect in human BRD4-dependent cancer cell lines (Figure 2.2B bottom). The addition of 7-N and the benzyl to t-butyl substitution clearly establish UMB32 as the front runner with dramatically improved biological activity.

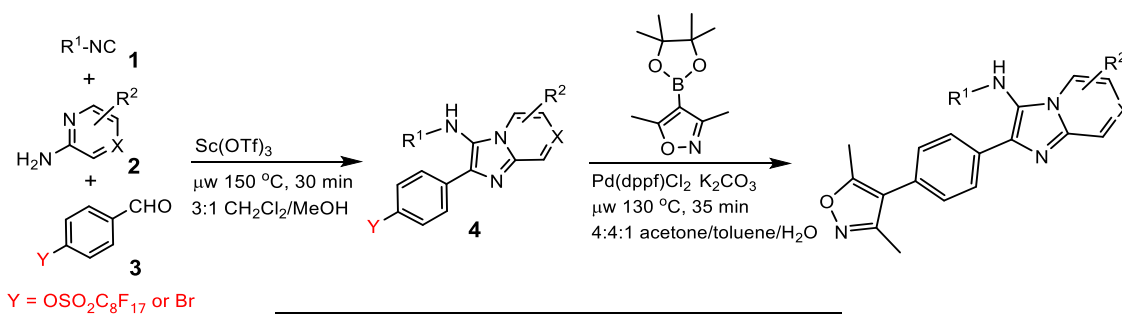
While BRD4 inhibitors already exist, it is important to develop novel chemistries in order to reach new classes of bromodomains and to have multiple potential paths toward therapeutics. The benzodiazepines⁹ and previous dimethyl isoxazoles³⁴ have been shown to be potent and selective against the BET bromodomain family. Here we report a new class of inhibitor that can potently inhibit BETs *in vitro* and in cell culture. UMB32 represents a promising lead compound developed with chemistry enabling facile derivatization toward ever more potent and selective compounds.

Moreover, it exhibits sub micromolar potency on a previously undrugged family of bromodomains in TAF1 and TAF1L. Indeed, oncogenic MYC causes inappropriate activation and localization of the STAGA complex containing TRRAP, GCN5, TFIID, CBP/P300, mediator,³⁵ and Sp1²⁰. TAF1 has been shown to block p53 activity,³⁶ and its removal by inactivation triggered a DNA damage response.³⁷ Finally, the TFIID complex of which TAF1 is a significant member is vital to stem cell reprogramming.³⁸ Thus, a probe to the bromodomain TAF1 will be valuable to expanding our understanding of transcriptional regulation in normal cell states as well as cancer.

Experimental:

General Synthetic Information. All chemicals and solvents were purchased from commercial suppliers and used as received. ^1H NMR (300 MHz) and ^{13}C NMR (75 MHz) spectra were recorded on a Varian NMR spectrometer. CDCl_3 was used as the solvent unless otherwise specified. LC-MS were performed on an Agilent 2100 system with a C_{18} (5.0 μm , 6.0 x 50 mm) LC column. The mobile phase is MeOH and water both containing 0.05% trifluoro acetic acid. A linear gradient was started from 75:25 MeOH/ H_2O to 100% MeOH in 5.0 min at a flow rate of 0.7 ml/min. The chromatograms were recorded at UV 210, 254, and 365 nm. Low resolution mass spectra were recorded in APCI (atmospheric pressure chemical ionization). Flash chromatography separation was performed on YAMAZEN AI-580 system with Agela silica gel (12 or 20 g, 230-400 μm mesh) cartridges. The microwave reactions were performed on a Biotage Initiator 8 system.

General procedures for the synthesis of UMB-6, -11, -20, -21, -23, -25, -28 to -32, -56, -57, -60 to -62, -65, -76, -82, and -83. The synthesis of these compounds was accomplished by a reported two-step synthesis shown in Scheme 2.2.¹ The three-component reaction (Groebke-Blackburn-Bienayme reaction) was followed by the Suzuki coupling.



| product | X | R ¹ | R ² |
|---------------|-----|--|-----------------------------------|
| UMB-6 | CH | PhCH ₂ | Me |
| UMB-11 | CH | PhCH ₂ | H |
| UMB-20 | CH | PhCH ₂ | Cl |
| UMB-21 | 7-N | PhCH ₂ | H |
| UMB-23 | CH | <i>p</i> -MeOC ₆ H ₄ | Cl |
| UMB-25 | 7-N | <i>p</i> -MeOC ₆ H ₄ | H |
| UMB-28 | CH | <i>c</i> -C ₆ H ₁₁ | H |
| UMB-29 | CH | <i>t</i> -Bu | H |
| UMB-30 | CH | <i>p</i> -EtC ₆ H ₄ | H |
| UMB-31 | CH | <i>t</i> -Bu | Cl |
| UMB-32 | 7-N | <i>t</i> -Bu | H |
| UMB-56 | 6-N | <i>t</i> -Bu | H |
| UMB-57 | 7-N | <i>i</i> -Pr | H |
| UMB-60 | 7-N | -CH ₂ CO ₂ tBu | H |
| UMB-61 | 7-N | <i>n</i> -Bu | H |
| UMB-62 | 7-N | (<i>S</i>)-1-PhEt | H |
| UMB-65 | CH | H | H |
| UMB-76 | CH | <i>t</i> -Bu | 6-Me |
| UMB-82 | CH | <i>t</i> -Bu | 6-CO ₂ CH ₂ |
| UMB-83 | CH | <i>t</i> -Bu | 6-COOH |

Scheme 2.2

Representative procedure for the three-component reaction. Synthesis of 2-(4-bromophenyl)-N-(t-butyl)imidazo[1,2-a]pyrazin-3-amine 4 ($X = N$, $R^1 = t\text{-Bu}$, $R^2 = H$).¹ A sealed 10 mL microwave tube charged with *t*-butylisocyanide (0.043 g, 0.52 mmol), 2-aminopyrazine (0.05 g, 0.52 mmol), 4-bromobenzaldehyde (0.074 g, 0.40 mmol), and $\text{Sc}(\text{OTf})_3$ (0.010 g, 0.02 mmol) in 2 mL of 3:1 $\text{CH}_2\text{Cl}_2/\text{MeOH}$) was heated under microwave at 150 °C for 30 min. The mixture was filtered and washed with EtOAc (4 ml). Concentration of the organic phase gave a crude product which was purified by flash chromatography eluted with 2:8 EtOAc/hexane to provide the product **4** as a yellow solid (110 mg, 80%).

*Representative procedure for the Suzuki-coupling reaction. Synthesis of N-(tert-butyl)-2-(4-(3,5-dimethylisoxazol-4-yl)phenyl)imidazo[1,2-a]pyrazin-3-amine UMB-32.*¹ A sealed 10 mL microwave tube charged with **4** ($X = N$, $R^1 = t\text{-Bu}$, $R^2 = H$, 0.110 g, 0.32 mmol), 3,5-dimethylisoxazole-4-boronic acid pinacol ester (0.093 g, 0.42 mmol), $\text{Pd}(\text{dppf})\text{Cl}_2 \cdot \text{CH}_2\text{Cl}_2$ (0.021 g, 0.026 mmol, 8% mol), and K_2CO_3 (0.088 g, 0.64 mmol) in 2 mL of 4:4:1 acetone/toluene/ H_2O was heated under microwave at 130 °C for 40 min. The mixture was filtered and washed with EtOAc (4 ml). Concentration of the organic phase gave a crude product which was purified by flash chromatography eluting with 3:7 EtOAc/hexane to give **UMB-32** as brownish solid (66 mg, 57%). ¹H NMR (300 MHz, CDCl_3) δ 9.01 (s, 1H), 8.16 (d, $J = 4.8$ Hz, 1H), 8.05(d, $J = 6.6$ Hz, 2H), 7.88 (d, $J = 4.8$ Hz, 1H), 7.38 (d, $J = 6.6$ Hz, 2H), 3.18 (s, 1H, NH), 2.46 (s, 3H), 2.33 (s, 3H), 1.11 (s, 9H); ¹³C NMR (75 MHz, CDCl_3) δ 165.0, 158.34, 143.0, 141.2, 137.1, 133.2, 129.8, 128.7, 128.6, 128.3, 124.9, 116.1, 116.1, 56.7, 30.2, 11.4, 10.6; MS(APCI) m/z 362.2 ($M^+ + 1$).

N-Benzyl-2-(4-(3,5-dimethylisoxazol-4-yl)phenyl)-6-methylimidazo[1,2- \square]pyridine-3-amine **UMB-6**. Yellow solid, 45% yield, ^1H NMR (300 MHz, CDCl_3) δ 7.99 (d, 1H), 7.96 (d, 1H), 7.62 (s, 1H), 7.39 (d, 2H), 7.27 (m, 5H), 6.97 (d, 2H), 4.14 (s, 2H), 3.42 (s, 1H), 2.44 (s, 3H), 2.36 (s, 3H), 2.28 (s, 3H). MS(APCI) m/z 409.2 ($\text{M}^+ + 1$).

N-Benzyl-2-(4-(3,5-dimethylisoxazol-4-yl)phenyl)imidazo[1,2- α]pyridin-3-amine **UMB-11**. Yellowish brown solid, 52% yield, ^1H NMR (300 MHz, CDCl_3) δ 8.24(d, 1H), 7.72 (d, 2H), 7.66 (d, 1H), 7.58 (d, 2H), 7.53 (t, 1H), 7.42 (t, 1H), 7.22 (m, 5H), 4.21 (s, 2H), 3.15 (s, 1H), 2.42 (s, 3H), 2.37 (s, 3H); ^{13}C NMR (75 MHz, CDCl_3) δ 165.2, 158.7, 141.7, 138.9, 133.5, 129.2, 128.7, 128.1, 127.7, 127.3, 125.7, 124.2, 122.3, 117.5, 116.4, 111.8, 52.5, 24.8, 11.7, 10.9; MS(APCI) m/z 395.2 ($\text{M}^+ + 1$).

N-Benzyl-6-chloro-2-(4-(3,5-dimethylisoxazol-4-yl)phenyl)imidazo[1,2- \square]pyridin-3-amine **UMB-20**. ^1H NMR (300 MHz, CDCl_3) δ 8.85 (s, 1H), 8.12 (d, 2H), 8.05 (d, 1H), 8.02 (d, 1H), 7.96 (d, 2H), 7.34 (m, 5H) 4.22 (s, 2H), 3.51 (s, 1H), 2.42 (s, 3H), 2.37 (s, 3H); MS(APCI) m/z 429.1 ($\text{M}^+ + 1$).

N-benzyl-2-(4-(3,5-dimethylisoxazol-4-yl)phenyl)imidazo[1,2- α]-pyrazin-3-amine **UMB-21**. ^1H NMR (300 MHz, CDCl_3) δ 8.11(d, 1H), 8.05 (d, 1H), 8.01 (s, 1H), 7.92 (d, 2H), 7.52 (d, 2H), 7.42 (t, 1H), 7.28 (m, 5H), 4.22 (s, 2H), 3.51 (s, 1H), 2.43 (s, 3H), 2.37 (s, 3H); ^{13}C NMR (75 MHz, CDCl_3) \square 165.4, 158.7, 143.6, 138.3, 133.9, 131.1, 129.3, 129.1, 128.9, 128.8, 128.1, 128.0, 126.3, 116.5, 115.2, 52.3, 11.6, 10.8; MS(APCI) m/z 396.2 ($\text{M}^+ + 1$).

6-Chloro-2-(4-(3,5-dimethylisoxazol-4-yl)phenyl)-*N*-(4-methoxy-phenyl)imidazo-[1,2- \square]pyridine-3-amine **UMB-23**. ^1H NMR (300 MHz, CDCl_3) δ 8.07 (s, 1H), 8.02 (d, 1H), 7.62 (d, 1H), 7.40 (d, 2H), 7.38 (d, 2H), 7.30 (d, 2H), 7.23 (d, 2H), .3.77 (s, 3H), 2.42 (s, 3H),

2.28 (s, 3H); ¹³C NMR (75 MHz, CDCl₃) □□187.0, 184.0, 173.0, 172.8, 167.0, 156.8, 146.4, 137.5, 129.3, 127.4, 126.6, 118.2, 117.6, 115.4, 114.6, 109.4, 100.0, 55.7, 29.7, 29.4; MS(APCI) m/z 445.9 (M⁺ + 1).

2-(4-(3,5-Dimethylisoxazol-4-yl)phenyl)-7-methoxy-N-(4-methoxy-phenyl)imidazo[1,2-c]pyrimidin-3-amine **UMB-24**. ¹H NMR (300 MHz, CDCl₃) δ 8.51 (s, 1H), 8.09 (d, J = 8.4Hz, 2H), 7.31 (d, J = 8.4Hz, 2H), 6.85 (d, J = 8.7Hz, 2H), 6.78 (s, 1H), 6.65 (d, J = 8.7Hz, 2H), 5.38 (s, 1H), .3.97 (s, 3H), 3.76 (s, 3H), 2.42 (s, 3H), 2.29 (s, 3H); MS(APCI) m/z 442.4(M⁺ + 1).

N-Benzyl-2-(3-(3,5-dimethylisoxazol-4-yl)phenyl)imidazo[1,2-α]pyridin-3-amine **UMB-26**. ¹H NMR (300 MHz, CDCl₃) δ 7.99 (d, 1H), 7.91 (s, 1H), 7.59 (d, 1H), 7.54 (t, 1H), 7.52 (d, 1H), 7.32 (m, 5H), 7.21 (t, 1H), 7.17 (d, 1H), 6.81 (t, 1H), 4.23 (s, 2H), 3.42 (s, 1H), 2.42 (s, 3H), 2.29 (s, 3H); MS(APCI) m/z 395.2 (M⁺ + 1).

N-Cyclohexyl-2-(4-(3,5-dimethylisoxazol-4-yl)phenyl)imidazo[1,2-α]pyridin-3-amine **UMB-28**. ¹H NMR (300 MHz, CDCl₃) δ 8.11(d, 1H), 8.05 (d, 2H), 7.57 (d, 1H), 7.35 (d, 2H), 7.08 (t, 1H), 6.81 (t, 1H), 3.01 (s, 1H), 2.42 (s, 3H), 2.27 (s, 3H), 1.12 (m, 11H); MS(APCI) m/z 387.2 (M⁺ + 1).

N-(*t*-Butyl)-2-(4-(3,5-dimethylisoxazol-4-yl)phenyl)imidazo[1,2-α]pyridin-3-amine **UMB-29**. ¹H NMR (300 MHz, CDCl₃) δ 8.15(d, 1H), 7.99 (d, 2H), 7.45 (d, 1H), 7.22 (d, 2H), 7.03 (t, 1H), 6.71 (t, 1H), 3.01 (s, 1H), 2.40 (s, 3H), 2.25 (s, 3H), 1.01 (s, 9H); MS(APCI) m/z 361.2 (M⁺ + 1).

2-(4-(3,5-Dimethylisoxazol-4-yl)phenyl)-*N*-(4-methoxyphenyl)imidazo-[1,2-α]pyridin-3-amine **UMB-30**. ¹H NMR (300 MHz, CDCl₃) δ 8.03 (d, J = 8.4Hz, 2H), 7.80 (d, J = 6.6Hz, 1H), 7.59 (d, J = 9Hz, 1H), 7.21 (d, J = 8.4Hz, 2H), 7.17 (t, 1H), 6.75 (d, J = 6.6Hz, 2H),

6.73 (t, 1H), 6.50 (d, J = 6.6Hz, 2H), 5.43 (s, 1H), 3.68 (s, 3H), 2.33 (s, 3H), 2.20 (s, 3H), 1.01 (s, 9H); \square MS(APCI) m/z 411.2 ($M^+ + 1$).

N-(t-Butyl)-6-chloro-2-(4-(3,5-dimethylisoxazol-4-yl)phenyl)imidazo[1,2- α]pyridin-3-amine **UMB-31**. ^1H NMR (300 MHz, CDCl_3) δ 8.19 (s, 1H), 7.93 (d, J = 6.6Hz, 2H), 7.44 (d, J = 9.6 Hz, 1H), 7.27 (d, J = 6.6 Hz, 2H), 7.07 (d, J = 9.6 Hz, 1H), 3.03 (s, 1H), 2.35 (s, 3H), 2.25(s, 3H), 1.01(s, 9H); MS(APCI) m/z 395.2 ($M^+ + 1$).

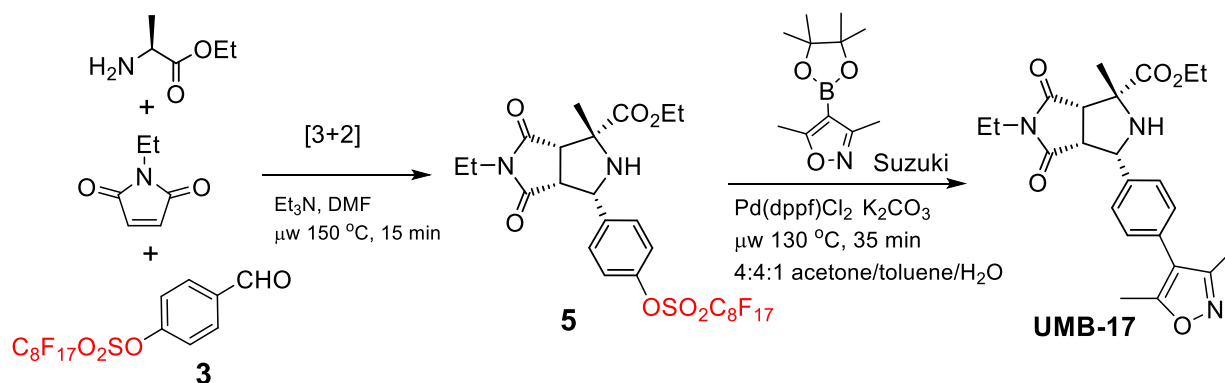
Tert-butyl (2-(4-(3,5-dimethylisoxazol-4-yl)phenyl)imidazo[1,2- α]pyrazin-3-yl)glycinate **UMB-60**. ^1H -NMR (300MHz, CDCl_3) δ 9.01 (s, 1H), 8.19 (m, 3H), 7.89 (d, J=4.5Hz, 1H), 7.38 (d, J=7.2Hz, 2H), 3.77 (s, 2H), 2.46 (s, 3H), 2.33(s, 3H), 1.47(s, 9H). MS (APCI) m/z 420.2 ($M^+ + 1$).

N-butyl-2-(4-(3,5-dimethylisoxazol-4-yl)phenyl)imidazo[1,2- α]pyrazin-3-amine **UMB-61**. ^1H -NMR (300MHz, CDCl_3) δ 9.02 (s, 1H), 8.07 (d, J=8.4Hz, 2H), 7.98 (d, J=4.2Hz, 1H), 7.89 (d, J=7.8Hz, 1H), 7.39 (d, J=8.1Hz, 2H), 3.15 (s, 2H), 2.46 (s, 3H), 2.34 (s, 3H), 1.64 (m, 2H), 1.48 (m, 2H), 0.95 (t, 3H). MS (APCI) m/z 362.2 ($M^+ + 1$).

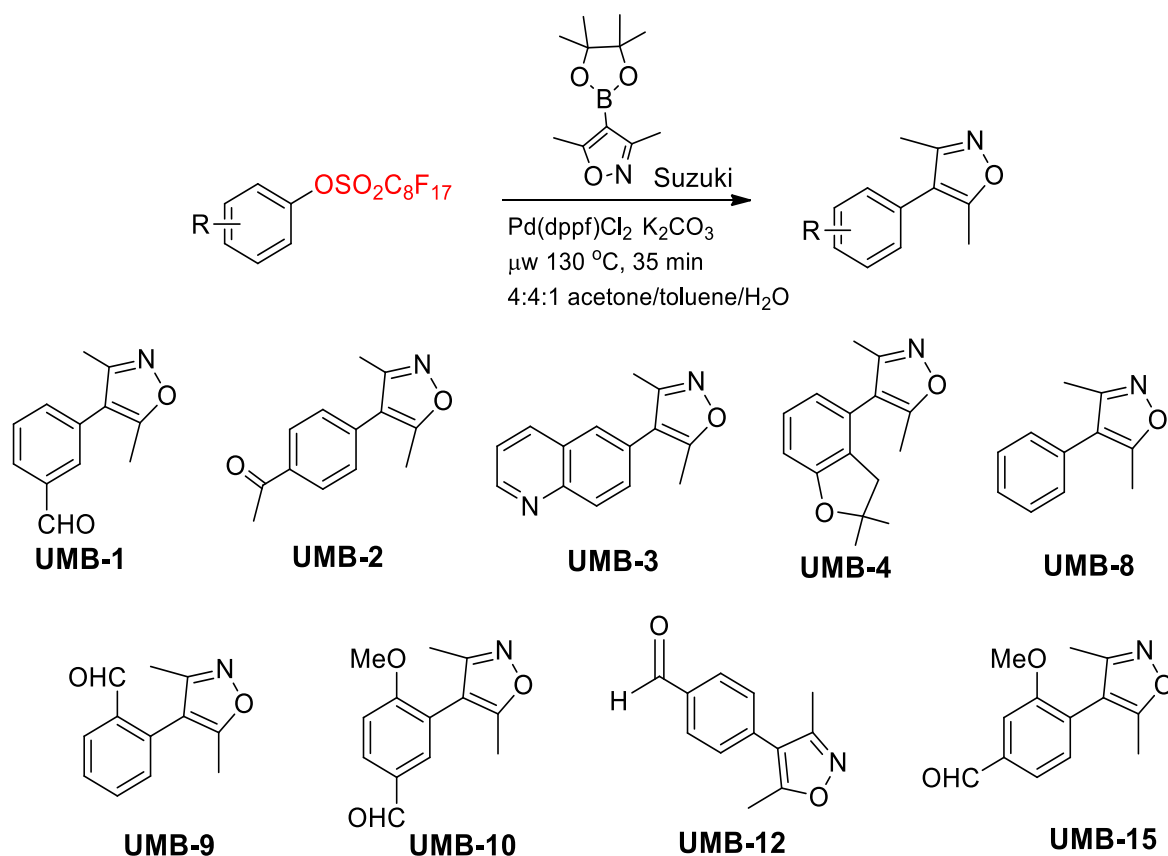
(S)-2-(4-(3,5-dimethylisoxazol-4-yl)phenyl)-N-(1-phenylethyl)imidazo[1,2- α]pyrazin-3-amine **UMB-62**. ^1H -NMR (300MHz, CDCl_3) δ 8.96 (s, 1H), 8.05 (m, 2H), 7.78 (d, J=9.6Hz, 2H), 7.36 (d, J=2.1Hz, 2H), 7.27 (m, 5H), 4.38 (m, 1H), 2.48 (s, 3H), 2.35 (s, 3H), 1.51 (s, 3H). MS (APCI) m/z 410.2 ($M^+ + 1$).

2-(4-(3,5-dimethylisoxazol-4-yl)phenyl)imidazo[1,2- α]pyridin-3-amine **UMB-65**. ^1H -NMR (300MHz, CDCl_3) δ 8.06 (m, 3H), 7.55 (m, 2H), 7.36 (d, J=6.3Hz, 2H), 7.15 (m, 1H), 6.83 (m, 1H), 3.45 (2, 2H), 2.44 (s, 3H), 2.31 (s, 3H). MS (APCI) m/z 305.1 ($M^+ + 1$).

N-(tert-butyl)-2-(4-(3,5-dimethylisoxazol-4-yl)phenyl)-6-methylimidazo[1,2- α]pyridin-3-amine **UMB-76**. $^1\text{H-NMR}$ (300MHz, CDCl_3) δ 8.06 (m, 3H), 7.55 (m, 2H), 7.36 (d, $J=6.3\text{Hz}$, 2H), 7.15 (m, 1H), 6.83 (m, 1H), 3.45 (2, 2H), 2.44 (s, 3H), 2.31 (s, 3H). MS (APCI) m/z 305.1 ($M^+ + 1$).



*Procedures for the synthesis of ethyl-3-(4-(3,5-dimethylisoxazol-4-yl)phenyl)-5-ethyl-1-methyl-4,6-dioxooctahydropyrrolo[3,4- c]pyrrole-1-carboxylate **UMB-17**. **UMB-17** was prepared by a reported two-step synthesis shown in Scheme 2.3.² The three-component [3+2] cycloaddition is followed by the Suzuki coupling to afford **UMB-17** as a yellow semi-solid in 10% yield. MS (APCI) m/z 426.1($M^+ + 1$).*



Scheme 2.4

*Procedures for the synthesis of **UMB-1**, **-2**, **-3**, **-4**, **-8**, **-9**, **-10**, **-12**, and **-15**.* These compounds were prepared by direct Suzuki coupling of fluorinated arylsulfonates with the boronic ester (Scheme 2.4). The Suzuki coupling reactions were carried out following the general procedure shown in Scheme 2.2.

3-(3,5-Dimethylisoxazol-4-yl)benzaldehydes **UMB-1**. Yellow oily compound, 63% yield, ¹H NMR (300 MHz, CDCl₃) δ 10.3 (s, 1H), 7.91 (d, 1H), 7.78 (s, 1H), 7.71 (d, 1H), 7.64 (t, 1H), 2.42 (s, 3H), 2.27 (s, 3H). MS (APCT) m/z 202.2 (M⁺ + 1).

1-(4-(3,5-Dimethylisoxazol-4-yl)phenyl)ethanone **UMB-2**. Yellow oily compound, 60% yield, ¹H NMR (300 MHz, CDCl₃) δ 8.05 (d, J = 8.7Hz, 2H), 7.38 (d, J = 8.7Hz, 2H), 2.64 (s, 3H), 2.44 (s, 3H), 2.30 (s, 3H). MS(APCT) m/z 216.2 (M⁺ + 1).

(3,5-Dimethyl-4-(quinolin-6-yl)isoxazole **UMB-3**. Yellow-brownish oily compound, 71% yield, $^1\text{H NMR}$ (300 MHz, CDCl_3) δ 8.95 (d, 1H), 8.21 (d, 1H), 7.75 (d, 1H), 7.62 (s, 1H), 7.61 (d, 1H), 7.55 (t, 1H), 2.44 (s, 3H), 2.34 (s, 3H). MS(APCT) m/z 225.1 ($\text{M}^+ + 1$).

4-(2,2-Dimethyl-2,3-dihydrobenzofuran-4-yl)-3,5-dimethylisoxazole **UMB-4**. Brown semi-solid, 37% yield, $^1\text{H NMR}$ (300 MHz, CDCl_3) δ 7.20 (d, 1H), 7.00 (d, 1H), 6.92 (t, 1H), 3.05 (s, 2H), 2.38 (s, 3H), 2.25 (s, 3H), 1.47 (s, 6H); MS(APCT) m/z 244.2($\text{M}^+ + 1$).

3,5-Dimethyl-4-phenylisoxazole **UMB-8**. Yellow oily compound, 58% yield, $^1\text{H NMR}$ (300 MHz, CDCl_3) δ 7.15-7.62 (m, 5H), 2.41 (s, 3H), 2.25 (s, 3H); MS(APCT) m/z 174.1 ($\text{M}^+ + 1$).

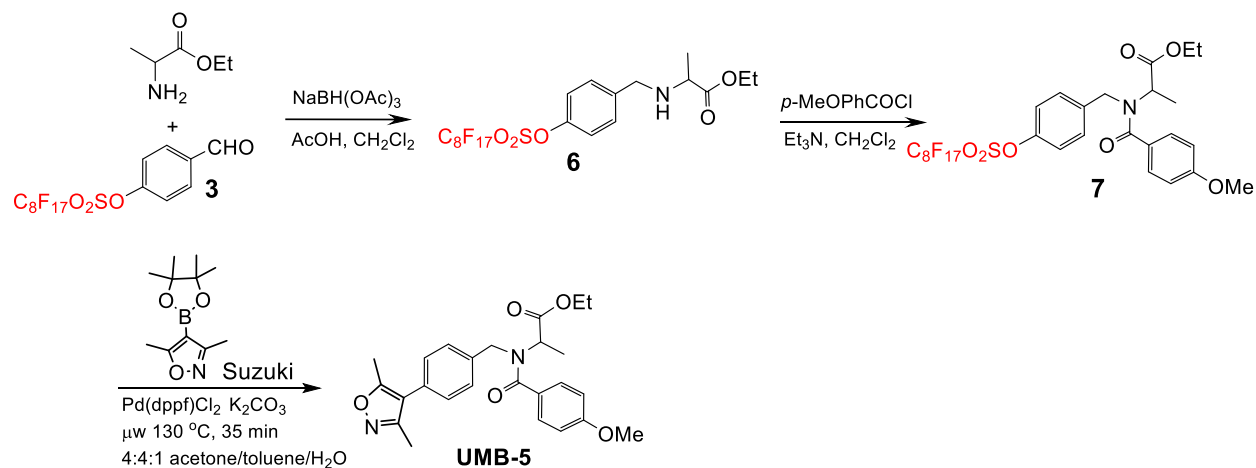
2-(3,5-Dimethylisoxazol-4-yl)benzaldehydes **UMB-9**. Yellow oily compound, 17% yield, $^1\text{H NMR}$ (300 MHz, CDCl_3) δ 9.92 (s, 1H), 8.06 (d, $J=7.2\text{Hz}$, 1H), 7.69 (m, 1H), 7.54 (m, 2H), 2.28 (s, 3H), 2.16 (s, 3H); MS(APCT) m/z 202.1 ($\text{M}^+ + 1$).

3-(3,5-Dimethylisoxazol-4-yl)-4-methoxybenzaldehyde **UMB-10**. Yellow oily compound, 27% yield; MS(APCT) m/z 232.1 ($\text{M}^+ + 1$).

4-(3,5-dimethylisoxazol-4-yl)benzaldehyde **UMB-12**. Yellow oily compound, 35% yield; $^1\text{H NMR}$ (300 MHz, CDCl_3) δ 10.07 (s, 1H), 7.99 (m, 2H), 7.46 (d, $J=6.6\text{Hz}$, 2H), 2.47 (s, 3H), 2.31 (s, 3H); MS(APCT) m/z 202.1 ($\text{M}^+ + 1$).

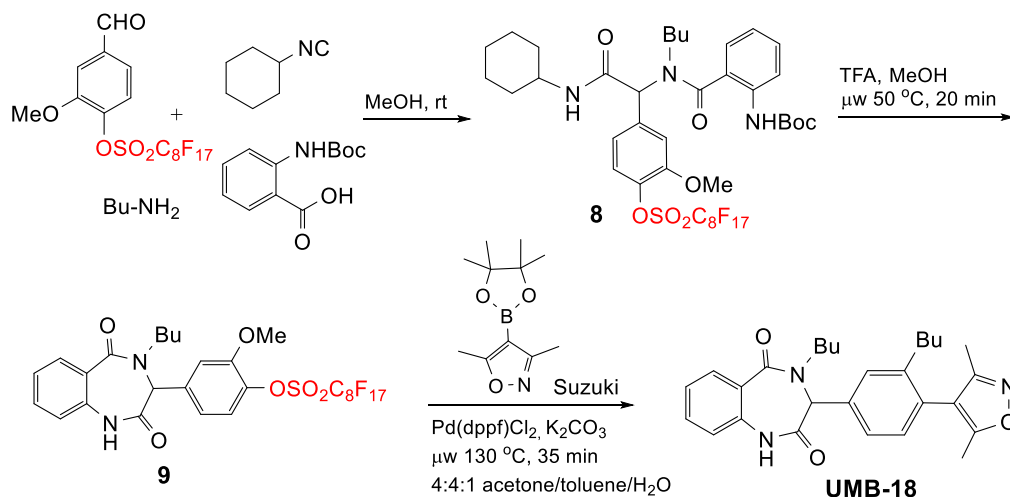
4-(3,4-Dimethylisoxazol-4-yl)-3-methoxybenzaldehyde **UMB-15**. Brown oily compound, 18% yield; MS(APCT) m/z 232.1 ($\text{M}^+ + 1$).

Synthesis of Ethyl-2-(*N*-(4-(3,5-dimethylisoxazol-4-yl)benzyl)-4-methoxybenzamido)-propanoate **UMB-5**. This compound was prepared following the reported procedure (Scheme 2.5).³ Reductive amination of **3** afforded compound **6**, which was then *N*-acylated to give compound **7**. The Suzuki coupling of **7** afforded **UMB-5** as a brown solid (17% yield). ¹H NMR (300 MHz, CDCl₃) δ 7.72 (d, *J* = 5.7 Hz, 2H), 7.70 (d, *J* = 5.7 Hz, 2H), 7.49 (d, *J* = 9.0 Hz, 2H), 7.46 (d, *J* = 9.0 Hz, 2H), 4.24 (q, 2H), 4.21 (s, 2H), 4.18 (m, 1H), 3.82 (s, 3H), 2.42 (s, 3H), 2.28 (s, 3H), 1.58 (m, 2H), 1.27 (d, 3H), 0.95 (t, 3H); MS(APCT) *m/z* 437.2 (*M*⁺ + 1).



Scheme 2.5

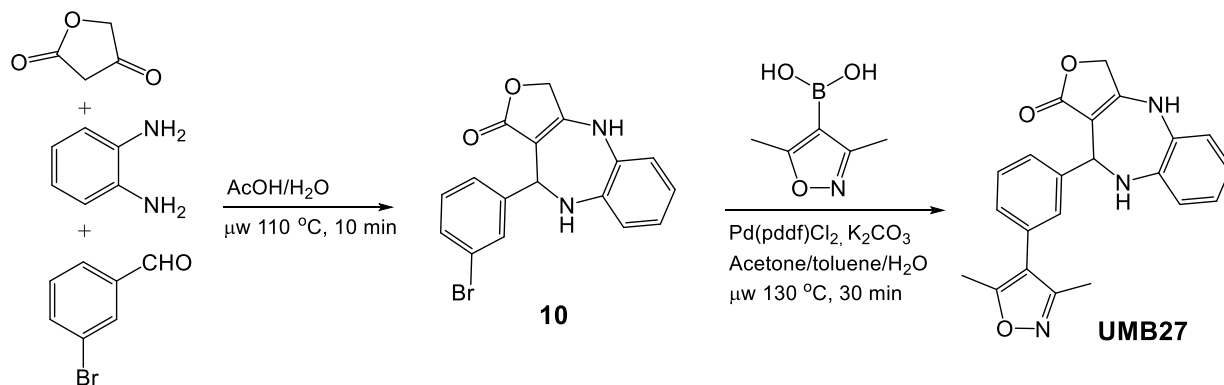
Synthesis of 4-butyl-3-(4-(3,5-dimethylisoxazol-4-yl)-3-methoxyphenyl)-3,4-dihydro-1*H*-benzo[*e*][1,4]diazepine-2,5-dione **UMB-18**. This compound was prepared following the reported procedures (Scheme 2.6).⁴ The Ugi 4-component reaction gave compound **8** which was cyclized to form **9**. The Suzuki coupling of **9** afforded **UMB-18** as a brown semisolid in 44% yield. MS(APCT) *m/z* 434.2 (*M*⁺ + 1).



Scheme 2.6

Synthesis of 10-(3-(3,5-dimethylisoxazol-4-yl)phenyl)-3,4,9,10-tetrahydro-1H-benzo[b]furo[3,4-e][1,4]diazepin-1-one UMB-27. The synthesis of **UMB-27** was accomplished by a two-step synthesis shown in Scheme 2.7. A mixture of benzene-1,2-diamine (54 mg, 0.5 mmol), tetronic acid (53.5 mg, 0.5 mmol), and acetic acid (3 μL) in 1 mL H₂O was stirred at room temperature for 30 min. Then 3-bromobenzaldehyde (92.5 mg, 0.5 mmol) was added to the reaction mixture and heated under microwave at 110 $^\circ\text{C}$ for 10 min. The reaction mixture was filtered and the residue was washed with 1 mL of 50% ethanol. The solid obtained was purified by flash chromatography (6:4 hexanes/EtOAc) to afford **10** (87 mg, 49% yield). A mixture of **10** (32 mg, 0.09 mmol), 3,5-dimethylisoxazole-4-yl boronic acid (19 mg, 0.135 mmol), Pd(pddf)Cl₂ (5.7 mg, 0.007 mmol), and K₂CO₃ (25 mg, 0.18 mmol) in 2 mL of 4:4:1 acetone:toluene:H₂O was heated under microwave at 130 $^\circ\text{C}$ for 30 min. The reaction mixture was filtered and the residue was washed with EtOAc. The concentrated filtrate was purified by flash chromatography

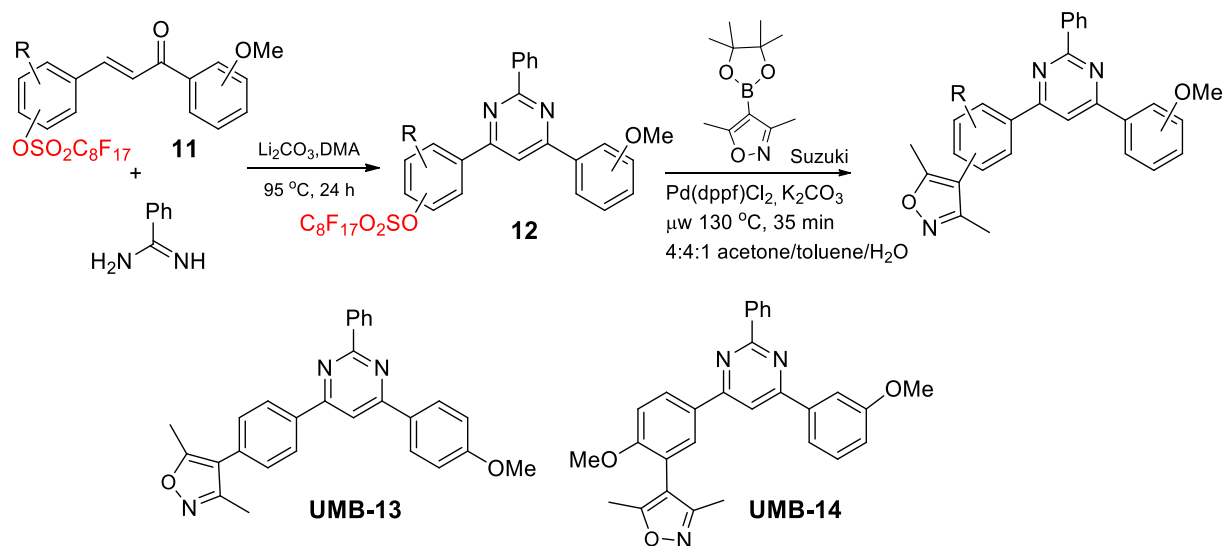
(6:4 hexanes/EtOAc) to afford **132 UMB-27** (18 mg, 54% yield). $^1\text{H NMR}$ (300 MHz, CDCl_3) δ 8.05 (d, $J = 8.4\text{Hz}$ 1 H), 7.96 (m, 2 H), 7.47 (m, 1 H), 6.9 (m, 3H), 6.5 (d, $J = 8.4\text{Hz}$ 1H), 5.1 (b, 1H), 4.87(s, 2H), 4.62 (s, 1H), 2.35 (s, 3 H), 2.21 (s, 3 H); MS (APCI) m/z : 374.1 ($\text{M}^{+}+1$).



Synthesis of UMB-13 and UMB-14. The synthesis of **UMB-13** and **UMB-14** were accomplished following the literature procedures (Scheme 2.8). The cycloaddition of α,β -unsaturated ketone **11** with benzimidamide afforded pyrimidine **12**.⁵ This compound was subjected to the Suzuki coupling to give the final product.

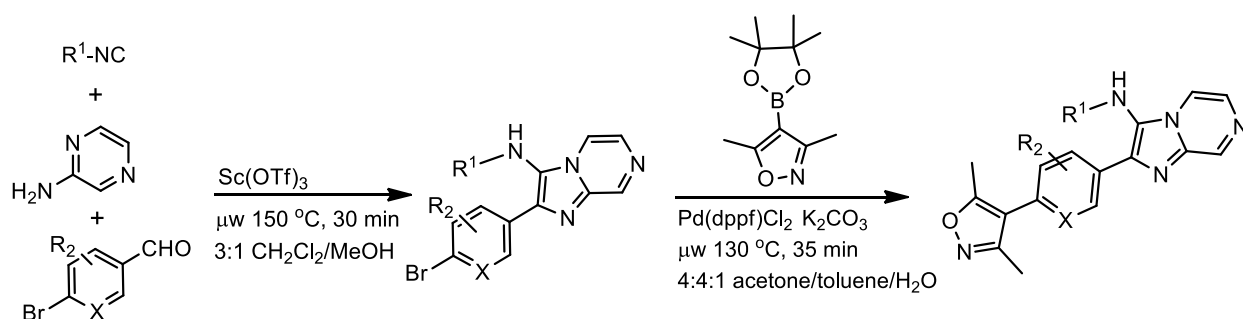
4-(4-(6-(4-Methoxyphenyl)-2-phenylpyrimidin-4-yl)phenyl)-3,5-di-methylisoxazole **UMB-13**. Yellow oily compound, 12% yielded, MS(APCT) m/z 434.1 ($\text{M}^{+} + 1$).

(4-(2-Methoxy-5-(6-(3-methoxyphenyl)-2-phenylpyrimidin-4-yl)phenyl)-3,5-dimethylisoxazole **UMB-14**. Brown semisolid, 11% yield, MS(APCT) m/z 464.2 ($\text{M}^{+} + 1$).



Scheme 2.8

General procedures for the synthesis of UMB-53 to -55, UMB-58 and -59. The synthesis of these compounds was accomplished by a two-step synthesis shown in Scheme 2.9. The three-component reaction (Groebke-Blackburn-Bienayme reaction) was followed by the Suzuki coupling.



| Compound | R ¹ | R ² | X |
|---------------|----------------|----------------|-----|
| UMB-53 | t-Bu | H | 2-N |
| UMB-54 | t-Bu | H | 3-N |
| UMB-55 | t-Bu | 2-F | CH |
| UMB-58 | t-Bu | 3-OMe | CH |
| UMB-59 | i-Pr | 3-OMe | CH |

Scheme 2.9

N-(tert-butyl)-2-(6-(3,5-dimethylisoxazol-4-yl)pyridin-3-yl)imidazo[1,2-a]pyrazin-3-amine

UMB-53. ¹H-NMR (300MHz, CDCl₃) δ 8.92 (s, 1H), 8.84 (d, J=2.1Hz, 1H), 7.87 (m, 1H), 7.52 (d, J=8.1Hz, 1H), 7.35 (d, J=4.8Hz, 1H), 2.65 (s, 3H), 2.50 (s, 3H), 1.46 (s, 9H); MS (APCI) m/z 363.1 (M⁺ + 1).

N-(tert-butyl)-2-(5-(3,5-dimethylisoxazol-4-yl)pyridin-2-yl)imidazo[1,2-a]pyrazin-3-amine

UMB-54. ¹H-NMR (300MHz, CDCl₃) δ 9.54 (s, 1H), 8.55 (s, 1H), 7.93 (d, J=6.3Hz, 1H), 7.65 (m, 2H), 7.35 (d, J=4.5Hz, 1H), 2.48 (s, 3H), 2.34 (s, 3H), 1.25 (s, 9H); MS (APCI) m/z 363.1 (M⁺ + 1).

N-(tert-butyl)-2-(4-(3,5-dimethylisoxazol-4-yl)-3-fluorophenyl)imidazo[1,2-a]pyrazin-3-

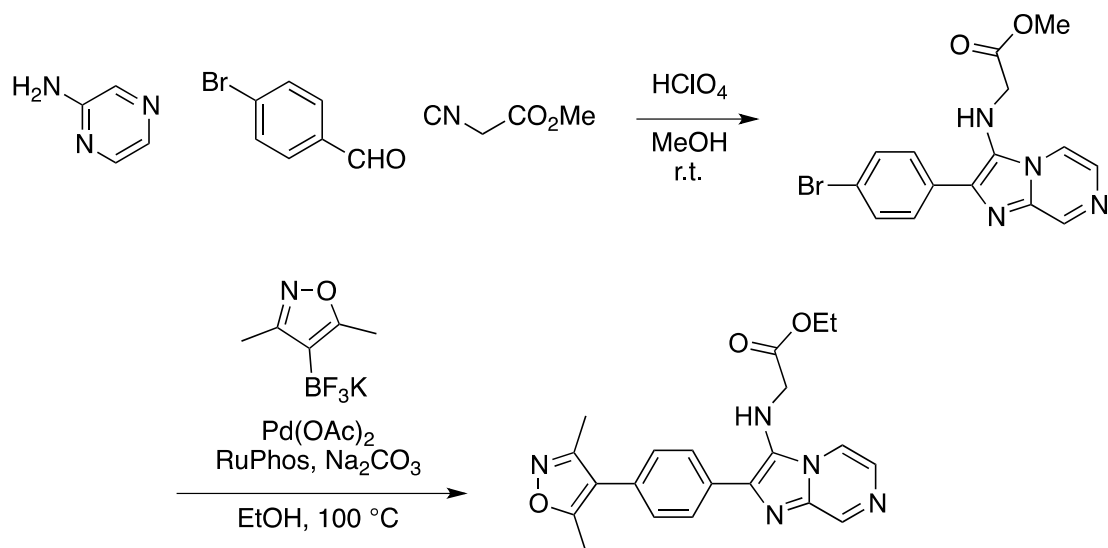
amine **UMB-55.** ¹H-NMR (300MHz, CDCl₃) δ 9.04 (s, 1H), 7.88 (d, J=5.4Hz, 1H), 7.36 (m, 4H), 2.43 (s, 3H), 2.31 (s, 3H), 1.51 (s, 9H); MS (APCI) m/z 380.1 (M⁺ + 1).

N-(tert-butyl)-2-(4-(3,5-dimethylisoxazol-4-yl)-2-methoxyphenyl)imidazo[1,2-a]pyrazin-3-

amine **UMB-58.** ¹H-NMR (300MHz, CDCl₃) δ 9.00 (s, 1H), 8.22 (d, J=4.5Hz, 1H), 7.88

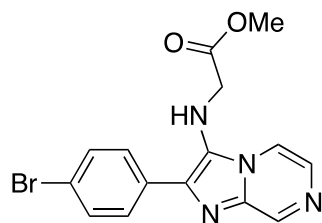
(m, 2H), 7.05 (d, J=7.8Hz, 1H), 6.89 (s, 1H), 3.94 (s, 3H), 3.82 (s, 1H), 2.47 (s, 3H), 2.33 (s, 3H), 1.01 (s, 9H); MS (APCI) m/z 392.2 (M⁺ + 1).

2-(4-(3,5-dimethylisoxazol-4-yl)-2-methoxyphenyl)-N-isopropylimidazo[1,2-a]pyrazin-3-amine **UMB-59**. ¹H-NMR (300MHz, CDCl₃) δ 9.00 (s, 1H), 8.05 (m, 1H), 7.89 (m, 2H), 7.05 (d, J=6.6Hz, 1H), 6.91 (s, 1H), 7.05 (d, J=7.8Hz, 1H), 3.94 (s, 3H), 3.15 (m, 1H), 2.48 (s, 3H), 2.34 (s, 3H), 1.03 (d, 6H); MS (APCI) m/z 378.1 (M⁺ + 1).



Scheme 2.10

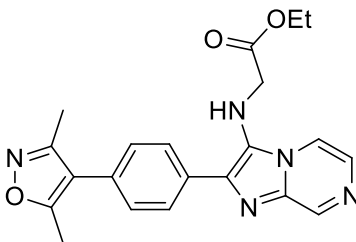
Methyl 2-((2-(4-bromophenyl)imidazo[1,2-a]pyrazin-3-yl)amino)acetate



Aminopyrazine (95.2 mg, 1.00 mmol, 1 eq), 4-bromobenzaldehyde (278 mg, 1.50 mmol, 1.5 eq) and methyl isocyanoacetate (0.105 mL, 1.15 mmol, 1.15 eq) were dissolved in methanol (2 mL). A 1M solution of perchloric acid in methanol (0.20 mL, 0.10 eq) was

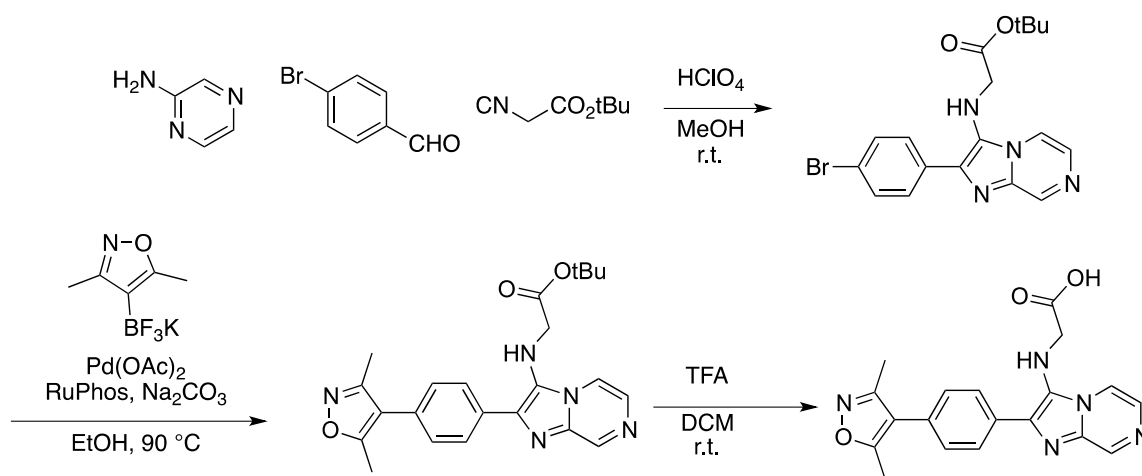
added and the solution was stirred for 12 hours at room temperature. The mixture was then diluted with EtOAc and washed with saturated sodium bicarbonate, water and brine. The crude material was purified by automated column chromatography (50 to 100% EtOAc/hexanes) to yield a cream colored solid (0.21 g, 0.581 mmol, 58%). **¹H NMR** (400 MHz, CDCl₃) δ 8.99 (d, *J* = 1.5 Hz, 1H), 8.18 (dd, *J* = 4.6, 1.5 Hz, 1H), 8.02 – 7.93 (m, 2H), 7.90 (d, *J* = 4.6 Hz, 1H), 7.68 – 7.51 (m, 2H), 3.83 (d, *J* = 5.6 Hz, 2H), 3.74 (s, 3H). **¹³C NMR** (100 MHz, CDCl₃) δ 172.22, 143.77, 137.20, 136.97, 132.25, 132.17, 129.48, 128.82, 122.67, 115.73, 110.16, 52.67, 49.03. **MS** (ESI) 361.69 (M+H).³⁹

Ethyl 2-((2-(4-(3,5-dimethylisoxazol-4-yl)phenyl)imidazo[1,2-*a*]pyrazin-3-yl)amino)acetate (DB-1-038)



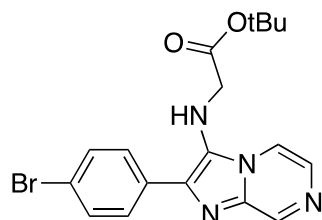
Methyl 2-((2-(4-bromophenyl)imidazo[1,2-*a*]pyrazin-3-yl)amino)acetate (147 mg, 0.408 mmol, 1 eq), potassium 3,5-dimethylisoxazole-4-trifluoroborate (108 mg, 0.530 mmol, 1.3 eq), palladium (II) acetate (4.5 mg, 0.020 mmol, 5 mol %) RuPhos (19.1 mg, 0.041 mmol, 10 mol %) and sodium carbonate (86.5 mg, 0.816 mmol, 2 eq) were dissolved in ethanol (2.1 mL) and degassed with nitrogen for roughly 1 minute. The mixture was placed in a heat block at 100 °C. After 16 hours, the mixture was filtered through a silica plug and concentrated. The crude mixture was purified by automated column chromatography (30 to 100% EtOAc/hexanes) to yield the ethyl ester (as a result of trans-esterification during the course of the cross-coupling) as a brown solid (88.9 mg,

0.227 mmol, 56%). **¹H NMR** (400 MHz, CDCl₃) δ 8.96 (d, *J* = 1.3 Hz, 1H), 8.21 (dd, *J* = 4.6, 1.4 Hz, 1H), 8.18 – 8.10 (m, 2H), 7.85 (d, *J* = 4.6 Hz, 1H), 7.39 – 7.31 (m, 2H), 4.18 (q, *J* = 7.2 Hz, 2H), 4.05 (t, *J* = 5.7 Hz, 1H), 3.86 (d, *J* = 5.7 Hz, 2H), 2.43 (s, 3H), 2.29 (s, 3H), 1.22 (t, *J* = 7.2 Hz, 3H). **¹³C NMR** (100 MHz, CDCl₃) δ 171.75, 165.45, 158.69, 143.50, 137.26, 136.86, 132.51, 130.39, 129.47, 129.18, 127.51, 126.60, 116.34, 115.87, 61.72, 49.27, 14.18, 11.77, 10.98. **MS** (ESI) 392.90 (M+H)⁴⁰



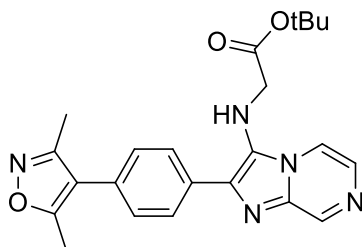
Scheme 2.11

***tert*-butyl 2-((2-(4-bromophenyl)imidazo[1,2-*a*]pyrazin-3-yl)amino)acetate**



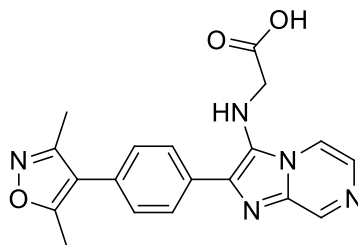
Aminopyrazine (95.2 mg, 1.00 mmol, 1 eq), 4-bromobenzaldehyde (278 mg, 1.50 mmol, 1.5 eq) and *tert*-butyl isocyanoacetate (0.167 mL, 1.15 mmol, 1.15 eq) were dissolved in methanol (2 mL). A 1M solution of perchloric acid in methanol (0.20 mL, 0.10 eq) was added and the solution was stirred for 12 hours at room temperature. The mixture was then diluted with EtOAc and washed with saturated sodium bicarbonate, water and brine. The crude material was purified by automated column chromatography (30 to 100% EtOAc/hexanes) to yield a yellow oil, which slowly crystallizes upon standing (0.34 g, 0.84 mmol, 84%). **¹H NMR** (400 MHz, CDCl₃) δ 8.87 (d, *J* = 1.4 Hz, 1H), 8.08 (dd, *J* = 4.6, 1.5 Hz, 1H), 7.93 – 7.78 (m, 2H), 7.75 (d, *J* = 4.6 Hz, 1H), 7.50 – 7.38 (m, 2H), 3.98 (t, *J* = 5.5 Hz, 1H), 3.62 (d, *J* = 5.6 Hz, 2H), 1.38 (s, 9H). **¹³C NMR** (100 MHz, CDCl₃) δ 170.74, 143.28, 136.53, 136.39, 132.09, 131.74, 129.01, 128.49, 126.77, 122.21, 115.65, 82.44, 49.72, 27.99. **MS** (ESI) 403.76 (M+H).³⁹

***tert*-butyl 2-((2-(4-(3,5-dimethylisoxazol-4-yl)phenyl)imidazo[1,2-*a*]pyrazin-3-yl)amino)acetate (DB-1-057)**



tert-butyl 2-((2-(4-bromophenyl)imidazo[1,2-*a*]pyrazin-3-yl)amino)acetate (0.34 g, 0.843 mmol, 1 eq), potassium 3,5-dimethylisoxazole-4-trifluoroborate (0.205 g, 1.01 mmol, 1.2 eq), palladium (II) acetate (5.7 mg, 0.0253 mmol, 3 mol %) RuPhos (23.6 mg, 0.0506 mmol, 6 mol %) and sodium carbonate (0.179 g, 1.69 mmol, 2 eq) were dissolved in ethanol (4.2 mL) and degassed with nitrogen for roughly 1 minute. The mixture was placed in a heat block at 90 °C. After 17 hours, the mixture was filtered through a silica plug and concentrated. The crude mixture was purified by automated column chromatography (30 to 100% EtOAc/hexanes) to yield the product as a brown foam (0.284 g, 0.677 mmol, 80%). **¹H NMR** (400 MHz, CDCl₃) δ 8.99 (d, *J* = 1.3 Hz, 1H), 8.20 (dd, *J* = 4.6, 1.3 Hz, 1H), 8.18 – 8.12 (m, 2H), 7.88 (d, *J* = 4.6 Hz, 1H), 7.40 – 7.34 (m, 2H), 3.89 (t, *J* = 4.5 Hz, 1H), 3.76 (d, *J* = 5.5 Hz, 2H), 2.45 (s, 3H), 2.32 (s, 3H), 1.46 (s, 9H). **¹³C NMR** (100 MHz, CDCl₃) δ 170.90, 165.50, 158.76, 143.59, 137.29, 136.88, 132.58, 130.45, 129.54, 129.30, 127.59, 126.90, 116.42, 115.76, 82.74, 50.12, 28.17, 11.83, 11.04. **MS** (ESI) 420.83 (M+H).⁴⁰

2-((2-(4-(3,5-dimethylisoxazol-4-yl)phenyl)imidazo[1,2-*a*]pyrazin-3-yl)amino)acetic acid (DB-1-064)



tert-butyl 2-((2-(4-(3,5-dimethylisoxazol-4-yl)phenyl)imidazo[1,2-*a*]pyrazin-3-yl)amino)acetate (0.284 g, 0.677 mmol, 1 eq) was dissolved in DCM (2.7 mL) and TFA

(2.7 mL) and stirred at room temperature. After 12 hours, the mixture was concentrated, and purified by preparative HPLC (5 to 95% MeCN/water with 0.1%TFA) and lyophilized to yield the product as an orange powder (187 mg, 0.515 mmol, 76%). **¹H NMR** (400 MHz, MeOD) δ 9.08 (s, 1H), 8.69 (d, J = 5.3 Hz, 1H), 8.16 (d, J = 8.2 Hz, 2H), 7.94 (d, J = 5.1 Hz, 1H), 7.66 – 7.46 (m, 2H), 3.99 (s, 2H), 2.48 (s, 3H), 2.32 (s, 3H). **¹³C NMR** (100 MHz, MeOD) δ 174.12, 167.40, 159.93, 140.98, 136.86, 135.29, 134.79, 132.95, 132.23, 130. **MS** (ESI) 364.76

Biologic and Biochemical Compound Evaluation

Reagents. Endogenous BRD4-NUT-expressing midline carcinoma cell lines, 797⁴¹ was described previously. Media, trypsin, and antibiotics for tissue culture were purchased from Mediatech.**Cloning.** cDNA encoding human BRD2, BRD3, BRD4, BRDT, CREBBP and WDR9 (NCBI accession number NP 005095, NP 031397.1, NP 055114.1, NP 001717.2, NP 004371.1, NP 061836.2) were obtained from different sources (BRD2: Synthetic, BRD3: Origene, BRD4: FivePrime, BRDT: IMAGE collection, CREBBP: Synthetic, WDR9: synthetic) and used as templates to amplify the bromodomain regions of the above proteins, using the polymerase chain reaction (PCR) in the presence of Platinum® Pfx DNA polymerase (Invitrogen™, UK). PCR products were purified (QIAquick PCR Purification Kit, Qiagen Ltd. UK) and further sub-cloned into a pET28 derived expression vector, pNIC28-Bsa4⁴², using ligation independent cloning⁴³. The constructs were transformed into competent Mach1™ cells (Invitrogen™, UK) to yield the final plasmid DNA.

Protein Expression and Purification. Colonies from freshly transformed plasmid DNA in competent *E. coli* BL21(DE3)-R3-pRARE2 cells (phage-resistant derivative of BL21(DE3) cell, Invitrogen™), with a pRARE plasmid encoding rare codon tRNAs were grown overnight at 37 °C in 5 ml of Luria-Bertani medium (LB-broth, Merck) with 50 µg/ml kanamycin and 34 µg/ml chloramphenicol (start-up culture). The start-up culture was diluted 1:1000 in fresh medium and cell growth was allowed at 37 °C to an optical density of about 0.5 (OD600) before the temperature was decreased to 18 °C. When the system equilibrated at 18 °C the optical density was about 0.8 (OD600) and protein expression was induced over night at 18 °C with 0.1 mM isopropyl-β-D-thiogalactopyranoside (IPTG). The bacteria were harvested by centrifugation (8,700 x g for 15 min at 4 °C, JLA 81,000 rotor, on a Beckman Coulter Avanti J-20 XP centrifuge) and were frozen at -20 °C as pellets for storage. Cells expressing His6 tagged proteins were re-suspended in lysis buffer (50 mM HEPES, pH 7.5 at 25 °C, 500 mM NaCl, 5 mM Imidazole, 5 % glycerol and 0.5 mM TCEP) in the presence of protease inhibitor cocktail (1 µl/ml) and lysed using an EmulsiFlex-C5 high pressure homogenizer (Avestin - Mannheim, Germany) at 4 °C. 0.15 % of PEI was added with an incubation of 30 min on ice and the lysate was cleared by centrifugation (16,000 x g for 1 h at 4 °C, JA 25.50 rotor, on a Beckman Coulter Avanti J-20 XP centrifuge) and was applied to a nickel-nitrilotriacetic acid agarose column (Ni-NTA, Qiagen Ltd., 5 ml, equilibrated with 20 ml lysis buffer). The column was washed once with 30 ml of lysis buffer then twice with 10 ml of lysis buffer containing 30 mM Imidazole. The protein was eluted using a step elution of imidazole in lysis buffer (50, 100, 150, 2x250 mM Imidazole in 50 mM HEPES, pH 7.5 at 25 °C, 500 mM NaCl). All fractions were collected and monitored by SDS-polyacrylamide gel electrophoresis (Bio-Rad Criterion™

Precast Gels, 4-12 % Bis-Tris, 1.0 mm, from Bio-Rad, CA. Gel run conditions: 180 V, 400 mA, 55 min in XT MES buffer). After the addition of 10 mM dithiothreitol (DTT), the eluted protein was treated overnight at 4 °C with TEV protease to remove the hexa-histidine tag. The protein was further purified with size exclusion chromatography on a Superdex 75 16/60 HiLoad gel filtration column (GE/Amersham Biosciences) on an ÄktaPrime™ plus system (GE/Amersham Biosciences). Samples were monitored by SDS-polyacrylamide gel electrophoresis and concentrated to 10-40 mg/ml in the elution buffer, 10 mM Hepes pH 7.5, 150 mM NaCl, 0.5 mM TCEP and were used for crystallization. Samples for isothermal calorimetry were dialysed over night at 4 °C in a D-Tube™ Dialyser Midi, MWCO 3.5 kDa to a final buffer of 50 mM HEPES, pH 7.4 (at 25 °C), 150 mM NaCl. Protein handling was carried out on ice or in a cold room in all the above steps.

AlphaScreen BRD Binding Assay. Assays were performed with minor modifications from the manufacturer's protocol (PerkinElmer, USA). All reagents were diluted in 50 mM HEPES, 150 mM NaCl, 0.1% w/v BSA, 0.01% w/v Tween20, pH 7.5 and allowed to equilibrate to room temperature prior to addition to plates. After addition of Alpha beads to master solutions all subsequent steps were performed in low light conditions. A 2x solution of components with final concentrations of BRD at 40 nM, Ni-coated Acceptor Bead at 25 µg/ml, and 20 nM bJQ1 was added in 10 µL to 384-well plates (AlphaPlate - 384, PerkinElmer, USA). Biotinylated JQ1 derivative was synthesized as previously described. After a 1 minute 1000rpm spin-down, 100 nL of compounds in DMSO from stock plates were added by pin transfer using a Janus Workstation (PerkinElmer, USA). The streptavidin-coated donor beads (25 µg/ml final) were added as with previous

solution in a 2x, 10 μ L volume. Following this addition, the plates were sealed with foil to block light exposure and to prevent evaporation. The plates were spun down again at 1000rpm for 1 minute. Next, the plates were incubated in the room with the plate reader (for temperature equilibration) for 1 hour prior to reading the assay. Signal is sTable 2.for up to 3 hours after donor bead addition. AlphaScreen measurements were performed on an Envision 2104 (PerkinElmer, USA) utilizing the manufacturer's protocol.

Cell Viability Assay. Cells were counted and adjusted to 60,000 cells/mL. Using a Biotek EL406, 50 μ L of cells are media were distributed into 384 well white plates from Thermo. Immediately after plating, compound in DMSO was distributed to plates. For large plate sets, cells were returned to 37°C incubator while not in use.

Compounds were added to plates using a 100nL 384 well pin transfer manifold on a Janus workstation. Stocks were arrayed in 10 point quadruplicate dose response in DMSO stock in 384 well Greiner compound plates. After addition of compound, plates were incubated for three days in a 37°C incubator.

Cell viability was read out using ATPlite from Perkin Elmer. Plates were removed from the incubator and brought to room temperature prior to use. Lyophilized powder was resuspended in lysis buffer and diluted 1:2 with DI water. 25 μ L of this solution was added to each well using the Biotek liquid handler. Plates were sealed with adherent aluminum seals prior to vortexing and spinning down at 1000g for 1 minute. Plates were incubated for 15 minutes at room temperature before signal was read on an Envision Plate Reader.

Isothermal Titration Calorimetry. Experiments were carried out on a VP-ITC titration microcalorimeter from MicroCal™, LLC (Northampton, MA). All experiments were

carried out at 15 °C while stirring at 295 rpm, in ITC buffer (50 mM HEPES pH 7.4 at 25 °C, 150 mM NaCl). The microsyringe (250 µl) was loaded with a solution of the protein sample (300 µM protein for the BETs, 950 µM protein for CREBBP and 600 µM for WDR9(2), in ITC buffer). All titrations were conducted using an initial control injection of 2 µl followed by 34 identical injections of 8 µl with a duration of 16 sec (per injection) and a spacing of 250 sec between injections. The heat of dilution was determined by independent titrations (protein into buffer) and was subtracted from the experimental data. The collected data were implicated in the MicroCal™ Origin software supplied with the instrument to yield enthalpies of binding (ΔH) and binding constants (K_B) as previously described by Wiseman and coworkers⁴⁴. Thermodynamic parameters were calculated ($\Delta G = \Delta H - T\Delta S = -RT\ln K_B$, where ΔG , ΔH and ΔS are the changes in free energy, enthalpy and entropy of binding respectively). In all cases a single binding site model was employed.

Computational Methods

All computational work was performed in Schrodinger Suite (Schrodinger, LLC). Conformational analysis of lead compounds was performed using Schrodinger's Conformational Search function. Possible poses were prepared for docking by Ligprep. In both cases, default settings were used (OPLS2005 force field, water solvent). Docking was conducted using Glide. The co-crystal of BR4 and JQ1 (PDB: 3MXF) was used to define the ligand receptor grid. Water molecules outside the binding pocket were excluded, and hydrogen bonding interactions were optimized prior to docking.

References:

- 1 Sanchez, R. & Zhou, M. M. The role of human bromodomains in chromatin biology and gene transcription. *Current opinion in drug discovery & development* **12**, 659-665 (2009).
- 2 Schreiber, S. L. & Bernstein, B. E. Signaling network model of chromatin. *Cell* **111**, 771-778 (2002).
- 3 Frank, S. R. *et al.* MYC recruits the TIP60 histone acetyltransferase complex to chromatin. *EMBO Rep* **4**, 575-580, doi:10.1038/sj.embor.embor861 embor861 [pii] (2003).
- 4 Vervoorts, J. *et al.* Stimulation of c-MYC transcriptional activity and acetylation by recruitment of the cofactor CBP. *EMBO Rep* **4**, 484-490, doi:10.1038/sj.embor.embor821 (2003).
- 5 You, J. S. & Jones, P. A. Cancer genetics and epigenetics: two sides of the same coin? *Cancer Cell* **22**, 9-20, doi:S1535-6108(12)00257-7 [pii] 10.1016/j.ccr.2012.06.008 (2012).
- 6 Berg, T. Inhibition of transcription factors with small organic molecules. *Curr Opin Chem Biol* **12**, 464-471, doi:S1367-5931(08)00119-1 [pii] 10.1016/j.cbpa.2008.07.023 (2008).
- 7 Frye, S. V. The art of the chemical probe. *Nat Chem Biol* **6**, 159-161, doi:10.1038/nchembio.296 (2010).
- 8 Delmore, J. E. *et al.* BET Bromodomain Inhibition as a Therapeutic Strategy to Target c-Myc. *Cell* **146**, 904-917, doi:S0092-8674(11)00943-3 [pii] 10.1016/j.cell.2011.08.017 (2011).
- 9 Filippakopoulos, P. *et al.* Selective inhibition of BET bromodomains. *Nature* **468**, 1067-1073, doi:10.1038/nature09504 (2010).
- 10 Zuber, J. *et al.* RNAi screen identifies Brd4 as a therapeutic target in acute myeloid leukaemia. *Nature*, doi:nature10334 [pii] 10.1038/nature10334 (2011).
- 11 Ott, C. J. *et al.* BET bromodomain inhibition targets both c-MYC and IL7R in high-risk acute lymphoblastic leukemia. *Blood*, doi:10.1182/blood-2012-02-413021 (2012).
- 12 Prinjha, R. K., Witherington, J. & Lee, K. Place your BETs: the therapeutic potential of bromodomains. *Trends in pharmacological sciences* **33**, 146-153, doi:10.1016/j.tips.2011.12.002 (2012).
- 13 Mujtaba, S. *et al.* Structural mechanism of the bromodomain of the coactivator CBP in p53 transcriptional activation. *Molecular cell* **13**, 251-263 (2004).
- 14 Mujtaba, S., Zeng, L. & Zhou, M. M. Structure and acetyl-lysine recognition of the bromodomain. *Oncogene* **26**, 5521-5527, doi:10.1038/sj.onc.1210618 (2007).
- 15 Filippakopoulos, P. *et al.* Histone recognition and large-scale structural analysis of the human bromodomain family. *Cell* **149**, 214-231, doi:10.1016/j.cell.2012.02.013 (2012).
- 16 Belkina, A. C. & Denis, G. V. BET domain co-regulators in obesity, inflammation and cancer. *Nat Rev Cancer* **12**, 465-477, doi:nrc3256 [pii] 10.1038/nrc3256 (2012).

- 17 Wu, S. Y. & Chiang, C. M. The double bromodomain-containing chromatin adaptor Brd4 and transcriptional regulation. *J Biol Chem* **282**, 13141-13145, doi:DOI 10.1071/jbc.R700001200 (2007).
- 18 Yang, Z. *et al.* Recruitment of P-TEFb for stimulation of transcriptional elongation by the bromodomain protein Brd4. *Molecular cell* **19**, 535-545, doi:10.1016/j.molcel.2005.06.029 (2005).
- 19 Yang, Z., He, N. & Zhou, Q. Brd4 recruits P-TEFb to chromosomes at late mitosis to promote G1 gene expression and cell cycle progression. *Molecular and cellular biology* **28**, 967-976, doi:10.1128/MCB.01020-07 (2008).
- 20 Schroder, S. *et al.* Two-pronged binding with bromodomain-containing protein 4 liberates positive transcription elongation factor b from inactive ribonucleoprotein complexes. *J Biol Chem* **287**, 1090-1099, doi:10.1074/jbc.M111.282855 (2012).
- 21 Rahman, S. *et al.* The Brd4 extraterminal domain confers transcription activation independent of pTEFb by recruiting multiple proteins, including NSD3. *Molecular and cellular biology* **31**, 2641-2652, doi:10.1128/MCB.01341-10 (2011).
- 22 Dey, A., Chitsaz, F., Abbasi, A., Misteli, T. & Ozato, K. The double bromodomain protein Brd4 binds to acetylated chromatin during interphase and mitosis. *Proceedings of the National Academy of Sciences of the United States of America* **100**, 8758-8763, doi:10.1073/pnas.1433065100 (2003).
- 23 Zhao, R., Nakamura, T., Fu, Y., Lazar, Z. & Spector, D. L. Gene bookmarking accelerates the kinetics of post-mitotic transcriptional re-activation. *Nat Cell Biol* **13**, 1295-1304, doi:10.1038/ncb2341
ncb2341 [pii] (2011).
- 24 French, C. A. Pathogenesis of NUT midline carcinoma. *Annu Rev Pathol* **7**, 247-265, doi:10.1146/annurev-pathol-011811-132438 (2012).
- 25 Zhang, W., Lu, Y. & Chen, C. H.-T. Combination of microwave reactions with fluororous separations in the palladium-catalyzed synthesis of aryl sulfides. *Molecular diversity* **7**, 199-202 (2003).
- 26 Zhang, W., Chen, C. H.-T., Lu, Y. & Nagashima, T. A highly efficient microwave-assisted Suzuki coupling reaction of aryl perfluorooctylsulfonates with boronic acids. *Organic letters* **6**, 1473-1476 (2004).
- 27 Zhang, W. & Chen, C. H.-T. Fluorous synthesis of biaryl-substituted proline analogs by 1, 3-dipolar cycloaddition and Suzuki coupling reactions. *Tetrahedron letters* **46**, 1807-1810 (2005).
- 28 Lu, Y. & Zhang, W. Microwave-assisted Synthesis of a 3-Aminoimidazo [1, 2-a]-pyridine/pyrazine Library by Fluorous Multicomponent Reactions and Subsequent Cross-coupling Reactions. *QSAR & combinatorial science* **23**, 827-835 (2004).
- 29 Zhou, H., Zhang, W. & Yan, B. Use of cyclohexylisocyanide and methyl 2-isocyanoacetate as convertible isocyanides for microwave-assisted fluororous synthesis of 1, 4-benzodiazepine-2, 5-dione library. *Journal of combinatorial chemistry* **12**, 206-214 (2009).
- 30 Zhang, W. & Nagashima, T. Palladium-catalyzed Buchwald–Hartwig type amination of fluororous arylsulfonates. *Journal of fluorine chemistry* **127**, 588-591 (2006).
- 31 Zhang, Z.-H., Lü, H.-Y., Yang, S.-H. & Gao, J.-W. Synthesis of 2, 3-dihydroquinazolin-4 (1 H)-ones by three-component coupling of isatoic anhydride, amines, and

- aldehydes catalyzed by magnetic Fe₃O₄ nanoparticles in water. *Journal of combinatorial chemistry* **12**, 643-646 (2010).
- 32 Hewings, D. S. *et al.* 3,5-dimethylisoxazoles act as acetyl-lysine-mimetic bromodomain ligands. *Journal of medicinal chemistry* **54**, 6761-6770, doi:10.1021/jm200640v (2011).
- 33 Dawson, M. A. *et al.* Inhibition of BET recruitment to chromatin as an effective treatment for MLL-fusion leukaemia. *Nature* **478**, 529-533, doi:10.1038/nature10509 (2011).
- 34 Dawson, M. A. *et al.* Inhibition of BET recruitment to chromatin as an effective treatment for MLL-fusion leukaemia. *Nature* **478**, 529-533, doi:10.1038/Nature10509 (2011).
- 35 Liu, X., Vorontchikhina, M., Wang, Y. L., Faiola, F. & Martinez, E. STAGA recruits Mediator to the MYC oncoprotein to stimulate transcription and cell proliferation. *Mol Cell Biol* **28**, 108-121, doi:10.1128/MCB.01402-07 [pii] 10.1128/MCB.01402-07 (2008).
- 36 Li, H. H., Li, A. G., Sheppard, H. M. & Liu, X. Phosphorylation on Thr-55 by TAF1 mediates degradation of p53: a role for TAF1 in cell G1 progression. *Mol Cell* **13**, 867-878, doi:10.1016/S1097276504001236 [pii] (2004).
- 37 Buchmann, A. M., Skaar, J. R. & DeCaprio, J. A. Activation of a DNA damage checkpoint response in a TAF1-defective cell line. *Mol Cell Biol* **24**, 5332-5339, doi:10.1128/MCB.24.12.5332-5339.2004 24/12/5332 [pii] (2004).
- 38 Pijnappel, W. W. *et al.* A central role for TFIID in the pluripotent transcription circuitry. *Nature* **495**, 516-519, doi:10.1038/nature11970 nature11970 [pii] (2013).
- 39 Bienayme, H. & Bouzid, K. A new heterocyclic multicomponent reaction for the combinatorial synthesis of fused 3-aminoimidazoles. *Angew Chem Int Edit* **37**, 2234-2237, doi:10.1002/(Sici)1521-3773(19980904)37:16<2234::Aid-Anie2234>3.0.Co;2-R (1998).
- 40 Molander, G. A., Canturk, B. & Kennedy, L. E. Scope of the Suzuki-Miyaura Cross-Coupling Reactions of Potassium Heteroaryltrifluoroborates. *J Org Chem* **74**, 973-980, doi:10.1021/Jo802590b (2009).
- 41 Toretsky, J. A. *et al.* Translocation (11;15;19): a highly specific chromosome rearrangement associated with poorly differentiated thymic carcinoma in young patients. *Am J Clin Oncol* **26**, 300-306 (2003).
- 42 This vector includes sites for ligation-independent cloning and a Tobacco Etch Virus (TEV)-cleavable N-terminal His₆-tag (extension MHHHHHSSGVDLGTENLYFQ*SM-) After digestion with TEV protease, the protein retains an additional serine and methionine on the N-terminus.
- 43 Stols, L. *et al.* A new vector for high-throughput, ligation-independent cloning encoding a tobacco etch virus protease cleavage site. *Protein Expression and Purification* **25**, 8-15 (2002).
- 44 Wiseman, T., Williston, S., Brandts, J. F. & Lin, L. N. Rapid Measurement of Binding Constants and Heats of Binding Using a New Titration Calorimeter. *Analytical Biochemistry* **179**, 131-137 (1989).

Chapter 3

Therapeutic Strategies to Inhibit MYC

McKeown MR, Bradner JE. 2014. Therapeutic strategies to inhibit MYC. Cold Spring Harb Perspect Med. doi: 10.1101/CSHPERSPECT.a014266.

¹Department of Medical Oncology, Dana-Farber Cancer Institute, Boston, MA; ²Center for the Science of Therapeutics, Broad Institute, Cambridge, MA; ³Department of Medicine, Harvard Medical School, Boston, MA.

Introduction:

As part of my research into chemical probes, I especially focused on potential methods to target cancer growth. While direct inhibition of MYC has proven difficult, it remains one of the most important undrugged cancer dependencies. Utilizing new biochemical techniques I led the screening effort in our lab to create a MYC inhibitor. The depletion of MYC in multiple myeloma¹ after treatment with JQ1 revealed the potential of alternative pathways to MYC inhibition. As consequence, Dr. Bradner and I did extensive literature searches on the topic. Our findings were eventually compiled into the book chapter contained herein. I co-authored the following chapter with Dr. Bradner, for Cold Spring Harbor Perspectives in Medicine.

The direct inhibition effort created a team with myself on biochemistry, Jason Marineau (formerly Bradner Lab) on synthetic chemistry, and Peter Rahl (formerly Young Lab) on MYC biology. Both of these collaborators were post-docs at the time and now work at Syros Pharmaceuticals. Due to the historical difficulties of developing small molecule inhibitors against protein-protein interactions, proteins lacking defined structures, and transcriptional complexes in general, MYC was chosen as a challenging target with strong therapeutic potential, and unmet need. Also, the lack of a chemical probe against MYC means that previous studies have had to rely on genetic manipulation of the system with tet-off²⁻⁴ or dominant negatives, like omomyc⁵⁻⁷. I hypothesize that small molecule inhibition of MYC will decrease the level of MYC on chromatin and its total protein amount. At the same time, MAX should stay constant and stay on chromatin. As a result, I will investigate the gene signature of MYC loss and its return after transient suppression by Affy array expression and CHIP for MYC and MAX

binding to chromatin. In addition, the binding of a small molecule to a poorly structured protein, such as MYC, may stabilize the structure.

A high throughput technology to screen for inhibitors of MYC/MAX dimerization and DNA binding

The *in vitro* high throughput assay uses AlphaScreen technology (Perkin Elmer), a bead-based proximity assay, purified biological components, nucleotide polymers containing protein binding sites and candidate inhibitors with full-length human MYC and MAX proteins. This reports on formation of the MYC/MAX/Ebox DNA ternary complex using singlet oxygen transfer between AlphaScreen beads resulting in production of luminescent signal. Inhibitors preventing complex formation will diminish signal intensity. Significantly, the assay was amenable to miniaturization, automation (automated plate filling and compound pin transfer) and high throughput screening in either 384- or 1536-well plate formats.

This assay is superior to alternative methodologies such as FRET or FP for a variety of reasons. First, the cost per well for protein is dramatically reduced by using protein concentrations in the tens of nanomolar or lower which is significantly lower than alternatives such as thermal melt or FP. The low concentration of protein components is important for detection of low affinity ligands that are often identified in high throughput screens. Second, the assay is unaffected by molecular orientation or proximity which can have a large impact on FRET. Third, AlphaScreen effectively displays an anti-Stokes shift greatly reducing the impact of intrinsically fluorescent molecules on the assay. Since the transfer of energy is mediated by singlet oxygen, the readout wavelength can be blue-shifted relative to the excitation wavelength, which is

impossible in traditional fluorescent assays. Fourth, the relatively long signal distance of 200 nm that singlet oxygen can travel allows reporting on full protein complexes and not just single target binding. Fifth, the assay proved highly amenable to miniaturization with and can be scaled down to smaller volumes with relative ease. Finally, neither the small molecules being assays nor the target protein, MYC, need to be chemically, conformationally or behaviorally altered by tethering them to a surface or reporter which can induce artifacts. We have the option of having MYC free in solution (as it is inside a cell) and having MAX and DNA bound to a bead. But as described below, this assay has the flexibility of alternative configuration where MYC and DNA are bound to a bead and MAX is free in solution. Thus, it allows for various configuration depending on the protein target.

Assay Development and Validation

Two complimentary assays have been developed to monitor MYC/MAX/Ebox DNA complex formation. The AlphaScreen assay (Perkin Elmer) is comprised of an acceptor and a donor bead in solution (Figure 3.1). The donor bead is illuminated at 680nm, which generates a singlet O₂ molecule. If the acceptor bead is within 200nm within 4 μsec of illumination (O₂ half-life), it will transfer the energy and generate luminescent signal at a wavelength of 520-620nm.

The assay consists of biotinylated Ebox DNA ([Biotin-triethyleneglycol]GGAAGCAGACCACGTGGTCTGCTTCC) used in conjunction with strepavidin donor bead. His₆-MAX is used with Ni⁺⁺ acceptor beads. Free MYC (purified as his₆-MYC, followed by a thrombin cleavage reaction to remove the his₆ tag)

is added free in solution. A reciprocal assay (not shown in schematic) uses biotinylated Ebox DNA with streptavidin donor beads. His₆-MYC is used in conjunction with the Ni⁺⁺ acceptor bead. Recombinant free MAX (purified as his₆-MAX followed by thrombin cleavage of the his₆ tag) is added free in solution. The different assay set-ups offer flexibility in which components are bound to beads or free in solution.

All reagents are diluted in reaction buffer (50 mM HEPES, 150 mM NaCl, 0.2% w/v BSA, 0.02% w/v Tween20, 40 µg/ml glycogen, 100 nM DTT, pH 8.0 and allowed to equilibrate to room temperature, where glycogen and DTT are added immediately prior to use.) prior to addition to plates. The composition of the reaction buffer can vary and be optimized depending on the complex of interest. We found that adjusting the pH from 7.4 to 8.0 better mimics the nuclear conditions and favours Myc/MAX heterodimer formation over MAX/MAX homodimer formation. Also, the BSA and Tween20 concentrations were optimized to reduce background, non-specific associations and aggregation. DTT was added to mimic the reducing conditions of the cellular interior. It is also thought that BSA reduces background signal by sequestering errant singlet oxygen. Early attempts to use automation were confounded by a gradient of signal across the plate, in the direction of plate filling, which we reasoned was caused by adsorption of oligos onto polypropylene tubing. We discovered that the addition of glycogen, serving as a carrier, corrected the defect in assay automation. Full automation is critical when screening compound libraries and therefore, this was an essential modification that we discovered had a profound effect on assay performance. The precise ratio of components proved very important for optimal signal to background and each was titrated as shown in Figure 3.1. Under fully optimized conditions, the

assay was found to be fully screening ready and generate a robust z-prime score using a positive control compound made by Jason Marineau called JJM288 (Figure 3.2). Having established the proper configuration (schema in Figure 3.3A). The assay gives IC50 values when used in dose response against screening hits and medicinal chemistry products (Figure 3.3B). In addition, over a several thousand compound screening effort, the assay showed good reproducibility between duplicates (Figure 3.3C) and clean normal distribution of hits (Figure 3.3D).

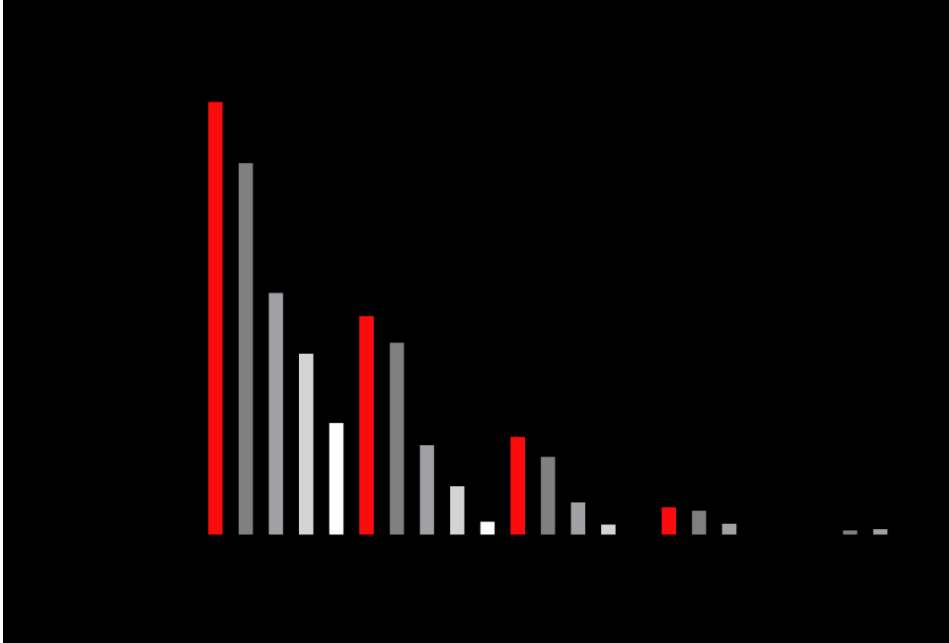


Figure 3.1: Assay optimization for MYC-dependent signal. Signal (RLUs) of bead proximity is dependent on MYC and Max protein concentrations. A fixed DNA concentration was used.

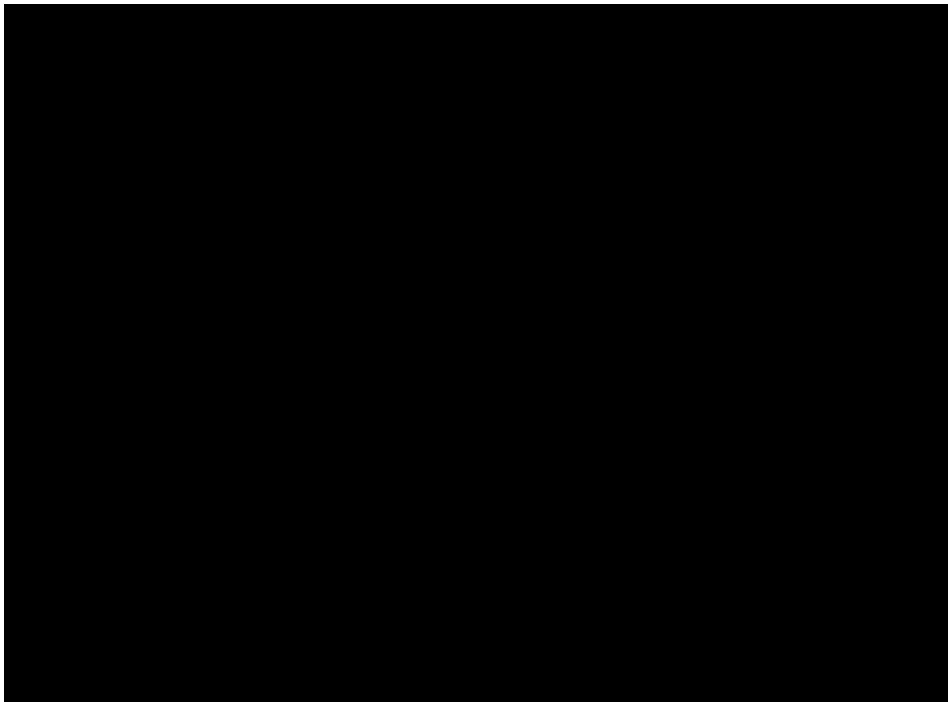


Figure 3.2: Z-prime analysis for assay robustness. This assay has a 0.82 Z-prime, indicating a highly robust assay. Z-prime in 16-plicate using JJM288 as a positive control compound (Positive). Leaving MYC out of the reaction (No Myc) also reduces signal, indicating MYC-dependent signal.

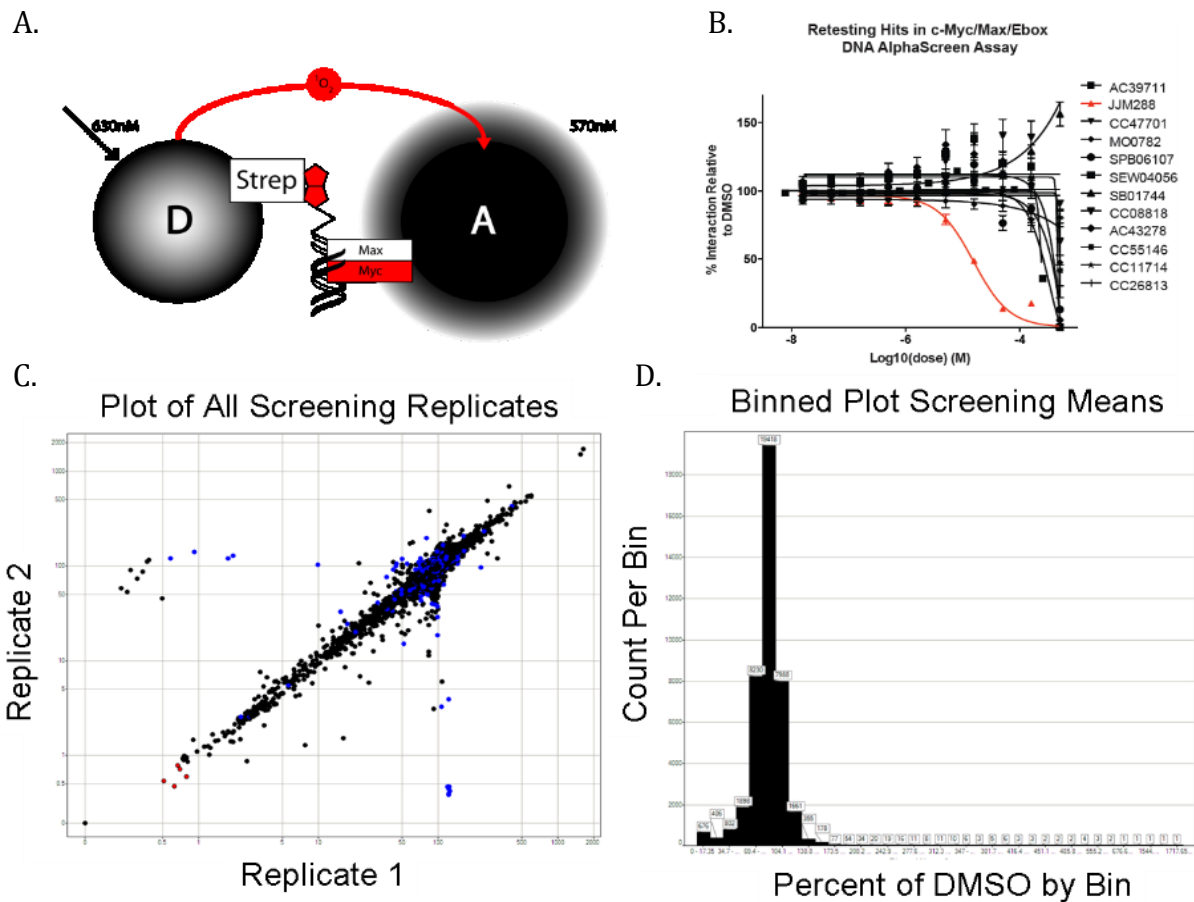


Figure 3.3: MYC Screening A) Schematic of cMyc assay. B) Characteristic dose response showing retest of hits from a library. C) Scatter Plot of all cMyc screening to date. D) Histogram showing performance of assay. 85% fall within 70-120% of DMSO mean.

MYC as a Target for Probe Discovery:

One particular compound series based on the hit resynthesized as JJM288, has shown potential. It had 4 μ M potency in biochemical assays and 19 μ M in H2171 lung cancer cell line, used due to its exceptionally high expression of MYC. Our collaborator Pete Rahl in the Young lab at the Whitehead performed gel shifts, nanostring of a MYC, ChIP, and caspase cleavage assays, which all looked favorable.

Having established a reasonable lead molecule, work on derivatization was performed in collaboration with Jason Marineau in the Bradner lab. Progressive iterations of compound development were pursued where biochemical and cell viability studies informed development of the next compound series. Based our own earlier work on a previous lead series with mitorubrinic acid and 10058-F4 (data not shown), we hypothesized that adding negative charge would be beneficial and were able to make a leap forward with a focused library that generated JJMII288-C02 (Figure 3.4A). Furthermore, we hypothesized that greater restriction of the bond angles and replacement of the hydrazide would increase potency which led to JJMIII-61 (Figure 3.4B). C02 has been further validated in gel shift assays, cellular viability, and reporter lines (Figure 3.4C&D). An important note caveat with regard to cellular assays is the use of an acetoxymethyl protecting group for free acids. Upon noting a lack of potency in cellular assays, it was hypothesized that masking the free acid would help deliver the molecule into cells. Moreover, an acetoxymethyl group was selected due to its preferential cleavage by cellular esterases, allowing accumulation in cells and preventing cleavage in media or the blood stream⁸.

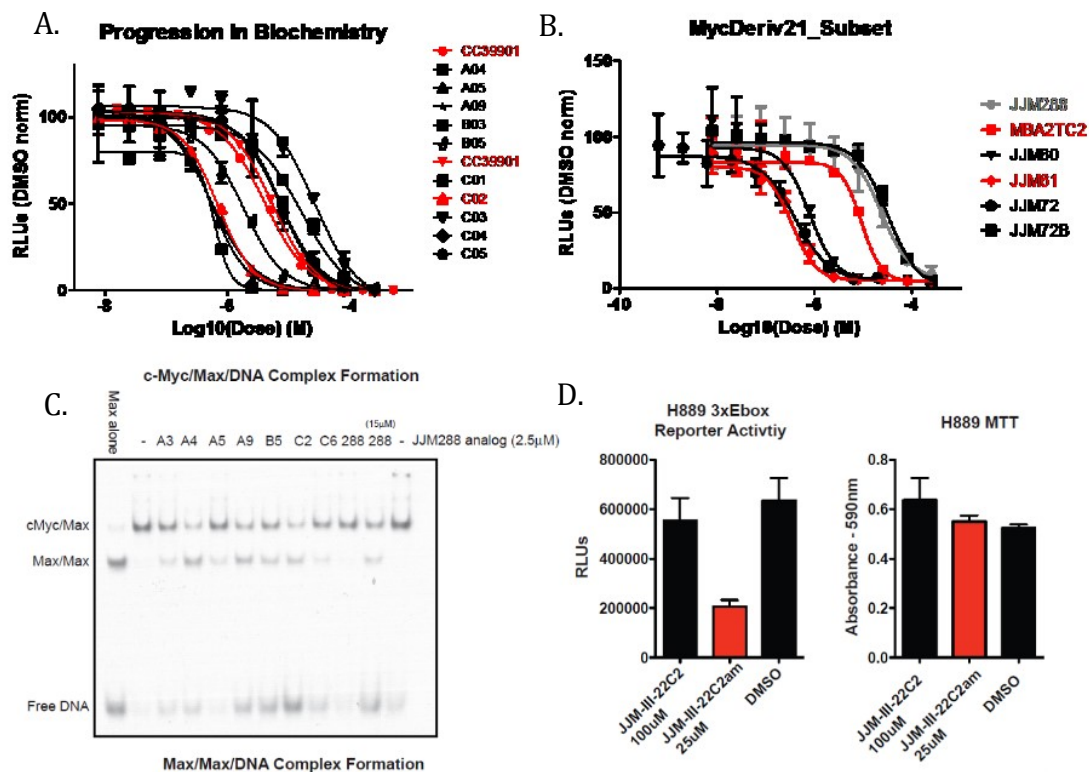
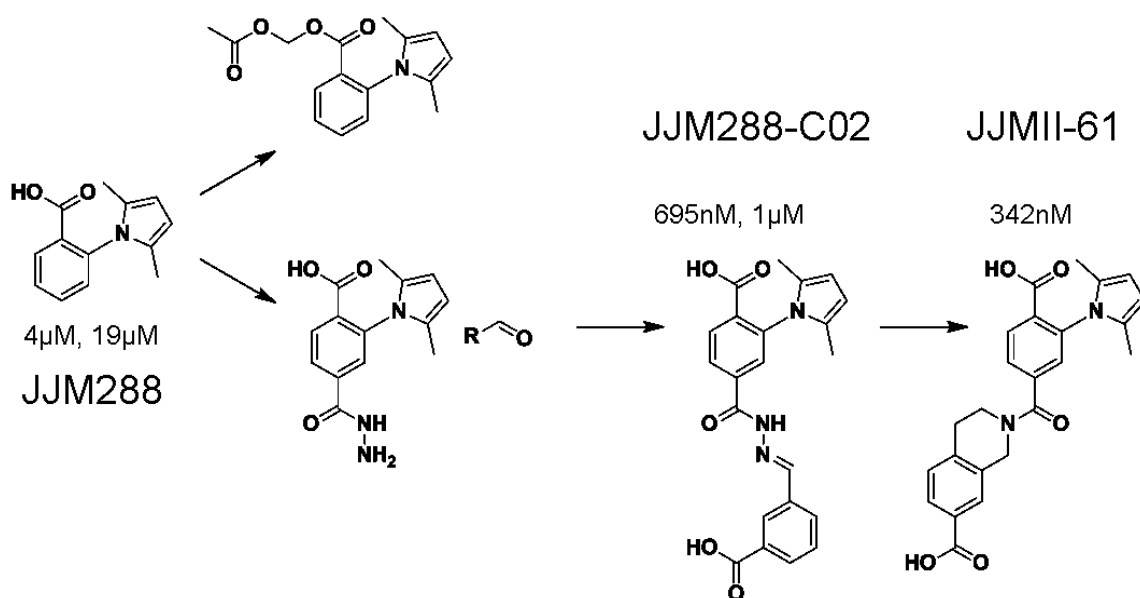


Figure 3.4: MYC dose response A) Alphascreen dose response of JJM288 derivatives made by hydrazide coupling. B) Alphascreen of constrained amides and ureas to replace hydrazide. C) Gel shift of JJM288 derivatives. Inhibition of Myc-Max-DNA complex results in increased Max homodimer and free DNA. D) Reporter assay with Ebox driven luciferase compared to MTT control assay for viability over 24 hours.



Scheme 3.1: Chemical Progression Chemical series starting from JJM288. The AM ester is used to make all compounds in the series functional on cells. Potency (Where tested) is given as biochemistry, cellular.

While numerous previous attempts have been made against the classically difficult target MYC it is an incredibly important target for drug discovery as the next section will elaborate on. Our approach using biochemical and cellular assays with large chemical libraries and focused libraries developed around hits identified in high throughput screens has shown success in developing inhibitors of transcription factor function that will require much ongoing work.

Background:

MYC (v-myc myelocytomatosis viral oncogene homologue) is a nuclear DNA-binding transcription factor that orchestrates transcriptional regulatory pathways underlying cell growth, cell cycle progression, metabolism and survival (Conacci-Sorrell et al. 2014) ¹. MYC was first described 30 years ago in the context of viral oncogenesis ²⁻⁴, and subsequently a human homologue was identified and characterized ^{5,6}. Since its discovery, MYC has emerged as a master regulator of numerous biological and disease processes.

MYC is the most frequently amplified oncogene in human cancers, and *MYC* alteration is observed in a wide range of tissue types including breast, lung, and prostate cancer ⁷. *MYC* overexpression occurs in 30% of all human cancers and frequently predicts for a poor clinical outcome, aggressive biological behavior, increased likelihood of relapse and advanced stage of disease ^{8,9}. An estimated 450,000 Americans each year are diagnosed with a *MYC*-dependent cancer. Deregulated expression of *MYC* is a hallmark feature of cancer (Conacci-Sorrell et al. 2014; Gabay et al. 2014), uncoupling physiologic growth-factor dependent proliferation. Deregulated expression of *MYC* in cancer occurs through gene amplification ¹⁰, chromosomal translocation ^{11,12}, focal enhancer amplification ¹³, germline enhancer polymorphism ¹⁴⁻¹⁸, or commonly through constitutive activation of upstream signaling pathways. Each of these mechanisms serves to uncouple physiologic, growth-factor dependent proliferation.

MYC has been multiply validated as essential for tumor initiation and maintenance in numerous tumor histologies (Gabay et al. 2014; Huang and Weiss

2013; Roussel and Robinson 2013; Schmitz et al. 2014). Studies in transgenic mouse models identify that MYC inactivation leads to prompt tumor regressions, often associated with phenotypes of differentiation and cellular senescence with or without apoptosis¹⁹⁻²⁴. In models of osteosarcoma, even brief *MYC* inactivation significantly improved survival rates owing to terminal differentiation of tumor cells²³.

The pleiotropic role of MYC in developmental biology and tissue homeostasis has prompted reasonable concern that targeting MYC may provoke severe, untoward toxicity. Indeed, genetic ablation of *MYC* in mice is embryonic lethal at an early stage of gestation (between days 9.5 and 10.5), with failed hematopoietic development²⁵ (Hurlin 2013). While subsequent studies have demonstrated tolerance of tissue-specific *MYC* loss or downregulation, such as in the liver and small intestine²⁶ (Hurlin 2013), concerns remain that pharmacologic inhibition of MYC may feature a narrow therapeutic index. For example, tolerance of *MYC* loss in intestinal epithelium could be conferred by compensatory upregulation of *MYCN*²⁶ (Hurlin 2013), suggesting that selective inhibition of MYC-family isoforms may be required to firmly establish a therapeutic index.

Recently, a powerful genetic instrument developed by Evan and colleagues has provided compelling evidence that a therapeutic index does exist for targeting MYC. Structure-guided design allowed the optimization and characterization of a 93 residue, dominant-negative peptide comprising the bHLHZ domain (see Conacci-Sorrell et al. 2014) called Omomyc^{24,27}. Four amino acid substitutions in the extended leucine zipper domain relieve repulsive charge interactions allowing for a coiled-coil binding event to occur, presumably with endogenous MYC. Thus, Omomyc functions to competitively

bind MYC in a manner preventing MYC:MAX heterodimerization, and expression of Omomyc prompts rapid growth arrest and downregulation of MYC target genes ^{28,29}. Tetracycline-inducible expression of Omomyc has allowed a simulation of what pharmacologic modulation of MYC function may hold, in vitro and in vivo. As described in Gabay et al. (2014), constitutive induction of Omomyc prompts tonic inhibition of MYC:MAX heterodimerization associated with significant toxicity in proliferative tissue compartments in rodents (bone marrow and bowel). However, periodic induction of Omomyc has proven well-tolerated. Dosing regimens have already been identified which provoke unprecedented responses in aggressive murine models of cancer, notably including the KRAS:TP53 model of non-small cell lung carcinoma ³⁰. This research further validates MYC as a therapeutic target in cancer, importantly downstream of other intractable protein targets and tumor suppressors, and establishes a therapeutic index for MYC inhibition, in vivo.

Beyond cancer, MYC is also a positive effector of tissue inflammation. Activation of MYC is observed in immune cells during inflammatory cell expansion ³¹. MYC amplifies the transcriptional response to inflammatory transcription factor signaling in conditions such as rheumatoid arthritis ³². MYC function has also been implicated in the pathophysiology of heart failure, during tissue remodeling associated with hypertrophy and dilatation ³³. Hence, the ability to inhibit MYC could extend beyond cancer therapy.

Toward direct inhibition of MYC

In the post-genomic era, the emergent paradigm of drug discovery is increasingly target directed. Disease biology identifies a critical effector mediating the

pathophysiology of illness or the maladaptive response, and target-directed ligand discovery is undertaken. Innovation in the science of therapeutics over the last three decades has generated diverse strategies, which may be deployed to realize direct-acting inhibitors of protein targets. Still, the prioritization of targets is heavily influenced by perceptions of success and the horizons of supported research ³⁴⁻³⁶.

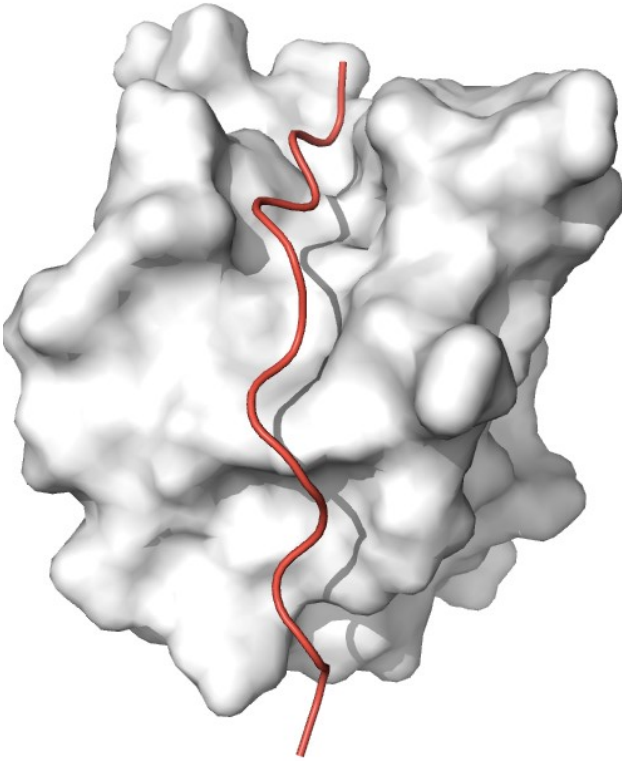
As a class, transcription factors have proven particularly evasive in the discipline of ligand discovery ^{37,38}. Transcription factors are master regulators of cell state, controlling gene expression programs driving cell type specification and contributing to the pathophysiology of a broad range of diseases ^{39,40}. As a class, transcription factors are highly desirable proteins for therapeutic targeting. Yet, also as a class, transcription factors biophysically associate through extensive inter-facial associations featuring large surface areas, a lack of hydrophobic invaginations, and noncontiguous contacts. These features are at odds with traditional binding models for small organic drug molecules ⁴¹. The number of transcription factors successfully approached to-date with discovery chemistry is therefore rather small. It has been our experience, developing the first direct-acting inhibitors of the NOTCH1 transactivation complex for probe and therapeutic development in T-cell acute lymphoblastic leukemia, that significant challenges exist in each phase of assay development, small molecule optimization, biophysical characterization, mechanistic validation and cellular permeability ⁴². For these and other reasons, despite a confluence of detailed mechanistic insights and unmet medical needs, direct inhibition of MYC remains a historic challenge ¹. Indeed, MYC has emerged as arguably the prototypical example of an “undruggable target,” a

term reserved for protein targets that have proven intractable to coordinated efforts in ligand discovery.

MYC presents specific, significant obstacles to discovery chemistry. MYC lacks enzymatic activity, limiting many effective approaches to direct inhibition. Rather, MYC functions via protein-protein interactions, which remain a technical and psychological barrier to organized efforts in drug discovery ⁴³. Structurally, MYC lacks globular functional domains, which might be approached with structure-based or empirical biochemical screening. MYC is comprised of a largely unstructured amino-terminal region involved in transactivation and protein stability (Conacci-Sorrell et al. 2014; Farrell and Sears 2014). Four highly conserved functional modules exist at the amino-terminus, termed MYC Boxes (MBI-IV). MBI possesses a degron targeted by FBW7 ^{44,45}. MBII recruits a chromatin modifying complex containing TRRAP, GCN5 and TIP60 (Hann 2014)⁴⁶. MBIII and MBIV contribute to MYC-specific phenotypes, such as MYC-induced apoptosis, but are not clearly relevant for MYC-induced cell proliferation and survival ^{47,48}. Among the MYC Boxes, structural data is only available for MBI. Arrowsmith and colleagues have reported a structural model for MBI binding to the SH3 domain of the BIN1 tumor suppressor ⁴⁹. However this interaction does not present a compelling therapeutic rationale, and the structure is limited to 13 residues of MYC (Figure 3.5A).

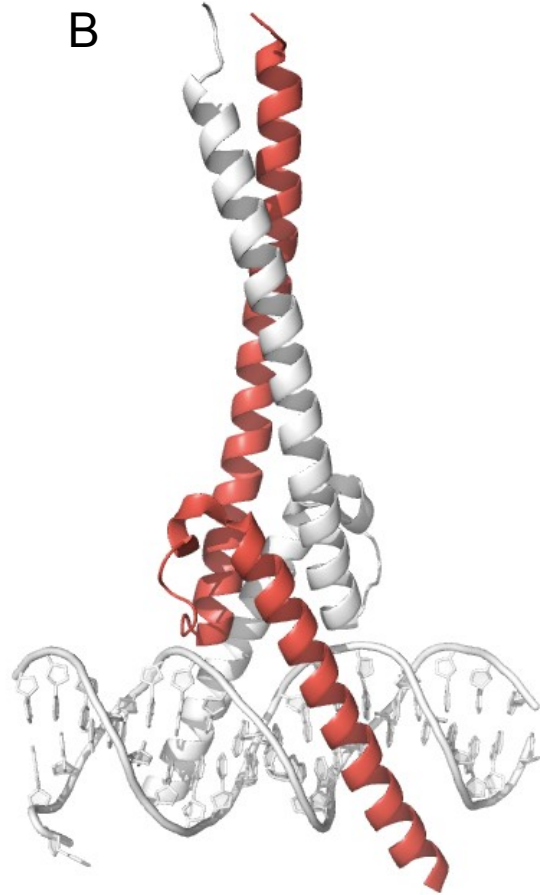
The carboxy-terminus of MYC encodes a 100 residue basic helix-loop-helix-leucine-zipper (bHLH-LZ) DNA binding domain. The leucine zipper forms a coiled coil heterodimer with a homologous region on the transcriptional repressor, MAX, which together engage E-box DNA binding sites (see Conacci-Sorrell et al. 2014). Localization

A



MYC Box 1 (PDB:

B



MYC:MAX (PDB:

Figure 3.5: Structural studies of MYC. Structural studies of MYC reveal challenges of developing directing inhibitors of (A) MYC Box I (MBI as red ribbon and BIN1 as white space-fill; PDB: 1MV0) and (B) the MYC:MAX heterodimer (MYC as red ribbon and MAX as white ribbon on white DNA; PDB: 1NKP).

of the heterodimer to promoter and enhancer regions positively regulates transcription of proliferation-associated genes through control of transcription elongation ^{1,50,51}. Heterodimerization of MYC and MAX is required for transcriptional activation and oncogenic transformation, validating this interaction for further study. A seminal structural study by Nair and Burley ⁵², however, elegantly displays the extended interaction between the two proteins that offers no apparent site for positioning a small molecule inhibitor (Figure 3.5B). The structurally and functionally similar *MYCN* and *MYCL* are comparably organized, posing then identical challenges for direct-acting therapeutic development in diseases attributable to these two oncogenes.

Intrinsically disordered proteins, such as MYC, comprise more than 30% of eukaryotic proteins ^{49,53,54}. Many such proteins are found at signaling nodes, where rapid physiologic response and dynamic cell state changes demand finely tuned post-translational regulatory mechanisms which may be facilitated by intrinsic disorder ⁵⁵. Disordered proteins are often encoded by transcripts featuring short polyA tails, which reduce mRNA stability, and feature amino-terminal degrons and internal PEST sequences allowing for precise control of protein half-life ⁵⁶. As discussed in detail in Farrell and Sears (2014), MYC has an ephemeral half-life (20–30 minutes), and is tightly regulated by E3 ubiquitin ligase recruitment and proteasomal degradation through at least two complexes (SKP2 and FBW7) and an evolutionarily conserved PEST domain ^{57,58}. Perhaps the intrinsic disorder of MYC and additional counter-regulatory measures (short protein and mRNA half-lives, transcriptional attenuation) are then ancient evolutionary safeguards to having such a dangerous oncogene in the genome.

Despite the apparent obstacles involved in studying the function of intrinsically disordered proteins, several research groups have organized around the challenge of developing first direct-acting inhibitors of MYC. The concept underlying these studies is theoretical in nature, arguing that the inherent, intrinsic disorder of native MYC^{52,59,60}, establishes an opportunity for small-molecule mediated induction of a neomorphic binding site, a perhaps extreme example of induced fit. Induced fit implies a conformational change in the protein target provoked by a ligand, which may be accompanied by target inhibition or functional modulation as has been characterized extensively in enzymology and protein-nucleic acid interactions^{61,62}. The concept of induced fit applied to intrinsically disordered proteins possesses additional considerations. The lack of secondary structure in proteins such as MYC limits competing native intramolecular interactions, which are often low affinity, yet is complicated by the need for significant binding energy to overcome entropic penalties⁵³, and the likelihood of multiple binding states. This latter consideration presents challenges in establishing modes of molecular recognition, capturing low energy assembly states for structural characterization, or even rigorously validating inhibitory biochemistry. As such, current described inhibitors of the MYC:MAX interaction serve as early, provocative examples of prototypical compounds, but as a group lack properties of target specificity, biophysical characterization and demonstrated utility in cell and model organism assays of MYC biology, that would define these compounds as chemical probes of MYC function and bona fide leads for therapeutic development⁶³.

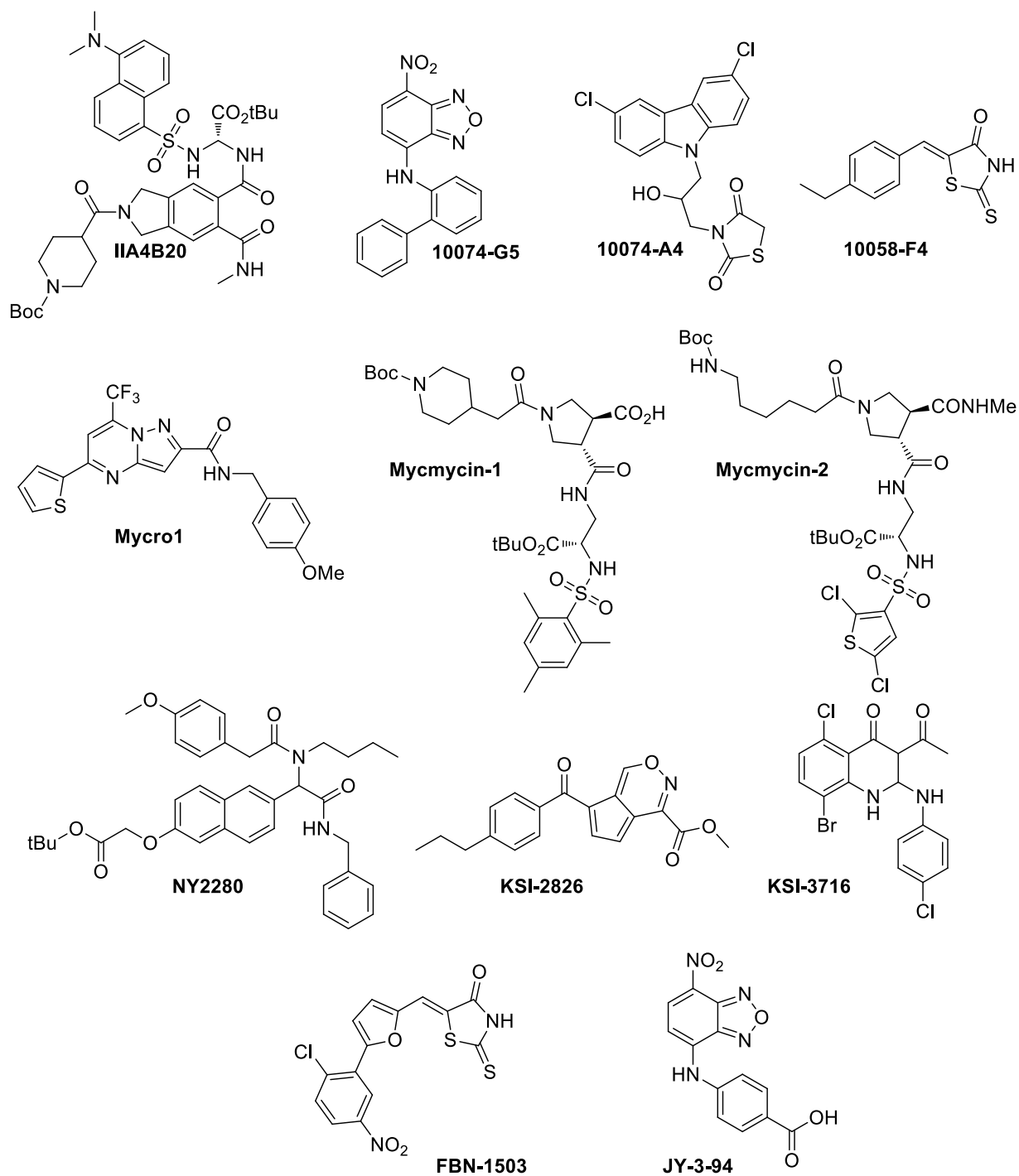


Figure 3.6: Small molecule inhibitors of MYC. From top left to bottom right: Berg et al. 2002, Yin et al. 2003, Kiessling et al. 2006 & 2007, Shi et al. 2009, Xu et al. 2006, Jeong et al. 2010, Yap et al. 2013. These compounds are the current putative direct inhibitors of MYC.

To our knowledge, the first efforts to inhibit MYC:MAX heterodimerization were reported by Vogt and colleagues in 2002⁶⁴. Using a CFP/YFP fluorescence resonance energy transfer (FRET) assay, the bHLH-LZ domains of MYC and MAX were studied for inhibition of dimerization by a library of 7,000 small molecules. These studies identified a series of related, substituted isoindolines (e.g., IIA4B20; Figure 3.6), which exhibited weak but reproducible inhibitory activity in FRET and ELISA assays (75–210 μ M). Soon thereafter, Prochownik and colleagues⁶⁵, studied a commercial library of 10,000 compounds using a Gal4-based yeast two-hybrid assay and the minimal bHLH-LZ interacting domains. Emerging from these studies were a series of structurally diverse compounds which impaired MYC:MAX binding by electrophoretic mobility shift assay (EMSA), including compounds which have been subsequently studied in cellular models of MYC biology (10074-A4, 10074-G5, and 10058-F4; Figure 3.6). A second study by Yang and co-workers reported curcuminoid inhibitors of MYC:MAX binding, in the context of a study aiming to establish binding constants for the heterodimeric interaction on DNA⁶⁶. By measuring binding of MYC:MAX heterodimers to a fluorescein-labeled oligonucleotide, Berg and colleagues screened 17,298 compounds to discover pyrazolo-pyrimidine inhibitors with measurable biochemical inhibitory activity for MYC (e.g., Mycro1; Figure 3.6; IC₅₀ = 30 μ M) and a narrow window of selectivity for MAX:MAX homodimers (IC₅₀ = 72 μ M)^{67,68}. Additional efforts to target the MYC:MAX heterodimerization event have been undertaken subsequently, including efforts using further FRET screens⁶⁹, cellular transformation assays⁷⁰, and further EMSA screens⁷¹. These and other studies have led to a list of structurally diverse compounds with reported activity against the MYC:MAX:DNA binding event (Figure 3.6)⁷².

As described above, this research comprises more than a decade of study to identify the first qualified chemical probes of MYC function, for mechanistic use in cellular biology. Medicinal chemistry efforts directed at improving the limited potency of these compounds are described in the published and patent literature (WO2010083404 A2). However, many of the active species belong to structural classes annotated as non-selective ligands in pharmaceutical screening libraries, so called pan-assay interference compounds (PAINS) ^{73,74}, establishing important first directions for follow-up chemistry. Perhaps consistent with this behavior, incisive and important studies have observed multiple binding events of bioactive compounds along the MYC protein by circular dichroism ⁶⁰, NMR ⁶⁰, and most recently by mass spectrometry ⁷⁵. The relatively low potency, demonstrable selectivity and durable biostability of lead compounds have prevented use in MYC model systems in vivo ^{76,77}, but insights are emerging from this work and structural modeling. Still needed are direct-acting MYC inhibitors with properties commensurate with a bona fide chemical probe, such as defined by Steven Frye ⁶³. There exists, therefore, an opportunity to revisit this biochemistry with new screening methodologies, new types of expansive chemical libraries and new measurements to characterize the mode of molecular recognition of candidate inhibitors.

Beyond the MYC:MAX heterodimerization interface, functional studies highlight MBII as a putative target for chemical probe development. The requirement for MBII in MYC-specific transactivation and cellular transformation highlights the emerging validation of this protein-protein interaction. Unfortunately, limited biochemical and no structural information is available for MBII. Focused biophysical and structural studies of

MBII may pave the way to miniaturized assays capable of interrogating MBII with discovery chemistry.

Inhibition of MYC-dependent transcriptional signaling

MYC-dependent transcription requires the assembly and function of critical transcriptional and chromatin-modifying enzyme complexes^{51,78} (also see Hann 2014) (Figure 3.7). Communication of transcriptional impulses is initiated by promoter- and enhancer-bound MYC, which serves to organize histone acetyltransferases (such as TIP60, GCN5, and CBP/P300) and the mediator complex. These events promote the preparation and stabilization of accessible euchromatin, as well as bridging interactions with initiated RNA Pol II. Recently, the Young laboratory described a pivotal role of MYC also in genome-wide transcriptional elongation mediated by proximal promoter pause release.⁵⁰ MYC importantly functions to promote CDK9-dependent phosphorylation of RNA Pol II, triggering the release of paused polymerase to execute definitive target gene transcription (see Rahl and Young 2014; Levens 2013; and Sabò and Amati 2014).

These insights support a model of targeting MYC via co-activator proteins critical to MYC-specific initiation and elongation. The pronounced effect of MYC on local chromatin acetylation (via HAT recruitment)^{79,80}, and the emerging role for MYC in elongation (via recruitment of CDK9), prompted our consideration that the bromodomain and extra-terminal domain (BET) family of co-activator proteins (BRD2, BRD3, BRD4, and BRDT) figure prominently in MYC-mediated transcriptional pause release. BET bromodomains bind to poly-acetylated histone tails via molecular recognition of ϵ -acetyllysine (Kac) by an anti-parallel bundle of four alpha-helices that forms a hydrophobic

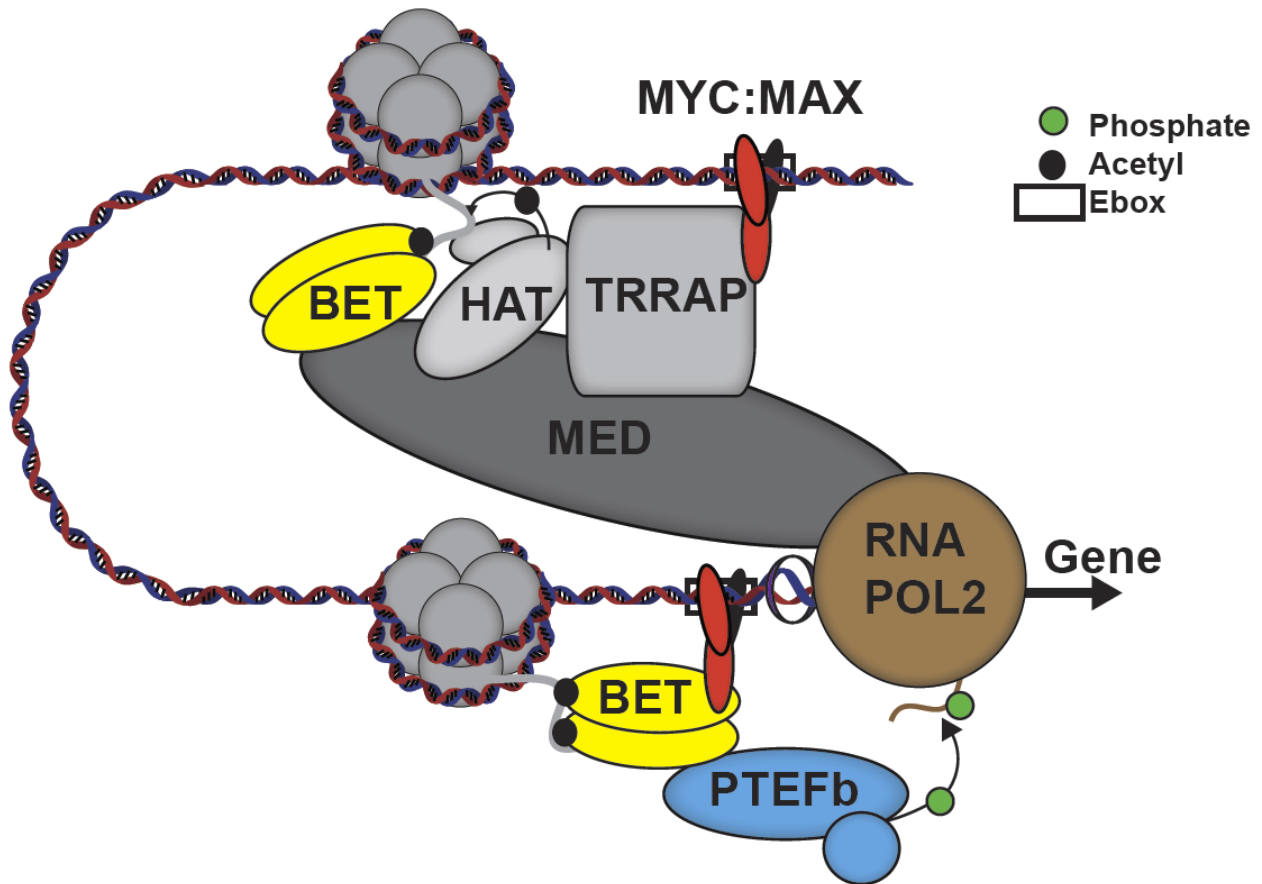


Figure 3.7: A model for MYC transcriptional complex. Chromatin-dependent MYC transcriptional signaling. MYC and MAX bind at Ebox motifs (boxes) in enhancers and promoters. Protein complex formation causes looping to engage promoters adjacent to MYC target genes (arrow to gene body), inducing RNA Pol II (RNA POL2) loading to initiation site. Recruitment of TRRAP and histone acetyltransferases (HAT) leads to covalent modification of nucleosomes (clustered gray spheres) with lysine side-chain acetylation (Kac; small black circles). Acetylated, open chromatin is bound by bromodomain containing proteins, including HATs (CBP, EP300, GCN5) and BET-family co-activators (BET; yellow). BET bromodomains recruit the P-TEFb elongation complex (CyclinT and CDK9; cyan) phosphorylates (small green circles) the carboxy terminal domain of RNA POL2, causing pause release and leading to elongation.

pocket with a conserved asparagine and an organized network of deep water molecules⁸¹⁻⁸⁴. Prior research established a role for BET bromodomains in cell cycle progression and mitotic memory⁸⁵. Biochemical studies in virology by Verdin and co-workers importantly established that BET bromodomains possess a high-affinity binding motif for the CDK9-containing positive transcription elongation factor complex (P-TEFb) at the distal carboxy-terminus⁸⁶. We thus hypothesized that BET bromodomains may function to recruit CDK9 to sites of hyperacetylated chromatin in cancer cells, thereby facilitating MYC-specific transcription elongation.

Having developed and characterized the first bromodomain inhibitor⁸⁷, targeting the BET family of bromodomains, we performed a chemical genetic study of BET inhibition on MYC transactivation in vitro and in vivo⁸⁸. Mechanistic studies performed in translational models of multiple myeloma (a MYC-dependent plasma cell malignancy), revealed that chemical displacement or genetic silencing of BET bromodomains results in the selective, coordinate down-regulation of the MYC transcriptional program. Concurrent, collaborative studies of BET inhibition in acute myeloid leukemia with Vakoc and Lowe, comparably demonstrated pronounced MYC pathway inhibition associated with marked downregulation of transcription of the *MYC* gene itself⁸⁹. In both studies, abrogation of chromatin-dependent *MYC* gene transcription via BET bromodomain inhibition elicited meaningful therapeutic responses in murine models of these aggressive hematological malignancies. Targeting MYC function via BET bromodomain inhibition has now been validated by studies in Burkitt lymphoma⁹⁰, B- and T-cell acute lymphoblastic leukemia⁹¹, non-small cell lung carcinoma⁹² and diffuse large B-cell lymphoma⁹³. In model systems of neuroblastoma,

MYCN transcription and function was found to be comparably sensitive to BET inhibition. This hypothesis is presently being assessed in clinical trials of BET bromodomain inhibitors in MYC-dependent solid and hematopoietic tumors.

Another noteworthy approach to targeting *MYC* transcription derives from a unique and well-characterized feature of the *MYC* locus, namely a predisposition for formation of G-quadruplex DNA^{94,95}. Small-molecule stabilizers of G-quadruplex DNA have been developed as tool compounds, which establish an impediment to RNA Pol II transcription of *MYC*. Further optimization is required before these compounds can be clinical deployed, but *MYC*-specific biological consequences have been observed with these compounds in experimental systems⁹⁶⁻¹⁰¹.

Beyond BET bromodomains, additional *MYC*-associated co-activator proteins may also then be considered for therapeutic development. As shown in Figure 3.8 (and as described in Conacci-Sorrell et al. 2004; Hann 2014) the *MYC* interactome features known critical mediators of transcriptional output, among them protein targets amenable to small molecule discovery. Through MBII, *MYC* recruits the TRRAP complex that includes the histone acetyltransferases TIP60 and GCN5. The successful development of P300 histone acetyltransferase inhibitors by Cole and colleagues^{102,103}, suggests that discovery chemistry directed at these validated effectors of *MYC*-dependent chromatin remodeling and transcription is within reach. As P300 is a known binding partner of *MYC* via interactions in the trans-activation domain¹⁰⁴, the C646 inhibitor of P300 could contribute to the further understanding of this enzyme in *MYC* stability and function. Downstream of enhancer-bound factors such as these, *MYC*-mediated recruitment of

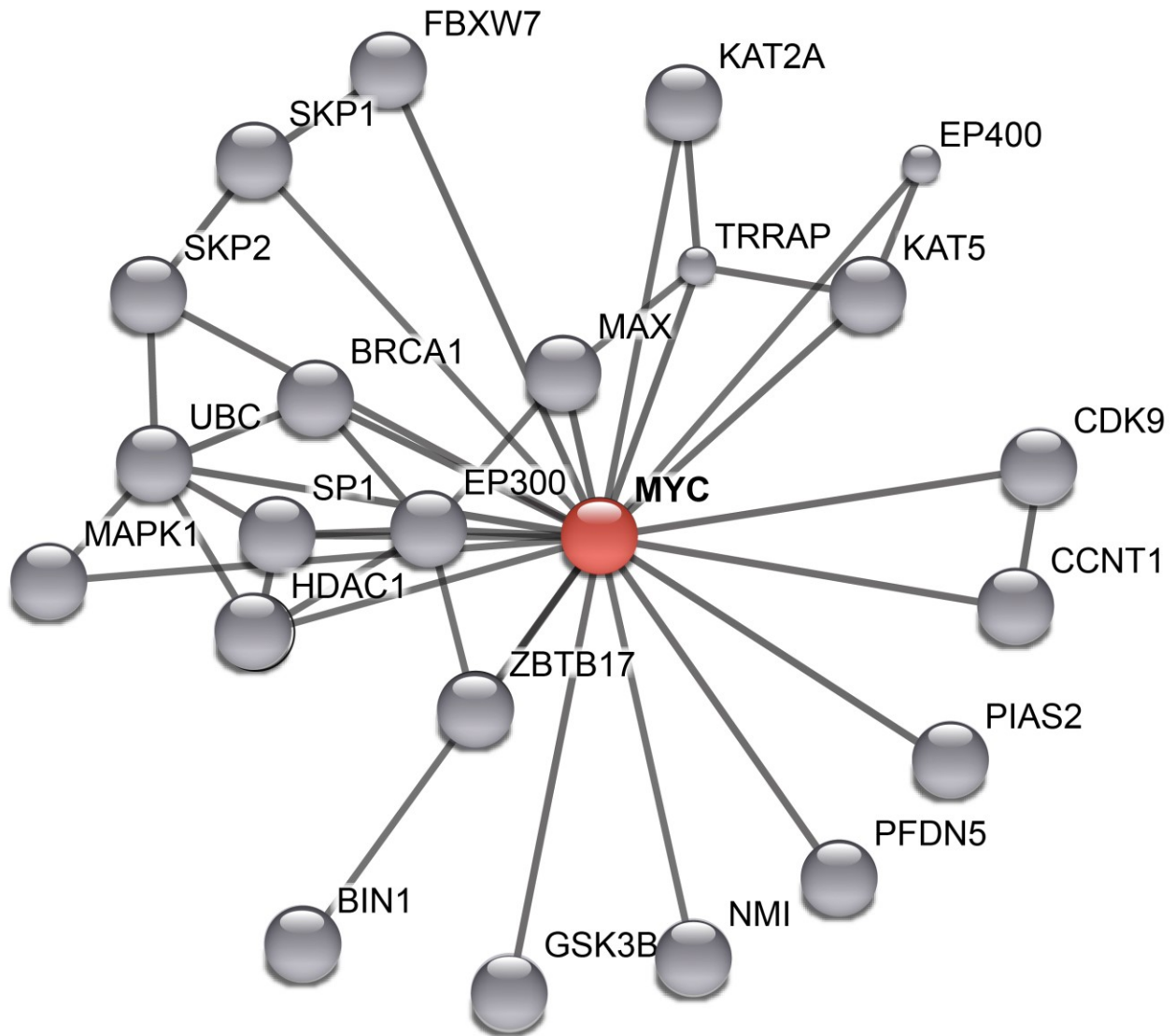


Figure 3.8: The MYC protein interactome (STRING). Connections between MYC and other critical regulatory proteins and complexes are shown.

mediator and TFIIH suggests consideration for the development of selective inhibitors of transcriptional kinases, such as CDK7, CDK8 and CDK9, as MYC-directed tools and prototype therapeutics. Small-molecule inhibitors of transcriptional kinases are being intensively pursued in academia and industry, and a partial list of emerging compounds is presented in Table 3.1.

Insights from developmental and disease biology suggest additional opportunities to target MYC function at the level of nuclear chromatin. Functioning alongside MYC-dependent transcription are parallel transcriptional networks which may be approached for synthetic lethality. Eisenman and colleagues discovered and characterized a functional interaction between *Drosophila* Myc and the Trithorax group protein Little imaginal discs (Lid)¹⁰⁵, a homologue of the human proto-oncogene JARID1. They hypothesize a role for JARID1 in MYC-dependent neoplasia^{106,107}, supported by recent evidence that the NUP98-JARID1A oncogene in AML functions, in part, through an essential interaction between a plant homeodomain (PHD) finger encoded by *JARID1A* and histone 3 lysine 4, providing functional validation of JARID1A in a MYC-dependent tumor^{108,109}.

Beyond chromatin-dependent MYC transcriptional signaling, other chromatin-associated factors such as the PIM1 kinase may contribute to high global transcriptional output at MYC target genes^{110,111}. PIM1 phosphorylates histone H3 and, interestingly and similar to MYC, PIM1 regulates transcriptional elongation^{112,113}. PIM1 inhibitors are in development as anti-tumor agents, including the ADP-competitive inhibitor SGI-1776. Additional small molecules targeting MYC-associated transcriptional regulators such as Table 3.1.

Table 3.1: MYC pathway and regulator inhibitors

| Compound Name | Class | Target |
|----------------------|-------------------------------|----------------------|
| Flavopiridol | CDK | CDK9 |
| SU9516 | CDK | CDK1 |
| Purvalanol A | CDK | CDK2, CDK9 |
| PHA 767491 HCl | CDK | CDK7, CDK9 |
| SNS-032 | CDK | CDK2, CDK7, and CDK9 |
| Cortistatin A | CDK | CDK8 |
| JQ1 | BET Bromodomain | BRD4, BRD3, and CDK9 |
| SGI-1776 | PIM kinase | Pim1 |
| EPZ004777 | Dot1L | Dot1L |
| C464 | p300/CBP Acetyltransferase | p300 |
| SAHA | HDAC | HDAC |
| Triptolide | TFIIH/XBP | XBP |
| Nutlin-3a | p53-MDM2 | p53-MDM2 |
| SB220025 | MAPK | p38 |
| LY294002 | PI3K | PI3K |
| VAV-939 | Wnt | Tankyrase 1,2 |
| Ly-411575 | γ Secretase | Notch1 |
| VX-680 | Aurora Kinase | Aurora Kinase |
| NSC71948 | BAG1 | BAG1 |
| ABT263 | BCL2 | BCL2 |
| VER-155008 | HSP70 | HSP70 |
| KW-2478 | HSP90 | HSP90 |
| SB 218078 | Chk1 | Chk1 |
| Leflunomide | DHODH | DHODH |

Targeting pathways upstream of MYC

As an end-effector of numerous upstream signal transduction pathways, it is highly likely that effective targeting of dominant growth-factor independent signaling networks will mute upstream activation of MYC. Often, mitogenic signaling pathways activate intermediary effector transcription factors that integrate upstream surface-to-nuclear signaling with the common transcriptional language of MYC-dependent cell proliferation. A classic example is KRAS activation, which is among the most prevalent alterations in human cancer. KRAS activation in cancer drives MYC activation. Both genetic (Omomyc)³⁰, and chemical (BET inhibition with JQ1)⁹², perturbation of MYC function arrest proliferation downstream of KRAS and validate MYC as a target in KRAS-dependent tumors.

Indeed, many other upstream signaling pathways lead to deregulated MYC function, including the MAPK, PI3K, Wnt/ β -catenin and Notch pathways (see Conacci-Sorrell et al. 2014;^{1,51}. The Wnt/ β -catenin pathway regulates MYC expression through signaling to the Tcf4 transcription factor that binds tissue-specific enhancers upstream of the *MYC* gene¹⁸. Stabilization of NOTCH1 by juxtamembrane or PEST domain alteration in T-ALL leads to deregulation of MYC expression and function. Targeting the Notch pathway with upstream inhibition of gamma-secretase¹¹⁴, or direct inhibition using stabilized alpha-helical peptides⁴², leads to prompt downregulation of MYC associated with anti-proliferative consequences. Exemplary, additional inhibitors of upstream signal transduction pathways, such as MAPK and PI3K are presented in Table 3.1. As targeted agents are brought forward for clinical trials, pre-clinical studies

assessing combinations of upstream and downstream modulators of MYC function should be pursued.

Modulating MYC stability

MYC has a naturally short half-life⁴⁹. Regulation and preservation of the short transcript and protein half-life is essential to long-term survival without cancer. MYC protein homeostasis is considered in detail in Farrell and Sears (2014) and elsewhere by Sears and colleagues¹¹⁵. Here, we describe only briefly the opportunity to target MYC protein stability using therapeutic approaches. The transactivating domain is subject to phosphorylation, acetylation, and ubiquitylation, which serve to regulate stability and binding interactions^{49,58}. Alterations in MYC and associated protein homeostatic pathway effectors are observed in human tumors, leading to the inappropriate post-translational processing and stability of the MYC oncoprotein.

The facile development of kinase inhibitors warrants consideration of approaches to target MYC degradation, as MYC degradation is heavily influenced by serine and threonine phosphorylation. Biochemical and functional studies have established that phosphorylation of serine 62 (pSer62) by ERK pathway kinase activity stabilizes MYC and promotes proliferation. In contrast, phosphorylation of threonine 58 (pThr58) by GSK-3 β destabilizes MYC. Notably, mutations of Thr58 are observed in Burkitt's lymphoma resulting in constitutive MYC stabilization. Thus, therapeutic approaches to MEK-ERK pathway inhibition, or efforts to inhibit GSK-3 β such as inhibition of PI3K-AKT signaling, may favorably modulate MYC stability for therapeutic benefit. This may be particularly true in tumors with upregulated MEK-ERK signaling (KRAS or EGFR

activated) or PTEN loss. Table 1 lists exemplary compounds, which may be used as chemical probes of pathway function.

Opposing MYC phosphorylation at serine 62 is protein phosphatase 2 (PP2A), which functions as a heterotrimeric enzyme complex to indirectly and directly modulate MYC protein stability. The Sears group has demonstrated that pSer62 is a direct target of PP2A, supporting a model where PP2A loss (a common tumor suppressor loss in cancer) promotes MYC stability. Presently, pharmaceutical compounds targeting PP2A do not exist. However, in collaborative research with the laboratories of Thomas Look, Jon Aster and Hanno Steen, we recently discovered PP2A as the anti-proliferative target of perphenazine (and other phenothiazines), by ligand-affinity chromatography¹¹⁶. As small molecules targeting and activating tumor suppressors are rarely described, we are interested now to optimize these compounds for enhanced PP2A binding and activation, to destabilize MYC and modulate other critical PP2A target proteins. Recently, Eilers and colleagues reported a novel approach to destabilize MYCN via inhibition of Aurora A kinases¹¹⁷. MYCN is targeted for degradation by the FBXW7 ubiquitin ligase. MYCN protein stability is promoted by an interaction with the Aurora A mitotic kinase. Though the kinase activity of AURKA is not required for MYCN protein stability, two ATP-competitive azepine inhibitors of AURKA (MLN-80545 and MLN-8237) disrupted binding to MYCN. In mechanistic and translational experiments performed in MYCN-dependent neuroblastoma models, AURKA inhibition prompted MYCN degradation and an anti-proliferative effect.

A final opportunity for therapeutic targeting of MYC protein stability is presented by MYC-associated histone acetyltransferases. Beyond their established role in

promoting chromatin remodeling, bromodomain recruitment and gene expression, acetylation of MYC by CBP/P300, GCN5 and TIP60 promotes MYC stability and transcriptional activity⁵⁸. As above, inhibition of these acetyltransferase enzymes may display favorable activity in cancer model systems, in support of further clinical development.

MYC and Synthetic Lethality

MYC addicted cancer cells may harbor unique dependencies that a normal cell may not require. Such synthetic lethal interactions with MYC may prompt the development of context-specific inhibitors. Two kinase targets have been identified which are required for cell survival in the context of enforced MYC expression, Aurora kinase B¹¹⁸ and Cdk1¹¹⁹. Inhibition of these kinases with cell-permeable small molecules has demonstrated compelling evidence of a leveraged anti-proliferative effect in MYC-dependent cancer models, albeit with a narrow therapeutic index. Emerging research approaches using highly parallel reverse genetic screens (RNA interference; RNAi), has reinvigorated efforts to identify MYC-specific tumor dependencies. Recently, two laboratories performed RNAi screening in a MYC-dependent context leading to the suggestion of CSNK1e kinase¹²⁰ and the SAE1/2 SUMO-activating enzyme¹²¹ as putative targets for the development of synthetic lethal small molecules. Rational approaches to synthetic lethality have included consideration of metabolic adaptation to MYC-mediated tumorigenesis. Observing therapy-associated cellular senescence in treated Eμ-MYC cells, Schmitt and colleagues targeted glucose uptake and autophagy with impressive anti-proliferative results¹²². Together, these studies establish a new path to MYC-specific therapeutic development, revealed by powerful new technologies

and a detailed mechanistic understanding of MYC biology at the interface of transcription, translation and metabolism.

Concluding Remarks

The centrality of MYC to the pathogenesis of cancer, illustrated in granular detail in the accompanying cited literature, demands the creativity and commitment of the allied fields of ligand discovery. In this review, we provide a rationale for targeting MYC that balances high-risk, high-reward approaches of direct MYC:MAX modulation with near-term opportunities to approach MYC transcriptional signaling via chromatin-dependent processes and pathways of protein homeostasis. Still, direct inhibition of MYC remains an elusive goal in cancer medicine—an inadequacy of current therapeutic science perhaps at the heart of our inability to eradicate this disease.

Acknowledgments

The authors thank Jason J. Marineau, Peter B. Rahl, Richard A. Young, Chi Dang, and Robert N. Eisenman for influential discussions regarding therapeutic strategies toward inhibiting MYC. I would also like to thank Jaime Reyes for help with graphic art for Figure 3.7.

References

- 1 Meyer, N. & Penn, L. Z. Reflecting on 25 years with MYC. *Nat Rev Cancer* **8**, 976-990, doi:nrc2231 [pii] 10.1038/nrc2231 (2008).
- 2 Duesberg, P. H. & Vogt, P. K. Avian acute leukemia viruses MC29 and MH2 share specific RNA sequences: evidence for a second class of transforming genes. *Proceedings of the National Academy of Sciences of the United States of America* **76**, 1633-1637 (1979).
- 3 Hu, S. S. & Vogt, P. K. Avian oncovirus MH2 is defective in Gag, Pol, and Env. *Virology* **92**, 278-284 (1979).
- 4 Sheiness, D. & Bishop, J. M. DNA and RNA from uninfected vertebrate cells contain nucleotide sequences related to the putative transforming gene of avian myelocytomatosis virus. *Journal of virology* **31**, 514-521 (1979).
- 5 Dalla-Favera, R. *et al.* Human MYC onc gene is located on the region of chromosome 8 that is translocated in Burkitt lymphoma cells. *Proceedings of the National Academy of Sciences of the United States of America* **79**, 7824-7827 (1982).
- 6 Taub, R. *et al.* Translocation of the MYC gene into the immunoglobulin heavy chain locus in human Burkitt lymphoma and murine plasmacytoma cells. *Proceedings of the National Academy of Sciences of the United States of America* **79**, 7837-7841 (1982).
- 7 Beroukhi, R. *et al.* The landscape of somatic copy-number alteration across human cancers. *Nature* **463**, 899-905, doi:10.1038/nature08822 (2010).
- 8 Gamberi, G. *et al.* MYC and c-fos in human osteosarcoma: prognostic value of mRNA and protein expression. *Oncology* **55**, 556-563, doi:oc155556 [pii] (1998).
- 9 Nesbit, C. E., Tersak, J. M. & Prochownik, E. V. MYC oncogenes and human neoplastic disease. *Oncogene* **18**, 3004-3016, doi:10.1038/sj.onc.1202746 (1999).
- 10 Sauter, G. *et al.* MYC copy number gains in bladder cancer detected by fluorescence in situ hybridization. *Am J Pathol* **146**, 1131-1139 (1995).
- 11 Leder, P. *et al.* Translocations among antibody genes in human cancer. *Science* **222**, 765-771 (1983).
- 12 Klein, G. Specific chromosomal translocations and the genesis of B-cell-derived tumors in mice and men. *Cell* **32**, 311-315, doi:0092-8674(83)90449-X [pii] (1983).
- 13 Herrmann, H. *et al.* Small-molecule inhibition of BRD4 as a new potent approach to eliminate leukemic stem- and progenitor cells in acute myeloid leukemia AML. *Oncotarget* **3**, 1588-1599 (2012).
- 14 Easton, D. F. *et al.* Genome-wide association study identifies novel breast cancer susceptibility loci. *Nature* **447**, 1087-1093, doi:nature05887 [pii] 10.1038/nature05887 (2007).
- 15 Greenman, C. *et al.* Patterns of somatic mutation in human cancer genomes. *Nature* **446**, 153-158, doi:nature05610 [pii] 10.1038/nature05610 (2007).

- 16 Kiemenev, L. A. *et al.* Sequence variant on 8q24 confers susceptibility to urinary bladder cancer. *Nat Genet* **40**, 1307-1312, doi:ng.229 [pii]
10.1038/ng.229 (2008).
- 17 Pomerantz, M. M. *et al.* The 8q24 cancer risk variant rs6983267 shows long-range interaction with MYC in colorectal cancer. *Nat Genet* **41**, 882-884, doi:ng.403 [pii]
10.1038/ng.403 (2009).
- 18 Wright, J. B., Brown, S. J. & Cole, M. D. Upregulation of MYC in cis through a large chromatin loop linked to a cancer risk-associated single-nucleotide polymorphism in colorectal cancer cells. *Mol Cell Biol* **30**, 1411-1420, doi:MCB.01384-09 [pii]
10.1128/MCB.01384-09 (2010).
- 19 Felsher, D. W. & Bishop, J. M. Reversible tumorigenesis by MYC in hematopoietic lineages. *Molecular cell* **4**, 199-207 (1999).
- 20 Flores, I., Murphy, D. J., Swigart, L. B., Knies, U. & Evan, G. I. Defining the temporal requirements for Myc in the progression and maintenance of skin neoplasia. *Oncogene* **23**, 5923-5930, doi:10.1038/sj.onc.1207796
1207796 [pii] (2004).
- 21 Pelengaris, S., Khan, M. & Evan, G. I. Suppression of Myc-induced apoptosis in beta cells exposes multiple oncogenic properties of Myc and triggers carcinogenic progression. *Cell* **109**, 321-334, doi:S0092867402007389 [pii] (2002).
- 22 Pelengaris, S., Littlewood, T., Khan, M., Elia, G. & Evan, G. Reversible activation of MYC in skin: induction of a complex neoplastic phenotype by a single oncogenic lesion. *Molecular cell* **3**, 565-577, doi:S1097-2765(00)80350-0 [pii] (1999).
- 23 Jain, M. *et al.* Sustained loss of a neoplastic phenotype by brief inactivation of MYC. *Science* **297**, 102-104, doi:10.1126/science.1071489 (2002).
- 24 Soucek, L. *et al.* Modelling Myc inhibition as a cancer therapy. *Nature* **455**, 679-683, doi:10.1038/nature07260 (2008).
- 25 Davis, A. C., Wims, M., Spotts, G. D., Hann, S. R. & Bradley, A. A null MYC mutation causes lethality before 10.5 days of gestation in homozygotes and reduced fertility in heterozygous female mice. *Genes & development* **7**, 671-682 (1993).
- 26 Bettess, M. D. *et al.* MYC is required for the formation of intestinal crypts but dispensable for homeostasis of the adult intestinal epithelium. *Mol Cell Biol* **25**, 7868-7878, doi:10.1128/MCB.25.17.7868-7878.2005 (2005).
- 27 Savino, M. *et al.* The action mechanism of the Myc inhibitor termed Omomyc may give clues on how to target Myc for cancer therapy. *PloS one* **6**, e22284, doi:10.1371/journal.pone.0022284 (2011).
- 28 Soucek, L. *et al.* Design and properties of a Myc derivative that efficiently homodimerizes. *Oncogene* **17**, 2463-2472, doi:10.1038/sj.onc.1202199 (1998).
- 29 Soucek, L. *et al.* Omomyc, a potential Myc dominant negative, enhances Myc-induced apoptosis. *Cancer Res* **62**, 3507-3510 (2002).

- 30 Soucek, L. *et al.* Inhibition of Myc family proteins eradicates KRas-driven lung cancer in mice. *Genes & development* **27**, 504-513, doi:10.1101/gad.205542.112 (2013).
- 31 Wang, R. *et al.* The transcription factor Myc controls metabolic reprogramming upon T lymphocyte activation. *Immunity* **35**, 871-882, doi:10.1016/j.immuni.2011.09.021 (2011).
- 32 Pap, T. *et al.* Cooperation of Ras- and MYC-dependent pathways in regulating the growth and invasiveness of synovial fibroblasts in rheumatoid arthritis. *Arthritis and rheumatism* **50**, 2794-2802, doi:10.1002/art.20461 (2004).
- 33 Ahuja, P. *et al.* Myc controls transcriptional regulation of cardiac metabolism and mitochondrial biogenesis in response to pathological stress in mice. *The Journal of clinical investigation* **120**, 1494-1505, doi:10.1172/JCI38331 (2010).
- 34 London, N., Raveh, B. & Schueler-Furman, O. Druggable protein-protein interactions - from hot spots to hot segments. *Curr Opin Chem Biol* **17**, 952-959, doi:10.1016/j.cbpa.2013.10.011 (2013).
- 35 Swinney, D. C. Phenotypic vs. target-based drug discovery for first-in-class medicines. *Clinical pharmacology and therapeutics* **93**, 299-301, doi:10.1038/clpt.2012.236 (2013).
- 36 Rask-Andersen, M., Almen, M. S. & Schioth, H. B. Trends in the exploitation of novel drug targets. *Nature reviews. Drug discovery* **10**, 579-590, doi:10.1038/nrd3478 (2011).
- 37 Darnell, J. E., Jr. Transcription factors as targets for cancer therapy. *Nat Rev Cancer* **2**, 740-749, doi:10.1038/nrc906 (2002).
- 38 Berg, T. Inhibition of transcription factors with small organic molecules. *Curr Opin Chem Biol* **12**, 464-471, doi:S1367-5931(08)00119-1 [pii] 10.1016/j.cbpa.2008.07.023 (2008).
- 39 Ptashne, M. & Gann, A. Transcriptional activation by recruitment. *Nature* **386**, 569-577, doi:10.1038/386569a0 (1997).
- 40 Ptashne, M. & Gann, A. *Genes & signals*. (Cold Spring Harbor Laboratory Press, 2002).
- 41 Fletcher, S. & Hamilton, A. D. Protein-protein interaction inhibitors: small molecules from screening techniques. *Curr Top Med Chem* **7**, 922-927 (2007).
- 42 Moellering, R. E. *et al.* Direct inhibition of the NOTCH transcription factor complex. *Nature* **462**, 182-188, doi:10.1038/nature08543 (2009).
- 43 Wells, J. A. & McClendon, C. L. Reaching for high-hanging fruit in drug discovery at protein-protein interfaces. *Nature* **450**, 1001-1009, doi:10.1038/nature06526 (2007).
- 44 Yada, M. *et al.* Phosphorylation-dependent degradation of MYC is mediated by the F-box protein Fbw7. *The EMBO journal* **23**, 2116-2125, doi:10.1038/sj.emboj.7600217 (2004).
- 45 Welcker, M. *et al.* The Fbw7 tumor suppressor regulates glycogen synthase kinase 3 phosphorylation-dependent MYC protein degradation. *Proceedings of the National Academy of Sciences of the United States of America* **101**, 9085-9090, doi:10.1073/pnas.0402770101 (2004).

- 46 McMahon, S. B., Van Buskirk, H. A., Dugan, K. A., Copeland, T. D. & Cole, M. D. The novel ATM-related protein TRRAP is an essential cofactor for the MYC and E2F oncoproteins. *Cell* **94**, 363-374 (1998).
- 47 Cowling, V. H., Chandriani, S., Whitfield, M. L. & Cole, M. D. A conserved Myc protein domain, MBIV, regulates DNA binding, apoptosis, transformation, and G2 arrest. *Mol Cell Biol* **26**, 4226-4239, doi:10.1128/MCB.01959-05 (2006).
- 48 Herbst, A. *et al.* A conserved element in Myc that negatively regulates its proapoptotic activity. *EMBO reports* **6**, 177-183, doi:10.1038/sj.embor.7400333 (2005).
- 49 Andresen, C. *et al.* Transient structure and dynamics in the disordered MYC transactivation domain affect Bin1 binding. *Nucleic acids research* **40**, 6353-6366, doi:gks263 [pii] 10.1093/nar/gks263 (2012).
- 50 Rahl, P. B. *et al.* MYC regulates transcriptional pause release. *Cell* **141**, 432-445, doi:10.1016/j.cell.2010.03.030 (2010).
- 51 Eilers, M. & Eisenman, R. N. Myc's broad reach. *Genes & development* **22**, 2755-2766, doi:10.1101/gad.1712408 (2008).
- 52 Nair, S. K. & Burley, S. K. X-ray structures of Myc-Max and Mad-Max recognizing DNA. Molecular bases of regulation by proto-oncogenic transcription factors. *Cell* **112**, 193-205, doi:S0092867402012849 [pii] (2003).
- 53 Metallo, S. J. Intrinsically disordered proteins are potential drug targets. *Curr Opin Chem Biol* **14**, 481-488, doi:10.1016/j.cbpa.2010.06.169 S1367-5931(10)00074-8 [pii] (2010).
- 54 Wright, P. E. & Dyson, H. J. Intrinsically unstructured proteins: re-assessing the protein structure-function paradigm. *Journal of molecular biology* **293**, 321-331, doi:10.1006/jmbi.1999.3110 (1999).
- 55 Gsponer, J. & Babu, M. M. The rules of disorder or why disorder rules. *Prog Biophys Mol Biol* **99**, 94-103, doi:S0079-6107(09)00043-1 [pii] 10.1016/j.pbiomolbio.2009.03.001 (2009).
- 56 Gsponer, J., Futschik, M. E., Teichmann, S. A. & Babu, M. M. Tight regulation of unstructured proteins: from transcript synthesis to protein degradation. *Science* **322**, 1365-1368, doi:322/5906/1365 [pii] 10.1126/science.1163581 (2008).
- 57 Herbst, A., Salghetti, S. E., Kim, S. Y. & Tansey, W. P. Multiple cell-type-specific elements regulate Myc protein stability. *Oncogene* **23**, 3863-3871, doi:10.1038/sj.onc.1207492 1207492 [pii] (2004).
- 58 Cowling, V. H. & Cole, M. D. Mechanism of transcriptional activation by the Myc oncoproteins. *Semin Cancer Biol* **16**, 242-252, doi:S1044-579X(06)00067-8 [pii] 10.1016/j.semcancer.2006.08.001 (2006).
- 59 Follis, A. V., Hammoudeh, D. I., Wang, H., Prochownik, E. V. & Metallo, S. J. Structural rationale for the coupled binding and unfolding of the MYC oncoprotein by small molecules. *Chem Biol* **15**, 1149-1155 (2008).
- 60 Hammoudeh, D. I., Follis, A. V., Prochownik, E. V. & Metallo, S. J. Multiple independent binding sites for small-molecule inhibitors on the oncoprotein MYC. *J Am Chem Soc* **131**, 7390-7401 (2009).

- 61 Williamson, J. R. Induced fit in RNA-protein recognition. *Nature structural biology* **7**, 834-837, doi:10.1038/79575 (2000).
- 62 Johnson, K. A. Role of induced fit in enzyme specificity: a molecular forward/reverse switch. *The Journal of biological chemistry* **283**, 26297-26301, doi:10.1074/jbc.R800034200 (2008).
- 63 Frye, S. V. The art of the chemical probe. *Nat Chem Biol* **6**, 159-161, doi:10.1038/nchembio.296 (2010).
- 64 Berg, T. *et al.* Small-molecule antagonists of Myc/Max dimerization inhibit Myc-induced transformation of chicken embryo fibroblasts. *Proceedings of the National Academy of Sciences of the United States of America* **99**, 3830-3835, doi:10.1073/pnas.062036999 (2002).
- 65 Yin, X., Giap, C., Lazo, J. S. & Prochownik, E. V. Low molecular weight inhibitors of Myc-Max interaction and function. *Oncogene* **22**, 6151-6159, doi:10.1038/sj.onc.1206641 (2003).
- 66 Park, S. *et al.* Determination of binding constant of transcription factor myc-max/max-max and E-box DNA: the effect of inhibitors on the binding. *Biochimica et biophysica acta* **1670**, 217-228, doi:10.1016/j.bbagen.2003.12.007 (2004).
- 67 Kiessling, A., Wiesinger, R., Sperl, B. & Berg, T. Selective inhibition of MYC/Max dimerization by a pyrazolo[1,5-a]pyrimidine. *ChemMedChem* **2**, 627-630, doi:10.1002/cmdc.200600294 (2007).
- 68 Kiessling, A., Sperl, B., Hollis, A., Eick, D. & Berg, T. Selective inhibition of MYC/Max dimerization and DNA binding by small molecules. *Chem Biol* **13**, 745-751, doi:10.1016/j.chembiol.2006.05.011 (2006).
- 69 Xu, Y. *et al.* A credit-card library approach for disrupting protein-protein interactions. *Bioorganic & medicinal chemistry* **14**, 2660-2673, doi:10.1016/j.bmc.2005.11.052 (2006).
- 70 Shi, J., Stover, J. S., Whitby, L. R., Vogt, P. K. & Boger, D. L. Small molecule inhibitors of Myc/Max dimerization and Myc-induced cell transformation. *Bioorg Med Chem Lett* **19**, 6038-6041, doi:S0960-894X(09)01301-8 [pii] 10.1016/j.bmcl.2009.09.044 (2009).
- 71 Jeong, K. C., Ahn, K. O. & Yang, C. H. Small-molecule inhibitors of MYC transcriptional factor suppress proliferation and induce apoptosis of promyelocytic leukemia cell via cell cycle arrest. *Mol Biosyst* **6**, 1503-1509, doi:10.1039/c002534h (2010).
- 72 Yap, J. L. *et al.* Pharmacophore identification of MYC inhibitor 10074-G5. *Bioorg Med Chem Lett* **23**, 370-374, doi:10.1016/j.bmcl.2012.10.013 (2013).
- 73 Baell, J. B. & Holloway, G. A. New substructure filters for removal of pan assay interference compounds (PAINS) from screening libraries and for their exclusion in bioassays. *J Med Chem* **53**, 2719-2740, doi:10.1021/jm901137j (2010).
- 74 Whitty, A. Growing PAINS in academic drug discovery. *Future medicinal chemistry* **3**, 797-801, doi:10.4155/fmc.11.44 (2011).
- 75 Harvey, S. R. *et al.* Small-molecule inhibition of MYC:MAX leucine zipper formation is revealed by ion mobility mass spectrometry. *J Am Chem Soc* **134**, 19384-19392, doi:10.1021/ja306519h (2012).

- 76 Clausen, D. M. *et al.* In vitro cytotoxicity and in vivo efficacy, pharmacokinetics, and metabolism of 10074-G5, a novel small-molecule inhibitor of MYC/Max dimerization. *J Pharmacol Exp Ther* **335**, 715-727, doi:jpet.110.170555 [pii] 10.1124/jpet.110.170555 (2010).
- 77 Guo, J. *et al.* Efficacy, pharmacokinetics, tissue distribution, and metabolism of the Myc-Max disruptor, 10058-F4 [Z,E]-5-[4-ethylbenzylidene]-2-thioxothiazolidin-4-one, in mice. *Cancer Chemother Pharmacol* **63**, 615-625, doi:10.1007/s00280-008-0774-y (2009).
- 78 Dang, C. V. *et al.* The MYC target gene network. *Semin Cancer Biol* **16**, 253-264, doi:S1044-579X(06)00065-4 [pii] 10.1016/j.semcancer.2006.07.014 (2006).
- 79 McMahan, S. B., Wood, M. A. & Cole, M. D. The essential cofactor TRRAP recruits the histone acetyltransferase hGCN5 to MYC. *Mol Cell Biol* **20**, 556-562 (2000).
- 80 Knoepfler, P. S. *et al.* Myc influences global chromatin structure. *The EMBO journal* **25**, 2723-2734, doi:10.1038/sj.emboj.7601152 (2006).
- 81 Prinjha, R. K., Witherington, J. & Lee, K. Place your BETs: the therapeutic potential of bromodomains. *Trends in pharmacological sciences* **33**, 146-153, doi:10.1016/j.tips.2011.12.002 (2012).
- 82 Mujtaba, S. *et al.* Structural mechanism of the bromodomain of the coactivator CBP in p53 transcriptional activation. *Molecular cell* **13**, 251-263 (2004).
- 83 Mujtaba, S., Zeng, L. & Zhou, M. M. Structure and acetyl-lysine recognition of the bromodomain. *Oncogene* **26**, 5521-5527, doi:10.1038/sj.onc.1210618 (2007).
- 84 Filippakopoulos, P. *et al.* Histone recognition and large-scale structural analysis of the human bromodomain family. *Cell* **149**, 214-231, doi:10.1016/j.cell.2012.02.013 (2012).
- 85 Dey, A., Chitsaz, F., Abbasi, A., Misteli, T. & Ozato, K. The double bromodomain protein Brd4 binds to acetylated chromatin during interphase and mitosis. *Proceedings of the National Academy of Sciences of the United States of America* **100**, 8758-8763, doi:10.1073/pnas.1433065100 (2003).
- 86 Bisgrove, D. A., Mahmoudi, T., Henklein, P. & Verdin, E. Conserved P-TEFb-interacting domain of BRD4 inhibits HIV transcription. *Proc Natl Acad Sci U S A* **104**, 13690-13695, doi:0705053104 [pii] 10.1073/pnas.0705053104 (2007).
- 87 Filippakopoulos, P. *et al.* Selective inhibition of BET bromodomains. *Nature* **468**, 1067-1073, doi:10.1038/nature09504 (2010).
- 88 Delmore, J. E. *et al.* BET Bromodomain Inhibition as a Therapeutic Strategy to Target MYC. *Cell* **146**, 904-917, doi:S0092-8674(11)00943-3 [pii] 10.1016/j.cell.2011.08.017 (2011).
- 89 Zuber, J. *et al.* RNAi screen identifies Brd4 as a therapeutic target in acute myeloid leukaemia. *Nature* **478**, 524-528, doi:10.1038/nature10334 (2011).
- 90 Mertz, J. A. *et al.* Targeting MYC dependence in cancer by inhibiting BET bromodomains. *Proceedings of the National Academy of Sciences of the United States of America* **108**, 16669-16674, doi:1108190108 [pii] 10.1073/pnas.1108190108 (2011).

- 91 Ott, C. J. *et al.* BET bromodomain inhibition targets both MYC and IL7R in high-risk acute lymphoblastic leukemia. *Blood* **120**, 2843-2852, doi:10.1182/blood-2012-02-413021 (2012).
- 92 Shimamura, T. *et al.* Efficacy of BET Bromodomain Inhibition in Kras-Mutant Non-Small Cell Lung Cancer. *Clinical cancer research : an official journal of the American Association for Cancer Research* **19**, 6183-6192, doi:10.1158/1078-0432.CCR-12-3904
1078-0432.CCR-12-3904 [pii] (2013).
- 93 Chapuy, B. *et al.* Discovery and characterization of super-enhancer-associated dependencies in diffuse large B cell lymphoma. *Cancer cell* **24**, 777-790, doi:10.1016/j.ccr.2013.11.003 (2013).
- 94 Mathad, R. I., Hatzakis, E., Dai, J. & Yang, D. MYC promoter G-quadruplex formed at the 5'-end of NHE III1 element: insights into biological relevance and parallel-stranded G-quadruplex stability. *Nucleic Acids Res* **39**, 9023-9033, doi:10.1093/nar/gkr612 (2011).
- 95 Siddiqui-Jain, A., Grand, C. L., Bearss, D. J. & Hurley, L. H. Direct evidence for a G-quadruplex in a promoter region and its targeting with a small molecule to repress MYC transcription. *Proceedings of the National Academy of Sciences of the United States of America* **99**, 11593-11598, doi:10.1073/pnas.182256799 (2002).
- 96 Han, H., Bennett, R. J. & Hurley, L. H. Inhibition of unwinding of G-quadruplex structures by Sgs1 helicase in the presence of N,N'-bis[2-(1-piperidino)ethyl]-3,4,9,10-perylenetetracarboxylic diimide, a G-quadruplex-interactive ligand. *Biochemistry* **39**, 9311-9316, doi:bi000482r [pii] (2000).
- 97 Han, H., Cliff, C. L. & Hurley, L. H. Accelerated assembly of G-quadruplex structures by a small molecule. *Biochemistry* **38**, 6981-6986, doi:10.1021/bi9905922
bi9905922 [pii] (1999).
- 98 Han, H. & Hurley, L. H. G-quadruplex DNA: a potential target for anti-cancer drug design. *Trends in pharmacological sciences* **21**, 136-142, doi:S0165-6147(00)01457-7 [pii] (2000).
- 99 Han, H., Hurley, L. H. & Salazar, M. A DNA polymerase stop assay for G-quadruplex-interactive compounds. *Nucleic Acids Res* **27**, 537-542, doi:gkc120 [pii] (1999).
- 100 Han, H., Langley, D. R., Rangan, A. & Hurley, L. H. Selective interactions of cationic porphyrins with G-quadruplex structures. *Journal of the American Chemical Society* **123**, 8902-8913, doi:ja002179j [pii] (2001).
- 101 Hurley, L. H., Von Hoff, D. D., Siddiqui-Jain, A. & Yang, D. Drug targeting of the MYC promoter to repress gene expression via a G-quadruplex silencer element. *Semin Oncol* **33**, 498-512, doi:S0093-7754(06)00186-2 [pii]
10.1053/j.seminoncol.2006.04.012 (2006).
- 102 Bowers, E. M. *et al.* Virtual ligand screening of the p300/CBP histone acetyltransferase: identification of a selective small molecule inhibitor. *Chemistry & biology* **17**, 471-482, doi:10.1016/j.chembiol.2010.03.006
S1074-5521(10)00117-1 [pii] (2010).

- 103 Zheng, Y. *et al.* Synthesis and evaluation of a potent and selective cell-permeable p300 histone acetyltransferase inhibitor. *J Am Chem Soc* **127**, 17182-17183, doi:10.1021/ja0558544 (2005).
- 104 Faiola, F. *et al.* Dual regulation of MYC by p300 via acetylation-dependent control of Myc protein turnover and coactivation of Myc-induced transcription. *Mol Cell Biol* **25**, 10220-10234, doi:10.1128/MCB.25.23.10220-10234.2005 (2005).
- 105 Secombe, J., Li, L., Carlos, L. & Eisenman, R. N. The Trithorax group protein Lid is a trimethyl histone H3K4 demethylase required for dMyc-induced cell growth. *Genes & development* **21**, 537-551, doi:10.1101/gad.1523007 (2007).
- 106 Secombe, J. & Eisenman, R. N. The function and regulation of the JARID1 family of histone H3 lysine 4 demethylases: the Myc connection. *Cell Cycle* **6**, 1324-1328 (2007).
- 107 de Rooij, J. D. *et al.* NUP98/JARID1A is a novel recurrent abnormality in pediatric acute megakaryoblastic leukemia with a distinct HOX gene expression pattern. *Leukemia* **27**, 2280-2288, doi:10.1038/leu.2013.87 (2013).
- 108 Wang, G. G. *et al.* Haematopoietic malignancies caused by dysregulation of a chromatin-binding PHD finger. *Nature* **459**, 847-851, doi:10.1038/nature08036 (2009).
- 109 Li, L., Greer, C., Eisenman, R. N. & Secombe, J. Essential functions of the histone demethylase lid. *Plos Genet* **6**, e1001221, doi:10.1371/journal.pgen.1001221 (2010).
- 110 Breuer, M. *et al.* Very high frequency of lymphoma induction by a chemical carcinogen in pim-1 transgenic mice. *Nature* **340**, 61-63, doi:10.1038/340061a0 (1989).
- 111 van Lohuizen, M. *et al.* Predisposition to lymphomagenesis in pim-1 transgenic mice: cooperation with MYC and N-myc in murine leukemia virus-induced tumors. *Cell* **56**, 673-682, doi:0092-8674(89)90589-8 [pii] (1989).
- 112 Zippo, A., De Robertis, A., Serafini, R. & Oliviero, S. PIM1-dependent phosphorylation of histone H3 at serine 10 is required for MYC-dependent transcriptional activation and oncogenic transformation. *Nat Cell Biol* **9**, 932-944, doi:ncb1618 [pii] 10.1038/ncb1618 (2007).
- 113 Zippo, A. *et al.* Histone Crosstalk between H3S10ph and H4K16ac Generates a Histone Code that Mediates Transcription Elongation. *Cell* **138**, 1122-1136, doi:S0092-8674(09)00911-8 [pii] 10.1016/j.cell.2009.07.031 (2009).
- 114 Weng, A. P. *et al.* MYC is an important direct target of Notch1 in T-cell acute lymphoblastic leukemia/lymphoma. *Genes & development* **20**, 2096-2109, doi:10.1101/gad.1450406 (2006).
- 115 Sears, R. *et al.* Multiple Ras-dependent phosphorylation pathways regulate Myc protein stability. *Genes & development* **14**, 2501-2514 (2000).
- 116 Gutierrez, A. *et al.* Phenothiazines induce PP2A-mediated apoptosis in T cell acute lymphoblastic leukemia. *The Journal of clinical investigation*, doi:10.1172/JCI65093 (2014).

- 117 Brockmann, M. *et al.* Small molecule inhibitors of aurora-a induce proteasomal degradation of N-myc in childhood neuroblastoma. *Cancer cell* **24**, 75-89, doi:10.1016/j.ccr.2013.05.005 (2013).
- 118 Yang, D. *et al.* Therapeutic potential of a synthetic lethal interaction between the MYC proto-oncogene and inhibition of aurora-B kinase. *Proc Natl Acad Sci U S A* **107**, 13836-13841, doi:1008366107 [pii] 10.1073/pnas.1008366107 (2010).
- 119 Goga, A., Yang, D., Tward, A. D., Morgan, D. O. & Bishop, J. M. Inhibition of CDK1 as a potential therapy for tumors over-expressing MYC. *Nat Med* **13**, 820-827, doi:nm1606 [pii] 10.1038/nm1606 (2007).
- 120 Toyoshima, M. *et al.* Functional genomics identifies therapeutic targets for MYC-driven cancer. *Proc Natl Acad Sci U S A* **109**, 9545-9550, doi:10.1073/pnas.1121119109 1121119109 [pii] (2012).
- 121 Kessler, J. D. *et al.* A SUMOylation-dependent transcriptional subprogram is required for Myc-driven tumorigenesis. *Science* **335**, 348-353, doi:10.1126/science.1212728 science.1212728 [pii] (2012).
- 122 Dorr, J. R. *et al.* Synthetic lethal metabolic targeting of cellular senescence in cancer therapy. *Nature* **501**, 421-425, doi:10.1038/nature12437 nature12437 [pii] (2013).

Chapter 4

Disruption of Super Enhancer-Driven Cancer Dependencies in Diffuse Large B-Cell Lymphoma

Bjoern Chapuy^{1,7}, Michael R. McKeown^{1,7}, Charles Lin^{2,9}, Stefano Monti³, Margaretha G.M. Roemer¹, Jun Qi¹, Peter B. Rahl², Heather Sun⁴, Kelly T. Yeda¹, John G Doench⁵, Elaine Reichert¹, Andrew J. Kung^{6,10}, Scott J. Rodig⁴, Richard A. Young², Margaret A. Shipp^{1,8,11}, James E. Bradner^{1,2,8,11}

¹ Department of Medical Oncology, Dana-Farber Cancer Institute, Boston, MA

² Whitehead Institute of Genome Research, Massachusetts Institute of Technology, Cambridge, MA

³ Section of Computational Biomedicine, Boston University School of Medicine, Boston, MA

⁴ Department of Pathology, Brigham & Women's Hospital, Boston, MA

⁵ Broad Institute of MIT & Harvard, Cambridge, MA

⁶ Department of Pediatric Oncology, Dana-Farber Cancer Institute, Boston, MA

⁷ These authors contributed equally to this work.

⁸ These authors contributed equally to this work.

Introduction

Diffuse Large B-Cell Lymphoma (DLBCL) is a biologically heterogeneous and clinically aggressive disease. Here, we explore the role of BET bromodomain proteins in DLBCL, using integrative chemical genetics and functional epigenomics. We observe highly asymmetric loading of BRD4 at enhancers, with approximately 33% of all BRD4 localizing to enhancers at 1.6% of occupied genes. These super enhancers prove particularly sensitive to bromodomain inhibition, explaining the selective effect of BET inhibitors on oncogenic and lineage-specific transcriptional circuits. Functional study of genes marked by super enhancers in DLBCL cell lines and primary tumors leads to the identification of novel dependencies. Translational studies performed on a comprehensive panel of DLBCLs establish a therapeutic rationale for evaluating BET inhibitors in this disease.

Although oncogenic transcription factors underlie the pathophysiology and biological heterogeneity of DLBCL, studies of transcriptional co-activator proteins are limited in this disease. In this chemical genetic study, we demonstrate the efficacy of BET inhibition and characterize the broad function of BET bromodomains in supporting the transcriptional growth program in all subclasses of DLBCL, including co-activation of E2F and MYC target genes. We define an asymmetry in the localization of BRD4 to enhancer regions nearby oncogenic and master regulatory genes and expand the finding to a representative panel of cell lines and primary samples. This finding likely explains the specific transcriptional effect of BET inhibition which modulates the expression of master transcription factors that control B-cell fate and germinal center formation.

The origins of this project came from a close collaboration between Michael McKeown (Bradner Lab) and Bjoern Chapuy (Shipp Lab). One of the most important questions that came out of the development of JQ1 was how it works to reduce proliferation in such a wide set of cancer backgrounds. Moreover, the heterogeneity of DLBCL has typically caused drugs to have varying effects based on the subtype was found to be conspicuously absent with JQ1. Therefore, we hypothesized that a deep study of the biology of JQ1 in DLBCL on the chromatin level would help to explain this effect. Our initial hypothesis that JQ1 was acting primarily through MYC and E2F1 proved incorrect and had a mild, partial impact. The resultant validation of large enhancers, BRD4 loading asymmetry, and discovery of novel dependencies is detailed below.

Originally, a large, exploratory cell screening effort involving forty experimental oncology compounds and sixty cell lines composed of DLCL, Hodgkin's Lymphoma, and Burkitt's Lymphoma was run (data not shown). The paper in *Cancer Cell*¹ from which this chapter is derived contains a subset of that data. Methods and operation of screening equipment including the Biotech EL406 liquid handler, Envision plate reader, and Janus pin transfer system were developed and executed by McKeown. In order to carry this out, optimized plate designs, cell loading volumes and concentrations, equipment protocols and programs, and data processing methods were developed. This amount of screening required large amounts of cells which were expanded and cared for by Chapuy and McKeown.

The mouse studies were carried out at the DFCI Lurie Center. However, processing of mice for pharmacodynamics measurements were carried out by Chapuy

and McKeown at the termination of these experiments. McKeown assisted with dissections by weighing spleens and prepping them for flow cytometry. In addition, McKeown prepped samples for histology and processed images in ImageScope and ScanScope software to prepare images.

The expansion of cells, treatment, and preparation for ChIP-seq was carried out by McKeown following a modified Agilent protocol. Methods for performing primary tissue ChIP-seq on human tissue were developed by McKeown as these had not previously been executed in the Bradner Lab. The concept of Super-Enhancers originated in experiment being carried out in the Young lab² and Bradner lab¹ at overlapping time frames. McKeown surveyed known oncogenes in DLBCL by viewing gene tracks and noted large enhancer regions in their proximity. This was found to agree with the Young lab findings in Multiple Myeloma. Charles Lin then developed metrics and analyses for genome wide characterization.

Based on the initial findings in cell lines, we expanded our search to look at primary tissues and confirmed the presence of Super-Enhancers here as well. Furthermore, the well transcriptionally characterized sub-types of DLBCL were hypothesized to correlate with enhancer placement, which ultimately proved accurate and allowed correct segregation of subtype by enhancer loci. Tracks and graphs used in figures for ChIP-seq data were prepared by Lin and McKeown.

Contribution:

MRM performed ChIP-seq, assisted with *in vivo* processing for pharmacodynamics, performed cellular screen, and wrote part of manuscript. BC performed cellular assays, transcriptional studies, and helped write. CL and ER worked on ChIP-seq processing. SM and JD processed expression data. JQ synthesized and provided chemical reagents. MR and KY assisted with cellular biology experiments. HS and SR processed histology samples. AK supervised *in vivo* work. PR advised on ChIP-seq methods and discussed super enhancers. RY, MS, and JB oversaw research.

Background

Diffuse large B-cell lymphoma (DLBCL) is the most common form of non-Hodgkin lymphoma in adults. The majority of DLBCLs arise from antigen-exposed B-cells during the germinal center (GC) reaction, a process that optimizes the affinity of antibodies for antigens ³. Despite significant advances in the biological understanding of DLBCL pathogenesis, current treatment regimens include empiric combination immuno/chemotherapy at induction and relapse. Mechanistic insights guiding the development of targeted therapeutic agents are urgently needed, as relapsed and refractory disease comprise significant unmet medical needs ⁴.

DLBCL exhibits significant biological heterogeneity. Gene expression profiling has allowed functional classification of tumors into distinct subgroups. Presently, DLBCL is described using two transcriptional classifications, commonly referred to as the cell of origin (COO) and the consensus clustering classification (CCC). The COO classification relates subsets of DLBCL to specific stages of normal B-cell development, assigning tumors to either a germinal center-B (GCB) or activated B-cell (ABC) subtype ⁵. The CCC classification defines 3 groups of DLBCLs on the basis of transcriptional heterogeneity solely within tumors. Here, DLBCL subtypes rely on B-cell receptor (BCR) survival signals and glycolysis (BCR), BCR-independent fuel utilization and oxidative phosphorylation (OxPhos), or exhibit an increased inflammatory and immune cell infiltrate (host response; HR) ⁶⁻⁸. Both classifications provide insights into disease pathogenesis and suggest potential tumor cell dependencies and rational therapeutic targets.

Several genome sequencing studies of DLBCL have revealed substantial genetic heterogeneity and defined the mutational landscape⁹⁻¹². In contrast to Burkitt lymphoma, another germinal center-derived tumor characterized by a hallmark t(8;14) translocation of *MYC* into the immunoglobulin heavy or light chain enhancer region, DLBCLs have high genotypic diversity. These tumors exhibit multiple low frequency copy number alterations (CNAs), additional chromosomal translocations and over 50 recurrent somatic mutations^{9,10,13}. In DLBCL, the underlying biological and genetic heterogeneity are associated with highly variable clinical outcomes, ranging from long-term overall survival (“cure”) to rapidly progressive disease¹³.

Mechanistically, the transcriptional heterogeneity of DLBCL is conferred, in part, by pathologic activation or inactivation of lineage-specific and growth-associated master regulatory transcription factors (TF), including NF- κ B⁵, BCL6¹⁴, MYC¹⁵ and p53¹³, and also through upstream pathway deregulation. Recently, we demonstrated that multiple, low-frequency CNAs converge functionally to deregulate p53 and cell cycle resulting in increased proliferation and enhanced signaling from the master regulatory transcription factor, E2F1¹³. In this study, deregulated cell cycle and increased expression of E2F1 target genes were associated with inferior outcome¹³. In recent studies, a newly defined subset of “double-hit” DLBCLs which overexpress MYC in association with BCL2 also have an unfavorable outcome^{16,17}. Together, these findings underscore the centrality of master regulatory TFs in DLBCL.

TFs control cancer cell state by binding proximal (promoter) and distal (enhancer) regulatory elements ¹⁸. The subsequent recruitment of multiprotein complexes leads to local remodeling of chromatin, which establishes mitotic memory, and transmission of transcriptional signals to RNA polymerase II (RNAP) poised at genes associated with growth and survival ^{19,20}. Chromatin associated with TF binding sites is markedly enriched in histone proteins post-translationally modified by lysine side-chain acetylation ²¹. This mark biophysically facilitates opening of chromatin and recruits an emerging class of co-activators which recognize ϵ -acetyl lysine through a specialized recognition motif or bromodomain ²².

Among the 47 known bromodomain-containing proteins ²³, the sub-family of bromodomain and extra-terminal domain (BET) co-activators (BRD2, BRD3 and BRD4) are particularly appealing targets in DLBCL. Structurally, BET proteins possess twin amino-terminal bromodomains that facilitate binding to hyperacetylated promoter/enhancer regions ^{23,24}, as well as a distal carboxy-terminal binding site for the positive transcription elongation factor (P-TEFb) ²⁵. In cancer, BET bromodomains promote M to G1 cell cycle progression ²⁶ and contribute to mitotic memory ^{27,28}. Collaborative research from our group and others has recently identified a role for BET bromodomains in supporting the transcription of known DLBCL oncogenes (*MYC* and *BCL2*) in studies of acute leukemia, multiple myeloma and Burkitt lymphoma ²⁹⁻³³. Interestingly, overexpression of *BRD2* from an engineered immunoglobulin heavy-chain promoter-enhancer construct caused an aggressive B-cell neoplasm resembling DLBCL in mice ³⁴. Together, the findings establish a compelling hypothesis that BET

bromodomains serve as chromatin-associated modulators of major gene regulatory pathways in DLBCL.

In an effort to study the role of BET bromodomains in cancer, we recently developed the first inhibitors of bromodomain and extra-terminal domain (BET) transcriptional co-activator proteins³⁵ including a prototypical triazolo-diazepine inhibitor of the acetyl-lysine binding site, JQ1. Here, we report first, detailed and genomewide mechanistic studies exploring the role of BET bromodomains in oncogenic transcription by master regulatory TFs, and an assessment of BRD4 as a therapeutic target in DLBCL.

BET bromodomain inhibition exerts pan-subtype growth arrest in DLBCL and in Burkitt lymphoma (BL)

To assess the role of BET bromodomains as cancer cell dependencies in DLBCL, we first studied the effects of four structurally dissimilar BET bromodomain inhibitors on a comprehensive panel of 34 human lymphoma cell lines (21 DLBCL, capturing all transcriptionally defined subtypes, 6 BL and 7 Hodgkin Lymphoma [HL]), in comparative high-throughput format. In addition to the prototypical BET inhibitor, JQ1 (JQ1S)³⁵, we resynthesized and tested an analogous thienodiazepine from Mitsubishi-Tanabe Pharmaceutical Corporation (Y803, OTX015; Oncoethix SA) which was developed for inflammatory bowel disease, (Figure 4.1A³⁶, a benzodiazepine inhibitor (iBET)³⁷ and a dimethylisoxazole inhibitor (iBET-151) from GlaxoSmithKline²⁹. Analyses of cellular proliferation at 72 hr revealed a potent (nanomolar) class effect of

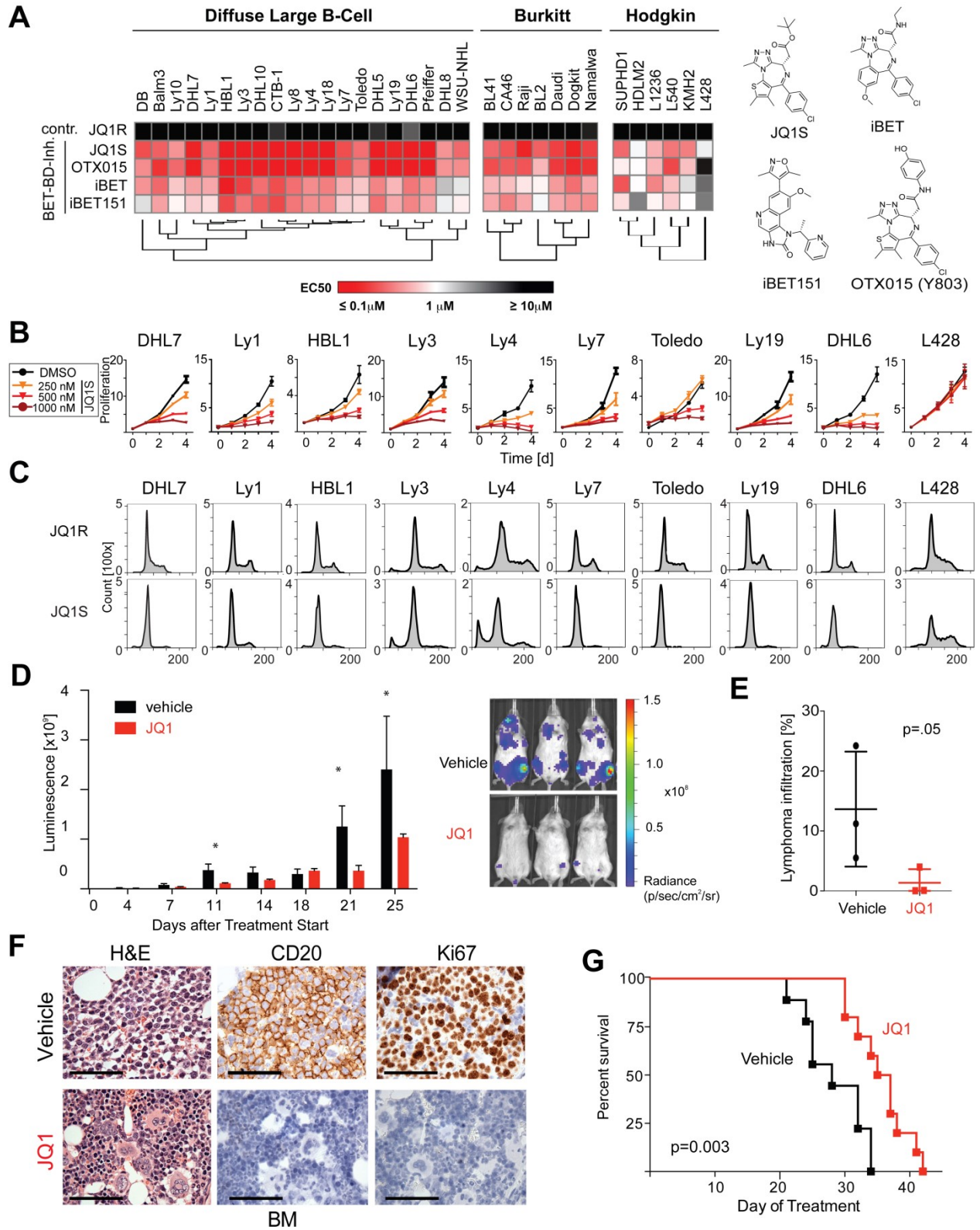
BET bromodomain inhibitors on the DLBCL and BL cell lines irrespective of subtype and the lack of effect of an inactive enantiomer, (JQ1R; Figure 4.1A). The HL cell lines were comparatively less sensitive to BET inhibition and HL line, L428, was resistant to all 4 compounds.

The effects of BET inhibition on growth over time, cell cycle progression, and apoptosis were then studied in a representative panel of nine DLBCL cell lines, using the L428 HL line as a negative control (Figure 4.1B-C; 4.2B-C). BET inhibition with JQ1 significantly attenuated growth in a dose-responsive manner in all tested DLBCL cell lines (Figure 4.1B). In three representative DLBCL cell lines, genetic depletion of BRD2 or BRD4 similarly decreased DLBCL proliferation, consistent with an on target effect of JQ1 (Figure 4.2D-G). We observed a profound S phase and G2 peak reduction following JQ1 treatment consistent with a G1 cell cycle arrest (Figure 4.1C, 4.2B). BET inhibition (500 nM) did not induce apoptosis in most cell lines studied, evidenced by low AnnexinV/7AAD staining (Figure 4.2C) and absence of a sub-G1 peak (Figure 4.1C). Neither enantiomeric (JQ1R) nor vehicle (DMSO) controls affected DLBCL proliferation or survival (Figure 4.1C; 4.2B-C). Treatment with 500 nM JQ1 was similarly cytostatic in Burkitt lymphoma cell lines (Figure 4.2C). The L428 HL cell line was resistant to BET inhibition in all tested assays.

Figure 4.1: *In vitro* analyses of BET Bromodomain inhibition in various B-cell lymphomas

(A) Hierarchical clustering of mean EC50s of the four BET inhibitors (72 hr treatment) in the indicated panel of B-cell lymphoma cell lines. EC50 values in a colorimetric scale: very sensitive ($\leq 1\mu\text{M}$) in red; sensitive ($=1\mu\text{M}$) in white; to resistant ($\geq 10\mu\text{M}$) in black. Corresponding structures are shown. (B) Proliferation of the indicated DLBCL and HL cell lines treated with vehicle or 250-1000 nM JQ1 for 1-4 days. (C) Cell cycle analysis following 72 hr treatment with JQ1 (500 nM) or inactive enantiomer JQ1R (500 nM). Error bars represent the SD of triplicates. (D) Bioluminescence of JQ1 (30mg/kg IP BID) or vehicle-treated NSG mice xenotransplanted with luciferized mCherry⁺ Ly1 cells. Asterisks indicate $p < .05$ using a one-sided t-test. Error bars represent SEM. (E) Lymphoma infiltration of bone marrow in a representative set of animals was assessed by flow cytometric analysis of mCherry⁺ cells and visualized as scatter plots (median, line; whiskers, SEM). p values were obtained with a one-sided Mann-Whitney U test. (F) Immunohistochemical analysis of lymphoma (Ly1) BM infiltration in JQ1- and in vehicle-treated mice: H&E; anti-human CD20, and anti-Ki67 immunostaining. Scale bar represents 100 μm . (G) Kaplan-Meier plot of the remainder of the Ly1 cohort ($n = 21$) treated with either vehicle or JQ1 30 mg/kg bid. The p value was obtained by Log-rank test.

Figure 4.1 (Continued)



Efficacy of BET inhibition in DLBCL xenograft models

We next explored the therapeutic potential of BET inhibition in two independent DLBCL xenotransplantation models (Figure 4.1D-G; 4.2H-K). First, the human DLBCL cell line Ly1 was engineered to ectopically express firefly luciferase and mCherry allowing surrogate measurement of tumor growth *in vivo*. NOD SCID Il2 γ ^{null} (NSG) mice xenotransplanted with Ly1-Luc-mCherry cells had a statistically significant reduction in tumor burden when treated with JQ1 (30 mg BID by intraperitoneal (IP) injection; Figure 4.1D). A representative cohort of animals was sacrificed on day 13 of treatment for full hematological analysis. JQ1-treated animals had significantly decreased lymphoma infiltration of the bone marrow (BM) as measured by flow cytometric assessment of mCherry⁺ cells (Figure 4.1E). Morphological and immunohistochemical analyses revealed that the highly proliferative (Ki67⁺) human CD20⁺ lymphoma cell infiltrate (Figure 4.1F, upper panel) was markedly reduced in animals treated with the BET bromodomain inhibitor (Figure 4.1F, lower panel). In the remainder of the Ly1 xenograft cohort, the JQ1-treated mice had a significant median overall survival advantage of 9 days ($p = 0.003$) (Figure 4.1G).

Figure 4.2: Dose response curves of OTX015 (Y803) and JQ1S *in vitro*, assessment of apoptosis in JQ1-treated lymphoma cell lines and proliferation in BRD2- and BRD4-depleted DLBCLs in three representative DLBCL cell lines and an additional xenograft model of JQ1 treatment.

(A) Potency of the Mitsubishi BET bromodomain inhibitor Y803 (licensed as OTX015), visualized in a dose-response curve. The competition assay uses AlphaScreen beads to observe the inhibited binding of bromodomain 2, 3, 4, and T site 1 against biotinylated acety-histone 4 tail in the presence of Y803 in a dose-dependent manner. Non-linear regressions were fit to the mean of four replicates over ten concentrations with the standard deviation at each point indicated by error bars. JQ1 was used as positive control. (B) Assessment of cell cycle following 72 hours of treatment with either 500nM of the active enantiomer, JQ1S, 500nM of the inactive enantiomer, JQ1R, or vehicle control (DMSO). (C) Apoptosis assessment by Annexin V-APC/7AAD staining in nine DLBCL, one Hodgkin lymphoma (L428) and two Burkitt lymphoma cell lines, Raji and CA46, following 72 hr of treatment with vehicle (DMSO), 500nM active JQ1S or 500nM of the inactive enantiomer JQ1R. (D/E) Assessment of proliferation following lentiviral-mediated knock down of BRD2 (D), and BRD4 (E) with two independent hairpins (sh1 and sh2) and a control (ev=empty vector) in representative DLBCL cell lines for each transcriptional-defined subtype (Ly1, BCR/GCB; Toledo, OxPhos/unclass.; HBL1, BCR/ABC). (F/G) Efficacy of knockdown of BRD2 (F) and BRD4 (G) was determined by immunoblot. Membranes were stripped and re-probed with GAPDH as loading control. (H) Bioluminescence of JQ1 (30mg/kg IP BID)- or vehicle-treated NSG mice xenotransplanted with luciferized mCherry⁺ Toledo cells. Asterisks indicate $p < .05$ using a one-sided t-test. Error bars represent SEM. (I) Spleen weights of JQ1- and vehicle-treated animals xenografted with Toledo cells are visualized as scatter plots (median, line; whiskers SEM). The p values were obtained with a one-sided Mann-Whitney U test. (J) Lymphoma infiltration of animals was assessed by flow cytometric analysis of mCherry⁺ cells and visualized as scatter plots (median, line; whiskers, SEM). The p values were obtained with a one-sided Mann-Whitney U test. (K) Immunohistochemical analysis of lymphoma (Toledo) cell infiltration in BM of JQ1 and DMSO-treated mice was assessed in JQ1- and in vehicle-treated mice: H&E; anti-human CD20, and anti-Ki67 immunostaining. Scale bar represents 100 μm .

Figure 4.2 (Continued)

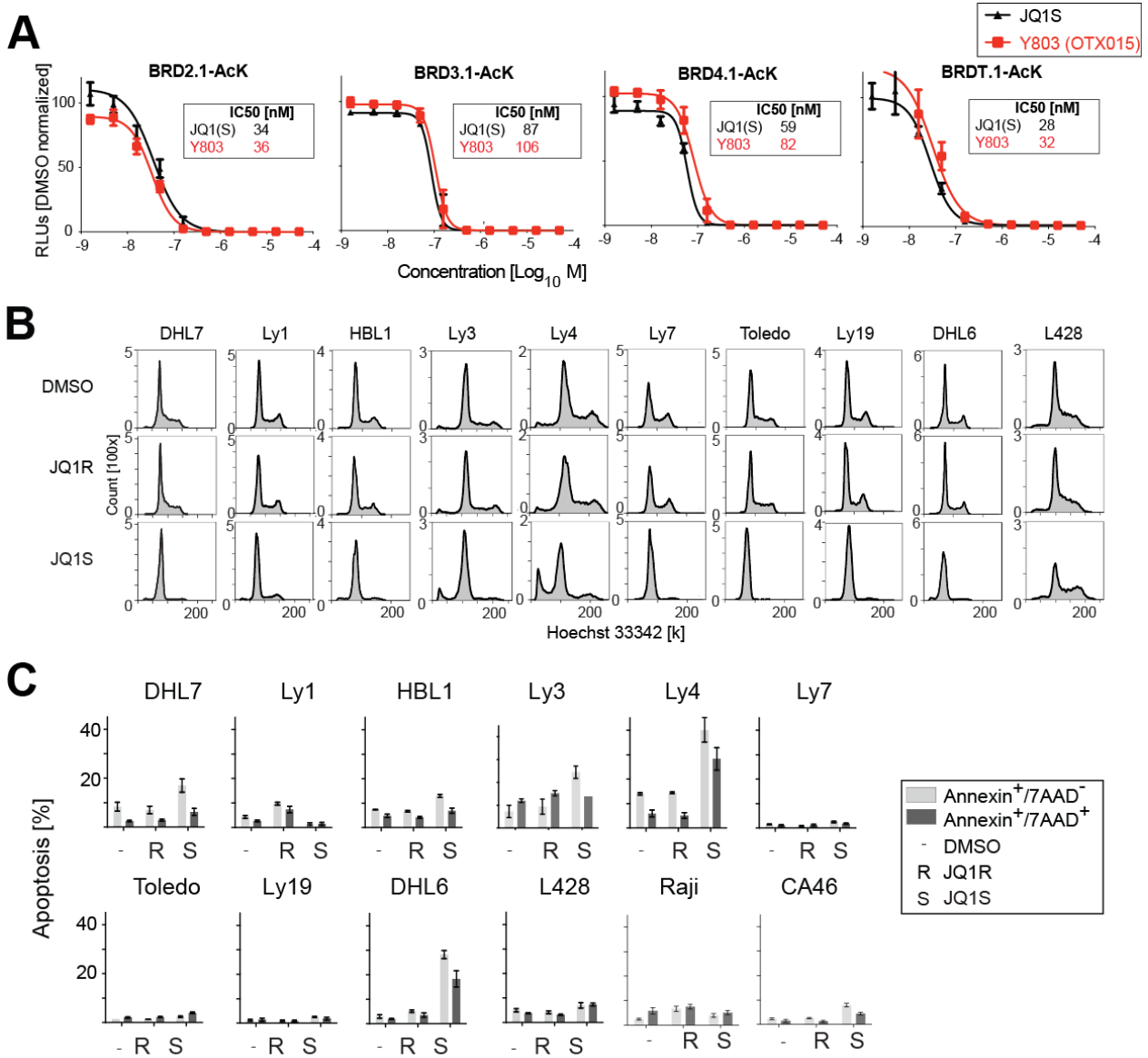
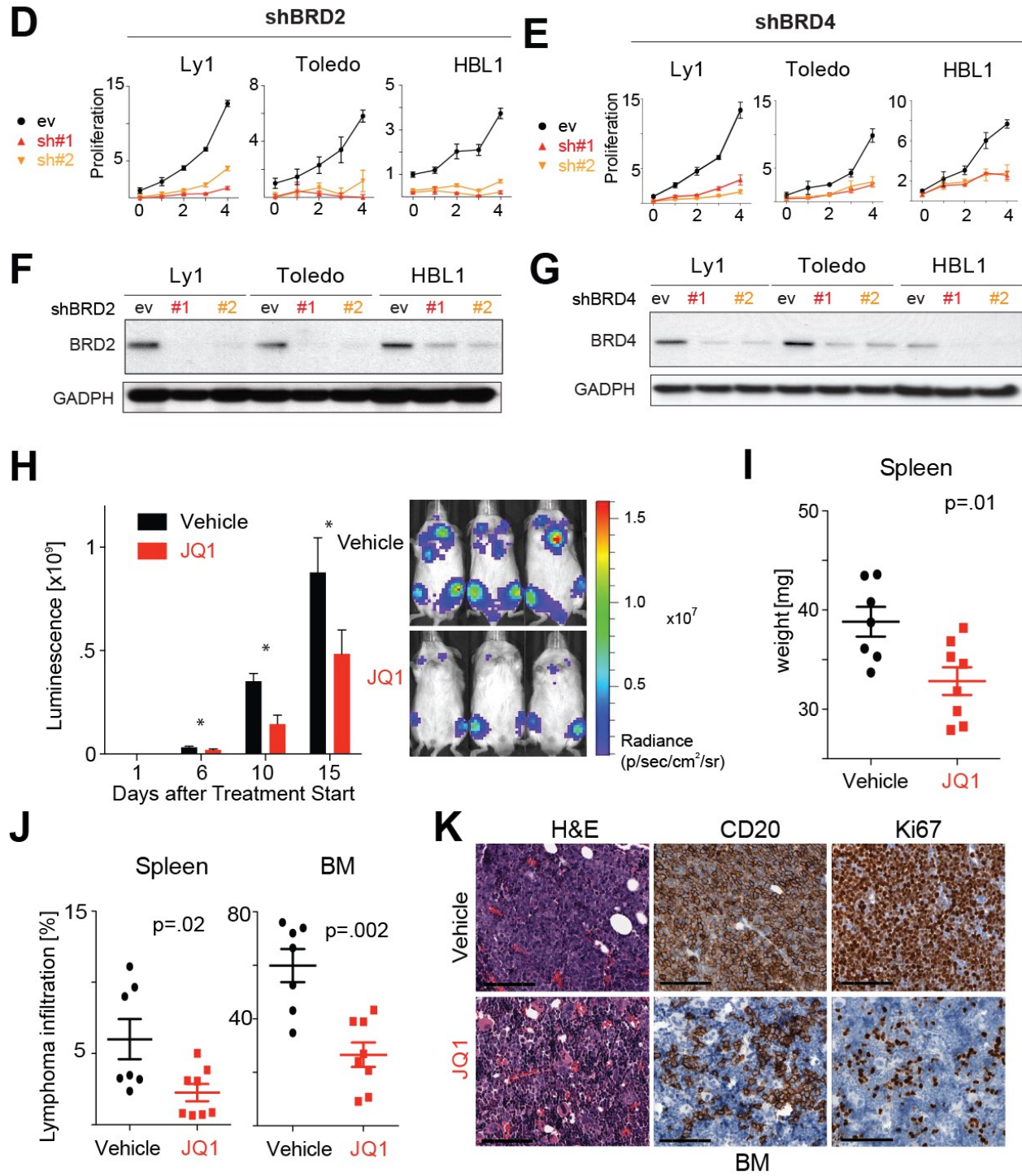


Figure 4.2 (Continued)



To confirm the pharmacodynamic findings, a second xenotransplantation model was established using the Toledo DLBCL cell line. NSG mice with established tumors had delayed tumor progression when treated with JQ1 (Figure 4.2H). Full hematological analysis revealed that JQ1-treated animals had decreased spleen weight (Figure 4.2I) and lymphomatous infiltration of bone marrow and spleen (Figure 4.2J). Morphological and immunohistochemical analysis of the BM revealed significantly reduced the infiltration of CD20⁺/Ki67⁺ human lymphoma cells following BET inhibition (Figure 4.2K).

BET inhibition downregulates oncogenic transcriptional pathways

To gain insights into the transcriptional pathways regulated by BET bromodomain co-activator proteins, we performed kinetic transcriptional profiling of vehicle and JQ1-treated DLBCL cell lines. Five human DLBCL cell lines which captured the recognized transcriptional heterogeneity (Ly1, BCR/GCB; DHL6, BCR/GCB; Ly4, OxPhos/unclass.; Toledo, OxPhos/unclass; and HBL1, BCR/ABC) were treated with JQ1 (500 nM) or vehicle control for 0, 2, 6, 12, 24, 48 hours. At each timepoint, differential analysis was performed between the vehicle and JQ1-treated samples (24 hr comparison, fold change (FC) > 1.3, false discovery rate (FDR) < 0.01, Figure 4.3A). Consistent with prior studies of BET bromodomain function and inhibition, HEXIM1 was markedly upregulated by JQ1 in all DLBCL cell lines (Figure 4.3B) ^{38,39}.

Figure 4.3: Transcriptional modulation of TLR pathway members and BCR signaling pathway components following BET inhibition, pathway enrichment analysis in COO subtypes, transcript and protein abundance of MYC and E2F1 following JQ1 treatment, transcription factor binding site enrichment in COO subtypes and MYC rescue experiments following JQ1 treatment.

(A) Heatmap of the most differentially expressed genes (FDR < 0.01, FC > 1.3) following 24 hr treatment with 500 nM JQ1 or vehicle. TLR10 and HEXIM1 are highlighted as representative genes. (B) Mean transcript abundance of HEXIM1 in all 5 lines treated with vehicle or JQ1 (500 nM) over time. (C) Heat map of TLR pathway components in vehicle- or JQ1-treated DLBCL cell lines over time (0 – 48hr). The row order is derived from unsupervised clustering in Ly1 cells and fixed across the remaining cell lines. (D) Heat map of BCR signaling pathway components in vehicle- or JQ1-treated DLBCL cell lines over time (0 – 48 hr). (E) Hyperenrichment analysis of differentially expressed genes (FDR < 0.05, FC > 1.3) in 2 GCB cell lines (DHL6, Ly1) treated with JQ1 (vs. vehicle) was performed using a pathway compendium (MSigDB, C2.CP). Results at each time point were ranked by FDR and visualized as a color-coded matrix. Intensity of color correlates with FDR significance levels as indicated. Highlighted down-regulated pathways included: MYD88/TLR signaling, blue; BCR signaling, green; and Cell cycle/E2F, turquoise). (F) Visualization of pathway enrichment analysis of differentially expressed genes (FDR < 0.05, FC > 1.3) in HBL1, an ABC cell line. See legend to (E) for details. (G) Transcription factor binding site motifs were analyzed in the most differentially expressed genes (FDR < 0.05, FC > 1.3) in 2 GCB (DHL6, Ly1) cell lines. Results at each timepoint were ranked using a color-coded matrix. Up-regulated motifs in red, down-regulated motifs in blue. Genes with MYC binding sites in blue and E2F binding sites in turquoise. (H) Transcription factor binding site motifs were analyzed in the most differentially expressed genes (FDR < 0.05, FC > 1.3) in one ABC (HBL1) cell line. (I) GSEA plots of functionally defined MYC and E2F target gene sets in two vehicle- vs. JQ1-treated GCB cells (DHL6, Ly1) at 24 hr. (J) GSEA plots of functionally defined MYC and E2F target gene sets in one vehicle- vs. JQ1-treated ABC cell (HBL1) at 24 hr. (K-N) Mean transcript abundance of MYC (K) and E2F1 (M) in all 5 DLBCL cell lines following JQ1 (red) or DMSO (black curve) treatment is plotted over time. Error bars represent SEM. Protein abundance of MYC (L) and E2F1 (N) was determined by western blot (Figure 4.2G), quantified using Image J (<http://rsb.info.nih.gov/ij/>,⁴⁰), and normalized to the quantified GAPDH signal. (O) Enforced expression of MYC in the three indicated DLBCL cell lines, Ly1, Toledo and HBL1, was not able to rescue JQ1-mediated proliferation inhibition. Proliferation was compared to enforced expression of a control insert, GFP, in the same vector. (P) Immunoblot analysis of the cell lines from (O) with enforced expression of either MYC or GFP. (Q) Quantification of protein abundance of (P) with ImageJ, see (K) for details.

Figure 4.3 (Continued)

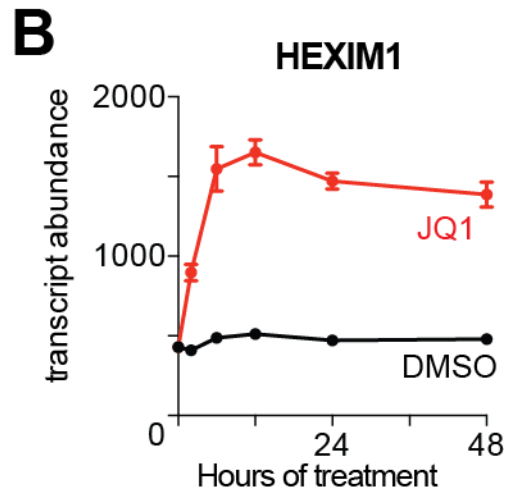
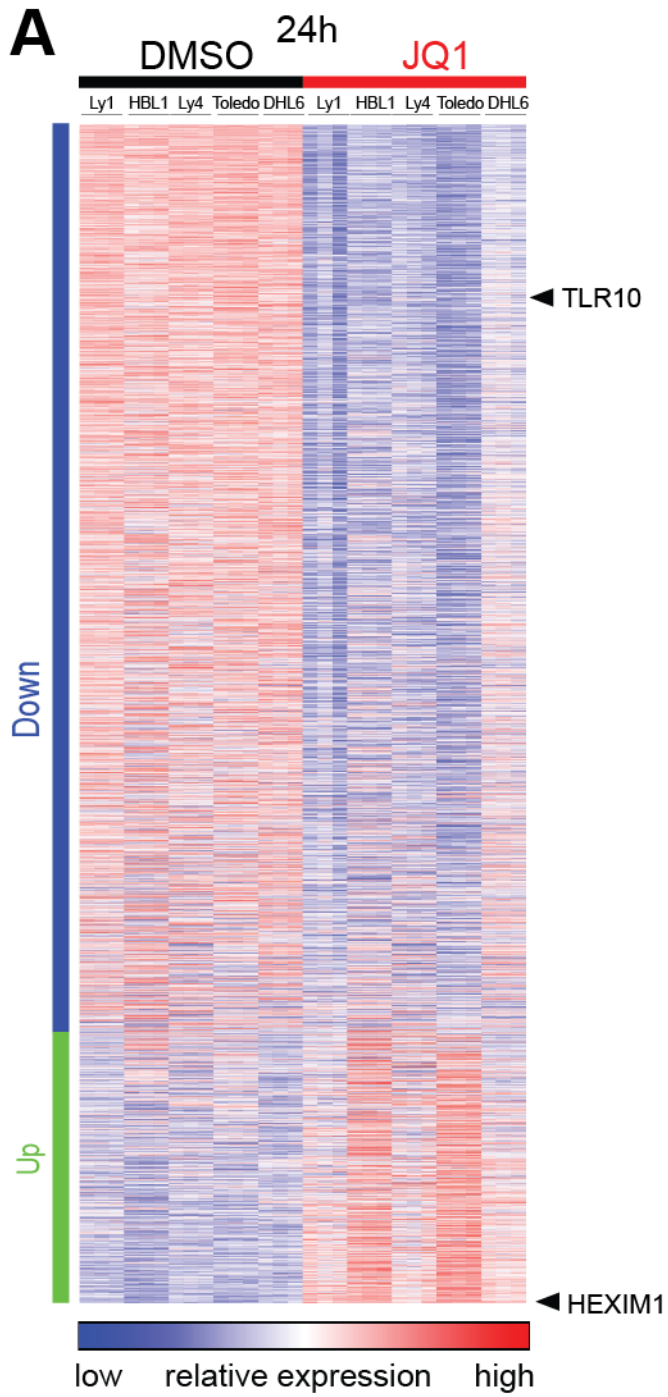


Figure 4.3 (Continued)

C

Leading edge TLR/MYD88 pathway components

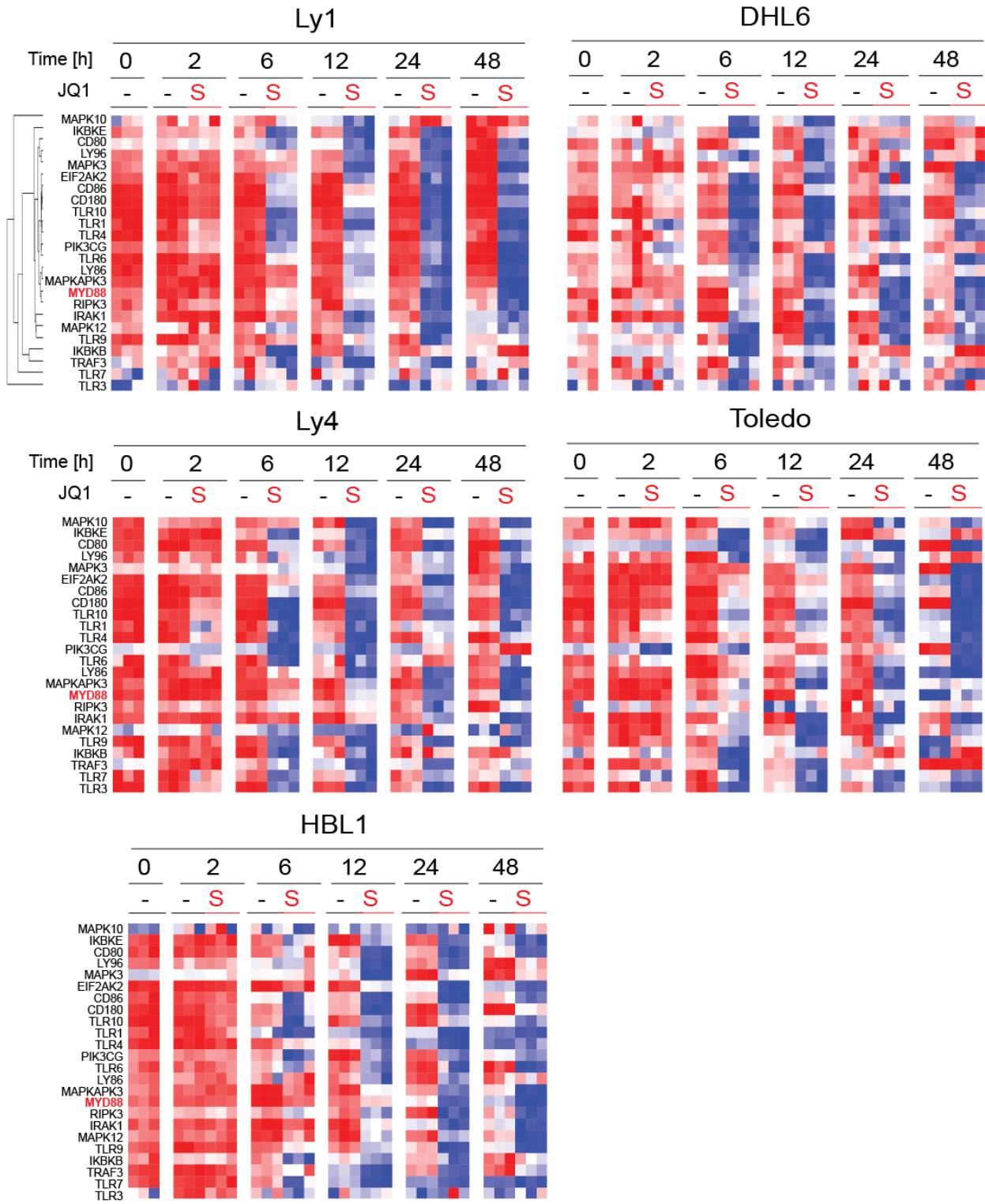


Figure 4.3 (Continued)

D

Leading edge BCR pathway components

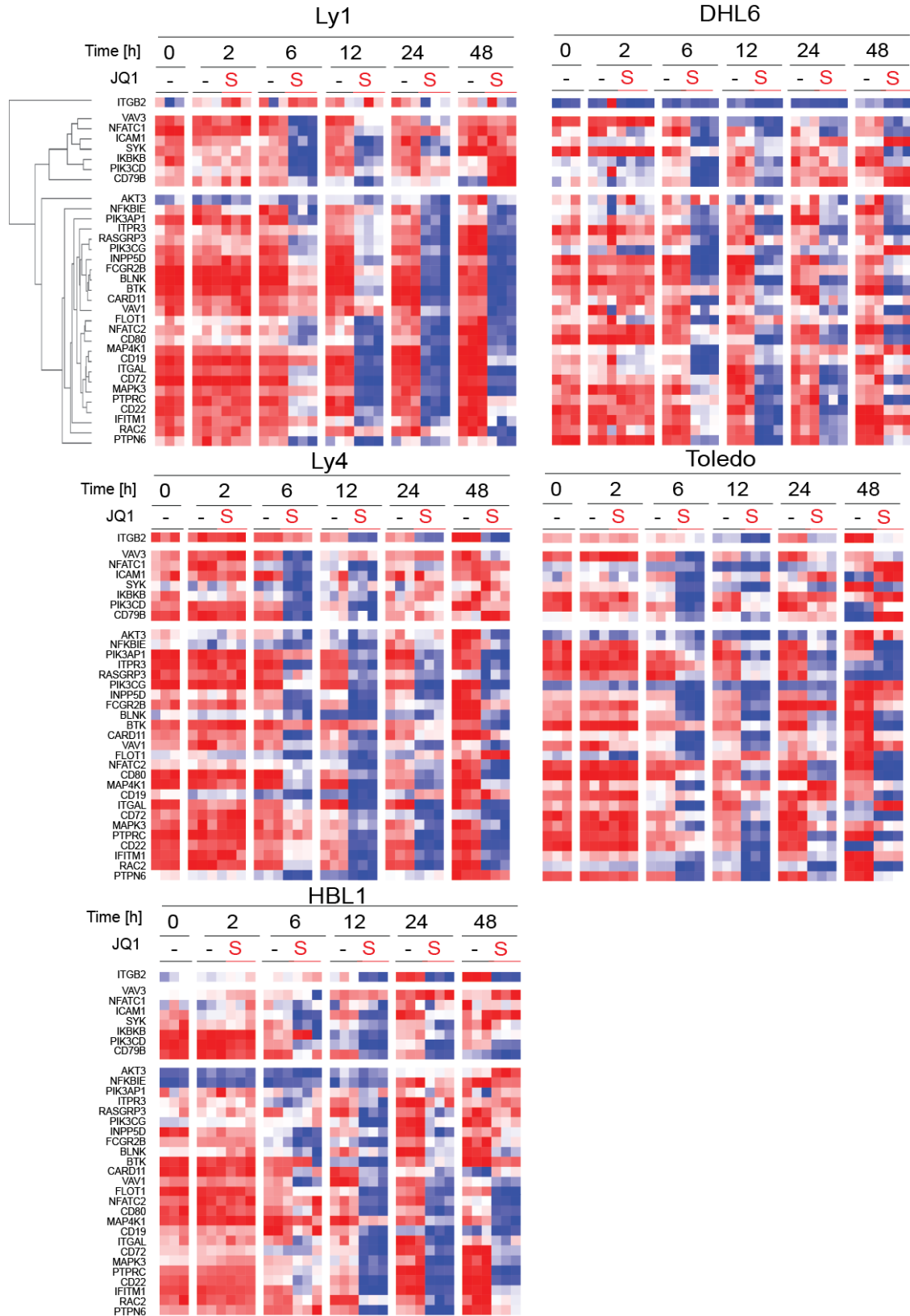


Figure 4.3 (Continued)

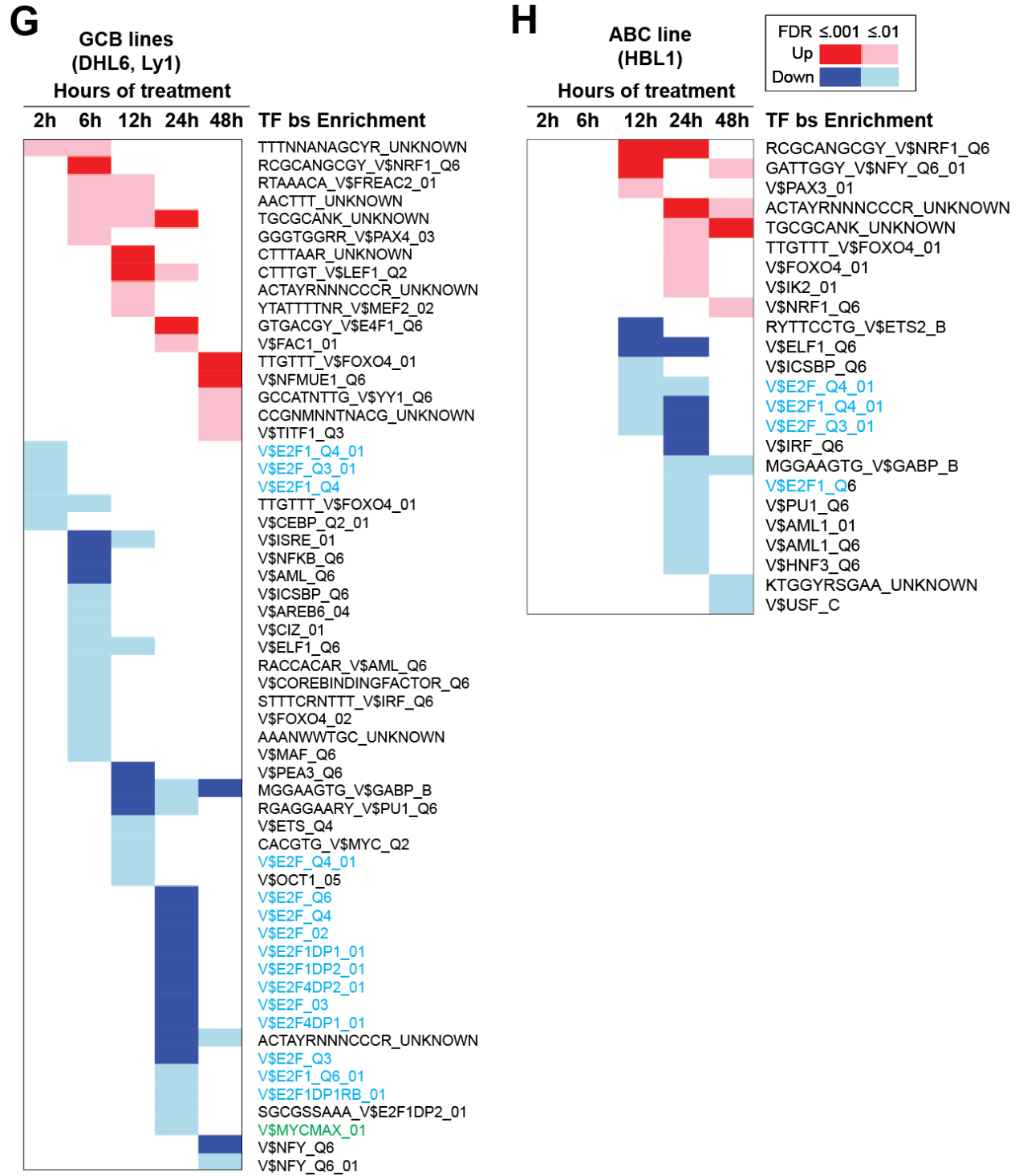


Figure 4.3 (Continued)

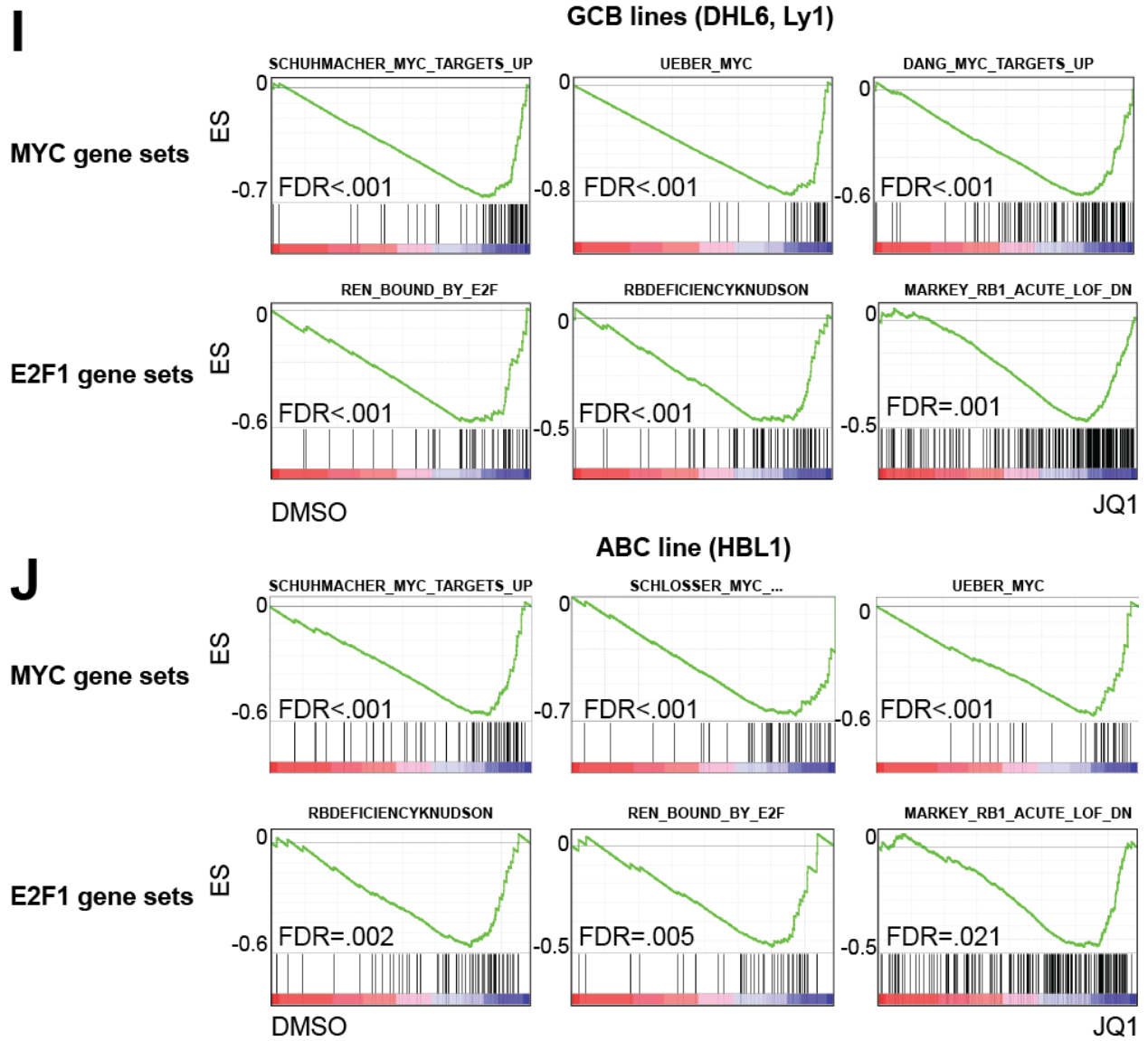
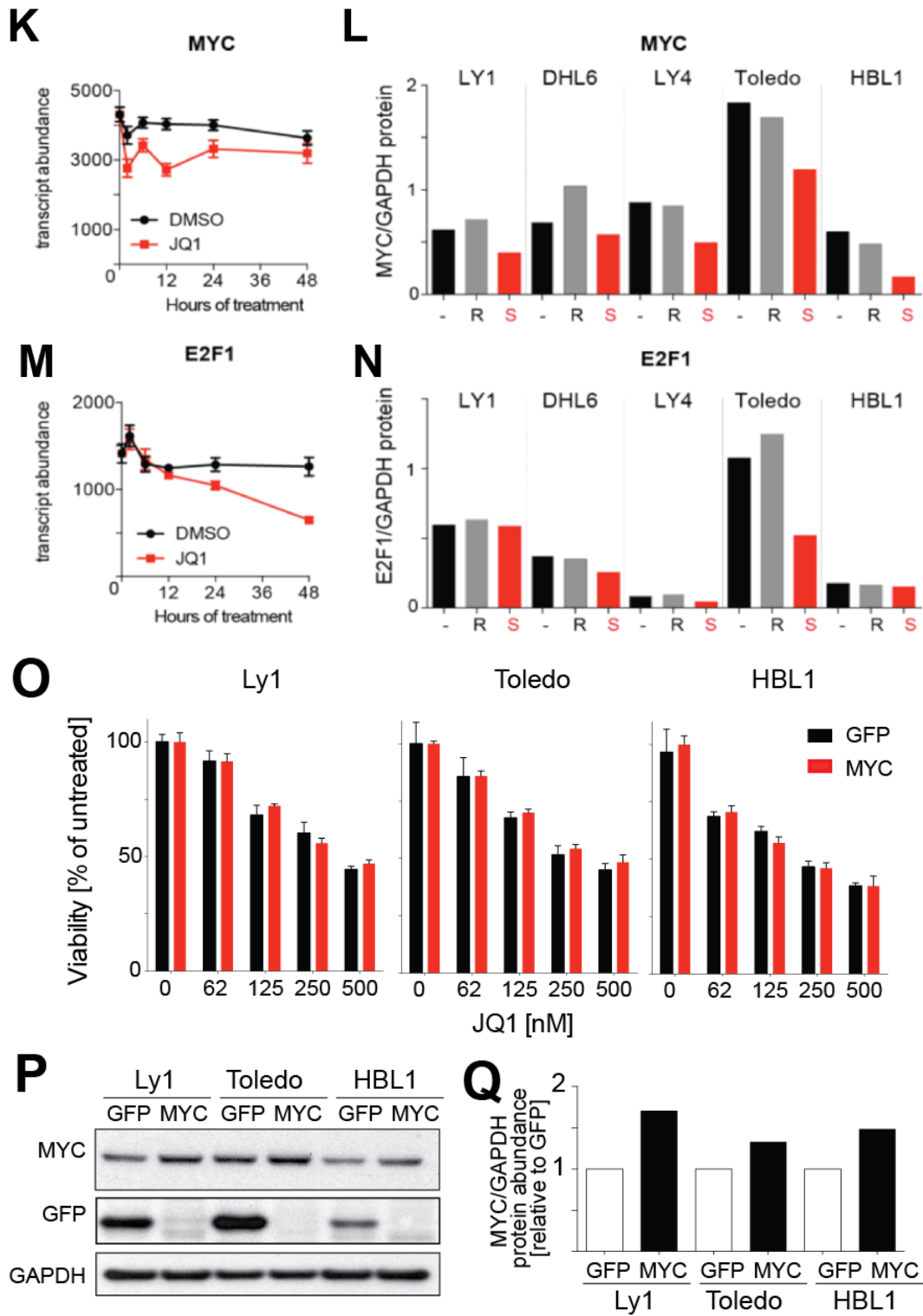


Figure 4.3 (Continued)



The most differentially expressed genes were assessed for pathway enrichment using a comprehensive pathway compendium (C2, CP; MSigDB 3.0) and each timepoint was ranked by FDR and visualized as a color-coded matrix (Figure 4.4A). We observed the early downregulation of MYD88/toll-like receptor (TLR) pathway components following JQ1 treatment, including TLR10 and MYD88 (Figure 4.3C; 4.4A-C). These data are consistent with previous studies in which the anti-inflammatory effect of BET inhibition in normal B cells was attributed to TLR pathway downregulation³⁷. In the JQ1-treated DLBCL cell lines, we also observed downregulation of multiple components of the BCR signaling pathway, E2F transcriptional targets and additional cell cycle transition gene sets (Figure 4.3D; 4.4A). Similar results were obtained when GCB and ABC DLBCL cell lines were analyzed separately (Figure 4.3E-F).

BET inhibition modulates MYC and E2F target gene transcription

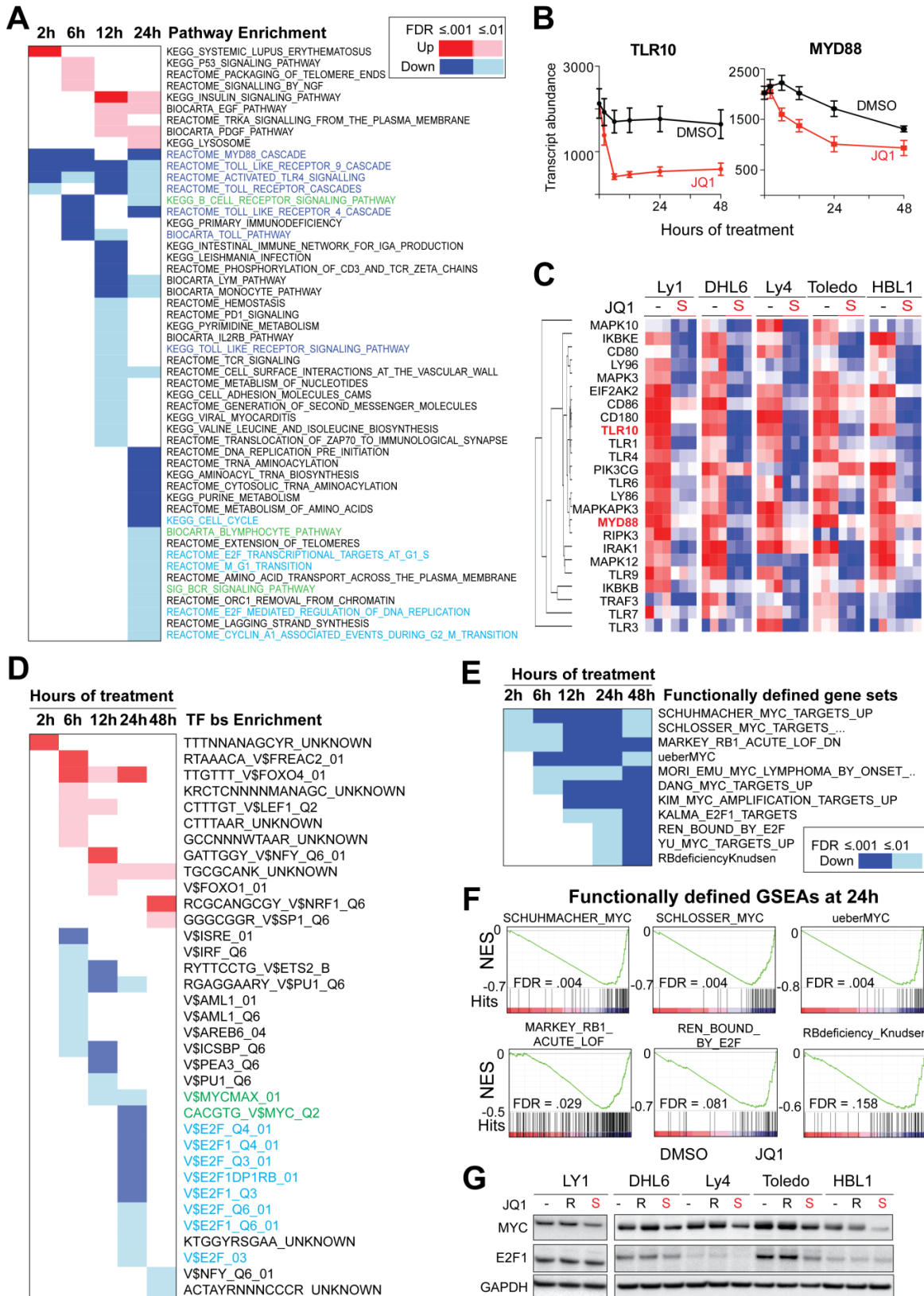
Cell state transitions are influenced by the function of specific regulatory TFs. To identify candidate TFs associated with BET bromodomain co-activators, we assessed the effects of JQ1 on sets of genes with common TF binding motifs (C3, MSigDB 3.0). The differentially expressed genes in vehicle vs. JQ1-treated DLBCL cell lines were tested for enrichment of candidate TF targets at 2 to 48 hr. Results at each timepoint were ranked by FDR and visualized as a color-coded matrix (Figure 4.4D).

Of interest, gene sets with MYC and E2F binding motifs were significantly downregulated following JQ1 treatment (Figure 4.4D). To further evaluate the effects of BET bromodomain inhibition on MYC and E2F transcriptional programs, we used

Figure 4.4: Transcriptional response to BET inhibition in representative DLBCL cell lines

(A) Hyperenrichment analysis of differentially expressed genes in all 5 lines (FDR < 0.01, FC > 1.3) following 24 hr of treatment with 500 nM JQ1 or vehicle was performed using a pathway compendium (MSigDB, C2.CP). Results at each timepoint were ranked by FDR and visualized as a color-coded matrix. Upregulated motifs in red, downregulated motifs in blue. Intensity of color correlates with FDR significance levels. Highlighted pathways included: Toll-like receptor MYD88, blue; BCR signaling, green; and Cell cycle/E2F, cyan. (B) Mean transcript abundance of TLR10 in all 5 lines (left) and MYD88 (right). (C) Heatmap of TLR pathway components in vehicle- or JQ1-treated DLBCLs (all 5 lines, 24 hr). (D) The most differentially expressed genes (FDR < 0.01, FC > 1.3) were analyzed for common transcription factor binding sites in the regulatory region using the MSigDB.C3 compendium. Results at each timepoint were ranked using a color-coded matrix as in (A). Genes with MYC binding sites in green and E2F binding sites in cyan. (E) GSEA of multiple functionally defined MYC and E2F transcription factor targets was performed. Results are reported over time in a color-coded matrix with color intensity reflecting significance level. (F) GSEA plots of functionally defined MYC and E2F target gene sets in vehicle- vs. Q1-treated cells (24 hr). (G) Protein abundance of MYC and E2F in the indicated DLBCL lines treated with vehicle or JQ1S or JQ1R (500 nm) (24 hr).

Figure 4.4 (Continued)



multiple functionally validated MYC and E2F target gene sets to perform directed pathway analyses. Following JQ1 treatment, there was highly significant early downregulation of well defined and functionally validated MYC and E2F target gene sets (Figure 4.4E-F). In complementary studies, we performed gene set enrichment analyses (GSEA) of multiple independent MYC and E2F target gene sets in vehicle versus JQ1-treated samples and found that MYC and E2F targets were significantly less abundant in JQ1-treated cells (Figure 4.3G-J; 4.4F).

BET bromodomain proteins may function as co-activators of the MYC and E2F proteins and/or direct modulators of MYC and E2F expression. To distinguish between these possibilities, we assessed the transcript abundance and protein levels of MYC and E2F in vehicle and JQ1-treated DLBCLs. BET bromodomain inhibition resulted in an apparent decrease in MYC transcripts and protein in each of the DLBCL cell lines (Figure 4.3K-L; 4.4G) suggesting that BET bromodomains directly modulate MYC transcription. In contrast, in 4 of 5 cell lines, JQ1 treatment did not measurably alter E2F1 transcript or protein abundance over 24 hrs (Figure 4.3M-N; 4.4G). These data suggest that BET bromodomains may function at regulatory elements at E2F1 target genes, rather than by influencing the abundance of E2F1 itself.

BET bromodomains as promoter-bound co-activators of E2F1-dependent transcription

The consequences of MYC downregulation following BET inhibition have been characterized by our group and others in hematologic malignancies ²⁹⁻³². However,

ectopic expression of MYC failed to rescue DLBCL cell lines from the anti-proliferative effects of JQ1 (Figure 4.3O-Q).

We next explored the role of BETs as co-activators of oncogenic E2F1. To further understand the role of BET bromodomains in oncogenic E2F transcriptional signaling, we performed chromatin immunoprecipitation with next-generation DNA sequencing (ChIP-Seq), using a chemical genetic approach. We selected Ly1 cells for mechanistic consideration owing to the robust downregulation of E2F target genes in the transcriptional profiling (Figure 4.5A) and the lack of effect of JQ1 on E2F1 protein expression (Figure 4.4G). Changes in BET localization, chromatin structure and RNA polymerase function were studied in Ly1 cells treated with JQ1 (500 nM) or vehicle control.

First, we established a chromatin landscape for Ly1 using H3K4me3 to identify promoters, H3K27ac to reveal enhancers and H3K27me3 to define repressive regions of the genome. Then, we assessed the genome-wide localization of E2F1 and the representative BET protein, BRD4, also by ChIP-seq using the respective antibodies. Rank-ordering of all transcriptionally active promoters based on H3K4me3 enrichment and RNA Pol II occupancy identifies pervasive binding of BRD4 and E2F1 to active promoter elements (Figure 6A). Analysis of enrichment data as a metagene of all active promoters centered on the transcription start site reveals spatial colocalization of E2F1 and BRD4 at all transcriptionally active promoters (Figure 4.6B).

Figure 4.5: Visualization of leading edge E2F1-target genes in all cell lines and knockdown of E2F1 in representative DLBCL cell lines.

(A) Heat map of leading edge genes from the E2F target GSEA (Figure 4.5E, top panel) in all five vehicle- or JQ1-treated DLBCL cell lines over time. See also legend of Figure 4.5. (B) Assessment of proliferation of three representative cell DLBCL cell lines (Ly1, BCR/GCB; Toledo, OxPhos/unclass.; HBL1, BCR/ABC) following lentiviral-mediated knockdown of E2F1 with two independent hairpins (shE2F1-#1 and shE2F1-#2) and a control hairpin (ev = empty vector). (C) Immunoblot of E2F1 of cells in (B) to demonstrate knockdown efficiency.

Figure 4.5 (Continued)

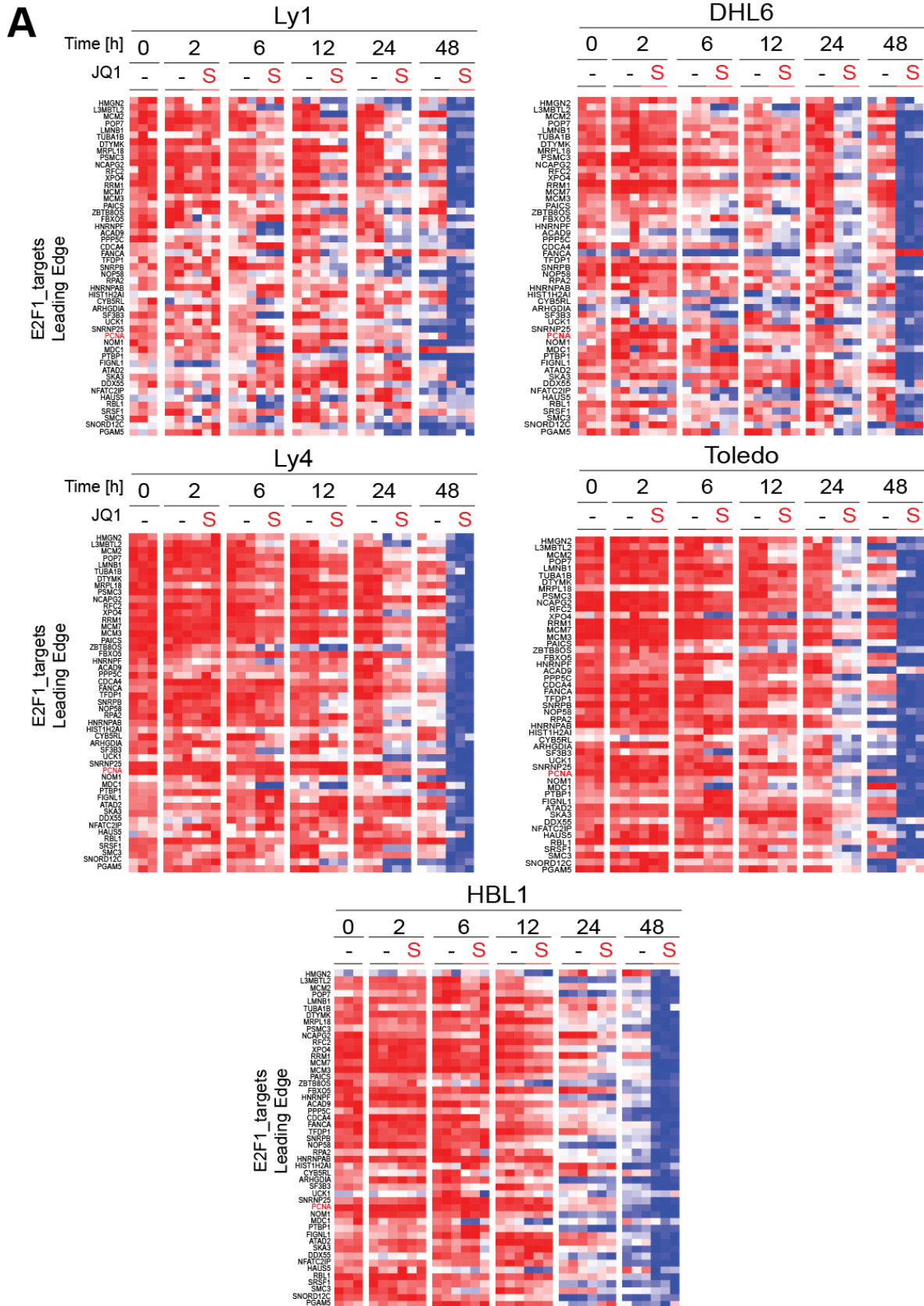
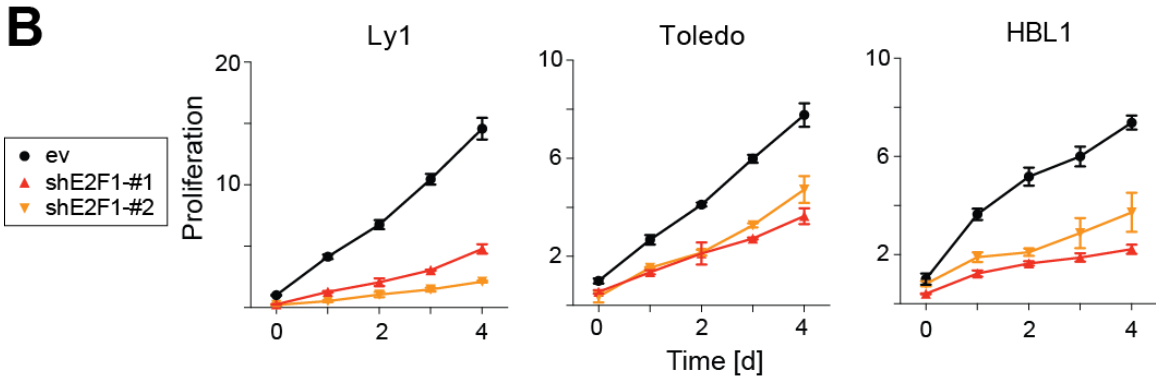


Figure 4.5 (Continued)



To understand the mechanism of BET inhibition on E2F1 target gene transcription, we assessed the effect of bromodomain inhibition on transcriptional elongation. As BRD4 is reported to recruit the positive transcription elongation factor complex (pTEFB) to prompt release of initiated but paused RNA Pol II ⁴¹, the colocalization of BRD4 and E2F1 at active promoters suggested a positive role of BRD4 in facilitating elongation at E2F1-driven genes. CHIP-Seq for E2F1 allowed the annotation of an E2F1 target gene set, based on the top promoter-bound genes in Ly1 cells. We then assessed the effect of BET inhibition on transcriptional pause release, by deriving traveling ratios for the top E2F1 target genes with or without JQ1 treatment, compared to a control gene set of non-E2F1 targets. The travel ratio is a genomewide measurement of pausing based on the gene-by-gene ratio of promoter to elongating RNA Pol II. We observed a statistically significant reduction of transcriptional elongation with JQ1 treatment, limited only to E2F1 target genes (Figure 4.6C).

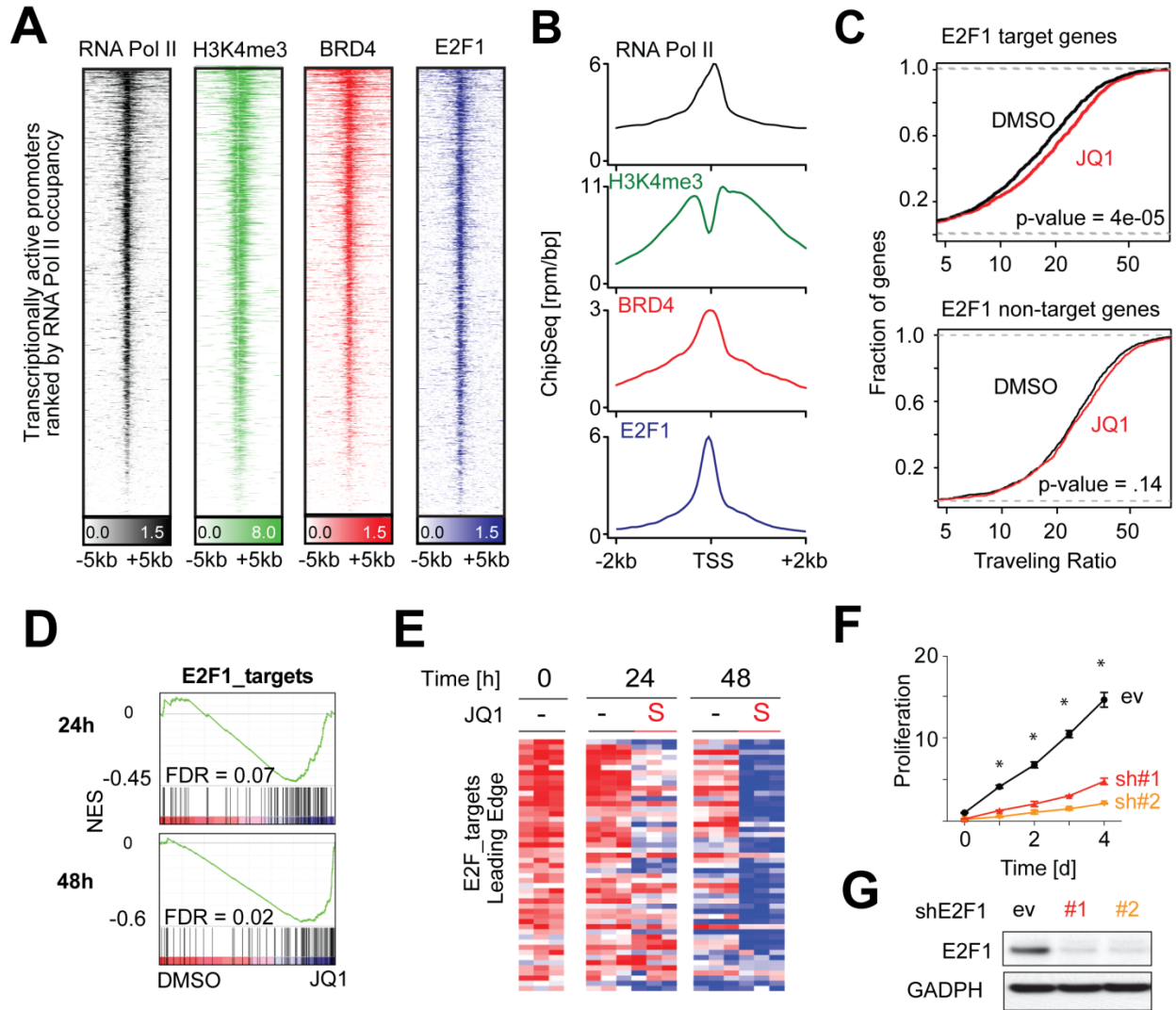
We next created a gene set of the top 100 ChIP-Seq defined E2F1 targets) and performed GSEA in Ly1 and additional DLBCL cell lines, DHL6, Ly4, Toledo, and HBL1. JQ1 treatment significantly decreased the transcript abundance of our functionally defined E2F1 targets at 24 hr and 48 hr in all cell lines studied (Figure 4.6D [GSEA] and E [heatmap]).

These data demonstrate that JQ1 treatment results in a defect in elongating RNA Pol II at E2F1 target genes, which is in agreement with the downregulation of E2F target genes (Figure 4.6D-E) and the G1 arrest (Figure 4.1B-C). In addition, these data define

Figure 4.6: Co-localization and function of BRD4 and E2F1 at active promoters

(A) Heatmap of CHIP-Seq reads for RNA Pol II (transcriptionally active; black), H3K4me3 (green), BRD4 (red), and E2F1 (blue) rank ordered from high to low RNA Pol II occupancy centered on a ± 5 kb window around the transcriptional start site (TSS) of all transcriptionally active promoters. Color density reflects enrichment; white indicates no enrichment. (B) Metagenes created from normalized genome-wide average of reads for designated factors centered on a ± 2 kb window around the TSS. Note the co-occupancy of BRD4 and E2F1 at the TSS. (C) RNA Pol II traveling ratio (TR) plots for E2F1 target genes (top panel) and non-target genes (bottom panel) following JQ1 (red) or DMSO (black) treatment. E2F1 targets and non-targets are defined by the 500 genes having the most or least E2F1 occupation at promoters. Increased TR values on x-axis indicate a higher ratio of paused promoter to elongating RNA Pol II. 24 hr of 500nM JQ1 treatment leads to statistically significant pause defects of E2F1 targets compared to non-targets. p values derived from a Welch's two-tailed *t*-test. (D) GSEA plots of a ChIP-Seq defined E2F1 target gene set in the 5 DLBCL cell lines treated with vehicle vs. JQ1 for 24 and 48 hr. (E) Heatmap of leading edge genes from the E2F target GSEA (D) in Ly1 cells treated with JQ1 or DMSO (24 hr). (F) Assessment of proliferation in Ly1 cell line following genetic depletion of E2F1 with two independent hairpins and a control hairpin (ev). Error bars represent SD, and asterisks show $p < 0.01$ by a two-sided Student's *t*-test. (G) Immunoblot of E2F1 of cells in (F) to demonstrate knockdown efficiency.

Figure 4.6 (Continued)



BRD4 functionally as an E2F1 co-activator protein in DLBCL. The E2F1 dependency of these DLBCL cell lines was previously reported¹³, but was further validated by genetic depletion in three representative cell lines (Figure 4.5B-C; 4.6F), suggesting that JQ1 disrupts the co-activator role of BETs for E2F1 signaling.

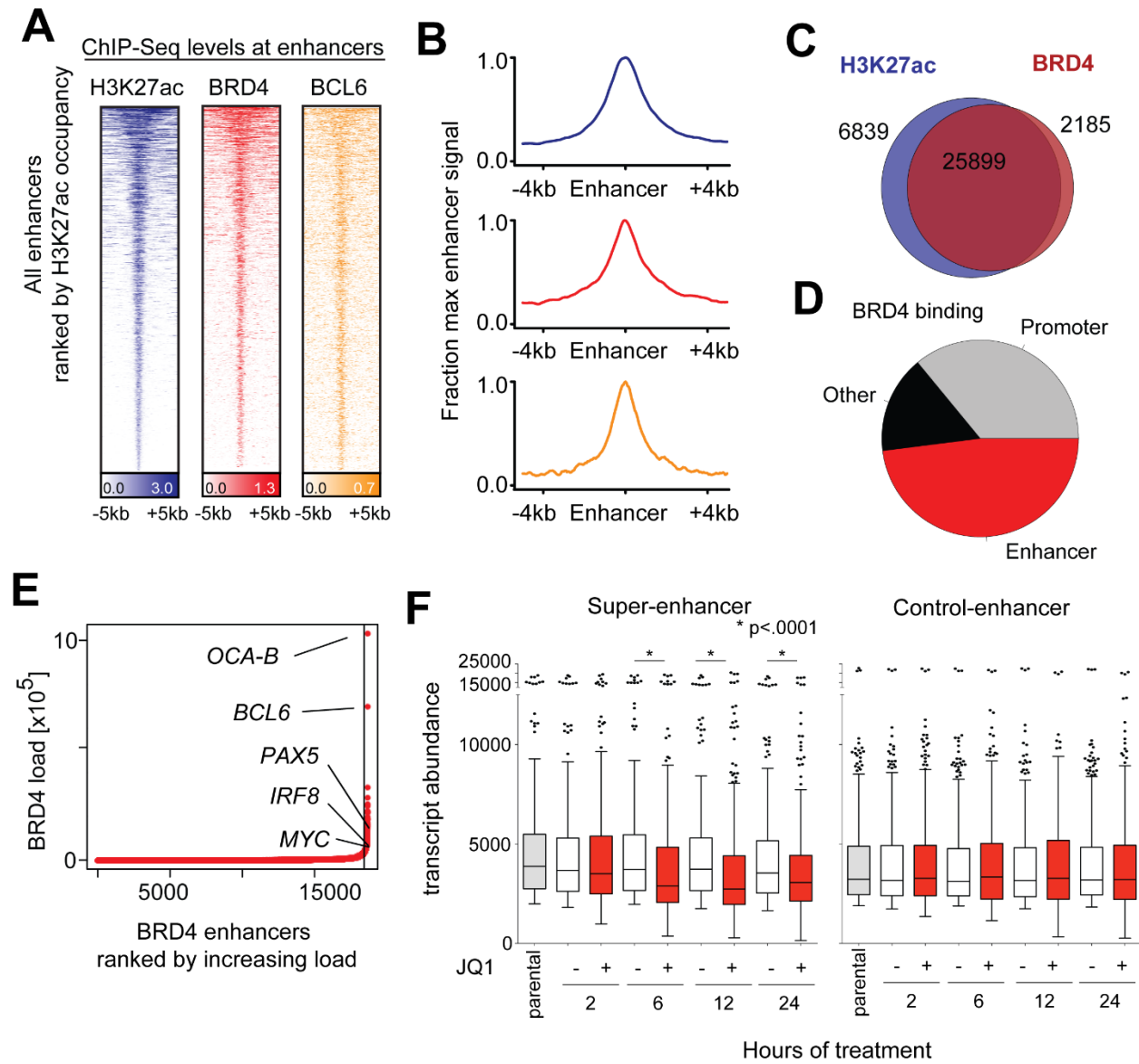
Disproportionate binding of BRD4 to overloaded enhancers

To date, studies of BET bromodomains have mainly focused on effects at promoter regions of the genome. Our research in multiple myeloma (MM) identified a role for BRD4 in enforcing MYC transcription from the translocated IgH enhancer locus³⁰. As oncogenic TFs may signal to RNA Pol II through distal enhancer elements, we sought to characterize the genome-wide localization of BRD4 to enhancers in DLBCL. Rank-ordering of enhancer regions by H3K27ac enrichment reveals that BRD4 binds to the vast majority of active enhancers in the Ly1 DLBCL genome (Figure 4.7A, blue and red tracks). Given the established role of BCL6 in the pathogenesis of DLBCL, we also documented genome-wide co-localization of BRD4 and BCL6 at H3K27ac-defined enhancers (Figure 4.7A, orange tracks). A metagene for active enhancers illustrates focal, superimposable enrichment for BRD4 with H3K27ac (Figure 4.7B). The correlation between BRD4 occupancy and H3K27 acetylation is extremely strong genome-wide, with 79.1% of H3K27ac regions containing BRD4 and 92.2% of all chromatin-bound BRD4 occurring in regions marked by H3K27ac (Figure 4.7C). Genome-wide binding data for BRD4 reveal that BRD4 is most commonly associated with enhancer regions, defined by the presence of H3K27ac and absence of H3K4me3 (Figure 4.7D).

Figure 4.7: Asymmetric BRD4 loading at enhancer elements of actively transcribed genes

(A) Heatmap of CHIP-Seq binding for H3K27ac (blue), BRD4 (red), and BCL6 (orange) rank ordered from high to low H3K27 occupancy centered on a ± 5 kb window around enhancers. Color density reflects enrichment, white indicating no enrichment. (B) Metagenes created from normalized genome-wide average of reads for designated factors centered on a ± 4 kb window around the enhancers. (C) Venn diagram of BRD4-binding and H3K27ac occupancy. 79.1% of H3K27ac regions contain BRD4 and 92.2% of all chromatin-bound BRD4 occurs within H3K27ac regions. (D) Pie chart of BRD4 binding to regions of the genome. BRD4 colocalization with H3K27ac without H3K4me3 defined as enhancer-bound (red); BRD4 colocalization with H3K4me3 reported as promoter-bound (grey); remaining genomic regions in “other” (black). (E) BRD4 loading/binding across enhancers of 18330 genes. 1.6% (285/18330) of enhancers contain 32 % of all enhancer-bound BRD4, with super-loading defined as surpassing the inflection point. Top BRD4-superloaded enhancers are indicated. (F) Mean transcript abundance of the genes associated with the 285 most and least BRD4-loaded enhancers (left and right panel, respectively) in 5 DLBCL cell lines treated with vehicle or JQ1 (2–24 hr). The p-values are obtained using a two-sided Mann-Whitney U test.

Figure 4.7 (Continued)



As predicted, BRD4 load is asymmetrically distributed throughout the genome at enhancer sites. Completely unexpected is the magnitude by which BRD4 load varies among active enhancer regions (Figure 4.7E). Only a small subset of BRD-loaded enhancers, 285/18330 (1.6%), account for 32% of all of the BRD4 enhancer binding in the cell (Figure 4.7E). The BRD4-loaded enhancers in the Ly1 DLBCL cell line are considerably larger than typical enhancer elements resembling the super-enhancers we recently described with Richard Young ².

Notably, the top two gene loci with BRD4-loaded enhancers, *POU2AF1* (which encodes the OCA-B transcriptional co-activator protein) and *BCL6* and additional genes with disproportionately BRD4-loaded enhancers, *PAX5* and *IRF8* (Figure 4.7E), are essential for B-cell fate determination and germinal center formation ^{3,14,42,43}. In fact, mice with genetic ablation of *OCA-B*, *BCL6*, *PAX5* or *IRF8* lack the ability to form germinal centers, the physiological structures from which most DLBCLs arise ⁴²⁻⁴⁶. Additionally, BRD4-superloaded enhancers are found adjacent to known oncogenes relevant to DLBCL biology, such as *CD79B* and *MYC* (Figure 4.8A-B).

Therefore, BRD4 is predominantly an enhancer-associated factor which distributes throughout DLBCL euchromatin in a highly asymmetric manner, adjacent to known oncogenes and lineage-specific transcription factors (Figure 4.7E). BET bromodomain inhibition selectively decreased the transcript abundance of the 285 genes with the most BRD4-loaded super enhancers, in contrast to the 285 genes with

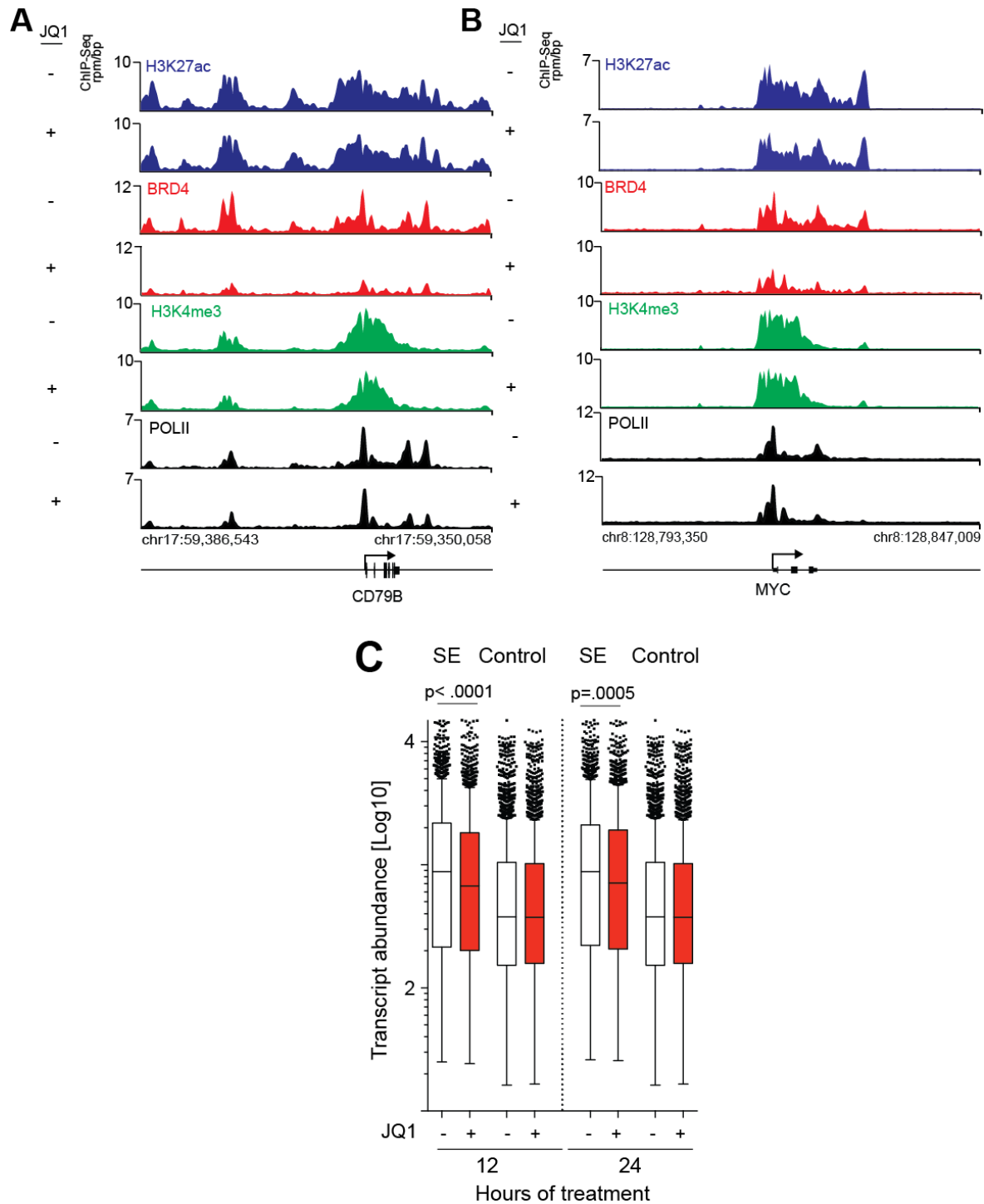


Figure 4.8: Modulation of BRD4 loading at *CD79B* and *MYC* enhancers following JQ1 treatment. ChIP-Seq binding density for H3K27ac (blue), and BRD4 (red) at the enhancer of *CD79B* (A) and *MYC* (B) with JQ1 (+) or DMSO (-). JQ1 treatment significantly reduced BRD4 occupancy at the enhancer element of both genes. ChIP-Seq reads at both gene promoters for RNA Pol II (black) and H3K4me3 (green) following JQ1 (+) or DMSO (-) treatment. (C) Mean transcript abundance of the genes associated with all most and least H3K27ac-loaded enhancers in Ly1 treated with vehicle or JQ1 (12 and 24 hr). The p values are obtained using a two-sided Mann-Whitney U test. See also Tab. S4, Fig. S4 and Tab. 4.

the least BRD4-loaded enhancers (Figure 4.7F). Similar results were obtained using H3K27ac as a surrogate enhancer mark (Figure 4.8C). Taken together, these data strongly suggest that BRD4 loading of select DLBCL enhancers determines the magnitude of the transcriptional effect of BET inhibition.

JQ1 targets the *POU2AF1* super enhancer and decreases OCA-B expression and activity

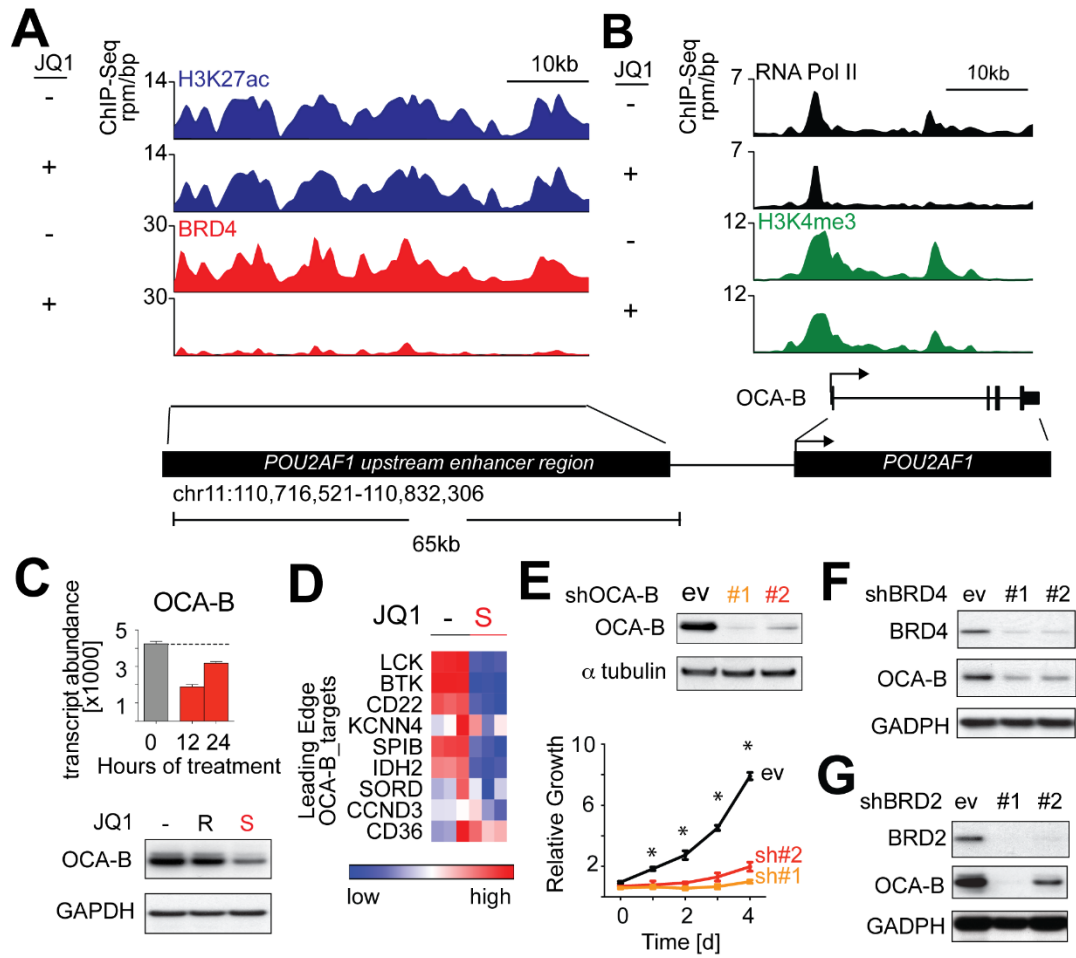
The *POU2AF1* locus emerged as the most BRD4-overloaded enhancer in the Ly1 DLBCL (Figure 4.7E), prompting further analysis of the effect of BET inhibition on OCA-B expression and function. OCA-B is a gene regulatory factor that interacts with the OCT1 and OCT2 TFs at octamer motifs and regulates B-cell development, maturation and GC formation⁴². Although OCA-B is expressed throughout B-cell development, it is most abundant in normal GC B cells and GC-derived tumors including DLBCL⁴⁷. *OCA-B* has a large H3K27ac-defined enhancer, with strong BRD4 binding that is abolished by JQ1 treatment (Figure 4.9A). Consistent with this observation, BET inhibition reduced RNA Pol II elongation of *OCA-B*, with a concomitant increase in promoter-paused RNA Pol II near the transcriptional start site (TSS; Figure 4.9B). JQ1 treatment (500 nM) also decreased OCA-B transcript abundance and protein expression in Ly1 (Figure 4.9C), as well as additional DLBCL cell lines (Figure 4.10A).

We next assessed the consequences of JQ1 treatment on the OCA-B transcriptional program by performing GSEA with a well-defined series of OCA-B target genes⁴². OCA-B targets were significantly less abundant in JQ1-treated

Figure 4.9: Modulation of BRD4 super-loading at the *POU2AF1* locus following JQ1 treatment

(A) ChIP-seq binding density for H3K27ac (blue), and BRD4 (red) at the enhancer of *POU2AF1* with JQ1 (+) or vehicle (DMSO) (-). JQ1 treatment significantly reduced BRD4 occupancy at the upstream enhancer element of *POU2AF1*. (B) ChIP-seq reads at the *POU2AF1* promoter for RNA Pol II (black) and H3K4me3 (green) following JQ1 (+) and DMSO (-) treatment. RNA Pol II showed increased pausing following JQ1 treatment. (C) OCA-B transcript and protein abundance in Ly1 cells treated with vehicle or 500 nM JQ1 or JQ1R (24 hr). (D) OCA-B-target genes (leading edge, OCA-B GSEA) in Ly1 cells treated with vehicle or 500 nM JQ1 (500 nM) are visualized as heatmap. (E) Knockdown efficacy of two independent shRNAs against OCA-B was detected by western blot (top panel). Proliferation of OCA-B-depleted cells was measured by alamar blue. The p values for NC vs. each OCA-B shRNA were delineated by two-sided Student's t-test; asterisks show $p < 0.01$. Knockdown efficiency of two independent shRNAs against BRD4 (F) or BRD2 (G) and the associated changes in OCA-B expression were evaluated by western blot.

Figure 4.9 (Continued)



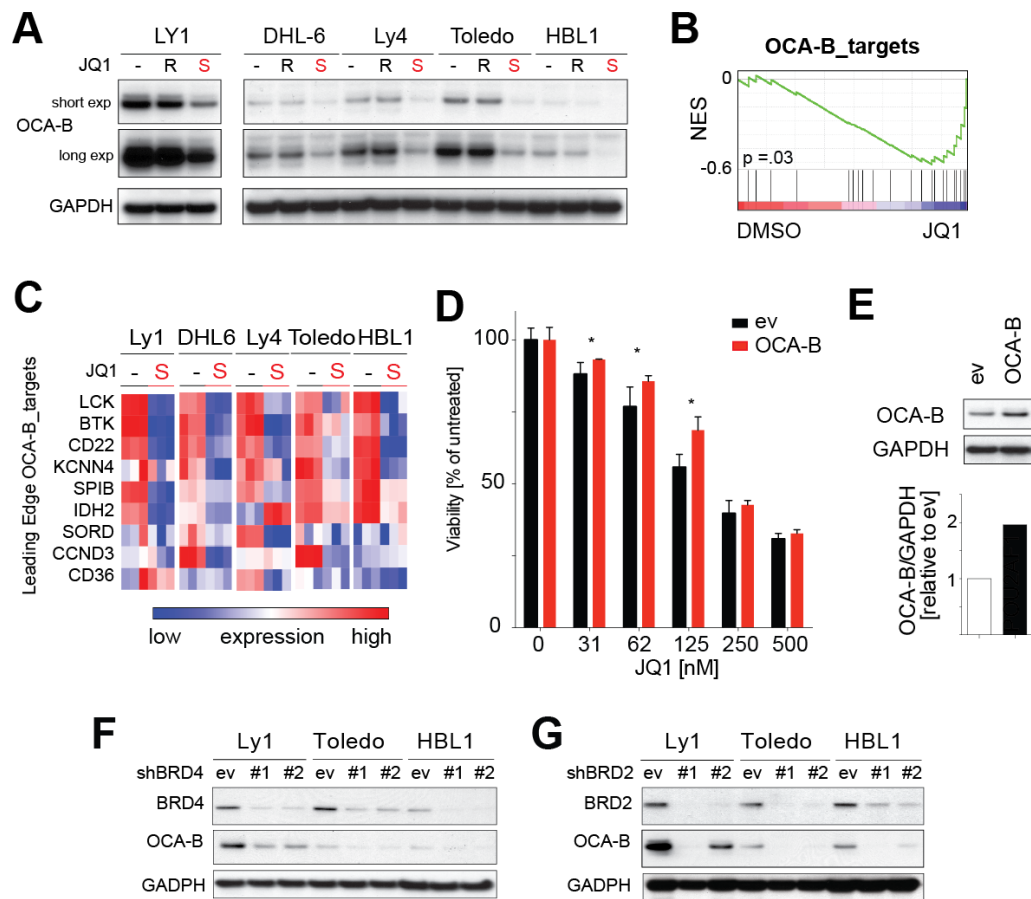


Figure 4.10: OCA-B abundance and target genes in DLBCL cell lines treated with JQ1.

(A) OCA-B protein abundance in each of the 5 DLBCL cell lines treated with vehicle or 500nM JQ1 or JQ1R (24 hr). (B) GSEA plot of a curated list of OCA-B targets in all 5 DLBCL cell lines treated with vehicle (DMSO) or JQ1 (24 hr). (C) Heat map of the OCA-B target genes (leading edge, OCA-B GSEA) in each of the DLBCL cell lines treated with vehicle or JQ1 (24 hr). (D) Enforced expression of OCA-B or control (ev=empty vector) in the pMIG expression vector resulted in a partial proliferative advantage for the OCA-B expressed cells at lower JQ1 concentrations following 72hr of JQ1 exposure. (E) Immunoblot for OCA-B after enforced expression (upper panel) and its quantification with ImageJ (lower panel). (F) Immunoblot of BRD4, OCA-B and GAPDH after genetic depletion of BRD4 with two independent hairpins (shBRD4-#1 and shBRD4-#2) and a control (ev=empty vector) in three representative DLBCL cell lines. (G) Western blot of BRD2, OCA-B and GAPDH after knockdown of BRD2 with two independent hairpins (shBRD4-#1 and shBRD4-#2) and a control (ev=empty vector).

DLBCLs as illustrated in Ly1 (Figure 4.9D) and the full DLBCL panel (Figure 4.10B-C). OCA-B depletion with two independent shRNAs significantly decreased the proliferation of Ly1 (Figure 4.9E), and enforced expression of OCA-B partially rescued the JQ1-mediated anti-proliferative effects (Figure 4.10D-E). Of note, genetic depletion of BRD2 or BRD4 (Figure 4.9F-G; 4.10F-G) phenocopied the JQ1-mediated reduction of OCA-B, indicating that BET inhibition acts partially via SE disruption.

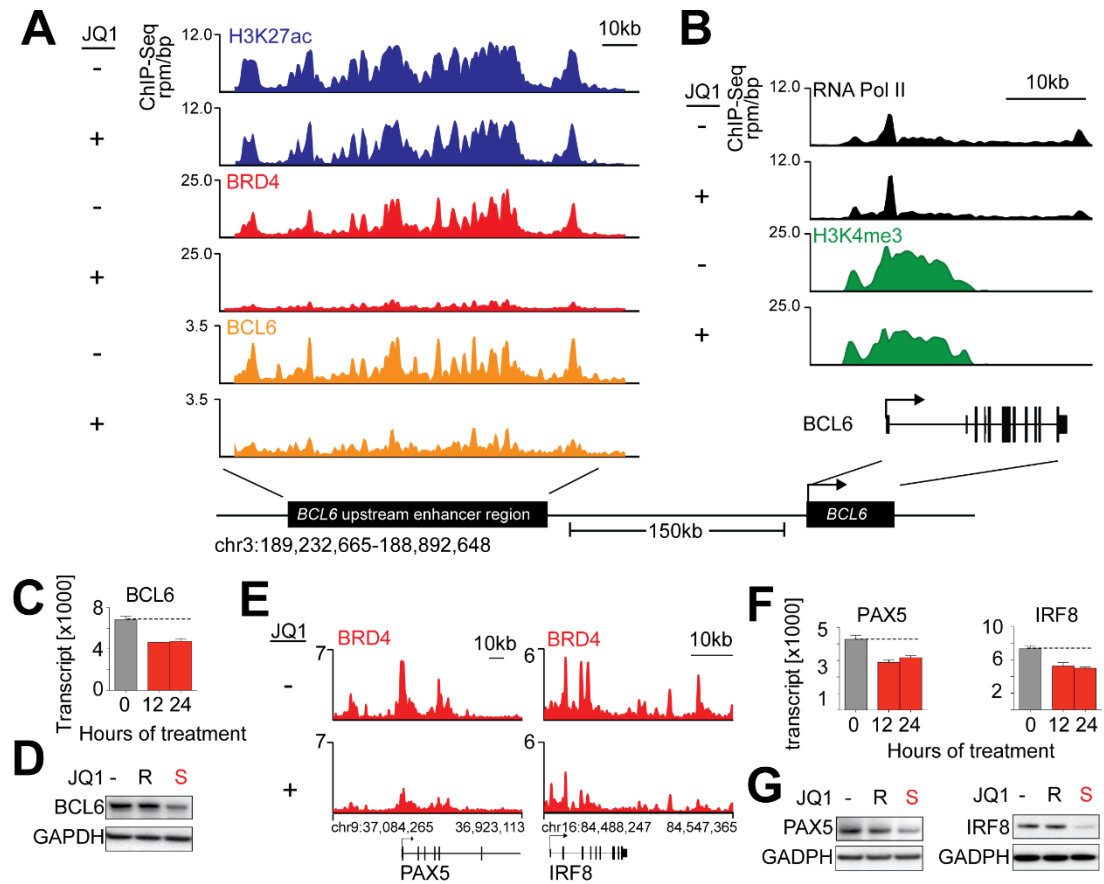
JQ1 targets the super enhancers of additional critical B-cell TFs and modulates the GC program

Three of the master regulatory TFs with BRD4-loaded super enhancers (*BCL6*, *IRF8* and *PAX5*), promote and maintain the B-cell gene expression program and limit differentiation into antibody-secreting plasma cells ⁴⁴. For these reasons, we further assessed the functional consequences of BET inhibition on the critical B-cell TFs with BRD4-loaded super enhancers.

Given the known oncogenic function of deregulated BCL6 in GC B-cells ¹⁴ and the sensitivity of certain DLBCLs to BCL6 depletion ⁴⁸, we first evaluated the consequences of BET inhibition on BCL6 expression and function. The *BCL6* locus includes a large previously defined upstream enhancer ⁴⁹ that is severely depleted of BRD4 upon JQ1 treatment (Figure 4.11A). Consistent with depletion of BRD4 from the *BCL6* enhancer, the promoter also shows increased RNA Pol II pausing and reduced elongating RNA Pol II (Figure 4.11B).

Figure 4.11: Modulation of super-enhancers of B-cell transcription factors following JQ1 treatment
(A) CHIP-Seq binding density for H3K27ac (blue), BRD4 (red), and BCL6 (orange) at the *BCL6* enhancer following JQ1 (+) or DMSO (-) treatment. JQ1 treatment significantly reduced BRD4 and BCL6 occupancy at the upstream enhancer element of *BCL6*. (B) ChIP-Seq reads at the *BCL6* promoter for RNA Pol II (black) and H3K4me3 (green) following JQ1 (+) and DMSO (-) treatment. RNA Pol II showed increased pausing following JQ1 treatment. (C) *BCL6* transcript abundance in Ly1 cells 12 and 24 hr following vehicle or JQ1 treatment (derived from GEP data). (D) *BCL6* protein abundance following treatment with vehicle or JQ1 or JQ1R (500 nM) (24 hr). (E) CHIP-Seq density of BRD4 (red) at super enhancers of the two additional B-cell TFs, *PAX5* and *IRF8*, following treatment with JQ1 (+) or DMSO (-). (F and G) *PAX5* and *IRF8* transcript (F) and protein abundance (G) in Ly1 cells following JQ1 treatment.

Figure 4.11 (Continued)



As BCL6 is known to bind its own enhancer, we used BCL6 localization by ChIP-Seq to explore the influence of BET inhibition on TF binding to this enhancer region. JQ1 treatment caused a marked reduction of BCL6 binding, demonstrating that BRD4 loss leads to diminished TF loading, enhancer accessibility, and BCL6 protein level (Figure 4.11A-B). In an independent ChIP-qPCR experiment, we confirmed that BET inhibition decreased TF loading at the BCL6 enhancer (Figure 4.12A). Consistent with these findings, JQ1 treatment markedly decreased *BCL6* transcript abundance and protein expression in Ly1 (Figure 4.11C-D), and additional DLBCL lines (Figure 4.12B). Similarly, *PAX5* and *IRF8* also have BRD4-loaded super enhancers that are severely depleted of BRD4 following JQ1 treatment (Figure 4.11E). BET inhibition also decreased *PAX5* and *IRF8* transcript abundance and protein expression (Figure 4.11F-G).

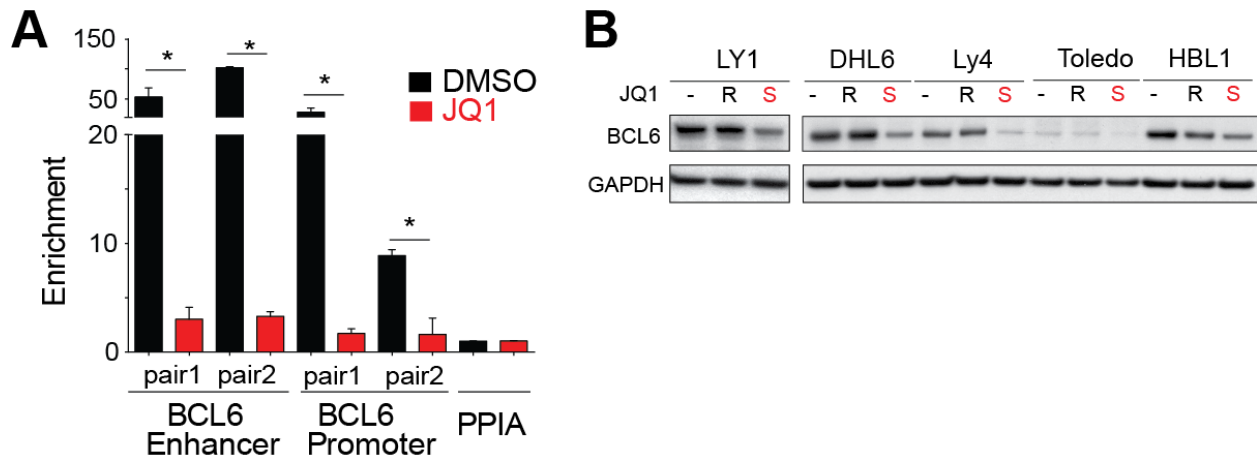


Figure 4.12: JQ1 effect on the *BCL6* locus, *BCL6* protein abundance and the germinal center B-cell signature

(A) ChIP-qPCR shows JQ1-mediated BRD4 depletion at the *BCL6* enhancer and promoter. Asterisks indicate statistically significant differences by two-sided Student's t-test with Welch's correction at a p-value <.05. PPIA serves as control. (B) *BCL6* protein abundance in DLBCL cell lines treated with vehicle or 500nM JQ1R vs. JQ1S (24 hr). GAPDH loading control.

Super enhancers define developmentally regulated TF in DLBCL cell lines and primary tumors

Using the robust H3K27ac mark to identify and discriminate super enhancers, we conducted ChIP-Seq SE analysis on five additional human DLBCL lines (DHL6, BCR/GCB; HBL1 and Ly3, BCR/ABC; Toledo and Ly4, OxPhos/Unclass) and a normal lymphoid sample (tonsil). Asymmetric enhancer loading was detected in all of the DLBCL cell lines (Figure 4.13A-C) and the normal tonsil (Figure 4.13D), confirming the ubiquitous nature of this epigenomic structural element.

In all of the DLBCL cell lines and normal tonsil, large SEs were identified adjacent to master TFs such as *PAX5*, *OCA-B*, and *IRF8* (Figure 13A-D; 13E-F, tracks and 4.14A) that maintain the B-cell program and limit plasma cell differentiation. Given the critical role of these master regulatory TFs in maintaining GC integrity and limiting GC exit⁴⁴, we assessed the consequences of BET inhibition on the GC program. To that end, we used a publically available compendium of GEPs of highly purified human B-cell subsets and defined a set of genes that are significantly more abundant in GC centrocytes and centroblasts than in post-GC plasma cells (Up_in_GCB_vs_PC). Using GSEA, we confirmed that the GC developmental program was downregulated in Ly1 and in all 5 DLBCL cell lines following JQ1 treatment (Figure 4.13G [GSEA]; 4.13H [Heatmap] and 4.14B).

Figure 4.13: Analysis of super enhancers in additional DLBCL cell lines and normal lymphoid tissue. (A-D) Rank order of increasing integrated H3K27ac fold enrichment at enhancer loci in DLBCL cell lines, GCB (A), ABC (B) unclassified (C) and normal tonsil (D). (E) H3K27ac ChIP-Seq fold enrichment at the *POU2AF1* locus showing the super-enhancer region. (F) H3K27ac ChIP-Seq reads at *IRF4* locus in the 2 GCB and 2 ABC cell lines. (G) GSEA plot of the “Up in GCB_vs_PC” signature in 5 DLBCL cell lines following JQ1 treatment. (H) The leading edge genes of the GSEA in (G) were visualized as heatmap. (I) Similarity matrix from unsupervised hierarchical clustering of each cell line by location of super-enhancers.

Figure 4.13 (Continued)

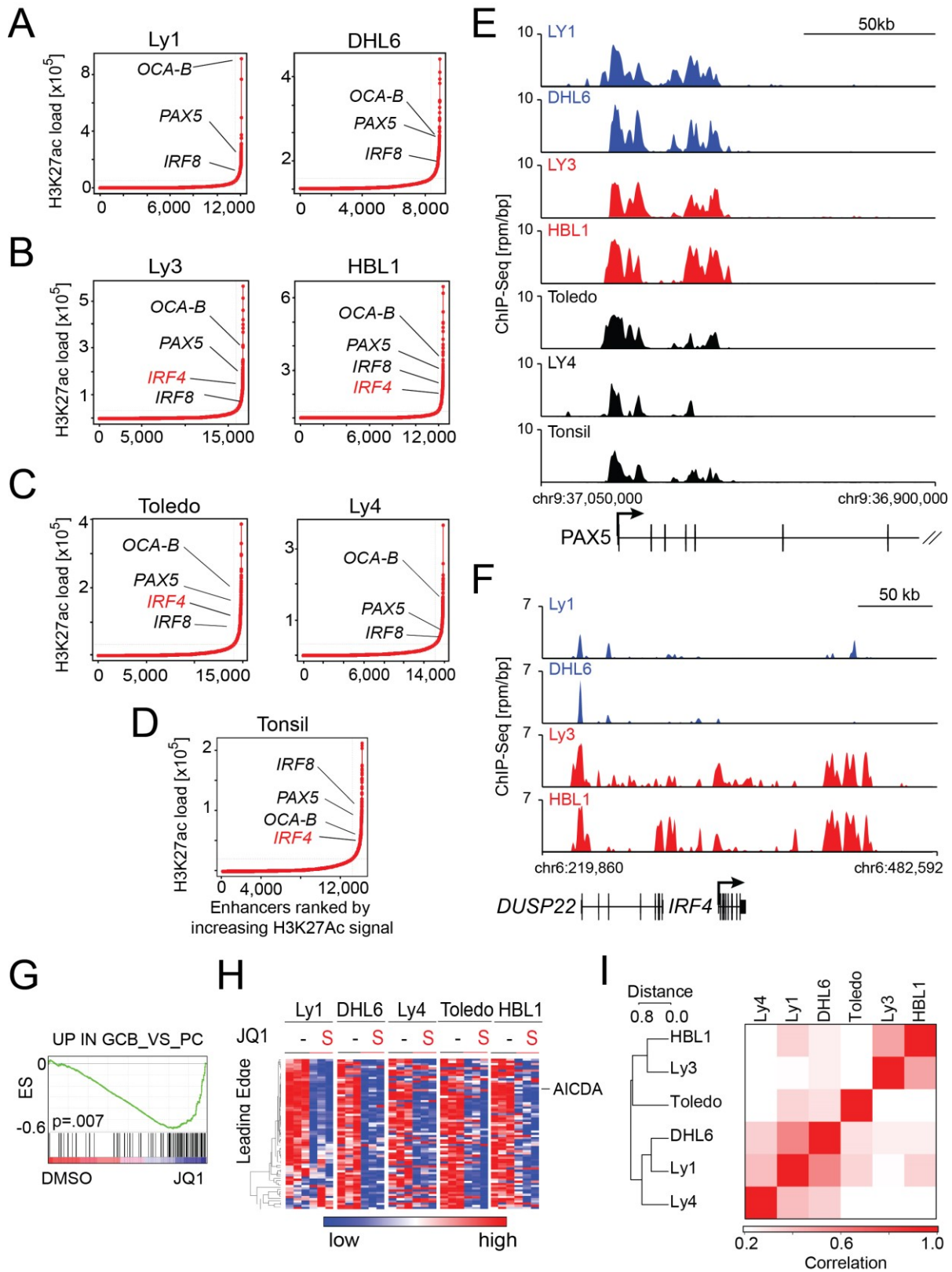
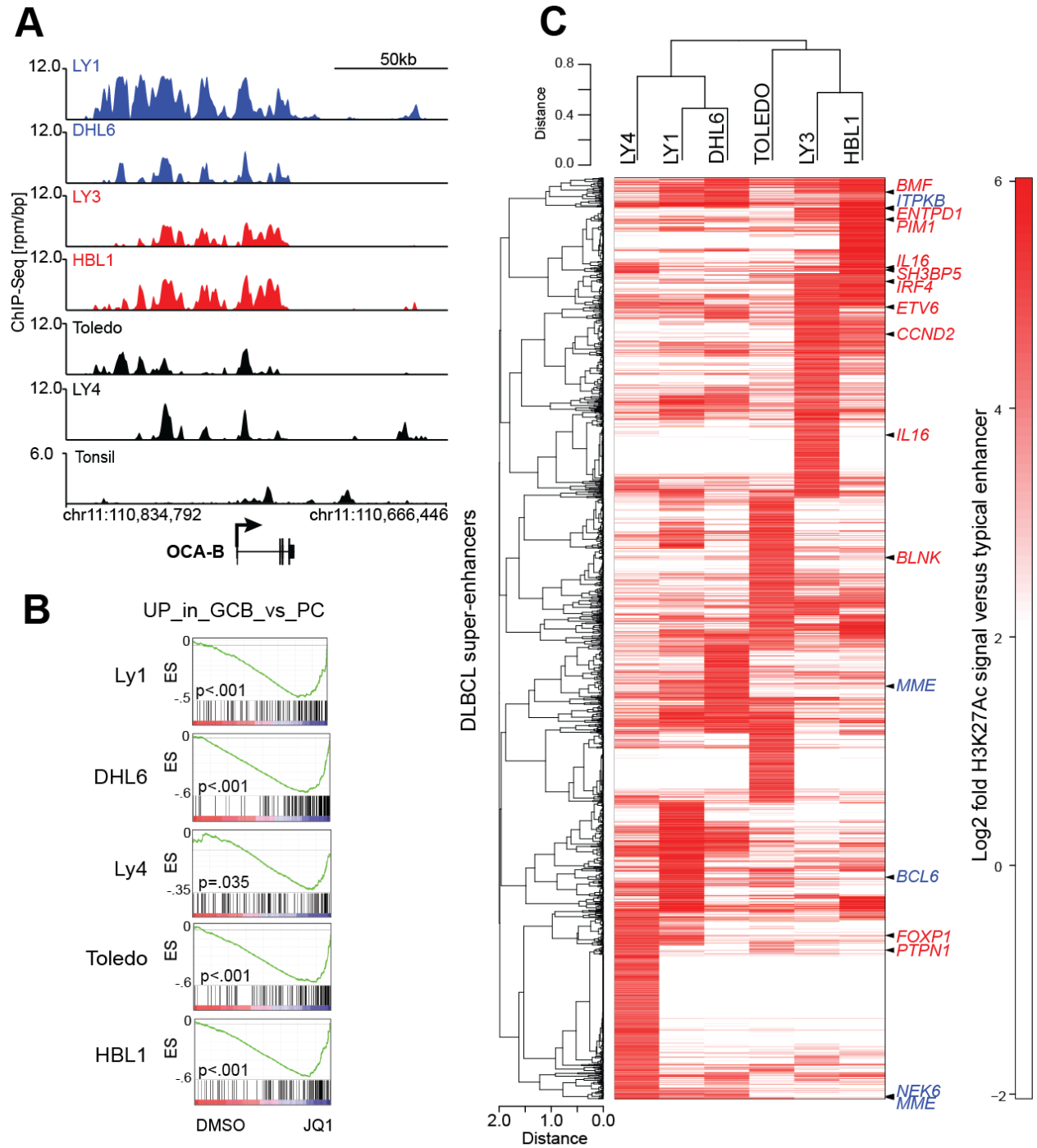


Figure 4.14: H3K27ac tracks of *POU2AF1* locus, GSEA plots of germinal center B-cell signature in individual cell lines and unsupervised hierarchical clustering of super-enhancers in DLBCL cell lines. (A) Tracks of the H3K27ac mark for the *POU2AF1* locus in indicated cell lines and a human tonsil. (B) GSEA plots of germinal center B-cell signature “Up_in_GC_vs_PC” in each of the DLBCL cell lines treated with vehicle vs. JQ1 (24 hr). (C) Unsupervised hierarchical clustering of super-enhancer loci in DLBCL cell lines. Magnitudes indicate the log 2 fold H3K27ac signal to typical enhancers. Genes within a 50kb range of the assigned super-enhancers loci comprising the Wright classifier ⁵⁰ are indicated with an arrowhead. Gene annotations are color coded with GCB, blue, and ABC, red.

Figure 4.14 (Continued)



We next asked whether genes that were differentially expressed in the developmentally defined COO subtypes had adjacent SEs (Figure 4.14C). In the ABC DLBCL cell lines, but not the GCB lines, the subtype-specific TF locus, *IRF4*, had an adjacent SE (Figure 4.13A-B and F). The *IRF4* SE was also detected in normal tonsil suggesting that it represented a developmental epigenetic mark rather than a tumor-specific feature. Additional genes associated with the developmental ABC signature, including *PIM1* and *CCND2*, had adjacent SE in ABC, but not GCB, cell lines (Figure 4.14C). Consistent with this finding, unsupervised bidirectional hierarchical clustering of the DLBCL cell lines by SEs distinguished the ABC from GCB lines (Figure 4.13I and 4.14C).

To evaluate the clinical significance of these findings, we performed ChIP-Seq and SE analysis on 4 primary DLBCLs that were previously subtyped as either GCB or ABC¹³. All primary DLBCLs exhibited the same characteristic asymmetry in H3K27ac enrichment, with readily identified regions consistent with SEs (Figure 4.15A-B). Again, SEs were found adjacent to lineage-specific TFs, such as *PAX5*, and subtype-associated TFs, such as *IRF4* (Figure 4.15A-B, tracks in Figure 4.15C-D). Notably, primary samples could also be clustered by SEs reflecting transcriptional developmental distinctions (Figure 4.15E).

Figure 4.15: Analysis of super enhancers in primary DLBCLs

(A and B) Rank order of increased H3K27ac fold enrichment at enhancer loci in primary DLBCLs (GCB#1 and #2 (A); ABC#1 and #2 (B)). (C) Gene tracks showing H3K27ac enrichment at the *PAX5* locus in all 4 primary DLBCLs. (D) Tracks as in (C) comparing the H3K27 enrichment at the *IRF4* locus in primary GCB vs. ABC DLBCLs. (F) Unsupervised hierarchical clustering of primary DLBCLs using the genomic location of all super-enhancers.

Figure 4.15 (Continued)

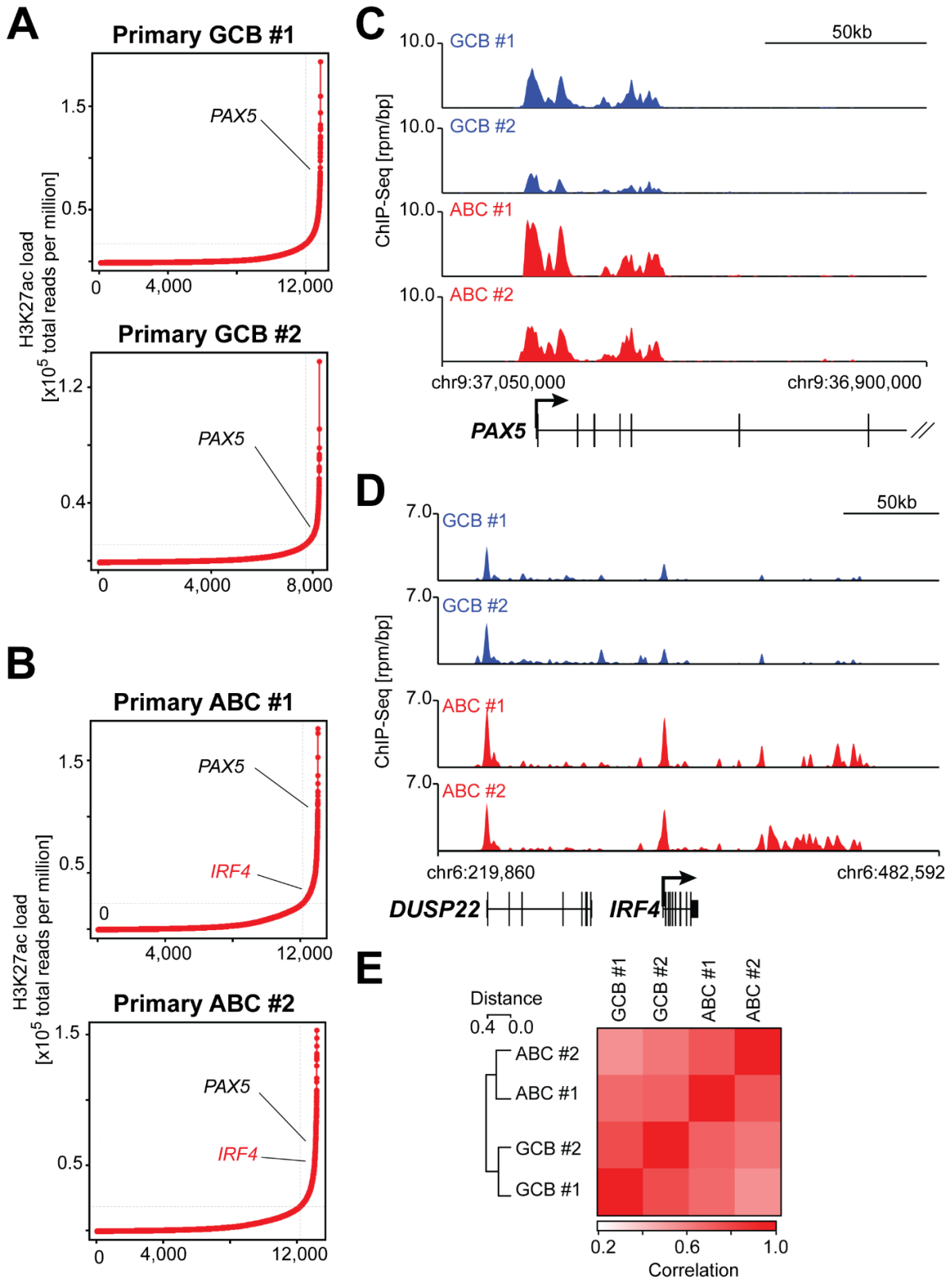
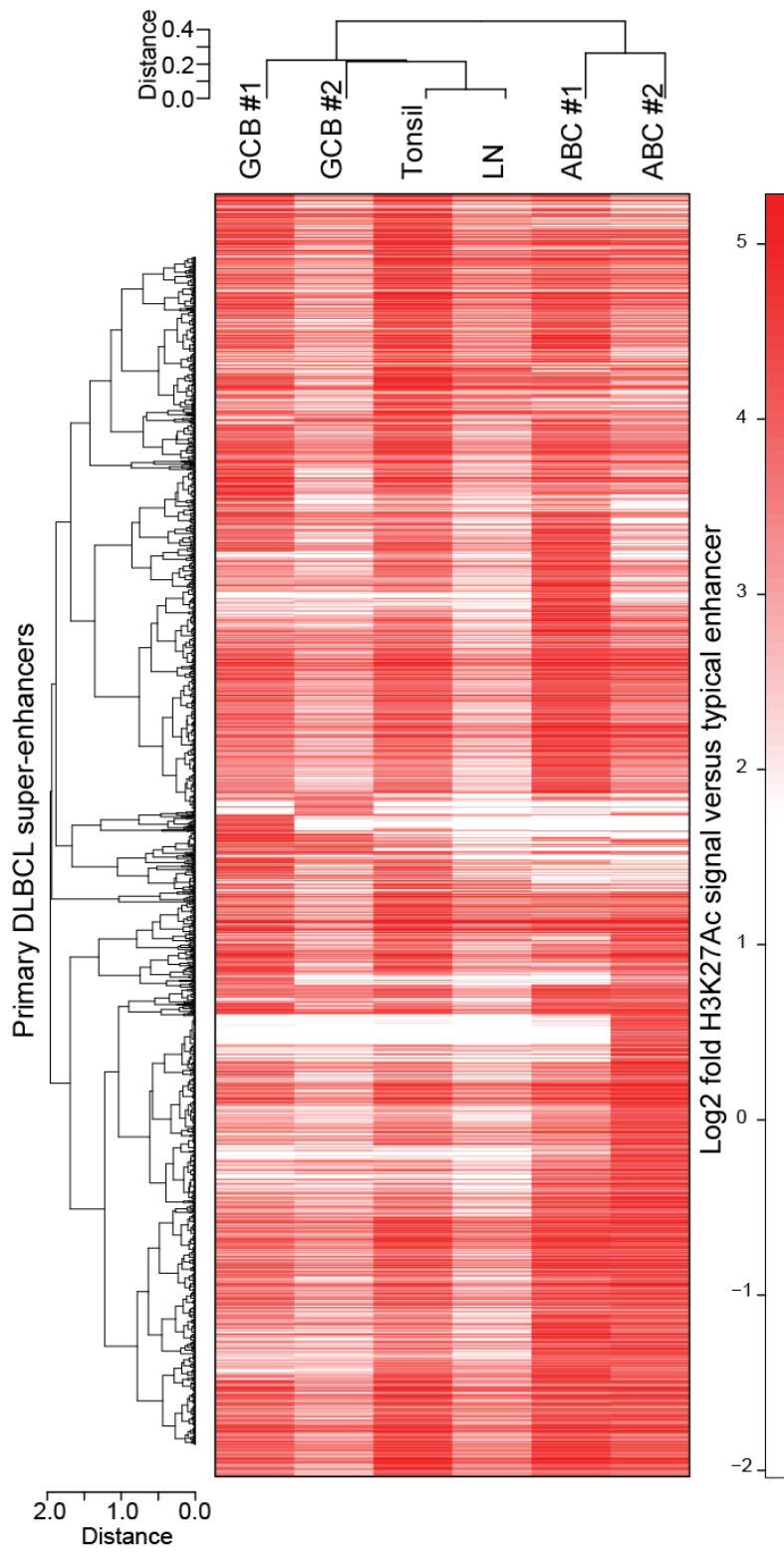


Figure 4.16: Unsupervised hierarchical clustering of super-enhancers in four primary DLBCL samples. Unsupervised hierarchical clustering of all super-enhancers loci in four primary DLBCL samples. Naming of primary samples indicates the previously assigned transcriptional COO subtype ¹³.

Figure 4.16 (Continued)



DISCUSSION

DLBCL is a clinically, biologically and genetically heterogeneous disease with distinctive transcriptional programs. As transcriptional circuits are ultimately controlled by master regulatory TFs and transcription and chromatin-associated factors rank among the most commonly altered genes in DLBCL^{9,10,13}, there is a pressing need to identify, characterize and target gene regulatory factors in this disease. We hypothesized that targeting oncogenic transcriptional activation at the chromatin level might act as a subclass-independent treatment in DLBCL. Here, we provide mechanistic evidence of BET bromodomains as transcriptional co-activators at large enhancers in addition to E2F1-driven promoters, and data supporting the study of BET inhibitors in all recognized subtypes of DLBCL.

In a broad panel of DLBCL cell lines representing all transcriptionally defined subtypes, nanomolar dose BET inhibition caused a profound G1 cell cycle arrest. BET inhibition also significantly delayed tumor growth in two independent DLBCL xenograft models. Gene expression profiling of multiple JQ1-treated DLBCL cell lines confirmed the previously described transcriptional downregulation of TLR pathway components, of interest in DLBCLs with activating mutations of MYD88^{37,51}. Transcriptional profiling also revealed coordinate downregulation of multiple B-cell receptor signaling components, of note given the role of BCR-mediated survival signals in specific DLBCL subtypes⁸. More broadly relevant for all subtypes of DLBCLs, we identified highly significant transcriptional downregulation of MYC and E2F1 target genes and the selective depletion of BRD4-loaded promoters and enhancers.

BET inhibition decreased the abundance of multiple functionally defined E2F target genes but did not measurably alter E2F1 protein levels. Epigenomic analyses confirmed the co-localization of BRD4 and E2F1 at active promoters and the selective decrease in BRD4 loading and transcriptional elongation of E2F1-driven genes following JQ1 treatment. Given the recently identified genetic signature of structural deregulated cell cycle and increased E2F activity in poor prognosis DLBCLs ¹³, BET inhibition may represent a promising targeted treatment strategy. Previous studies suggested a role of BET proteins in E2F1-mediated transcription ^{52,53}.

Studies from our lab and others have highlighted the important role of BRD4 as a co-activator of MYC mediated transcription ^{30,32,33}. In multiple myeloma cell lines with *Ig/MYC* translocations, BRD4 was postulated to function via long-range interactions with the distal *IgH* enhancer ³⁰. However, emerging data indicate that BET inhibitors suppress MYC transcription in the context of translocated, amplified or wild-type *MYC* alleles and BRD4 localizes to *MYC* promoter and enhancer elements ^{2,30,32,33}. In the current studies, we identify a BRD4-loaded *MYC* enhancer and find that BET inhibition decreases MYC transcription and expression in DLBCL cell lines with translocated, amplified or wild-type *MYC* alleles. In this extensive DLBCL cell line panel, the functional consequences of BET inhibition – cell cycle arrest and decreased cellular proliferation – were largely comparable. Although JQ1 treatment broadly downregulated the transcriptional targets of MYC and E2F, we sought additional bases for the effect of BET inhibition across multiple DLBCL subtypes.

We observed that a small subset of genes had a disproportionately high BRD4 load at their proximal enhancers. These unusual regulatory elements were \approx 12-fold larger than typical enhancer regions. Integrated epigenomic and transcriptional studies established that such super enhancer-marked genes were particularly sensitive to BET inhibition. As SEs were found adjacent to genes encoding known lineage factors and DLBCL oncoproteins, we surmised that SE analysis may identify novel, unrecognized tumor dependencies. The functional exploration of OCA-B, encoded by SE-marked *POU2AF1*, validates this factor as a cancer dependency in DLBCL. Mechanistic research has established OCA-B as a co-activator protein which binds into the OCT1-OCT2 transcriptional complex, enhancing IgH promoter-enhancer communication^{54,55}. Mice lacking OCA-B expression due to germline knock-out of *POU2AF1* are developmentally normal, even capable of early transcription from immunoglobulin promoters, however they lack an apparent germinal center reaction to antigen^{42,56}. Collectively, the earlier studies and the current research support a putative therapeutic window to targeting OCA-B, potentially by protein-protein inhibition via the POU domain. More generally, these studies establish a rationale to systematically explore SEs for unrecognized tumor dependencies, and potentially use SEs as biomarkers for targeted therapeutic development.

In this first comparative epigenomic analysis of human DLBCL cell lines, primary tumor specimens and normal lymphoid samples, we analyzed patterns of H3K27ac enrichment to understand the relevance of enhancer variation and function. These

studies reveal SEs as characteristic features of human lymphoid tissues, both benign and malignant. Preservation of tissue-specific SEs is observed comparing non-malignant nodal tissue to primary DLBCL samples, as well as in patient-derived human DLBCL cell lines.

In summary, our data suggest that the BET inhibition limits the growth of DLBCLs by at least two complementary activities: a specific effect on genes that define a given cell type by high BRD4 loading at enhancers and a more general suppression of transcription at E2F- and MYC-driven target genes. Thus, an E2F/MYC pathway effect is combined with massive depletion of proteins driven by BRD4 overloaded enhancers preventing cell cycle progression and leading to growth arrest. The majority of DLBCLs have a structural basis for increased E2F1-mediated cell cycle progression; however, these tumors may differ in BRD4 super-loading of cell fate-determining enhancers, including MYC, depending on their molecular context. This framework of BET inhibition explains its broad subclass- and tumor-type independent mechanism of action and reconciles the apparent pleiotropic effects and cell type-specific outcomes. Importantly, these data provide a compelling rationale for further human clinical investigation.

Experimental procedures

High throughput screening of BET bromodomain inhibitors in B-cell lymphoma cell line panel

Using a semi-automated screen we tested the indicated compounds in 34 human lymphoma lines in a 384-well format. Cell viability at 72 hr was evaluated using ATPlite (Perkin Elmer). The mean of absolute EC50s from two independent screens were visualized and clustered using GENE (<http://www.broadinstitute.org/cancer/software/GENE-E/index.html>).

Animal Studies

All animal studies were performed according to Dana-Farber Cancer Institute Institutional Animal Care and Use Committee (IACUC)-approved protocols as previously described¹³ and Supplemental Experimental Procedures.

Analyses of cellular proliferation and apoptosis, immunohistochemistry, immunoblotting, transcriptional profiling, GSEA and lentiviral mediated shRNA, chromatin immunoprecipitation with massively parallel sequencing (CHIP-Seq) and analysis of CHIP-Seq data

A full description of these methods is listed in Supplemental Experimental Procedures.

Accession Numbers

The Gene Expression Omnibus accession numbers for the gene expression and CHIP-Seq data reported in this paper is GSE45630 and GSE46663, respectively.

Cell Culture

The identities of the diffuse large B-cell and Hodgkin lymphoma cell lines used in this study were confirmed via STR profiling (PowerPlex ®1.2 system [Promega]) and the online verification services of the cell banks JCRB, DSMZ

(http://cellbank.nibio.go.jp/cellbank_e.html, <http://www.dsmz.de/STRanalysis>) and the Arizona Lymphoid Tissue and Blood Repository (L. Rimsza). The Burkitt lymphoma cell lines were recently purchased from the German Cell Line bank DSMZ (Braunschweig, Germany). HBL1 was kindly provided by Georg Lenz (Charité, Berlin, Germany).

All cell lines were cultured at 37°C in 5% CO₂. Balm3, BL2, BL41, CA46, CTB-1, Daudi, Dogkit, DB, HBL1, HDLM2, KM-H2, L428, L1236, L540, Namalwa, Pfeiffer, Raji, SU-DHL-5, SU-DHL-6 (hereafter DHL6), SU-DHL-7, SU-DHL-8, SU-DHL-10, Toledo and WSU-NHL were propagated in RPMI (Cellgro); OCI-Ly1 (hereafter Ly1), OCI-Ly3, OCI-Ly4 (hereafter Ly4), OCI-Ly7, OCI-Ly8, OCI-Ly10, OCI-Ly18 and OCI-Ly19 were grown in IMDM (Invitrogen). SUP-HD-1 was cultured in McCoy's media (Invitrogen). HEK293T cells for lentiviral particle production were cultured in DMEM (Cellgro). All media were supplemented with 10mM HEPES buffer, 2mM L-glutamine, 50U/mL penicillin, 50U/mL streptomycin and 10% heat-inactivated fetal bovine serum (FBS, all from Invitrogen); only BL2, L540, OCI-Ly10, HDLM2, SUP-HD1 were cultured in 20% FBS. The growth media of HBL1 was supplemented with 1mM sodium pyruvate. All cell lines were adjusted to 200,000 cells/ml 48 hr prior to an experiment.

Compounds

All compounds used in this study were resynthesized in-house or by contract with ChemPartner. Materials were stored as dry powders or 10 mM DMSO stock aliquots. JQ1 in this document refers to the JQ1S active species. The inactive JQ1R enantiomer is noted as such where used.

Screening of BET bromodomain inhibitors in B-cell lymphoma cell line panel

On the day of the experiment, cells were counted and adjusted to 60,000 cells/ml in appropriate growth media. Using a Biotek EL406, 50 μ l of cells were distributed into white 384-well plates (Thermo). Immediately after plating, compound in DMSO was distributed to plates. For large plate sets, cells were returned to 37°C incubator while not in use. Compounds were added to plates using a 100 nl 384-well pin transfer manifold on a Janus workstation. Stocks were arrayed in 10 point quadruplicate dose response in DMSO stock in 384-well Greiner compound plates. After addition of compound, plates were incubated for 72 hr in a 37°C incubator.

Cell viability was read out using ATPlite (Perkin Elmer). Plates were removed from the incubator and brought to room temperature prior to use. Lyophilized powder was resuspended in lysis buffer and diluted 1:2 with distilled water. 25 μ l of this solution was added to each well using the Biotek liquid handler. Plates were sealed with adherent aluminum seals prior to vortexing and spinning down at 1000g for 1 min. Plates were incubated for 15 min at room temperature before the luminescence signal was read on an Envision Plate Reader.

Data acquired as described was stored and grouped in Microsoft's Excel and analyzed using GraphPad Prism Software. Curve fits to calculate EC50 were done in GraphPad

Prism version 6.0a using four parameter (Hill slope not assumed to be equal to 1) non-linear regressions of the data with the log₁₀ transformed data of the compound concentrations plotted against the percent viability of the cells when normalized to DMSO only treated wells included on the plate. Edge wells were excluded. The mean of absolute EC₅₀s from two independent screen experiments were visualized and clustered in a color-coded heat map using GENE (<http://www.broadinstitute.org/cancer/software/GENE-E/index.html>).

Assessment of proliferation, cell cycle and apoptosis following BET

Bromodomain Inhibition

Proliferation of a smaller panel of cell lines (as listed in Figure 4.1) following treatment with increasing doses of JQ1 was assessed with the alamarBlue assay (Invitrogen, Carlsbad, CA) according to the manufacturer's recommendation. Briefly, 10,000 cells were plated in a round-bottom 96-well with indicated final concentrations of JQ1 or vehicle in 100µl of growth media. After adding 10µl of resazurin-containing alamar blue solution per well, plates were incubated for 2h at 37C to allow reduction to resorufin. Viability was determined compared to background on subsequent days by reading the fluorescence emission of resorufin on a Spectramax M3 plate reader (Molecular Devices, Sunnyvale, CA) using an excitation wavelength of 544 nm and reading the emission at 590 nm with 10 readings per well.

Cell cycle analysis was performed 72 hr after JQ1 treatment using Hoechst 33342. Cells were resuspended in 1 ml of growth medium supplemented with 10µg/ml Hoechst 33342 (Molecular Probes, Invitrogen) as final concentration. After 60 min at 37°C in the

dark, analysis was performed on a FACS Ariall cytometer (BD Biosciences) using the UV laser 350 nm with 20 mW. The cell cycle was plotted as histogram after excluding doublets.

Cellular apoptosis was analyzed with an APC AnnexinV/7ADD Apoptosis Detection kit (BD Pharmingen). AnnexinV/7AAD assessments and cell cycle graphics were generated using FlowJo software V7.6.1 for Windows (Tree Star).

In vivo studies

All animal studies were performed according to Dana-Farber Cancer Institute Institutional Animal Care and Use Committee (IACUC)-approved protocols as previously described¹³. The DLBCL cell lines, Toledo and Ly1, were engineered for *in vivo* imaging by transduction with the VSV-G-pseudotyped lentivirus encoding the firefly luciferase, mCherry, and a puromycin-N-acetyltransferase, each separated by picornavirus ribosomal slippage peptides as previously described¹³. Subsequently, 5×10^6 viable Luc-mCherry-expressing lymphoma cells in 250 μ l sterile PBS were injected via the lateral tail veins of 8-week old NOD SCID Il2r α ^{null} mice (Charles River Laboratories, Wilmington, MA).

Disease burden was quantified using bioluminescence imaging as previously described¹³ and data are presented as mean \pm SEM with statistical significance determined by one-sided t-test. One week following tumor inoculation, animals with established disease documented by imaging were divided into two cohorts with equal mean bioluminescence and treated with 30 mg/kg JQ1S or vehicle (10% DMSO in D5W) BID by intraperitoneal injection. Following 16 days of treatment, the entire Toledo cohort

was sacrificed and subjected to a complete hematologic analysis. One third of the spleen and one tibia were fixed in 10% neutral-buffered formalin over night and then stored in preparation for immunohistochemical analyses in 70% ethanol. Flow cytometry was used to analyze single cell suspensions of spleen and bone marrow for the presence of mCherry-positive Toledo cells (excitation of 561 nm using a yellow-green laser on a BD LSRFortessa [BD Biosciences]), which were confirmed to co-express human CD45 and CD19 by flow cytometry with anti-human CD45-FITC (BD) and anti-human CD19-PE-Cy7 (BD) antibodies (data not shown, see ¹³).

To measure survival as endpoint, we used a second independent DLBCL cell line, Ly1, which were injected into 25 mice (see details above). At day 13 of treatment three animals from each group were sacrificed and subjected to a full hematological analysis with vehicle or JQ1, validate the PD of the drug and mirror our analysis in Toledo. The remainder of the cohort was treated until the end point of the study (overall survival) were reached. Animals with paralysis, emaciation or severe dyspnea were scarified according to the protocol.

Immunohistochemistry of mouse tissues

Immunohistochemistry (IHC) for human CD20 and Ki67 was performed using 4- μ m-thick, formalin-fixed, paraffin-embedded tissue sections of explanted mice spleen or tibia as previously described (Monti et al., Cancer Cell 2012). Prior to embedding, mice tibia was subjected to decalcification following standard protocols in order to soften the bone tissue for sectioning. Slides were baked, deparaffinized in xylene, passed through graded alcohols, and then antigen retrieved with either 10mM citrate buffer, pH6.0

(Invitrogen), for CD20 or 1mM EDTA, pH8.0 (Invitrogen), for Ki67 in a steam pressure cooker (Decloaking Chamber; BioCare Medical) as per manufacturer's instruction. All further steps were carried out at room temperature in a hydrated chamber. Slides were pretreated with Peroxidase Block (Dako) for 5 minutes to quench endogenous peroxidase activity, and then washed in 50mM Tris-Cl, pH7.4. Slides were blocked using Protein Block (Dako) as per manufacturer's instruction, and subsequently incubated with α CD20cy (clone L26 , ready to use; Dako) and α Ki67 (clone MIB-1, 1:500 dilution; in diluent (Dako)) for 1 hr. Slides were then washed in 50mM Tris-Cl, pH7.4 and treated with anti-mouse horseradish peroxidase-conjugated antibody (Envision Plus; Dako) for 30 min. After further washing, immunoperoxidase staining was developed using a 3,3'diaminobenzidine (DAB) chromogen (Dako) for 5 min. Slides were counterstained with hematoxylin, dehydrated in graded alcohol and xylene, and mounted and coverslipped. Slides were loaded into an Aperio ScanScope XT and scanned at 40x magnification (0.25 μ m/pixel) via the semi-automated method. Slides were checked for image quality using visual inspection.

Gene expression profiling

The 5 DLBCL cell lines, Ly1, DHL6, Ly4, Toledo and HBL1, were incubated in biological triplicates for 2, 6, 12 and 24 hr with 500nM of JQ1 or DMSO at a concentration of 1×10^6 cells/ml. Untreated cells in triplicates per cell line at baseline (0 hr) were harvested directly without treatment. Total RNA was extracted using the standard Trizol extraction method. RNAs were measured and quality controlled on a Bioanalyzer, and

subsequently profiled on an Affymetrix human ST1.0 gene chip in the Dana-Farber Microarray Core (<http://chip.dfci.harvard.edu>).

Data processing

The gene-by-sample expression matrix used for subsequent analyses was obtained from the raw '.CEL' files by performing Robust Multichip Average (RMA) normalization⁵⁷ using a custom CDF based on entrez annotation⁵⁸. Variation filtering was performed by ranking genes according to an F-statistic measuring the ratio of their between- to within-replicate variation, and by then selecting the top 8000 transcripts⁶.

Temporal response analysis

At each time point (2, 6, 12, and 24 hours), differential analysis was performed between the DMSO-treated and the JQ1-treated samples, using a t-statistic and a permutation-based p-value calculation to identify the transcripts most significantly up- and down-regulated in response to the treatment⁵⁹. Permutations were constrained so as to control for cell type (Good P Springer book). The up-regulation and down-regulation signatures at each time point were defined as the sets of genes with FDR-corrected q-value $\leq .01$ and fold-change ≥ 1.3 .

Enrichment analysis

The signatures thus defined were then tested for enrichment based on the hypergeometric distribution with respect to the canonical pathways included in the MSigDB c2_cp compendium, as well as with respect to the list of transcription factor targets included in the MSigDB c3_tft compendium⁶⁰. Gene sets significantly enriched with FDR q-value ≤ 0.25 were reported, with the multiple-hypothesis correction accounting both for the multiple gene sets as well as the multiple signatures tested. Functionally

defined gene sets were derived from the C2.CGP MSigDB depository (<http://www.broadinstitute.org/gsea/msigdb/index.jsp>). For OCA-B, we curated a gene signature from previously published work. The ChiP-Seq defined E2F1 target gene set was composed of the top 100 genes with transcription factor-occupied proximal regulatory regions, defined as signal ± 5 kb of the transcription start side in vehicle-treated Ly1 cells. The binding signal of the E2F1 chip was normalized to the signal of the whole cell lysate. To define a developmental signature of germinal center B-cells, we utilized publically available gene expression profiles of purified human B-cell subsets (GSE12453)⁶¹. We performed a differential analysis between the union of centrocytes/centroblasts and plasma cells in gene pattern (Broad Institute,⁶²) using the comparative marker selection module. The 150 most up-regulated genes in normal germinal center centrocytes and centroblasts vs. normal plasma cells were defined as (UP_in_GCB_vs_PC).

SDS-PAGE Western Bot

SDS-PAGE and Western Blot was performed as previously described in¹³ with the following antibodies in 0.1% Tween 20/PBS: BCL6, sc-858 (N-3, 1:500); BACH2, sc-14702 (1:500); GAPDH, sc-25778 (FL-335, 1:2000) (all from Santa Cruz Biotechnology). BRD2 was analyzed with HPA042816 (1:1000) from Sigma and BRD4 (A301-985A, 1:500) with a commercial antibody from Bethyl. POU2AF1 (OCA-B) was detected with PA5-26105 (1:1000) from Thermo Scientific, PAX5 from BD (#610863, 1:500), IRF8 from Cell Signaling (D20D8, 1:1000) and alpha-Tubulin with the clone

DM1A (CP06, 1:2000) from Calbiochem. Secondary antibodies were purchased from Santa Cruz Biotechnology.

Chromatin immunoprecipitation with massively parallel sequencing from cell lines (ChIP-Seq)

ChIP-Seq was performed as described⁶³ with minor changes. In brief, approximately 1×10^8 cells were treated per condition at a concentration of 1×10^6 cells/ml with 500 nM JQ1 or DMSO for 24 hr and then cross-linked with 1.1% formaldehyde (10 X crosslink solution contains: 11% formaldehyde, 50 mM HEPES pH 7.3, 100 mM NaCl, 1 mM EDTA pH 8.0, 0.5 mM EGTA pH 8.0) followed by two washes with PBS. Cells were pelleted, flash frozen in dry ice/isopropanol and stored at -80°C until final use.

100 μl of Dynal magnetic beads per sample (Invitrogen) were blocked with 0.5% BSA (w/v) in PBS. Magnetic beads were loaded with 10 μg of each antibody over night at 4°C . Antibodies used were as follows: Pol II (Rpb1 N-terminus): Santa Cruz sc-899; Histone H3K27Ac: Abcam ab4729; Histone H3K4me3: Millipore 07-473; Histone H3K27me3: Abcam ab6002; E2F1: Cell Signaling #3742; BRD4: Bethyl A301-985A; BCL6: Santa Cruz sc-858. Cross-linked cells were lysed with lysis buffer 1 (50 mM HEPES pH 7.3, 140 mM NaCl, 1 mM EDTA, 10% glycerol, 0.5% NP-40, and 0.25% Triton X-100) for a total of 4.5 min on with 30 s pulses separated by 1 min pauses at 18 amps. Pellets were then washed with lysis buffer 2 (10 mM Tris-HCl pH 8.0, 200 mM NaCl, 1 mM EDTA pH 8.0 and 0.5 mM EGTA pH 8.0). Cells were resuspended and sonicated in lysis buffer 3 (50 mM Tris-HCl pH 7.5, 140 mM NaCl, 1 mM EDTA, 1 mM EGTA, 1% Triton X-100, 0.1% Na-deoxycholate, 0.1% SDS) on ice for 10 cycles at 30 s

(18 W) with 60 s on ice between cycles. All lysis and sonication buffers contain Complete Protease Inhibitor Cocktail (Roche). Sonicated lysates were cleared by centrifuging at 20,000g for 10 min and incubated overnight on a spinning wheel at 4°C with magnetic beads prebound with antibody. Beads were washed three times with sonication buffer, one time with sonication buffer with 500 mM NaCl added, one time with LiCl wash buffer (20 mM Tris pH 8.0, 1 mM EDTA, 250mMLiCl, 0.5% NP-40, 0.5% Na-deoxycholate) and once with TE. DNA was eluted in elution buffer (50 mM Tris-HCl pH 8, 10mM EDTA, and 1% SDS). Cross-links were reversed overnight at 65°C. RNA and protein were digested with 0.2mg/mL RNase A for two hr followed by 0.2mg/mL Proteinase K for one hr. DNA was purified with phenol chloroform extraction and ethanol precipitation.

Libraries for Illumina sequencing were prepared following the Illumina TruSeq™ DNA Sample Preparation v2 kit protocol with the following exceptions. After end-repair and A-tailing, immunoprecipitated DNA (~10-50ng) or whole cell extract DNA (50ng) was ligated to a 1:50 dilution of Illumina Adapter Oligo Mix assigning one of 24 unique indexes in the kit to each sample. Following ligation, libraries were amplified by 18 cycles of PCR using the HiFi NGS Library Amplification kit KAPA Biosystems. Amplified libraries were then size-selected using a 2% gel cassette in the Pippin Prep™ system from Sage Science set to capture fragments between 200 and 400 bp. Libraries were quantified by qPCR using the KAPA Biosystems Illumina Library Quantification kit according to kit protocols. Libraries with distinct TruSeq indexes were multiplexed by mixing at equimolar ratios and running together in a lane on the Illumina HiSeq 2000 for 40 bases in single read mode.

ChIP-Seq from primary tissue

Primary tissue samples from two ABC-DLBCL, two GCB-DLBCL flash-frozen and stored in OCT were collected in 10 slices at 20 μ m. After two washes and spin downs in PBS (300g, 5 min), these were then cross-linked with 1.1% formaldehyde in PBS for 10 min. The formaldehyde was quenched by adding 60 μ l/ml of 2.5 M glycine. Glycine and fixative were removed with two washes in cold PBS. Samples were homogenized with a Dounce homogenizer using 10 strokes with pestle A and 10 strokes pestle B in a solution of 10 mM Tris HCl pH8, 10 mM NaCl, 3 mM MgCl₂, and 1% NP40. Sample was then transferred to a 15 ml conical tube and rotated in the cold room for 60 min. After this incubation, nuclei were spun down at 1350g for 10 min and transferred to a 3.5 ml tube in 50 mM Tris-HCl pH 7.5, 140 mM NaCl, 1 mM EDTA, 1 mM EGTA, 1% Triton X-100, 0.1% Na-deoxycholate, 0.7% SDS. Samples were then sonicated on ice for 10 cycles at 30 s (18 W) with 60 s on ice between cycles. All lysis and sonication buffers contain Complete protease inhibitor cocktail (Roche). Sonicated lysates were cleared by centrifuging at 20,000g for 10 min and incubated overnight on a spinning wheel at 4°C with magnetic beads prebound with antibody after diluting sample to 0.1% SDS final. 100 μ l of Dynal magnetic beads per sample (Invitrogen) were blocked with 0.5% BSA (w/v) in PBS. Magnetic beads were loaded with 10 μ g of each antibody overnight at 4°C. Antibodies used were as follows: Histone H3K27Ac: Abcam ab4729 ; BRD4: Bethyl A301-985A.

Beads were washed three times with sonication buffer, one time with sonication buffer supplemented with 500 mM NaCl, one time with LiCl wash buffer (20 mM Tris pH 8.0, 1

mM EDTA, 250 mM LiCl, 0.5% NP-40, 0.5% Na-deoxycholate) and once with TE. DNA was eluted in elution buffer (50 mM Tris-HCl pH 8, 10mM EDTA, and 1% SDS). Cross-links were reversed overnight at 65°C. RNA and protein were digested with 0.2mg/mL RNase A for two hr followed by 0.2 mg/ml Proteinase K for one hr. DNA was purified with phenol chloroform extraction and ethanol precipitation.

Library preparation and sequencing was performed as described for ChIP-Seq from cell lines.

Analysis of ChIP-Seq data

Gene sets and annotations

All analyses were performed using RefSeq (NCBI36/HG18) ⁶⁴ human gene annotations.

ChIP-Seq data processing

All ChIP-Seq datasets were aligned using Bowtie (version 0.12.2) ⁶⁵ to build version NCBI36/HG18 of the human genome. Alignments were performed using the following criteria: -n2, -e70, -m1, -k1, --best. These criteria preserved only reads that mapped uniquely to the genome with 1 or fewer mismatches.

Calculating read density

We used a previously described method to calculate the normalized read density of a ChIP-Seq dataset in any region ⁶⁶. ChIP-Seq reads aligning to the region were extended by 200bp and the density of reads per base pair (bp) was calculated. In order to eliminate PCR bias, multiple reads of the exact same sequence aligning to a single position were collapsed into a single read. Only positions with at least 2 overlapping extended reads contributed to the overall region density. The density of reads in each

region was normalized to the total number of million mapped reads producing read density in units of reads per million mapped reads per bp (rpm/bp).

Identifying ChIP-Seq enriched regions

We used the MACS version 1.4.1 (Model based analysis of ChIP-Seq)⁶⁷ peak finding algorithm to identify regions of ChIP-Seq enrichment over background. A p value threshold of enrichment of $1e-9$ was used for all datasets.

Defining transcribed genes

A gene was defined as transcribed if an enriched region for either H3K4me3 or RNA Pol II was located within +/- 5kb of the TSS. H3K4me3 is a histone modification associated with transcription initiation⁶⁸.

Defining E2F1 target genes

Because E2F1 has been shown to regulate genes through binding at cis-regulatory elements near genes, we defined E2F1 target genes based on total E2F1 ChIP-Seq occupancy near transcription start sites of genes. We first calculated total E2F1 occupancy at E2F1 enriched regions genome wide. For the top 5,000 transcribed genes (determined by RNA Pol II occupancy in the +/- 1kb TSS region), the total E2F1 occupancy was summed for all E2F1 enriched regions within +/- 50kb of the TSS. The top 1,000 genes ranked by total TSS proximal E2F1 occupancy were called "E2F1 target genes", whereas the bottom 1,000 genes ranked by TSS proximal E2F1 occupancy were called "E2F1 non-target genes". See Figure 4.9C.

Defining active enhancers

Active enhancers were defined as in ⁶⁶ as regions of enrichment for H3K27Ac outside of promoters (greater than 5kb away from any TSS). H3K27Ac is a histone modification associated with active enhancers ^{69,70}.

Heatmap representations of ChIP-Seq data

In order to display ChIP-Seq levels at promoters or enhancers, we used a heat map representation. In the heatmap representation, each row represents the +/- 5kb centered on the TSS (for promoter heatmaps) or H3K27Ac enriched region center (for enhancer heatmaps). Each 50bp bin in each row was shaded based on intensity of ChIP-Seq occupancy (in units of rpm/bp). See Figure 4.9A and Figure 4.11A

Creating meta representations of ChIP-Seq occupancy at active enhancers and promoters

Genome-wide average “meta” representations of ChIP-Seq occupancy at active enhancers and promoters were created by mapping ChIP-Seq read density to the 5kb regions flanking the center of active enhancer regions or transcription start sites (TSS) of active genes. Each active enhancer or TSS region was split into one hundred 50bp bins. All active enhancer or TSS regions were then aligned and the average background subtracted ChIP-Seq factor density in each bin was calculated to create a meta genome-wide average in units of rpm/bp. See Figure 4.9B and Figure 4.11B.

Determination of RNA Pol II traveling ratio

We determined the ratio of background subtracted RNA Pol II ChIP-Seq levels in initiating to elongating regions, a measure known as the traveling ratio (TR) ⁶³ in each cell line. We defined the initiating region as +/-300bp around the TSS. We defined the elongating region as +300bp from the TSS to +3,000bp after the gene end. In order to

make higher confidence comparisons, we limited our analysis to genes with detectable signal above noise in the initiating and elongating regions across all samples. The statistical significance of changes in the distribution of traveling ratios was determined using a Welch's two-tailed *t* test. See Figure 4.9C.

BRD4 and H3K27Ac overlap

BRD4 and H3K27Ac regions were considered overlapping if they were within 5kb of one another. See Figure 4.11B.

BRD4 location analysis

We examined the location of BRD4 enriched region centers relative to active promoters and enhancers. Promoters and enhancer regions were defined as the +/- 5kb region flanking the TSS or +/-5kb region flanking the center of enhancers respectively. See Figure 4.11D.

Calculating BRD4 load at enhancers

In order to accurately capture dense clusters of BRD4 bound enhancers, we allowed TSS distal BRD4 regions within 12.5kb of one another to be stitched together, a method described in ^{2,71}. This analysis defined BRD4 bound enhancer regions in the Ly1 genome. The total BRD4 ChIP-Seq occupancy signal at BRD4 bound enhancers was calculated by first determining the average ChIP-Seq read density in the entire enhancer region (rpm/bp). This value was multiplied by the length of the region to produce total ChIP-Seq occupancy in units of total rpm. See Figure 4.11E.

Identifying super-enhancers

We observed disproportionately high occupancy of BRD4 at a subset of enhancers, similar to recent descriptions of “super-enhancers”⁷². In Ly1 cells, super-enhancers were defined similarly to. Briefly, we first ranked all enhancers by increasing total background subtracted ChIP-Seq occupancy of BRD4 (x-axis), and plotted the total background subtracted ChIP-Seq occupancy of BRD4 in units of total rpm (y-axis). This representation revealed a clear inflection point in the distribution of BRD4 at enhancers (Figure 4.11E). We geometrically defined the inflection point and used it to establish the cut off for super-enhancers.

Assigning enhancers to genes

Enhancers tend to loop to and associate with adjacent genes in order to activate their transcription⁷³. Using a simple proximity rule, we assigned the closest expressed and transcriptionally active gene (distance from enhancer center to TSS) within 1mb to each enhancer as its most likely target gene.

Clustering of super-enhancers

DLBCL super-enhancers were hierarchically clustered to display relationships between individual enhancers and samples. Within a set of DLBCLs, all unique super-enhancer containing regions were identified. In each super-enhancer containing region, for each sample, background subtracted H3K27Ac was calculated relative to the median enhancer. Pairwise pearson correlations were determined for all patterns of H3K27Ac signal and this correlation score was used to hierarchically cluster super-enhancer containing regions together. Individual DLBCLs were also clustered together using the pearson correlation of H3K27Ac signal across all super-enhancer containing

regions. Patterns of H3K27Ac signal at super-enhancer containing regions were displayed in two-dimensionally clustered heatmaps with each super-enhancer containing region displayed as a row color encoded by H3K27Ac fold signal over the median enhancer. Likewise, similarities between DLBCLs were displayed in hierarchically clustered two dimensional heatmaps in which each cell was colored by pairwise pearson correlation of H3K27Ac signal at all super-enhancer containing regions.

Lentiviral-mediated knockdown of BRD2, BRD4, E2F1 and OCA-B.

Hairpin-containing PLKO.1 plasmids were obtained from the RNAi platform at the Broad Institute. The following hairpins were used:

| Gene | Hairpin | TRC number |
|-----------------|--------------------|-------------------|
| BRD2 | #sh1 | 0000006312 |
| | #sh2 | 0000006310 |
| BRD4 | #sh1 | 0000199427 |
| | #sh2 | 0000196576 |
| E2F1 | #sh1 | 0000010328 |
| | #sh4 | 0000000250 |
| POU2AF1 (OCA-B) | #sh1 | 0000431764 |
| | #sh2 | 0000423580 |
| Control | ev (=empty vector) | 025 |

The lentivirus was packaged by co-transfection of the lentiviral hairpin containing plasmid PLKO.1 and the helper plasmids. pCMV-dR8.91 and pMD2.G-VSV-G into HEK293T cells using Lipofectamin (Invitrogen), as previously described¹³ with minor modifications. Following transduction via spinoculation for 2 hr at 1000g and 30°C in the presence of 8 ug/ml hexadimethrine bromide (Sigma, St. Louis, MO) and selection with 1 ug/ml puromycin for 48 hr (Sigma, St. Louis, MO), knockdown efficacy was determined by western blotting and cells were seeded for proliferation assays as described above.

Enforced Expression of MYC and OCA-B.

Enforced expression of OCA-B was conducted with the pMSCV-IRES-GFP (pMig) vector. POU2AF1 (OCA-B) was obtained from the DF/HCC DNA Resource Core (<http://plasmid.med.harvard.edu/PLASMID/Home.jsp>) in pDONR221 (HsCD00042886) and subsequently cloned into pMig using a standard Gateway LR reaction according to the manufacturer's recommendation.

The vector pMX-MYC was ordered from Addgene (plasmid #17220, ⁷⁴) and pDONR-GFP was obtained from the Broad ORF consortium. MYC was subcloned into pDONR223 using a Gateway BP reaction according to the manufacturer's recommendation. Both, GFP and MYC, were then subsequently subcloned with a Gateway LR reaction into the final destination vector for enforced expression of MYC and GFP, pMSCV-puro. All inserts used for enforced expression were confirmed to contain the reference sequence by classical Sanger sequencing.

Retroviral particles were packaged by cotransfecting HEK293T cells with the pMSCV construct, VSV-G and PKAT in the ratio 10:5:10 ug using TransIT following the manufacturer's recommendation. Viral particles were collected for 48 hr in DMEM supplemented with 30% FBS before indicated cell lines were transduced in a spinoculation for 1 hr/1000g/30°C.

Ly1, Toledo and HBL1 cells were selected 48 hr after infection with its pMSCV-puro constructs for 2 d with 1 μ g/ml puromycin before plated for an experiment. Ly1 cells transduced with OCA-B or control vector (pMMSCV-GFP) were sorted 48hr after infection using the concordant expressed GFP as marker.

Acetyl-Histone Binding Assay.

Assays were performed with minor modifications from the manufacturer's protocol (PerkinElmer, USA). All reagents were diluted in 50 mM HEPES, 150 mM NaCl, 0.1% w/v BSA, 0.01% w/v Tween20, pH 7.5 and allowed to equilibrate to room temperature prior to addition to plates. After addition of Alpha beads to master solutions all subsequent steps were performed in low light conditions. A 2x solution of components with final concentrations of 6xHis-tagged bromodomain protein at 80 nM, Ni-coated Acceptor Bead at 25 µg/ml, and 80 nM biotinylated Histone 4-tetra acetyl tail was added in 10 µL to 384-well plates (AlphaPlate - 384, PerkinElmer, USA). Biotinylated peptide for BRD4.1 was synthesized in-house on a CEM Liberty 9008005 microwave peptide synthesizer: H4-tetra acetyl, Biotin-PEG2-SGRGKacGGKacGLGKacGGAKacRHRK-COOH. Addition to wells was performed with a Biotek EL406 liquid handler. After a 1 min 1000rpm spin-down, 100 nL of compounds from stock plates were added by pin transfer using a Janus Workstation (PerkinElmer, USA). The streptavidin-coated donor beads (25 µg/ml final) were added as with previous solution in a 2x, 10 µL volume. Following this addition, the plates were sealed with foil to block light exposure and to prevent evaporation. The plates were spun down again at 1000rpm for 1 min. Next, the plates were incubated in the room with the plate reader (for temperature equilibration) for 1.5 hr prior to reading the assay. AlphaScreen measurements were performed on an Envision 2104 (PerkinElmer, USA) utilizing the manufacturer's protocol.

ChIP-qPCR

ChIP-qPCR analysis for BRD4 was performed on Ly1. Following treatment of 1×10^6 cells/ml with 500 nM JQ1 or DMSO for 24 hr in growth medium, 1×10^6 cells were fixed with 1.1% formaldehyde (10 X crosslink solution contains: 11% formaldehyde, 50 mM HEPES pH 7.3, 100 mM NaCl, 1 mM EDTA pH 8.0, 0.5 mM EGTA pH 8.0) followed by two washes with PBS. Cells were pelleted and flash frozen in dry ice/isopropanol. 50 μ l of Dynal magnetic beads per sample (Invitrogen) were blocked with 0.5% BSA (w/v) in PBS. Magnetic beads were bound with 2 μ g of an anti-BRD4 antibody (Bethyl A301-985A). Cross-linked cell pellets were lysed with 10% SDS, 0.5M EDTA, 1M Tris, and Roche Complete protease cocktail at pH 7.5. Samples at 500 μ L were sonicated at 35 amps for a total of five min with 1 s pulses followed by 2 s off. Lysates were cleared and incubated overnight at 4°C with magnetic beads preloaded with antibody. Beads were washed three times with sonication buffer, once with sonication buffer supplemented with 500 mM NaCl, once with LiCl wash buffer (20 mM Tris pH 8.0, 1 mM EDTA, 250mMLiCl, 0.5% NP-40, 0.5% Na-deoxycholate) and one time with TE. DNA was eluted in elution buffer before cross-links were reversed overnight at 65°C. RNA and protein were digested using RNase A and Proteinase K, respectively, and DNA was purified with phenol chloroform extraction and subsequent ethanol precipitation. ChIP and input DNA were analyzed using SYBR Green real-time PCR analysis (Applied Biosystems).

Real Time SYBR Green primer For CHIP-PCR:

| Gene Symbol | Primer | |
|----------------------|--|---|
| PPIA | IDT Hs.PT.51.23155197 | |
| BCL6-promoter-pair 1 | forward reverse forward | 5'- CAA CCT GAA ACA CAG CTT GTC-3' 5'- CAC TCT GGC TGG TTC TAC TAC T-3' 5'- CAG TAT CAC AGA TAC TGC CTG T -3' |
| BCL6-promoter-pair 2 | reverse | 5'- GGA AAG AAT TTC TCC TTC TTC TCT AC-3' |
| BCL6-enhancer-pair 1 | forward reverse forward reverse | 5'- GCA TAT CAG TTA CAC TAT TTC TGA GC-3' 5'- AGC CAC GCA CAG GAA AGT GAG AG-3' 5'- AGT GGG TAG CAG AGA ACA TGA GAC AT-3' 5'- TAC ACT TGC ATC TGG TTG CGC AGC T-3' |
| BCL6-enhancer-pair 2 | | |

References

- 1 Chapuy, B. *et al.* Discovery and characterization of super-enhancer-associated dependencies in diffuse large B cell lymphoma. *Cancer cell* **24**, 777-790, doi:10.1016/j.ccr.2013.11.003 (2013).
- 2 Loven, J. *et al.* Selective inhibition of tumor oncogenes by disruption of super-enhancers. *Cell* **153**, 320-334, doi:10.1016/j.cell.2013.03.036 (2013).
- 3 Klein, U. & Dalla-Favera, R. Germinal centres: role in B-cell physiology and malignancy. *Nat Rev Immunol* **8**, 22-33, doi:nri2217 [pii] 10.1038/nri2217 (2008).
- 4 Gisselbrecht, C. *et al.* Salvage regimens with autologous transplantation for relapsed large B-cell lymphoma in the rituximab era. *J Clin Oncol* **28**, 4184-4190, doi:10.1200/JCO.2010.28.1618 (2010).
- 5 Lenz, G. & Staudt, L. M. Aggressive lymphomas. *N Engl J Med* **362**, 1417-1429, doi:362/15/1417 [pii] 10.1056/NEJMra0807082 (2010).
- 6 Monti, S. *et al.* Molecular profiling of diffuse large B-cell lymphoma identifies robust subtypes including one characterized by host inflammatory response. *Blood* **105**, 1851-1861, doi:10.1182/blood-2004-07-2947 (2005).
- 7 Caro, P. *et al.* Metabolic signatures uncover distinct targets in molecular subsets of diffuse large B cell lymphoma. *Cancer cell* **22**, 547-560, doi:10.1016/j.ccr.2012.08.014 (2012).
- 8 Chen, L. *et al.* SYK inhibition modulates distinct PI3K/AKT- dependent survival pathways and cholesterol biosynthesis in diffuse large B cell lymphomas. *Cancer cell* **23**, 826-838, doi:10.1016/j.ccr.2013.05.002 (2013).
- 9 Morin, R. D. *et al.* Frequent mutation of histone-modifying genes in non-Hodgkin lymphoma. *Nature* **476**, 298-303, doi:10.1038/nature10351 (2011).
- 10 Pasqualucci, L. *et al.* Analysis of the coding genome of diffuse large B-cell lymphoma. *Nat Genet* **43**, 830-837, doi:10.1038/ng.892 (2011).
- 11 Lohr, J. G. *et al.* Discovery and prioritization of somatic mutations in diffuse large B-cell lymphoma (DLBCL) by whole-exome sequencing. *Proc Natl Acad Sci U S A* **109**, 3879-3884, doi:10.1073/pnas.1121343109 (2012).
- 12 Zhang, J. *et al.* Genetic heterogeneity of diffuse large B-cell lymphoma. *Proc Natl Acad Sci U S A* **110**, 1398-1403, doi:10.1073/pnas.1205299110 (2013).
- 13 Monti, S. *et al.* Integrative analysis reveals an outcome-associated and targetable pattern of p53 and cell cycle deregulation in diffuse large B cell lymphoma. *Cancer cell* **22**, 359-372, doi:10.1016/j.ccr.2012.07.014 (2012).
- 14 Basso, K. & Dalla-Favera, R. Roles of BCL6 in normal and transformed germinal center B cells. *Immunological reviews* **247**, 172-183, doi:10.1111/j.1600-065X.2012.01112.x (2012).
- 15 Slack, G. W. & Gascoyne, R. D. MYC and aggressive B-cell lymphomas. *Advances in anatomic pathology* **18**, 219-228, doi:10.1097/PAP.0b013e3182169948 (2011).
- 16 Hu, S. *et al.* MYC/BCL2 protein coexpression contributes to the inferior survival of activated B-cell subtype of diffuse large B-cell lymphoma and demonstrates high-risk gene expression signatures: a report from The International DLBCL Rituximab-CHOP Consortium Program. *Blood* **121**, 4021-4031; quiz 4250, doi:10.1182/blood-2012-10-460063 (2013).

- 17 Johnson, N. A. *et al.* Concurrent expression of MYC and BCL2 in diffuse large B-cell lymphoma treated with rituximab plus cyclophosphamide, doxorubicin, vincristine, and prednisone. *J Clin Oncol* **30**, 3452-3459, doi:10.1200/JCO.2011.41.0985 (2012).
- 18 Lee, T. I. & Young, R. A. Transcriptional regulation and its misregulation in disease. *Cell* **152**, 1237-1251, doi:10.1016/j.cell.2013.02.014 (2013).
- 19 Schreiber, S. L. & Bernstein, B. E. Signaling network model of chromatin. *Cell* **111**, 771-778 (2002).
- 20 Fuda, N. J., Ardehali, M. B. & Lis, J. T. Defining mechanisms that regulate RNA polymerase II transcription in vivo. *Nature* **461**, 186-192, doi:10.1038/nature08449 (2009).
- 21 Marushige, K. Activation of chromatin by acetylation of histone side chains. *Proc Natl Acad Sci U S A* **73**, 3937-3941 (1976).
- 22 Owen, D. J. *et al.* The structural basis for the recognition of acetylated histone H4 by the bromodomain of histone acetyltransferase gcn5p. *EMBO J* **19**, 6141-6149, doi:10.1093/emboj/19.22.6141 (2000).
- 23 Filippakopoulos, P. *et al.* Histone recognition and large-scale structural analysis of the human bromodomain family. *Cell* **149**, 214-231, doi:10.1016/j.cell.2012.02.013 (2012).
- 24 Zhang, W. *et al.* Bromodomain-containing protein 4 (BRD4) regulates RNA polymerase II serine 2 phosphorylation in human CD4⁺ T cells. *J Biol Chem* **287**, 43137-43155, doi:10.1074/jbc.M112.413047 (2012).
- 25 Bisgrove, D. A., Mahmoudi, T., Henklein, P. & Verdin, E. Conserved P-TEFb-interacting domain of BRD4 inhibits HIV transcription. *Proc Natl Acad Sci U S A* **104**, 13690-13695, doi:10.1073/pnas.0705053104 (2007).
- 26 Yang, Z., He, N. & Zhou, Q. Brd4 recruits P-TEFb to chromosomes at late mitosis to promote G1 gene expression and cell cycle progression. *Molecular and cellular biology* **28**, 967-976, doi:10.1128/MCB.01020-07 (2008).
- 27 Dey, A., Chitsaz, F., Abbasi, A., Misteli, T. & Ozato, K. The double bromodomain protein Brd4 binds to acetylated chromatin during interphase and mitosis. *Proceedings of the National Academy of Sciences of the United States of America* **100**, 8758-8763, doi:10.1073/pnas.1433065100 (2003).
- 28 Zhao, R., Nakamura, T., Fu, Y., Lazar, Z. & Spector, D. L. Gene bookmarking accelerates the kinetics of post-mitotic transcriptional re-activation. *Nat Cell Biol* **13**, 1295-1304, doi:10.1038/ncb2341 (2011).
- 29 Dawson, M. A. *et al.* Inhibition of BET recruitment to chromatin as an effective treatment for MLL-fusion leukaemia. *Nature* **478**, 529-533, doi:10.1038/nature10509 (2011).
- 30 Delmore, J. E. *et al.* BET Bromodomain Inhibition as a Therapeutic Strategy to Target c-Myc. *Cell* **146**, 904-917, doi:S0092-8674(11)00943-3 [pii] 10.1016/j.cell.2011.08.017 (2011).
- 31 Zuber, J. *et al.* RNAi screen identifies Brd4 as a therapeutic target in acute myeloid leukaemia. *Nature* **478**, 524-528, doi:10.1038/nature10334 (2011).
- 32 Mertz, J. A. *et al.* Targeting MYC dependence in cancer by inhibiting BET bromodomains. *Proceedings of the National Academy of Sciences of the United States of America* **108**, 16669-16674, doi:1108190108 [pii] 10.1073/pnas.1108190108 (2011).

- 33 Ott, C. J. *et al.* BET bromodomain inhibition targets both c-Myc and IL7R in high-risk acute lymphoblastic leukemia. *Blood* **120**, 2843-2852, doi:10.1182/blood-2012-02-413021 (2012).
- 34 Greenwald, R. J. *et al.* E mu-BRD2 transgenic mice develop B-cell lymphoma and leukemia. *Blood* **103**, 1475-1484, doi:10.1182/blood-2003-06-2116
2003-06-2116 [pii] (2004).
- 35 Filippakopoulos, P. *et al.* Selective inhibition of BET bromodomains. *Nature* **468**, 1067-1073, doi:10.1038/nature09504 (2010).
- 36 Miyoshi, S., Ooike, S., Iwata, K., Hikawa, H. & Sugaraha, K. Antitumor agent. **International Patent No. PCT/JP2008/073864 (WO/2009/084693)** (2009).
- 37 Nicodeme, E. *et al.* Suppression of inflammation by a synthetic histone mimic. *Nature* **468**, 1119-1123, doi:Doi 10.1038/Nature09589 (2010).
- 38 Bartholomeeusen, K., Xiang, Y., Fujinaga, K. & Peterlin, B. M. Bromodomain and Extra-terminal (BET) Bromodomain Inhibition Activate Transcription via Transient Release of Positive Transcription Elongation Factor b (P-TEFb) from 7SK Small Nuclear Ribonucleoprotein. *The Journal of biological chemistry* **287**, 36609-36616, doi:M112.410746 [pii]
10.1074/jbc.M112.410746 (2012).
- 39 Puissant, A. *et al.* Targeting MYCN in neuroblastoma by BET bromodomain inhibition. *Cancer discovery* **3**, 308-323, doi:10.1158/2159-8290.CD-12-0418 (2013).
- 40 Schneider, C. A., Rasband, W. S. & Eliceiri, K. W. NIH Image to ImageJ: 25 years of image analysis. *Nature methods* **9**, 671-675 (2012).
- 41 Yang, Z. *et al.* Recruitment of P-TEFb for stimulation of transcriptional elongation by the bromodomain protein Brd4. *Molecular cell* **19**, 535-545, doi:10.1016/j.molcel.2005.06.029 (2005).
- 42 Teitell, M. A. OCA-B regulation of B-cell development and function. *Trends in immunology* **24**, 546-553 (2003).
- 43 Wang, H. *et al.* IRF8 regulates B-cell lineage specification, commitment, and differentiation. *Blood* **112**, 4028-4038, doi:10.1182/blood-2008-01-129049 (2008).
- 44 Nutt, S. L., Taubenheim, N., Hasbold, J., Corcoran, L. M. & Hodgkin, P. D. The genetic network controlling plasma cell differentiation. *Seminars in immunology* **23**, 341-349, doi:10.1016/j.smim.2011.08.010 (2011).
- 45 Ye, B. H. *et al.* The BCL-6 proto-oncogene controls germinal-centre formation and Th2-type inflammation. *Nat Genet* **16**, 161-170, doi:10.1038/ng0697-161 (1997).
- 46 Cobaleda, C., Schebesta, A., Delogu, A. & Busslinger, M. Pax5: the guardian of B cell identity and function. *Nat Immunol* **8**, 463-470, doi:10.1038/ni1454 (2007).
- 47 Greiner, A. *et al.* Up-regulation of BOB.1/OBF.1 expression in normal germinal center B cells and germinal center-derived lymphomas. *Am J Pathol* **156**, 501-507, doi:10.1016/S0002-9440(10)64754-2 (2000).
- 48 Polo, J. M. *et al.* Transcriptional signature with differential expression of BCL6 target genes accurately identifies BCL6-dependent diffuse large B cell lymphomas. *Proc Natl Acad Sci U S A* **104**, 3207-3212, doi:10.1073/pnas.0611399104 (2007).
- 49 Ramachandrareddy, H. *et al.* BCL6 promoter interacts with far upstream sequences with greatly enhanced activating histone modifications in germinal center B cells. *Proc Natl Acad Sci U S A* **107**, 11930-11935, doi:10.1073/pnas.1004962107 (2010).

- 50 Wright, G. *et al.* A gene expression-based method to diagnose clinically distinct subgroups of diffuse large B cell lymphoma. *Proceedings of the National Academy of Sciences* **100**, 9991-9996 (2003).
- 51 Ngo, V. N. *et al.* Oncogenically active MYD88 mutations in human lymphoma. *Nature* **470**, 115-119, doi:nature09671 [pii] 10.1038/nature09671 (2011).
- 52 Peng, J. *et al.* Brd2 is a TBP-associated protein and recruits TBP into E2F-1 transcriptional complex in response to serum stimulation. *Molecular and cellular biochemistry* **294**, 45-54, doi:10.1007/s11010-006-9223-6 (2007).
- 53 Sinha, A., Faller, D. V. & Denis, G. V. Bromodomain analysis of Brd2-dependent transcriptional activation of cyclin A. *The Biochemical journal* **387**, 257-269, doi:10.1042/BJ20041793 (2005).
- 54 Luo, Y. & Roeder, R. G. Cloning, functional characterization, and mechanism of action of the B-cell-specific transcriptional coactivator OCA-B. *Molecular and cellular biology* **15**, 4115-4124 (1995).
- 55 Qin, X. F., Reichlin, A., Luo, Y., Roeder, R. G. & Nussenzweig, M. C. OCA-B integrates B cell antigen receptor-, CD40L- and IL 4-mediated signals for the germinal center pathway of B cell development. *The EMBO journal* **17**, 5066-5075, doi:10.1093/emboj/17.17.5066 (1998).
- 56 Kim, U. *et al.* The B-cell-specific transcription coactivator OCA-B/OBF-1/Bob-1 is essential for normal production of immunoglobulin isotypes. *Nature* **383**, 542-547, doi:10.1038/383542a0 (1996).
- 57 Irizarry, R. A. *et al.* Exploration, normalization, and summaries of high density oligonucleotide array probe level data. *Biostatistics* **4**, 249-264, doi:10.1093/biostatistics/4.2.249 4/2/249 [pii] (2003).
- 58 Dai, M. *et al.* Evolving gene/transcript definitions significantly alter the interpretation of GeneChip data. *Nucleic acids research* **33**, e175, doi:33/20/e175 [pii] 10.1093/nar/gni179 (2005).
- 59 Gould, J., Getz, G., Monti, S., Reich, M. & Mesirov, J. P. Comparative gene marker selection suite. *Bioinformatics* **22**, 1924-1925, doi:btl196 [pii] 10.1093/bioinformatics/btl196 (2006).
- 60 Subramanian, A. *et al.* Gene set enrichment analysis: a knowledge-based approach for interpreting genome-wide expression profiles. *Proceedings of the National Academy of Sciences of the United States of America* **102**, 15545-15550, doi:10.1073/pnas.0506580102 (2005).
- 61 Brune, V. *et al.* Origin and pathogenesis of nodular lymphocyte-predominant Hodgkin lymphoma as revealed by global gene expression analysis. *J Exp Med* **205**, 2251-2268, doi:10.1084/jem.20080809 (2008).
- 62 Reich, M. *et al.* GenePattern 2.0. *Nat Genet* **38**, 500-501, doi:10.1038/ng0506-500 (2006).
- 63 Rahl, P. B. *et al.* c-Myc regulates transcriptional pause release. *Cell* **141**, 432-445, doi:10.1016/j.cell.2010.03.030 (2010).
- 64 Pruitt, K. D., Tatusova, T. & Maglott, D. R. NCBI reference sequences (RefSeq): a curated non-redundant sequence database of genomes, transcripts and proteins. *Nucleic acids research* **35**, D61-65, doi:gkl842 [pii]

- 10.1093/nar/gkl842 (2007).
- 65 Langmead, B., Trapnell, C., Pop, M. & Salzberg, S. L. Ultrafast and memory-efficient alignment of short DNA sequences to the human genome. *Genome biology* **10**, R25, doi:10.1186/gb-2009-10-3-r25 gb-2009-10-3-r25 [pii] (2009).
- 66 Lin, C. Y. *et al.* Transcriptional amplification in tumor cells with elevated c-Myc. *Cell* **151**, 56-67, doi:10.1016/j.cell.2012.08.026 (2012).
- 67 Zhang, Y. *et al.* Model-based analysis of ChIP-Seq (MACS). *Genome Biol* **9**, R137, doi:10.1186/gb-2008-9-9-r137 (2008).
- 68 Guenther, M. G., Levine, S. S., Boyer, L. A., Jaenisch, R. & Young, R. A. A chromatin landmark and transcription initiation at most promoters in human cells. *Cell* **130**, 77-88, doi:S0092-8674(07)00681-2 [pii] 10.1016/j.cell.2007.05.042 (2007).
- 69 Creyghton, M. P. *et al.* Histone H3K27ac separates active from poised enhancers and predicts developmental state. *Proc Natl Acad Sci U S A* **107**, 21931-21936, doi:10.1073/pnas.1016071107 1016071107 [pii] (2010).
- 70 Rada-Iglesias, A. *et al.* A unique chromatin signature uncovers early developmental enhancers in humans. *Nature* **470**, 279-283, doi:10.1038/nature09692 nature09692 [pii] (2011).
- 71 Whyte, W. A. *et al.* Master transcription factors and mediator establish super-enhancers at key cell identity genes. *Cell* **153**, 307-319, doi:10.1016/j.cell.2013.03.035 (2013).
- 72 Whyte, W. A. *et al.* Enhancer decommissioning by LSD1 during embryonic stem cell differentiation. *Nature* **482**, 221-225, doi:10.1038/nature10805 nature10805 [pii] (2012).
- 73 Ong, C. T. & Corces, V. G. Enhancer function: new insights into the regulation of tissue-specific gene expression. *Nat Rev Genet* **12**, 283-293, doi:10.1038/nrg2957 nrg2957 [pii] (2011).
- 74 Takahashi, K. *et al.* Induction of pluripotent stem cells from adult human fibroblasts by defined factors. *Cell* **131**, 861-872, doi:10.1016/j.cell.2007.11.019 (2007).